TAL TECH

DOCTORAL THESIS

Design and Modeling of Contoured Airgap Topology for Additively Manufactured Electrical Machines

Muhammad Usman Naseer

TALLINNA TEHNIKAÜLIKOOL
TALLINN UNIVERSITY OF TECHNOLOGY
TALLINN 2025

TALLINN UNIVERSITY OF TECHNOLOGY
DOCTORAL THESIS
32/2025

Design and Modeling of Contoured Airgap Topology for Additively Manufactured Electrical Machines

MUHAMMAD USMAN NASEER

TAL TECH PRESS

TALLINN UNIVERSITY OF TECHNOLOGY
School of Engineering
Department of Electrical Power Engineering and Mechatronics
This dissertation was accepted for the defence of the degree 29/04/2025

Supervisor: Prof. Ants Kallaste
Department of Electrical Power Engineering and Mechatronics,
School of Engineering,
Tallinn University of Technology,
Tallinn, Estonia

Co-supervisor: Dr. Toomas Vaimann
Department of ELectrical Power Engineering and Mechatronics,
School of Engineering,
Tallinn University of Technology,
Tallinn, Estonia

Opponents: Prof. David A. Lowther
Department of Electrical and Computer Engineering,
McGill University
Montreal, QC, Canada

Prof. Avo Reinap
Division for Industrial Electrical Engineering and Automation,
LUND University,
Lund, Sweden

Defence of the thesis: 09/06/2025, Tallinn

Declaration:
Hereby I declare that this doctoral thesis, my original investigation and achievement, submitted for the doctoral degree at Tallinn University of Technology has not been submitted for doctoral or equivalent academic degree.

Muhammad Usman Naseer

---
signature

European Union
European Regional
Development Fund

Investing
in your future

Copyright: Muhammad Usman Naseer, 2025
ISSN 2585-6898 (publication)
ISBN 978-9916-80-301-1 (publication)
ISSN 2585-6901 (PDF)
ISBN 978-9916-80-302-8 (PDF)
DOI https://doi.org/10.23658/taltech.32/2025

Naseer, M. U. (2025). *Design and Modeling of Contoured Airgap Topology for Additively Manufactured Electrical Machines* [TalTech Press]. https://doi.org/10.23658/taltech.32/2025

TALLINNA TEHNIKAÜLIKOOL
DOKTORITÖÖ
32/2025

Kõverdatud õhupilu topoloogiaga kihtlisandusmeetodil valmistatud elektrimasinate projekteerimine ja modelleerimine

MUHAMMAD USMAN NASEER

TAL TECH
KIRJASTUS

Contents

List of Publications 7
Author's Contribution to the Publications 8
Introduction 9
1.1 Limitations of Conventional Manufacturing 9
1.2 Opportunities Introduced by Additive Manufacturing 10
1.3 Definition of the Research Problem 12
1.4 Hypotheses 13
1.5 Research Tasks 13
1.6 Contributions of the Thesis 14
1.6.1 Scientific Novelties 14
1.6.2 Practical Novelties 14
1.7 Thesis Layout 15
Abbreviations 16
2 Theoretical Foundations of Contoured Airgap Topology in Electrical Machines 17
2.1 Fundamentals of Torque Production in Electrical Machines 17
2.1.1 Airgap Reluctance and its Influence on Torque Production 18
2.2 Contoured Airgap Topology for Improved Performance Parameters 19
2.2.1 Methodology 20
2.2.2 Design and Analysis of the Benchmark Electromagnetic Circuit 23
2.2.3 Comparative Analysis of Contoured Airgap Topologies 25
3 Implementation of Contoured Airgap Topology in Rotating Electrical Machines 31
3.1 Machine Selection Considerations 31
3.1.1 Flux Orientation, Radial Versus Axial 31
3.1.2 Machine Type consideration 33
3.1.3 Proposed Path Forward 33
3.2 Methodology 33
3.3 Implementation of Contoured Airgap in Axial Flux SRM 36
3.3.1 Integration and Evaluation of Sinusoidal Airgap Contour 38
3.3.2 Practical Validation through Static Torque Measurements 41
3.4 Implementation of Contoured Airgap in Radial Flux SynRM 48
3.4.1 Implementation and Evaluation of Airgap contour 50
3.5 Conclusion 51
4 Modified Winding Function Analysis for Iterative Design Process Optimization 56
4.1 State-of-the-art and Fundamental Principles Of MWFA 57
4.1.1 Inductance Calculation 58
4.1.2 Turn Function and Winding Function 59
4.1.3 Airgap Permeance Function 60
4.1.4 Rotor Flux-Barrier Translation 61
4.1.5 Torque Calculation 61
4.1.6 Results And Analysis 62
4.1.7 Characteristics of MWFA 65
4.2 Incorporation of Core Material's Electromagnetic Characteristics 66
4.2.1 The Proposed Strategy 66
4.2.2 Determination of Machine Core's Operating Point on the BH-Curve 67

4.2.3 Results and Validation 70
4.3 Incorporation of Three-Dimensional Design Features 74
4.3.1 The Proposed Strategy 74
4.3.2 Formulation for Contoured Airgap Topology 75
4.3.3 Formulation for Slot Skewing 81
5 Conclusions and Future Work 89
5.1 Future Works 90
References 92
Acknowledgements 97
Abstract 98
Lühikokkuvõte 99
Author's Publications 101
Curriculum vitae 229
Elulookirjeldus 230

List of Publications

The list of author's publications, based on which the thesis has been prepared:

I M. U. Naseer, A. Kallaste, B. Asad, T. Vaimann, and A. Rassõlkin, "A Review on Additive Manufacturing Possibilities for Electrical Machines," Energies, vol. 14, no. 7, p. 1940, Mar. 2021, doi: 10.3390/en14071940.

II M. U. Naseer, A. Kallaste, and T. Vaimann, "A method for contouring an airgap profile in an electromagnetic device," Estonian Patent Office, P202500004, 2025.

III M. U. Naseer, A. Kallaste, T. Vaimann, and B. Asad, "Curved Airgap Topology: A Promising Strategy for Enhancing Axial- Flux Machine Performance Metrics," in 25th International Conference on the Computation of Electromagnetic Fields, Naples, Italy: IEEE, Jun. 2025

IV M. U. Naseer, A. Kallaste, B. Asad, T. Vaimann, and A. Rassõlkin, "Design Procedure and Preliminary Analysis for the Introduction of Axial Asymmetry in the Synchronous Reluctance Machines," Proceedings - 2023 IEEE Workshop on Electrical Machines Design, Control and Diagnosis, WEMDCD 2023, 2023, doi: 10.1109/WEMDCD55819.2023.10110903.

V M. U. Naseer, A. Kallaste, B. Asad, T. Vaimann, and A. Rassõlkin, "Modified Initial Design Procedure for Synchronous Reluctance Motor," in ICEM 2022 XXV International Conference on Electrical Machines, 2022.

VI M. U. Naseer, A. Kallaste, B. Asad, T. Vaimann, and A. Rassolkin, "Analytical modelling of synchronous reluctance motor including non-linear magnetic condition," IET Electr Power Appl, Jan. 2022, doi: 10.1049/ELP2.12172.

VII M. U. Naseer, A. Kallaste, B. Asad, T. Vaimann, and A. Rassolkin, "Modified Winding Function Analysis of Synchronous Reluctance Motor for Design Iteration Purposes," IEEE Trans Magn, pp. 1–1, 2022, doi: 10.1109/TMAG.2022.3164189.

VIII B. Asad, T. Vaimann, A. Belahcen, A. Kallaste, A. Rassõlkin, H. V. Khang, P. S. Ghahfarokhi, M. U. Naseer, and M. N. Iqbal, "The Modeling and Investigation of Slot Skews and Supply Imbalance on the Development of Principal Slotting Harmonics in Squirrel Cage Induction Machines," IEEE Access, vol. 9, pp. 165932–165946, 2021, doi: 10.1109/ACCESS.2021.3134331.

Author's Contribution to the Publications

Contribution to the papers in this thesis are:

I M. U. Naseer is the primary author of this article. He conducted the literature review on the state-of-the-art in AM techniques and possibilities for electrical machines, structured the content, and wrote the initial draft.

II M. U. Naseer is the lead inventor. He originated the concept, developed the mathematical formulation, and prepared the technical documentation for patent submission.

III M. U. Naseer is the primary author. He performed analytical and numerical modeling, validated the concept through simulations, and prepared the conference paper and presentation.

IV M. U. Naseer is the primary author. He proposed the asymmetric design concept, developed the automated design and analysis algorithms, performed FEA modeling to assess the correlations of interplay of various design variables against performance gains.

V M. U. Naseer developed and implemented the modified design procedure, performed simulations, and wrote the initial draft.

VI M. U. Naseer extended MWFA to account for nonlinear magnetic conditions and validated it against FEA. He is the lead author of the paper.

VII M. U. Naseer enhanced MWFA for iterative design application, formulated the hybrid FEA-analytical approach, and led the writing of the article.

VIII M. U. Naseer contributed to development of segmented approach for MWFA modeling, formulated the mathematical expressions for incorporation of slot skew in analytical modeling and reviewed the manuscript for technical consistency.

Introduction

With increasing global energy demands, system-level energy utilization and sustainability become critical. Electrical machines utilize around 53% of electric consumption globally [1] owing to their widespread use for a vast range of applications in modern industry and all the aspects of everyday life [2], [3], [4]. Consequently, enhancing their performance parameters such as torque densities and efficiencies, is critical to overall energy and material utilization from their production stage to operational utilization. This translates into the need for paradigm shift towards compact, efficient, and application-specific electrical machines.

Historically, the design of electrical machines has been significantly limited by conventional manufacturing methods, mainly involving laminated steel sheets [5]. Although effective for mass production, these traditional methods inherently restrict designs to planar, two-dimensional geometries, severely limiting electromagnetic optimization possibilities. As a result, decades of research have focused on improvements within this restricted design space such as winding layouts [6], [7], material enhancements [8], [9], and cooling strategies [10], [11]. However, these traditional design optimization possibilities are now approaching saturation, with limited performance gains. The increased demand for improved performance parameters and the limitations on design optimization possibilities originating from the conventional manufacturing techniques necessitates a fundamental shift towards the utilization of advanced manufacturing techniques such as additive manufacturing (AM).

1.1 Limitations of Conventional Manufacturing

Conventional electrical machine manufacturing, primarily based on stacking stamped or laser-cut laminated steel sheets, has long imposed limitations on structure and evolution of machine design. Consequently, all electromagnetic and structural features, such as slot shapes, winding configurations, or components for thermal management, must conform to two-dimensional planar constraints. This approach has general implications on design flexibility for improved performance parameters of all types of electrical machines [12], [13]. Whereas the applications requiring special-purpose geometrical structures with integrated-functionalities are particularly impacted by this limiting approach.

Advanced fields such as robotics, biomedical devices, aerospace, and wearable technologies can benefit the most from complex customized geometries with integrated design features. Achieving such geometries through conventional manufacturing often requires custom-tooling, segmented assemblies and extensive post-processing. This makes their production economically less viable when also considering the low-volume production demand of such machines [9], [14], [15], [16].

In contrast, additive manufacturing (AM) eliminates many of these constraints, enabling the direct realization of complex and three-dimensional geometries. This unlocks new opportunities for improved performance through electromagnetic design innovation and supports rapid, application-specific machine development, something conventional techniques inherently struggle to achieve.

1.2 Opportunities Introduced by Additive Manufacturing

Additive manufacturing, especially metal-AM techniques such as Laser Powder Bed Fusion (LPBF), Directed Energy Deposition (DED), and Binder Jetting, offers an innovative shift in how electrical machines can be designed and built [17], [18], [19], [20], [21]. Unlike traditional subtractive methods, AM fabricates components layer-by-layer, enabling complex, three-dimensional geometries that were previously unfeasible [13], [22], [23], [24].

For electrical machines, this opens the door to novel electromagnetic design possibilities beyond the limitations of 2D-planar laminations. Design features like non-uniform airgaps, axial slot modulation, integrated cooling channels, spatial windings, and embedded structural elements can now be implemented directly, without segmentation or separate assembly [6], [7], [9], [25]. This geometric freedom not only enhances performance but also allows true application-specific customization, including robotics, aerospace, biomedical devices, and autonomous systems. Additionally, AM enables the integration of multiple functionalities into single parts – reducing parasitic losses, part count, cost and assembly complexity [11], [12], [16], [18], [24], [26], [27], [28], [29], [30]. Its digital nature supports rapid prototyping and iterative development, ideal for low-volume, high-performance designs.

AM allows tailored material distributions, functionally graded regions, and even localized magnetic property control through build orientation or thermal gradients. These capabilities support performance tuning within a single part, something conventional processes cannot offer [31], [32].

Despite these advantages, the full potential of AM in electromagnetic design remains underexplored. Most of the research emphasizes isolated part-wise structural or thermal improvements, with limited focus on exploiting 3D topological freedom for fundamental electromagnetic enhancement [5], [33], [34]. To bridge this gap and allow high performance parameters for AM enabled machines, innovations in design and computational tools-capable of efficiently modeling and optimizing AM-enabled features are essential.

Table-I presents a brief comparison between AM and conventional manufacturing methods based on factors such as material composition, production nature, and the capacity of fabricating complicated structures.

Table-I. Comparison of characteristics and capabilities of Conventional Manufacturing Techniques and AM [5].

S. No	Traditional manufacturing method	Additive manufacturing method	Ref.
1	Employ subtractive methods or material removal such as machining and milling, leading to considerable negative environmental impacts, material waste which may lead to higher cost production.	In AM, an object is created by sequentially depositing and consolidating layers of material, which lead to $(35-80\%)$ reduced material utilization and convenient low-cost production.	[16], [18], [35]
2	Traditional EM manufacturing may be constrained by material composition. Incorporating novel materials composition with enhanced electrical and magnetic properties into traditional production method can pose challenges.	AM offers the opportunity to integrate materials at different scales, it becomes possible to customize the properties of components, such as thermal, magnetic, electrical, mechanical, and multifunctional.	[36], [37], [38], [39]
3	Fabrication of the required winding shape/profile with the capability of reduced losses and thermally stable behavior is quite complex and challenging using conventional manufacturing methods.	The utilization of metal AM has the capacity to revolutionize traditional winding design by eliminating limitations on conductor shapes, configurations, and integrated thermal mechanisms.	[40], [41], [42].
4	The conventionally laminated structure of an EM was essential and favorable due to low eddy current losses, but its basic limitation is its anisotropic property of magnetic flux. Creating complex structure by joining lamination and attaining the required structure is challenging or perhaps not possible.	With the help of AM technology, it is now possible to create a ferromagnetic core that allows the flow of magnetic flux in 3D. SMC core materials also enable 3D magnetic flux flow, however hysteresis loss, low permeability, and reduced mechanical strength are the main issues.	[8], [39], [43], [44], [45]
5	The EMs with intricate flux path and mechanical structure complexity such as axial flux machine, transverse flux machine, claw pole machines, spherical machine and tubular linear actuator are significantly constrained by limitations imposed by traditional manufacturing techniques.	AM constructs a 3D object by layering material and has gained significant attention and acceptance in various fields. This is mostly owing to its capability to produce intricate components that would be extremely challenging or perhaps unattainable using traditional manufacturing techniques.	[45], [46], [47], [48], [49]
6	Structural design with multiple functionalities integrated with individual machine part can offer improved performance parameters. Conventional manufacturing techniques have the limitation of producing an integrated structure for an EM, due to their structural complexity and proper material consideration.	By utilizing AM, it is possible to integrate internal features into components, allowing for enhanced thermal management and improved overall performance. Accomplishing this task using conventional approaches can be quite difficult or even unattainable.	[7], [9], [14], [40]

1.3 Definition of the Research Problem

While AM has demonstrated clear advantages in structural integration, thermal management, and part consolidation for electrical machines, its full potential in electromagnetic design remains largely unexploited [7], [50], [51]. Most existing efforts focus on adapting traditional topologies to AM rather than leveraging AM to redefine them. Specifically, the opportunity to expand electromagnetic design into the third dimension – enabled by AM – has received limited attention. Concepts like contoured airgaps or 3D flux-paths have been proposed, but few studies systematically explore their impact on key performance indicators such as torque density, efficiency, or flux linkage.

A second critical gap lies in the design process itself. While 3D finite-element-analysis (FEA) tools can simulate complex geometries, their high computational cost makes them impractical for iterative design - especially in the AM context, where production is most suitable for low-volume and application-specific needs. Analytical methods, though faster, typically cannot handle nonlinear material properties or 3D design features like contoured airgaps, limiting their utility for modern machine design.

Despite the significant potential of additive manufacturing to enhance the design and performance of electrical machines, the research gaps identified as follows, limit its broader integration into electromagnetic design and production processes.

1. **Three-dimensional Design Topologies**: The current state-of-the-art in AM of electrical machines demonstrates significant efforts and potential for performance parameter enhancement through different aspects of its integration in machine design and production process. These aspects include improved electromagnetic characteristics of the materials, improved thermal management solutions, structural topology optimization and integrated functionalities. Through very limited research, the current literature also suggests the potential of expanding the electromagnetic design space to 3D [52], [53]. Yet, there is a lack of research into the fundamental electromagnetic design innovation and its validation.
2. **Computationally Efficient Iterative Design Process**: While conventional numerical methods like FEA very well handle the complex 3D geometries, they require extensive computational resources, limiting the rapid, iterative design processes essential for low-volume production of application-specific electrical machines through AM. This dependence on numerical models is further imposed by the lower accuracy, inability to incorporate magnetic material characteristics and three-dimensional design features, of current state-of-the-art in analytical modeling techniques.

In the context of stated facts about electromagnetic design and modeling for AM-enabled electrical machines, the research problem converges on investigation of improved electromagnetic performance parameters of electrical machines through the utilization of three-dimensional design space, and to improve the computational efficiency of the iterative design process for incorporation of non-linear material characteristics and the three-dimensional design features.

1.4 Hypotheses

This thesis addresses the research gaps identified in the problem statement, through the following proposed hypotheses:

1. Contoured airgap topology enabled by additive manufacturing enhances the electromagnetic performance of electrical machines.
2. The hybrid FEA-Analytical approach reduces computational time and complexity in the machine design analysis, thereby enhancing its suitability for iterative design process.
3. Enhancing MWFA through segmented machine geometry improves its ability to handle 3-dimensional design features, such as contoured airgap topology and skewed machine structures.

1.5 Research Tasks

To prove the hypotheses put-forward in this thesis, a series of targeted research tasks were defined. These tasks are designed to investigate and verify the viability of AM-enabled three-dimensional contoured airgap topology, for enhanced electromagnetic performance of electrical machines. The other tasks relate to the improving the computational efficiency of the iterative design process through enhanced analytical modeling approach for precise modeling of machine performance across various regions of core material's permeability and the integration of complex three-dimensional design features. The specific research tasks are outlined as follows:

1. Formulation of geometric equations to enable the introduction of various contour shapes into the airgap structure of electrical machines.
2. Development of an airgap contouring strategy for effective implementation within the airgap structure of electrical machines.
3. Implementation of planar and contoured airgap topologies in a simple benchmark magnetic circuit, to demonstrate and theoretically validate the comparative flux linkage improvements offered by contoured topology, along with the design implications for optimal shape selection and contour sizing.
4. Implementation of selected contoured airgap topology in case-study electrical machines and optimizing the contour amplitude against performance gains using numerical modeling.
5. Validation of performance gains from contoured airgap topology through practical measurements.
6. Enhancing modified-winding-function-analysis based analytical model to incorporate the electromagnetic characteristics of the machine's core material into its performance estimation process.
7. Validation and benchmarking the computational performance of the enhanced analytical model against numerical modeling.
8. Extending the modified-winding-function-analysis, to incorporate three-dimensional design features such as contoured airgap topology and slot skewing and validate its performance against numerical modeling.

1.6 Contributions of the Thesis

1.6.1 Scientific Novelties

1. Design innovation for the electromagnetic performance enhancement of electrical machines through the development of a contoured airgap topology.
2. Methodology for effective contour implementation in airgap structures of electrical machines.
3. Simplifying the multi-objective problem of contour amplitude optimization through its iterative refinement methodology against the performance gains at selected operating points of electrical machine.
4. Enhanced torque density of electrical machines, for space-constrained applications through contoured airgap topology.
5. Support for diverse machine types and flux topologies, due to the fundamental nature of the design innovations introduced.
6. Enhanced accuracy of modified-winding-function-analysis achieved by introducing a hybrid FEA-analytical approach to incorporate core material's non-linear characteristics in the performance estimation of electrical machines, in a computationally efficient manner.
7. Extension of modified-winding-function-analysis's state-of-the-art, to incorporate three-dimensional design features, enabling skewed slots and contoured airgaps to be accurately represented in an analytical model.

1.6.2 Practical Novelties

1. Development of an automated design, implementation, and analysis tool that enables characterization of contoured airgap topologies and significantly streamlines the design iteration process.
2. Practical adaptation of the contoured airgap strategy in radial-flux synchronous reluctance and axial-flux switched reluctance machines, assessing torque and efficiency improvements via comprehensive numerical modeling.
3. Fast and accurate design capability provided through refined analytical and hybrid methods, which expedite the design iteration process over traditional, numerically intensive workflows.
4. Enabling synthetic data generation for AI-based training and optimization that enhances the learning and predictive accuracy of machine learning models, particularly in data-scarce scenarios.
5. Seamless integration from CAD software to 3D printers, facilitating modern-era industrial production with rapid design-to-manufacturing transitions.
6. Bridging the gap between theoretical design and practical implementation with the fabrication of contoured airgap surfaces using metal additive manufacturing.
7. Integration of contoured rotor/stator sections with standard machine components while maintaining compatibility with conventional windings, bearings, and couplings.

1.7 Thesis Layout

The thesis structure is as follows:

- **Chapter 2** describes the fundamental electromagnetics behind torque production, the role of airgap reluctance, and the basic equations for the proposed methodology of reducing the airgap reluctance.
- **Chapter 3** outlines how the proposed method is applied to both radial-flux SynRM and axial-flux SRM. Describes the design constraints, iterative amplitude sweeps, initial FEA results and practical validation of the concept.
- **Chapter 4** details the enhancements made to MWFA, including the incorporation of material's non-linear magnetic characteristics and segmentation for 3D topologies.
- **Chapter 5** summarizes key findings and suggests directions for further research.

Abbreviations

AM	Additive Manufacturing
LPBF	Laser Powder Bed Fusion
DED	Directed Energy Deposition
FEA	Finite Element Analysis
SRM	Switched Reluctance Motor
SynRM	Synchronous Reluctance Motor
WFA	Winding Function Analysis
MWFA	Modified Winding Function Analysis
MMF	Magnetomotive Force
MTPA	Maximum Torque per-Ampere
CAD	Computer-Aided-Design

2 Theoretical Foundations of Contoured Airgap Topology in Electrical Machines

2.1 Fundamentals of Torque Production in Electrical Machines

Torque production in electromechanical systems can be fundamentally explained by the basic physical phenomena such as the Lorentz force on current-carrying elements or the interaction of magnetic fields with the dipoles in the magnetic material. For practical purposes, analytical approximation techniques serve as the best characterization tools for the force and torque production in complex electromechanical energy conversion systems. These analytical approximations provide simplistic mathematical relations but don't include factors such as magnetic non-linearity. However, the results of such analytical relations can, if necessary, be corrected through semi-empirical methods. The most effective and widely utilized analytical techniques for estimating the force or torque production of an electromechanical system with reasonable engineering accuracy are tangential stress analysis and, the energy and co-energy analyses.

Considering the radial flux topology in electrical machines, as illustrated in Figure. 2.1, the analytical expression for the determination of torque T production through tangential strass analysis [54] is as follows.

$$T = \sigma_{tan}\, r_r\, S_r \tag{2.1}$$

$$\sigma_{tan} = A_s\, B_n \tag{2.2}$$

where σ_{tan} is the tangential stress acting on the rotor surface area S_r with a moment arm of r_r. A_s and B_n represent the average values of linear current density and normal flux density in the airgap, respectively. Substituting the expression of tangential stress in (2.1) and re-arranging yields

$$T = r_r\, A_s\, \phi \tag{2.3}$$

where $\phi = B_n\, S_r$ represents the average airgap flux. The analytical expression of (2.3) dictates the interpretation that the torque production is directly proportional to the magnitude of flux available in the airgap for a fixed value of linear current density and the machine's main geometrical parameters.

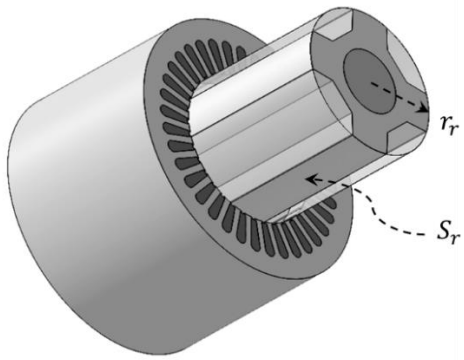


Figure 2.1. Illustration for machine structure for radial flux topology in electrical machines.

2.1.1 Airgap Reluctance and its Influence on Torque Production

Having established previously that the extent of torque production in an electromechanical system depends strongly on the magnetic flux in the airgap, following discussion describes the impact of airgap geometry on the flux production in a magnetic circuit. Consider the simple magnetic circuit with its core having a planar airgap topology, which is uniform in the third dimension, as shown in Figure 2.2. Provided that the airgap thickness is sufficiently small, the two series components of the circuit illustrated in Figure 2.2 i.e. the core with mean length l_c and cross-sectional area A_c, and the airgap with the thickness l_g and cross-sectional area A_g can be considered to carry the same flux.

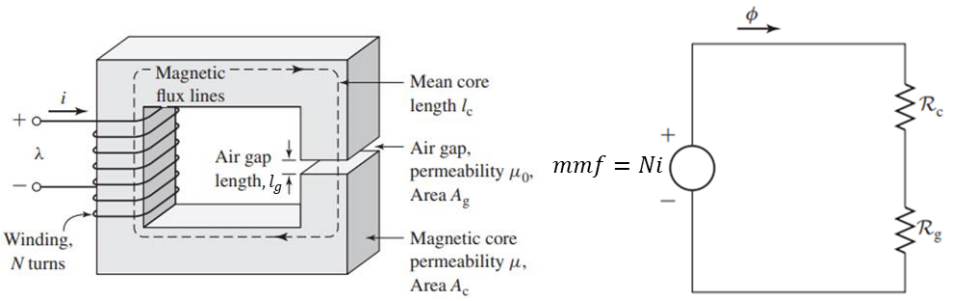


Figure 2.2. Magnetic circuit with planar airgap topology and its equivalent circuit representation [55].

Considering the linear magnetic permeability, the relation between magnetomotive force ($mmf = Ni$) and magnetic flux is given by,

$$mmf = \phi\,(\mathcal{R}_c + \mathcal{R}_g) \tag{2.4}$$

The reluctance of core $\mathcal{R}_c$ and airgap $\mathcal{R}_g$ are calculated as follows,

$$\mathcal{R}_c = \frac{l_c}{\mu\, A_c} \tag{2.5}$$

$$\mathcal{R}_g = \frac{l_g}{\mu_o\, A_g} \tag{2.6}$$

where $\mu = \mu_o\, \mu_r$ is the permeability of the core material ($\mu_r \gg 1$ for ferromagnetic materials and $\mu_r \approx 1$ for air). With the higher magnetic permeability and consequently very low reluctance of the core material, the airgap reluctance dominates and the total mmf drop can be approximated only across the airgap. Reducing the airgap reluctance has a direct impact on the electromagnetic performance of the machine, i.e. a lower airgap reluctance increases the total flux leading to higher flux linkage and consequently, higher torque production.

The dominance of airgap reluctance has an important implication, small geometric changes to the airgap (its thickness or cross-sectional area) can yield significantly large impacts on the flux, inductance, and consequently the torque production. For conventional electromagnetic designs, reducing the airgap reluctance is often attempted by decreasing the airgap thickness l_g or increasing its surface area A_g through increase in dimensions of the core components forming the airgap. However, these strategies come with practical

engineering constraints such as mechanical clearances, thermal expansion allowances, and the risk of underutilizing core material i.e., pushing the machine's flux density to a less optimal region on the $B - H$ curve. These constraints emphasize the importance of carefully managing the airgap to ensure it becomes neither so small as to compromise mechanical reliability nor so large that overall flux weakens significantly. Hence, any innovative approach aiming to improve torque density, particularly in advanced or high-performance rotating machines, must focus on ways to reduce the effective airgap reluctance without incurring impractical mechanical or material disadvantages. In the subsequent sections, a novel contoured airgap topology for increasing the effective surface area of the airgap (and thereby reducing its reluctance) is presented, while maintaining the same normal gap thickness and major machine dimensions.

2.2 Contoured Airgap Topology for Improved Performance Parameters

It is evident from the previous discussion that the airgap in electrical machines is crucial to their overall performance, particularly in terms of torque production capability and efficiency. While decreasing the airgap thickness reduces magnetic reluctance and increases flux linkage λ, mechanical and thermal limitations often dictate how thin the airgap can realistically be. Thermal expansion, manufacturing tolerances, and certain electromagnetic design considerations (such as mitigating surface eddy currents) all necessitate a minimum feasible airgap thickness.

Traditionally, to reduce airgap reluctance without altering its thickness, the dimensions of the airgap-facing components need to be increased. This approach, however, leads to an overall increase in the machine's size and volume, resulting in lower torque or power density, a critical drawback in modern-day applications where space and weight are of extreme importance.

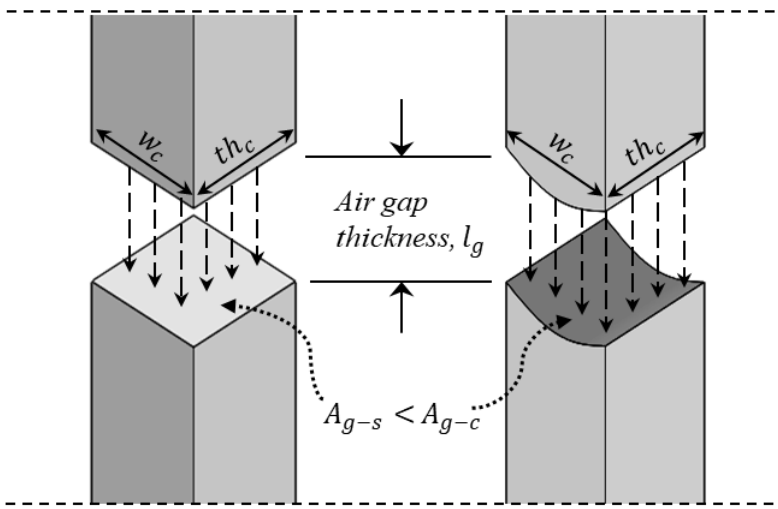


Figure 2.3. Ai gap in the magnetic core: conventional and contoured airgap topology.

To address these limitations, the proposed strategy introduces a novel approach, i.e. contouring the airgap facing surfaces to increase the effective airgap surface area without changing the machine's main dimensions or the airgap thickness itself. As illustrated in Figure 2.3, this approach maintains the same core dimensions and the

airgap thickness, yet the surface area of the contoured airgap is higher than the straight (planar) topology. By modifying the geometry of the airgap surfaces, while maintaining the required mechanical clearance, the magnetic path reluctance can be reduced. This reduction enhances flux linkage and torque production, leading to improved performance parameters such as higher torque or power density. The following subsections will address the theoretical validation of the concept by comparing the electromagnetic performance indicator, i.e. flux linkage of various contoured airgap topologies with a benchmark magnetic circuit having planar airgap topology.

2.2.1 Methodology

2.2.1.1 Contour Shape Definition and Implementation Strategy

Several geometric profiles can be employed to contour the airgap surfaces. The scope of the current work spans three primary contouring profiles: triangular, circular, and sinusoidal. The selection of these specific shapes is made considering their mathematically constrained implementation on airgap structures of the machine and subsequent ability to analytically correlate the performance parameters enhancements with the geometric equation of the contour. This fact will be later illustrated in Chapter 4 of this thesis when analytical incorporation of contoured airgap topology in MWFA will be presented.

As part of the airgap contouring strategy, a central contour guideline is established at the mid-height of the airgap based on specified geometrical equations that follow. The contour is offset by $l_g/2$ on both sides of the guide-profile, ensuring a consistent normal distance between the offset lines. These offset lines subsequently define the surfaces of the core components adjacent to the airgap. The conditional geometric equations [Publication-II] defining the central airgap contour are as follows and are illustrated in Figure 2.4.

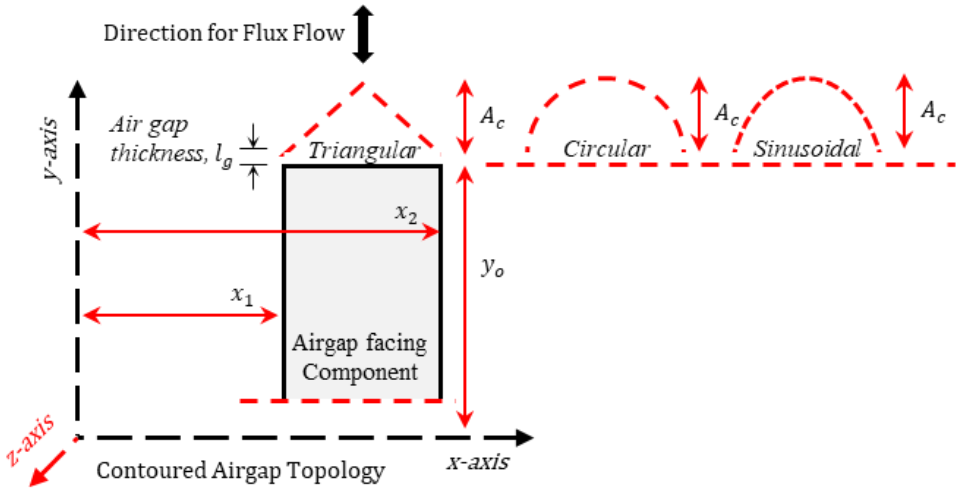


Figure 2.4. Illustration of the central contour defining the airgap.

Triangular airgap contour

$$y = y_o + \frac{l_g}{2} + \frac{2A_c}{(x_2 - x_1)}(x - x_1) \qquad (2.7)$$

$$x_1 < x < \frac{(x_1 + x_2)}{2}$$

$$y = y_o + \frac{l_g}{2} + 2A_c - \frac{2A_c}{(x_2 - x_1)}(x - x_1) \qquad (2.8)$$

$$\frac{(x_1 + x_2)}{2} < x < x_2$$

Circular airgap contour

$$r = \left| \frac{\left(\frac{x_2 - x_1}{2}\right)^2 + {A_c}^2}{2A_c} \right| \qquad (2.9)$$

$$\left(x - \frac{x_1 + x_2}{2}\right)^2 + \left(y - \frac{l_g}{2} + \sqrt{r^2 - \left(\frac{x_1 - x_2}{2}\right)^2} - y_o\right)^2 = r^2 \qquad (2.10)$$

$$for \ 0 < |A_c| < \frac{x_2 - x_1}{2}$$

$$\left(x - \frac{x_1 + x_2}{2}\right)^2 + \left(y - \frac{l_g}{2} - \sqrt{r^2 - \left(\frac{x_1 - x_2}{2}\right)^2} - y_o\right)^2 = r^2 \qquad (2.11)$$

$$for \ \frac{x_2 - x_1}{2} < |A_c| < \frac{y_o}{2}$$

Sinusoidal airgap contour

$$y = y_o + \frac{l_g}{2} + A_c \sin\frac{\pi(x - x_1)}{(x_2 - x_1)} \qquad (2.12)$$

$$0 < A_c < \frac{y_o}{2}$$

where x_1, x_2 and y_o are the dimensions of the airgap-facing components, in the plane perpendicular to the flow of flux, with x_1 being the starting point, x_2 being the endpoint and y_o being the height. A_c is the contour amplitude.

2.2.1.2 Material Properties Consideration

To accurately simulate magnetic performance while isolating the geometric effects of the airgap contours and the effects of material's magnetic characteristics, two different sets of performance analyses with different material characteristics are performed on each airgap geometry, i.e. one with a high but constant relative permeability chosen for the linear magnetic material representing the core. A sensitivity analysis was conducted to determine the optimal value of μ_r that effectively mimics an infinitely permeable material without introducing numerical instability or excessive computational demands. The relative permeability was incrementally increased, and the simulations were repeated for each value. It was observed that beyond a certain threshold, further increases in μ_r resulted in negligible changes in key performance metrics such as flux linkage and magnetic field distribution. At this point, the material is effectively behaving as an ideal magnetic conductor, and the magnetic reluctance of the core becomes insignificant compared to that of the airgap. The final value selected for the relative permeability was $\mu_r = 1 \times 10^7$, as increases beyond this value showed less than 0.002% variation in simulation results. This approach ensures that core material properties do not influence the magnetic circuit's behavior and any performance improvements observed in contoured topologies can be directly attributed to airgap geometry changes rather than material properties variations, ensuring a fair and meaningful comparison and isolating the effect of airgap contouring on key magnetic performance parameter such as flux linkage.

In contrast to the linear magnetic permeability, practical ferromagnetic materials (e.g., M400-50A) exhibit non-linear magnetic characteristics which can also impact the performance gains from the contoured geometry of the airgap-forming circuit components. To systematically investigate such impact of material's non-linear magnetic permeability, a separate set of analysis is conducted on the benchmark and contoured airgap geometry.

2.2.1.3 Numerical Modeling Consideration

FEA is utilized to characterize and validate the performance of magnetic circuits with and without the contouring. Since mesh size is critical for achieving accurate FEA results, especially when modeling geometries with fine features like the contoured airgap profiles. A mesh sensitivity analysis was performed to identify the optimal mesh size that balances computational efficiency with accuracy.

The analysis involves simulating the magnetic circuit with progressively finer mesh sizes. Starting from a coarse mesh, the mesh element size was reduced in steps (e.g., from 1 mm to 0.5 mm, 0.3 mm, and so on), and the resulting flux linkage values were recorded. It was found that mesh sizes larger than 0.3 mm led to noticeable discrepancies in the simulation results due to insufficient resolution of the geometric contours. As the mesh size was reduced to 0.2 mm, the changes in flux-linkage between successive refinements became less than 0.002%, indicating convergence of the solution. A mesh size of 0.2 mm was thus selected as the optimal choice for the current analyses. This provided a high level of accuracy in capturing the detailed geometry of the contoured airgap while maintaining reasonable computation times. Using this mesh size ensured that the simulations accurately reflected the electromagnetic behavior influenced by the airgap contours without any unnecessary computational overhead. This practice of mesh sensitivity analyses is consistently utilized in all the FEA modeling presented in this thesis.

2.2.2 Design and Analysis of the Benchmark Electromagnetic Circuit

2.2.2.1 Description of Benchmark Design

To assess and compare the effectiveness of the contoured airgap topologies, a benchmark magnetic circuit with a conventional straight (planar) airgap topology is established and illustrated in Figure 2.5. This circuit serves as the reference point against which different contoured designs will be compared. The benchmark magnetic circuit consists of a core with a central limb and two outer limbs forming a closed magnetic path. The central limb is equipped with two coils on each side that generate the MMF required for magnetic flux circulation. The airgap is introduced in the central limb. The specific shape of the magnetic circuit is formulated to have a uniformly distributed flux density in the airgap and the immediate core components which formulate the airgap.

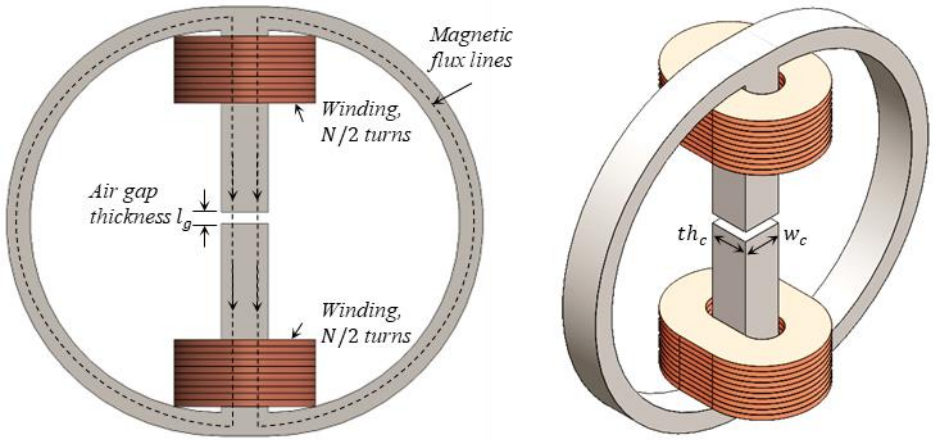


Figure 2.5. Benchmark magnetic circuit with straight (planar) airgap topology.

The design parameters of the benchmark magnetic circuit are selected to ensure the magnetic core operation at specified magnetic conditions. The key parameters are outlined in Table 2.1.

Table 2.1. Design Parameters of the Benchmark Magnetic Circuit.

Parameters	Units	Values
Core Material	-	M400-50A
Core Flux Density	T	1.6
Coil Current (I)	A	6
Airgap Thickness	mm	0.5
Core thickness at central limb (th_c)	mm	5
Core Width at central limb (w_c)	mm	5
Number of Turns in Coil	-	106

2.2.2.2 Analysis Of the Benchmark Design

The flux distribution obtained from the FEA simulation at a coil current of 6 A is shown in Figure 2.6. The results confirm that the core operates at the selected average flux density of 1.6 Tesla for the design-rated current of 6 A. The flux distribution is uniform in the central limb and across the airgap.

The relationship between flux linkage and coil current is plotted in Figure 2.7 (a) and (b) for magnetic material with constant and high relative permeability, and for M400-50A steel with non-linear relative permeability, respectively. In subsequent analyses, these baseline values will be used to quantify the improvements achieved and the performance implications by the contoured airgap topologies.

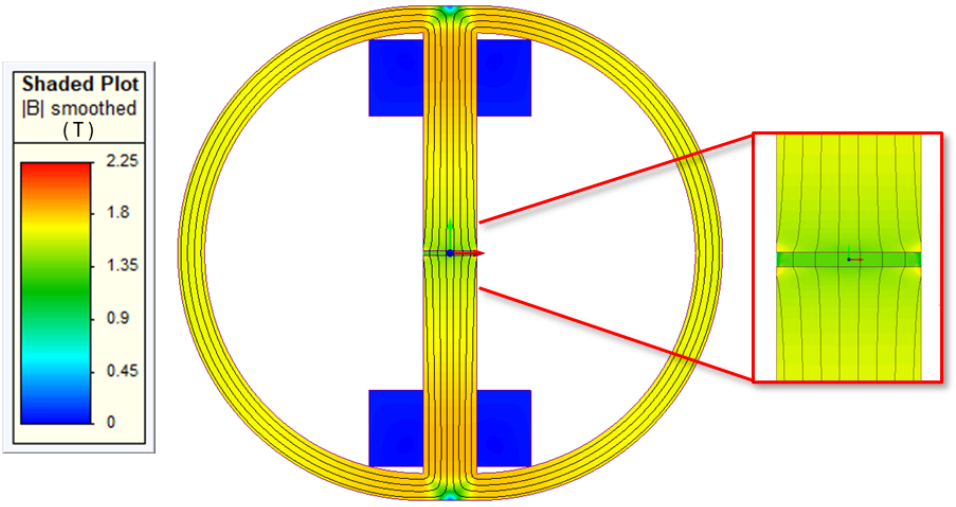


Figure 2.6. Flux Distribution in Benchmark Circuit at I = 6 A.

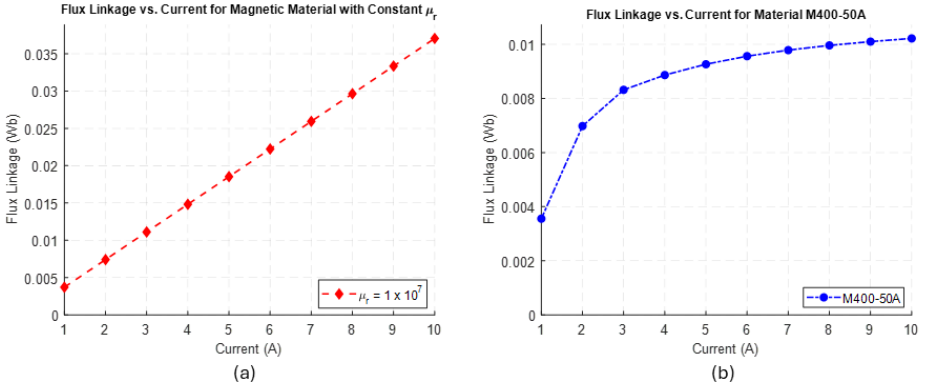


Figure 2.7. Coil flux linkage versus input coil current for (a) core material with constant magnetic permeability, (b) M400-50A core material.

The baseline for comparison, the straight air gap topology with the air gap surface area of 25 mm², produced a steady flux linkage increase with current, ranging from approximately 0.0037 Wb at 1 A to 0.0371 Wb at 10 A. This serves as the reference flux linkage against which all contour designs are compared, enabling direct assessment of each topology's effectiveness in enhancing magnetic performance.

2.2.3 Comparative Analysis of Contoured Airgap Topologies

2.2.3.1 Analysis With Constant Linear Magnetic Permeability

In the first stage of the comparative analysis, the core is assumed to have a high and constant relative permeability (effectively mimicking infinite). By neglecting non-linear magnetic behavior, any observed performance improvements or drawbacks can be attributed directly to geometric factors.

The airgap topologies used for the analysis along with their results for gains in flux linkage versus the input current to the coil, and the increase in per-unit surface area of the airgap for each of the chosen three topologies are presented in Figure 2.8–2.10. The preliminary analysis of the results presented in these figures show specific numerical improvements in flux linkage. This improvement is due to the direct impact of the increase in effective air gap surface area and consequently reduced overall magnetic reluctance.

The further evaluation of presented results enhances the understanding of the impact, that contoured airgap topology has, specifically in terms of flux linkage and the utilization of airgap surface area. The findings highlight both analytical and simulation-based considerations that arise from each topology's specific geometry.

- **Linear Flux Linkage Response to Current:** Across all topologies, flux linkage increases linearly with current, a direct result of using materials with constant magnetic permeability in the analyses. This choice removes saturation effects, simplifying the interpretation by ensuring that any performance variations arise solely from variations in geometry rather than non-linear material behavior. This linear response provides a clear baseline for comparing the impact of different contours.
- **Airgap Surface Area and Magnetic Reluctance:** As expected, contouring the airgap increases its effective surface area, thereby reducing magnetic reluctance and improving flux linkage. The higher surface area correlates with lower reluctance, allowing more magnetic flux production for the same applied MMF, which enhances the flux linkage. For example, the sinusoidal topology with the largest amplitude reaches a flux linkage of 0.0660 Wb at 10 A – an 80% improvement over the straight topology. This pattern reinforces the concept that air gap contouring is an effective strategy for increasing magnetic performance within compact machine designs.
- **Non-Proportional Flux Linkage Gains Relative to Surface Area/ Effect of Localized Core Cross-Section Reductions:** However, the increase in flux linkage is not directly proportional to the increase in air gap surface area, as illustrated in each topology's results, Figure 2.8 (c)–2.10 (c). While theoretical formulations suggest that flux linkage should increase proportionally with surface area (given a constant airgap thickness), FEA results deviate from this ideal due to a key factor: localized increases in core reluctance in the vicinity of the contoured airgap. While the reluctance of the core remains largely unaffected everywhere else and is predominantly very small as compared to the air gap reluctance, in the regions where the air gap is contoured, the cross-sectional area of the core is effectively reduced in the direction of the flux flow. This causes a significant increase in core reluctance (since however high the value of magnetic permeability was set; it is still a finite number having some extent of implications) that partially offsets the expected gains from the enlarged air gap surface area. This is highlighted in Figure 2.11 (a) and (b) and the effect is particularly evident through the higher flux densities in those regions.

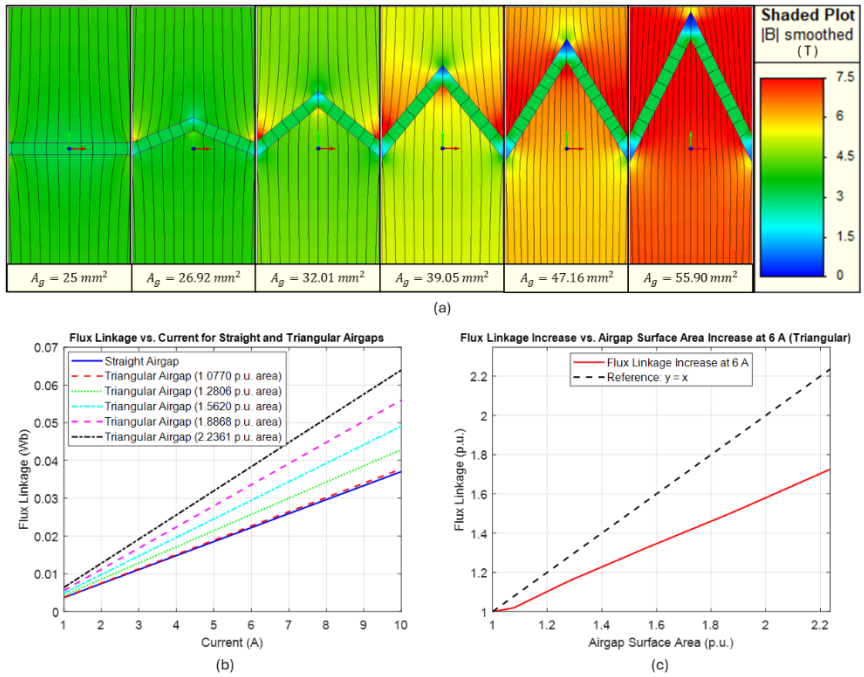


Figure 2.8. FEA results for triangular airgap topology (a) geometry progression and the flux distribution for I = 6 A, (b) flux linkage versus coil current for various airgap surface areas, (c) per-unit flux linkage increase versus the per-unit airgap surface area increase for coil currents of 6 A.

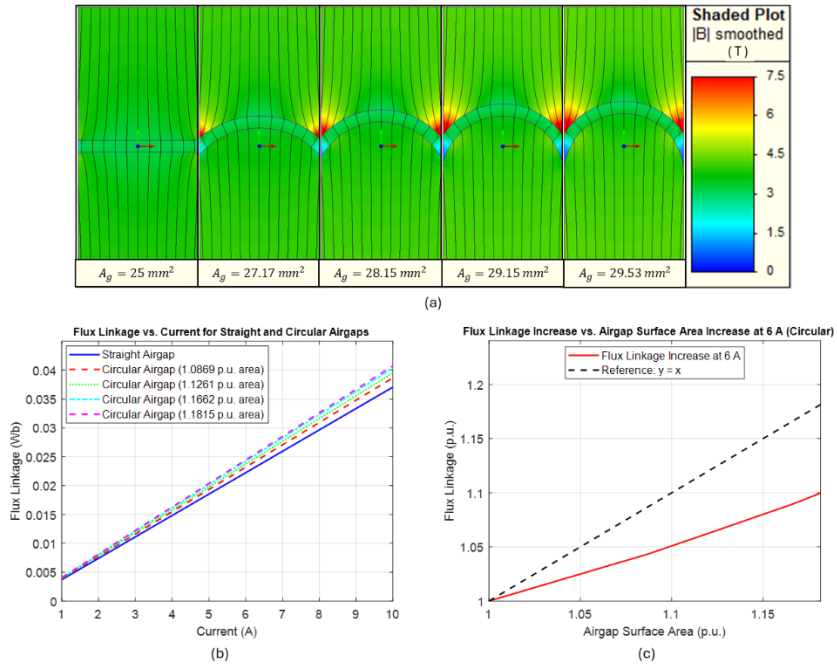


Figure 2.9. FEA results for circular airgap topology (a) geometry progression and the flux distribution for I = 6 A, (b) flux linkage versus coil current for various airgap surface areas, (c) per-unit flux linkage increase versus the per-unit airgap surface area increase for coil currents of 6 A.

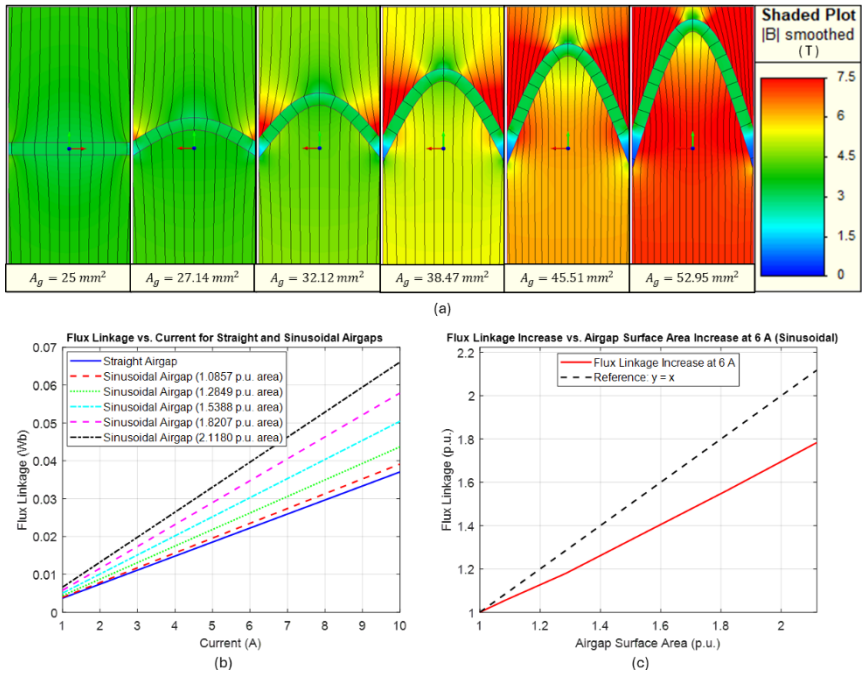


Figure 2.10. FEA results for sinusoidal airgap topology (a) geometry progression and the flux distribution for I = 6 A, (b) flux linkage versus coil current for various airgap surface areas, (c) per-unit flux linkage increase versus the per-unit airgap surface area increase for coil currents of 6 A.

2.2.3.2 Conclusions from Linear Magnetic Permeability Analysis

When the core material is assumed to have constant, high permeability (i.e., no saturation), the contoured airgap topologies consistently demonstrate higher flux linkage than the straight (planar) airgap. However, these improvements are not strictly proportional to the increase in airgap surface area. The following points summarize the key observations:

- **Contour Shape and Amplitude:** Shape (triangular, circular, or sinusoidal) directly influences how much additional surface area is introduced in the airgap. Amplitude controls the magnitude of this increase. Larger amplitudes provide a more substantial boost in airgap surface area – and thus lower the airgap reluctance – but also produce a more significant reduction in the local cross-sections of the core.

As the contour amplitude grows, the adjacent core geometry narrows in the vicinity of the contoured airgap. This localized reduction in core cross-section raises the local reluctance, partially offsetting the gains from the enlarged airgap surface area. Despite the offsetting effect of localized core narrowing, all contoured topologies still outperform the straight airgap baseline under linear assumptions.

The balance between reduced airgap reluctance (via increased surface area) and increased core reluctance (via reduced cross-sections) is contour-dependent, making both shape and amplitude critical design variables.

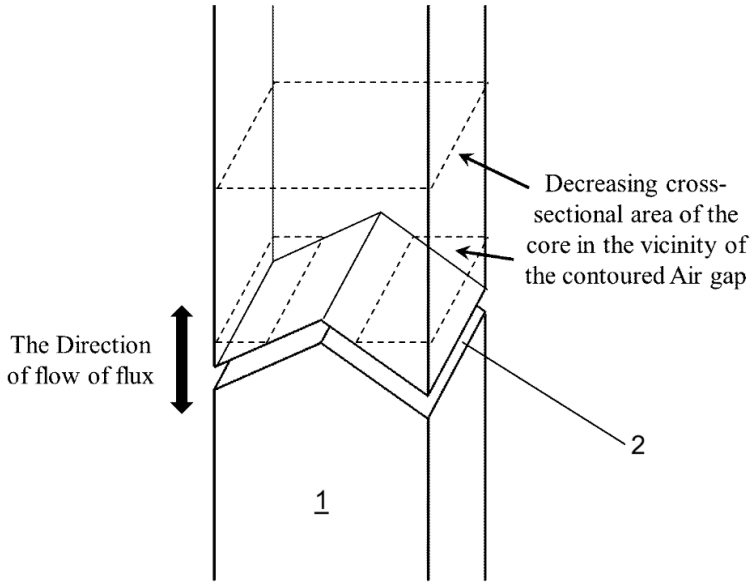


Figure 2.11. (a) Illustration of decreasing cross-sectional area of the core in the vicinity of the triangularly contoured air gap.

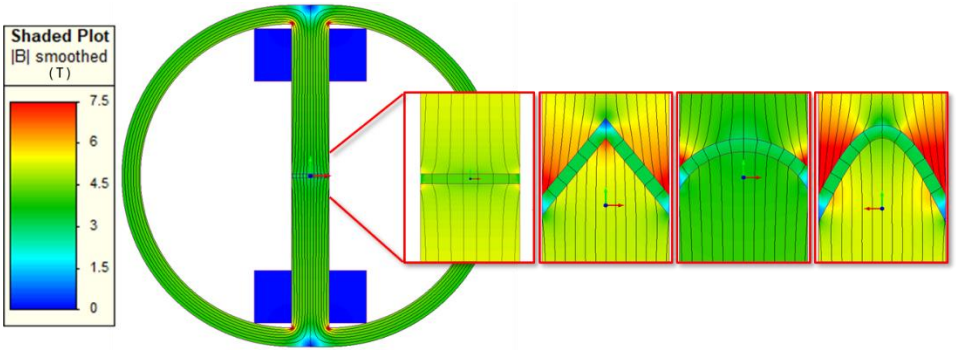


Figure 2.11. (b) Illustration of varying core cross-sections in the vicinity of the contoured air gap and the respective increased flux densities in the core's contoured portions.

2.2.3.3 Analysis with Non-Linear Magnetic Permeability

In contrast to the linear permeability scenario, practical ferromagnetic materials (e.g., M400-50A) exhibit non-linear magnetic characteristics. As the magnetomotive force (mmf) increases, local saturation can arise in the core, especially near regions where the cross-sectional area is reduced by contouring. Consequently, the overall flux linkage gains observed at lower currents may diminish at higher values for input current.

In the second stage of the comparative analysis, practical non-linear magnetic permeability (e.g., M400-50A steel) is introduced, allowing core saturation effects to appear at higher MMF levels. The same set of triangular, circular, and sinusoidal airgap contours are investigated to quantify how material non-linearity modifies each topology's potential gains. The specific flux linkage gains versus the input current to the coil, of various airgap surface areas for each of the chosen three topologies are presented in Figure 2.12–2.14.

The analysis of these results presents additional performance considerations, i.e. the expected proportional increase in flux linkage with the enlarged airgap surface area is further compromised by saturation effects. While analytical expressions might predict a linear relationship between increased surface area and flux linkage (assuming constant airgap thickness), incorporation of material's magnetic characteristics show that as saturation sets in, the incremental gains become progressively smaller. This leads to a marked deviation from the idealized linear behavior. This effect is particularly evident in contoured topologies with higher amplitudes, where the local flux densities exceed the material's linear operating range.

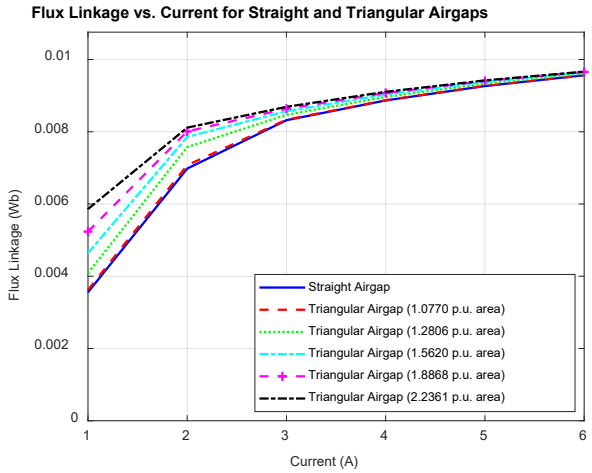


Figure 2.12. FEA results for triangular airgap topology, flux linkage versus coil current for various airgap surface areas.

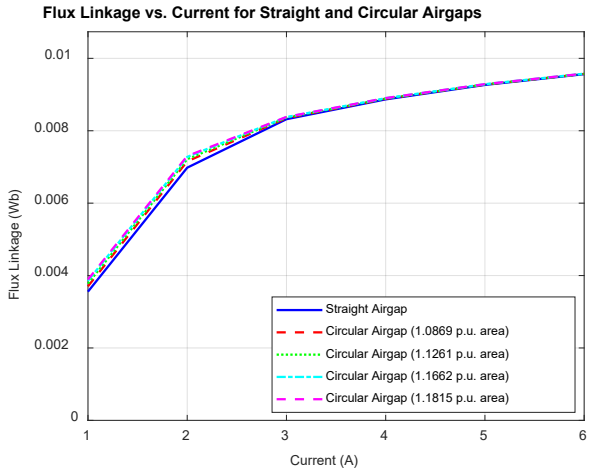


Figure 2.13. FEA results for circular airgap topology, flux linkage versus coil current for various airgap surface areas.

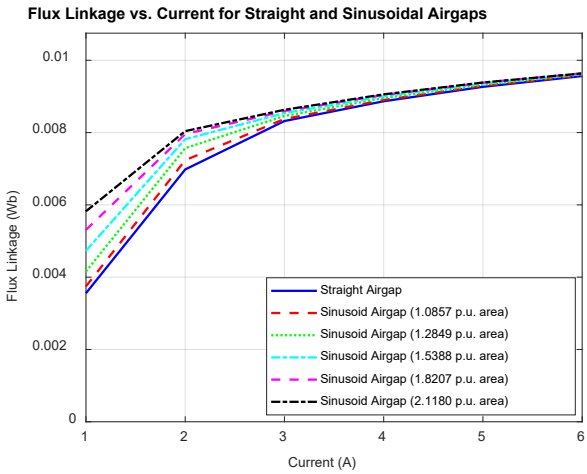


Figure 2.14. FEA results for sinusoidal airgap topology, flux linkage versus coil current for various airgap surface areas.

2.2.3.4 Conclusions from non-linear Magnetic Permeability Analysis

In summary, under non-linear magnetic permeability conditions, the performance benefits of airgap contouring are influenced not only by the contour's shape and amplitude – as was observed with linear materials – but also significantly by the operating point. At moderate currents, contoured topologies continue to outperform the straight airgap baseline; however, at higher currents, localized saturation in the narrowed core regions limits the net gains. This highlights the need for a multi-objective optimization strategy that considers both geometric design and the expected use-case scenarios to maximize overall machine performance.

Additionally, it should be noted that the airgap area adjacent to the contour edges also exhibits a non-uniform flux distribution, affecting the overall flux-linkage gains per-unit contoured airgap area. However, as this characteristic is consistently present across all contour shapes, it has been omitted from the primary comparative analysis.

3 Implementation of Contoured Airgap Topology in Rotating Electrical Machines

From the comparative analysis of results from the previous chapter it is evident that triangular contouring results in a non-uniform flux distribution across the airgap and lowers the flux linkage gains per-unit increase in airgap surface area. This is due to the occurrence of larger normal-airgap thickness at and around the tip of the triangular contour. By contrast, sinusoidal and circular contours produce relatively uniform airgap flux distribution and thus achieve higher flux linkage gains per-unit increase in the airgap surface area.

Among circular and sinusoidal profiles, the circular shape is inherently limited in contour amplitude by its geometric constraints, since the contour amplitude cannot be extended beyond half of the core width. On the other hand, the sinusoidal shape offers greater flexibility in the contour amplitude all the while offering comparatively uniform flux distribution in the airgap.

Having identified the sinusoidal profile as the most feasible airgap contour, the subsequent task is to integrate this concept into a rotating electrical machine design. Depending on the specific operating point of the machine, the varying contour amplitudes can yield different degrees of gains in performance parameters. An evaluation of amplitude sweep is necessary to optimize the reduction in airgap reluctance against potential local reductions in core cross-sectional area and the respective onset of magnetic saturation at specific operating points.

This chapter focuses on integration and subsequent validation of contoured airgap topology into rotating electrical machine designs. The following are the considerations for the selection of machine type, flux orientation (radial or axial) and the methodology for the design implementation and analysis of the case studies.

3.1 Machine Selection Considerations

In principle, every rotating electrical machine could benefit from a contoured airgap, as lower reluctance is universally advantageous. However, practical concerns regarding the latest state-of-the-art in manufacturing technology limit which machine types and flux topology are most suitable for practical validation. In context of primary selection of manufacturing technique, additive manufacturing provides a possibility to produce the 3-dimensional geometry of a contour, but current constraints on multi-material printing influence the choice of both machine type and flux topology.

This section details how these constraints shape the final choice of machine design and flux orientation for implementing (and experimentally validating) the proposed sinusoidal airgap topology in the rotating electrical machines.

3.1.1 Flux Orientation, Radial Versus Axial

A radial flux machine with contoured airgap structures, whether designed with an outer rotor configuration or vice versa, usually demands that one component be split into sections. That is because, in the contoured design for such machine topology, the “barrel-like” shape of the internal component (as shown in Figure 3.1) prevents its direct insertion into the fully fabricated counterpart. If the machine is configured with an outer rotor, the rotor must be segmented so it can be assembled around the stator. Mechanical seams, introduced by joining these rotor pieces, can degrade performance

through small but consequential airgap misalignments and increased reluctance at the seam boundaries. Alternatively, in an outer stator configuration, if the stator is composed of multiple segments and the rotor is kept in one piece, the challenges associated with increased reluctance at the seam boundaries shift to the segmented stator side while also demanding a sacrificed winding configuration.

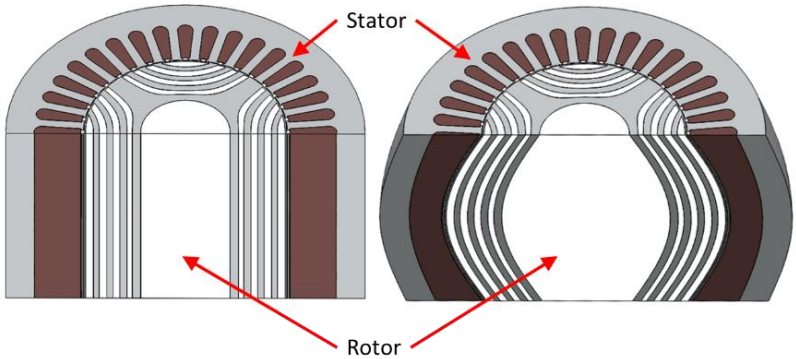


Figure 3.1. Comparative illustration of contoured airgap topology implementation on outer-stator, radial-flux electrical machine.

Axial flux machines are more naturally accommodating to contouring, owing to their nature of disc-like stator and rotor assembly in an axially stacked manner (as shown in Figure 3.2). This means that the machine components can be fabricated in or near their final shape, and there is no need for segmentation that later must be joined. However, the windings are predominantly of the concentrated type leading to a higher degree of ripple in torque/speed profile in comparison with the superior distributed winding configuration of radial flux topology. Nevertheless, in an electrical machine with axial flux topology, the contoured airgap can be achieved without creating segments or mechanical discontinuities that ought to complicate the assembly process and impact the performance parameters significantly. Thus, the axial flux topology is chosen for direct implementation and prototyping.

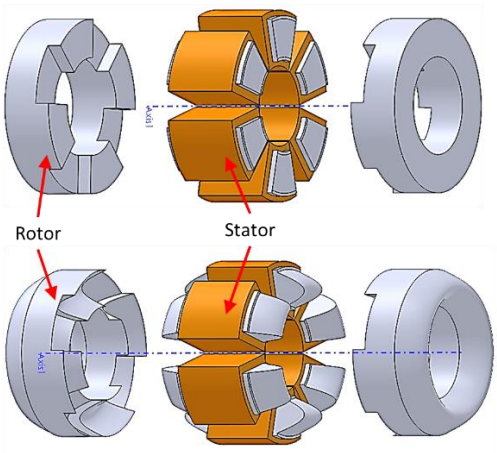


Figure 3.2. Comparative illustration of contoured airgap topology implementation on dual-rotor, axial-flux electrical machine.

3.1.2 Machine Type consideration

Current state-of-the-art in multi-material AM is less suited for designs requiring integrated permanent magnets or specifically different magnetic-electrical materials. Hence, the machines relying solely on reluctance-based torque production (i.e., no magnets or conduction-based rotor cages) naturally fit the available single-material AM approach.

In the category of reluctance machines, although both synchronous reluctance machines (SynRMs) and switched reluctance machines (SRMs) can benefit from reduced magnetic path reluctance, rotor flux barriers for axial flux topology in SynRMs require extensive internal support structures during printing and more extensive postprocessing to remove them. In contrast, SRM rotor typically consists of solid salient pole structure without the complex flux barriers seen in SynRMs and have a more mechanically straightforward rotor construction suited for AM production. Considering these points, an SRM is selected for the actual protype validation. Its rotor geometry avoids multi-material and post-processing issues, and its stator can be printed in a form that accommodates the contoured airgap without complicating the winding design.

Meanwhile, the broad potential of contoured airgaps is still relevant for SynRMs. A radial flux SynRM can be evaluated numerically to illustrate how the airgap contouring concept extends beyond flux orientation and machine type, even if it may require more complex printing and assembly processes to produce physically.

3.1.3 Proposed Path Forward

The axial flux SRM, combining a straightforward single-material rotor and a planar disc assembly, appears as the best candidate for prototyping a sinusoidally contoured airgap. In this arrangement, a systematic sweep of contour amplitudes can be conducted to identify which amplitude level maximizes torque and efficiency under the selected operating conditions.

In parallel, the radial flux SynRM remains valuable for simulation-based analyses, particularly given its commercial relevance in certain drives and industrial applications. By running FEA simulations on a SynRM with a contoured airgap, it becomes possible to demonstrate that the same principles underlying the axial flux prototype hold true in a radial flux setting, although with the previously mentioned assembly complications.

The combination of practical validation on the axial flux SRM and numerical validation on the radial flux SynRM provides convincing evidence of the contoured airgap topology's potential. It also points out how practical manufacturing constraints guide the choice of machine design for any practical implementation. This dual evaluation, through physical prototyping on an axial flux SRM and computational validation on a radial flux SynRM, ensures that the key impacts of airgap contouring can be generalized and adapted for different industrial applications.

3.2 Methodology

Having established the basis for machine type selection and flux orientation, this section provides a generalized framework for the design, simulation, and iteration process utilized for the implementation and analysis of the contoured airgap in the previously mentioned SynRM and SRM machine types. The detailed implementation and results for that specific machine follow in subsequent sections.

The iterative procedure is governed by establishing an OLE-Automation-server within the MATLAB environment, utilizing ActiveX/COM interfaces to control and communicate with geometry developing CAD-tool i.e. SolidWorks and the FEA tools i.e. FEMM, Simcenter MAGNET and JMAG for machine design analysis and iterative optimization. MATLAB provides the initial analytical design calculations, dimensional parameterizations (including stepwise variations of the contour amplitude), and supervisory scripting for the automated control and communication with other involved CAD and FEA software. SOLIDWORKS generates the 3D geometry based on these parameters, enabling exact representation of the contoured airgap in a solid model. The geometry is then imported into a FEA environment to compute electromagnetic performance. Finally, these results are returned to MATLAB for post-processing and comparative analysis. Figures 3.3 and 3.4 present a high-level block diagram and illustration of the methodology utilized for the subsequently presented studies[56], [Publication-III], [Publication-IV].

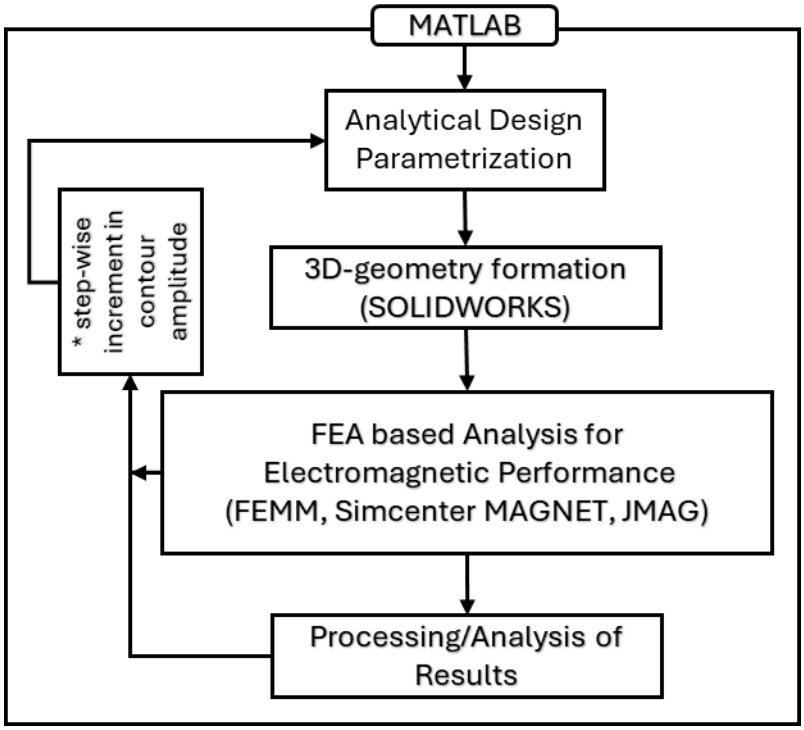


Figure 3.3. Block diagram for implementation of contoured airgap in electrical machines and subsequent analysis.

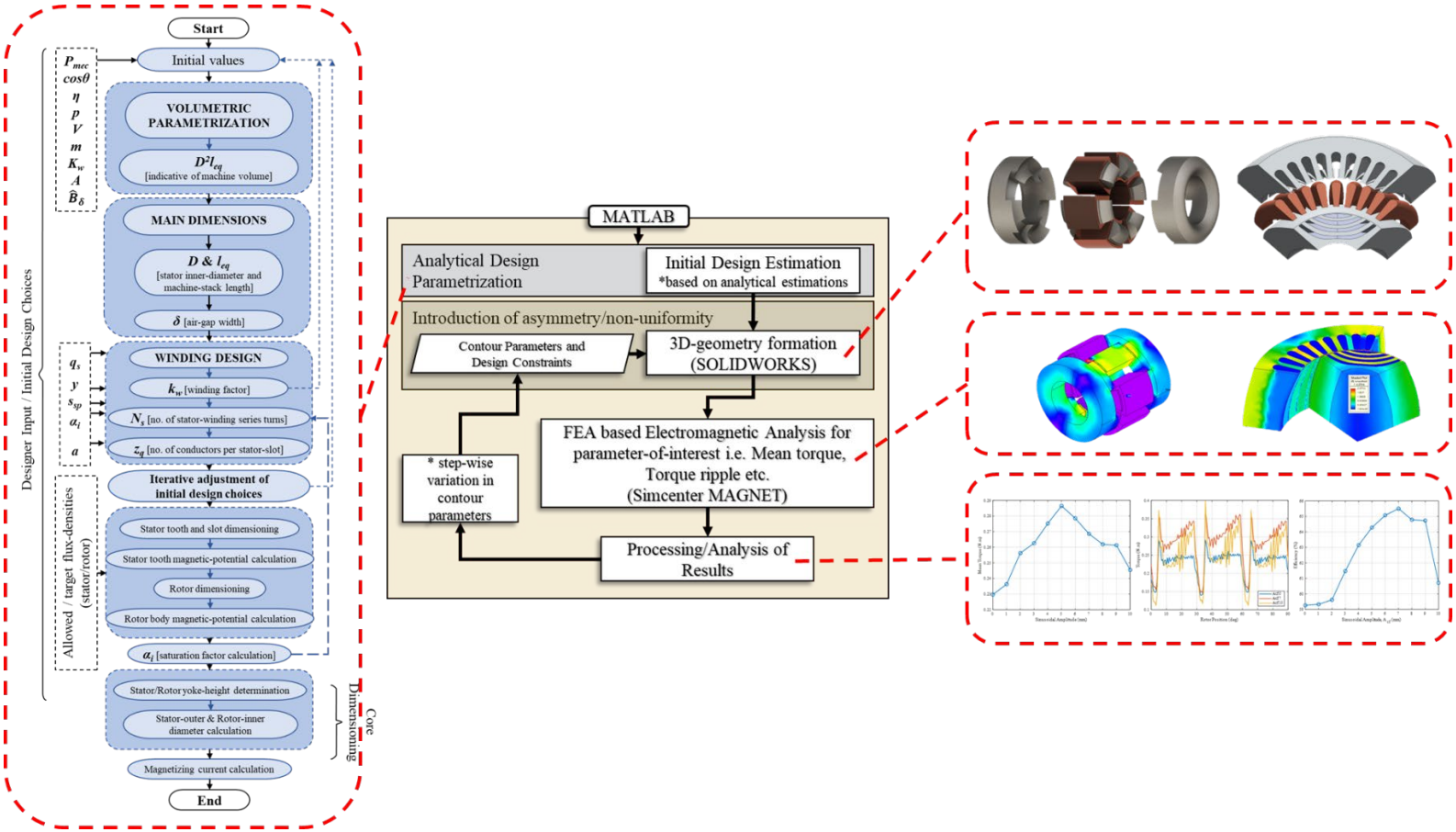


Figure 3.4. Illustration of workflow for contoured airgap implementation and analysis[56], [57], [58].

3.3 Implementation of Contoured Airgap in Axial Flux SRM

The axial-flux SRM design of [59], [60], having a planar airgap topology is considered reference point for this case study [Publication-III]. This reference design provides the geometry and performance characteristics against which the characteristics of implemented contoured airgap topology will be analyzed. Its key design and design parameters are presented in Table 3.1.

Table 3.1. Design Parameters of the Benchmark Axial Flux SRM.

Parameters	**Units**	**Values**
Rated Voltage	V	96
Rated Phase Current (peak)	A	4.03
Rated Speed	rpm	7000
Stator Rotor Pole Ratio	-	6/4
No. of Turns/coil	No.	150
Electric Loading	A/mm	28.485
RMS Current Density	A/mm^2	5
Airgap Length	mm	0.25
Outer Diameter	mm	60
Inner Diameter	mm	33.6
Stator Tooth-width	mm	13.1
Coil Width	mm	3
Stator Tooth Height	mm	13.2
Stator Axial Length	mm	25.3
Rotor Pole Width	mm	19.6
Rotor Pole Height	mm	5
Rotor Back Iron Height	mm	12.3
Phase Resistance	Ω	0.7535

Finite element analysis, conducted under steady-state conditions using tools such as FEMM and Simcenter MAGNET, confirms that the baseline SRM design produces an average torque of approximately 0.23 Nm aligning closely with analytical design estimation. The performance metrics, including load conditions, torque production, and efficiency, are documented to form the reference for subsequent contour amplitude sweeps. Figure 3.5 presents the current and torque profile at rated voltage and speed. Figure 3.6 presents the respective magnetic flux density distribution in the machine parts at the rated current, generated by FEA. At rated parameters, the FEA calculated values for torque production, ripple rate and efficiency are approximately 0.23Nm, 66% and 59% respectively. The output characteristics of benchmark design are also presented in Table 3.2. The ripple rate is calculated by

$$Ripple\ rate = \frac{T_{max} - T_{min}}{T_{avg}} \times 100 \tag{3.1}$$

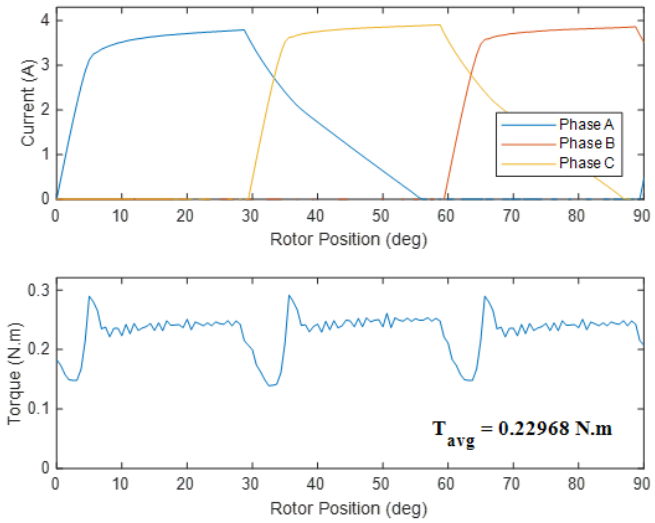


Figure 3.5. Current and torque profile of benchmark machine at rated voltage.

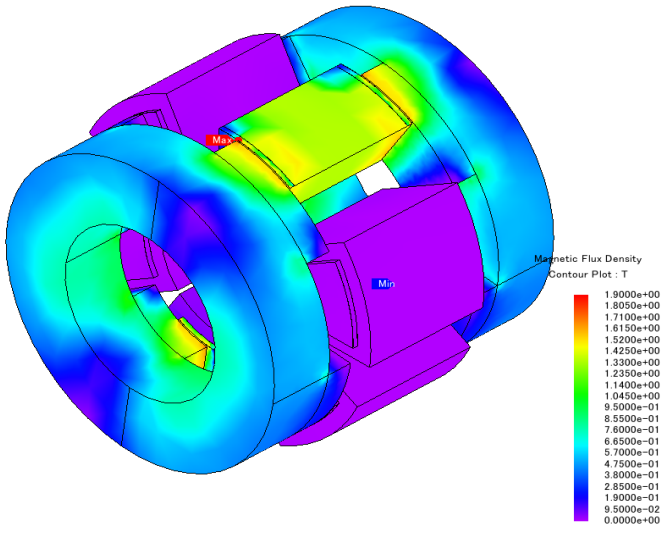


Figure 3.6. Magnetic Flux-Density Distribution in Machine Parts at Rated Current.

Table 3.2. Output Characteristics of Benchmark Axial-flux SRM Design.

Parameters	**Units**	**Values**
Average Torque (T_{av})	Nm	0.229
Torque Ripple Rate (T_{RR})	%	66.27
Torque Density ($T_{density}$)	Nm/kg	0.249
Efficiency	%	59.2

Next subsections will detail how this reference design is modified, simulated iteratively, and ultimately optimized for enhanced torque production and efficiency.

3.3.1 Integration and Evaluation of Sinusoidal Airgap Contour

To enhance the electromagnetic performance of the axial flux SRM, the conventional planar airgap is modified into a sinusoidally contoured profile. This integration aims to increase the effective airgap surface area, reducing the airgap reluctance and consequently increasing the flux linkage, without altering the nominal airgap thickness. The sinusoidal airgap contour is mathematically defined by (2.12). The depiction of increased airgap surface area from implementation of contour is made in Figure 3.7.

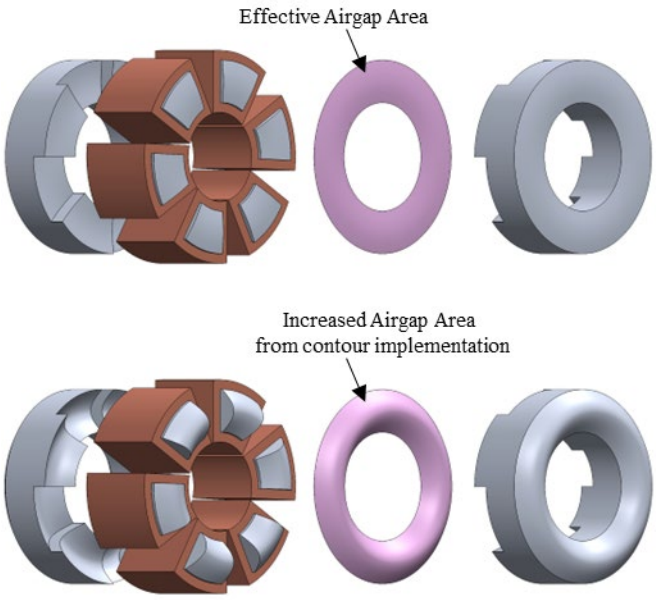


Figure 3.7. Illustration of increased airgap surface area from contour implementation.

During the contour implementation process, specific design constraints are imposed to preserve key parameters associated with the magnetic core. That means as the adjacent stator and rotor pole faces were contoured, the contouring was also translated similarly to other surfaces of the rotor back iron. This constraint is key in preserving the saliency ratio of the rotor. The other parameters such as outer diameter, inner diameter, and winding configuration were kept unchanged.

This case study iteratively implements and analyses varying contour amplitude from 1mm to 10mm in discrete consecutive steps of 1mm. Each contour amplitude is analyzed for key performance indicators – including average torque, torque ripple, flux density distribution, and efficiency – under identical operating conditions.

The generated torque profile as a function of rotor position, for various values of contour amplitude is shown in Figure 3.8. The analysis of the torque profiles shows that from the rotor position of unaligned to aligned, initially, the increase in generated torque for contoured geometry is not very distinct. That is because of the higher local magnetic saturation at sharp teeth edges of rotor poles. This increased local saturation limits the increase in flux linkage and hence the torque production initially but diminishes when rotor-stator poles start aligning with each other.

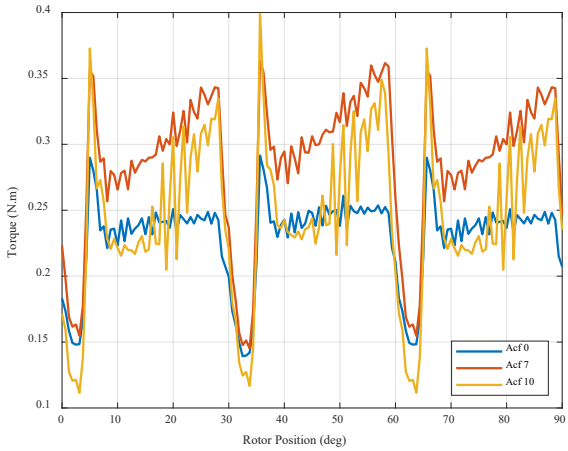


Figure 3.8. Machine's Torque Profile with varying contour amplitude.

The generated mean torque at rated input parameters, as a function of varying contour amplitude is presented in Figure 3.9. Figure 3.10 presents the variation of torque density as a function of contour amplitude. Figures 3.11 and 3.12 present the variation in electromagnetic efficiency and the torque ripple rate as a function of contour amplitude. All the presented results are for rated input parameters, identical to the benchmark design with planar airgap topology. The analysis of the results showcases consistent behavior as to the conclusions drawn from the analyses made in previous chapter. The torque production, torque density and efficiency values demonstrate the effect of decreased airgap reluctance in the form of increasing trend for increasing values of contour amplitude. The reason for the increase in torque density and efficiency is that, with a comparatively smaller increase in stator volume (contoured stator-teeth face), a larger gain in air gap surface area and hence the torque generation occurs. On the other hand, the small volume of added material in the stator core causes only iron losses and these losses are a very small portion of the total losses in the machine, i.e. iron losses and copper losses. That is so until a specific point from where the extent of localized saturation in the vicinity of contoured airgap is ought to dominate the gains from reduced airgap reluctance. After that, with further increase in contour amplitude deteriorates the output performance. The results indicate the increased output performance parameters of the machine at a cost of increased torque ripple rate. This increased torque ripple rate is associated with increased slope of reluctance profile from unaligned to aligned position, i.e. the aligned reluctance is comparatively lower than the benchmark design of planar airgap. For the operating conditions of the current analysis, the presented results indicate the design with contour amplitude of 5mm to be the optimal. The specific performance variation of the selected optimal design in comparison with the benchmark design is presented in Table 3.3.

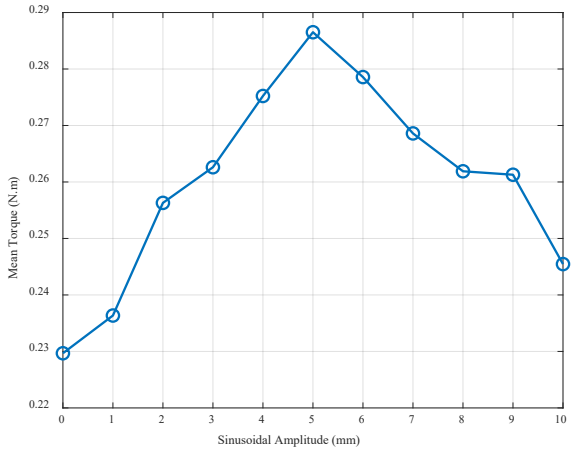


Figure 3.9. Mean torque production of machine at rated voltage, as a function of varying contour amplitude.

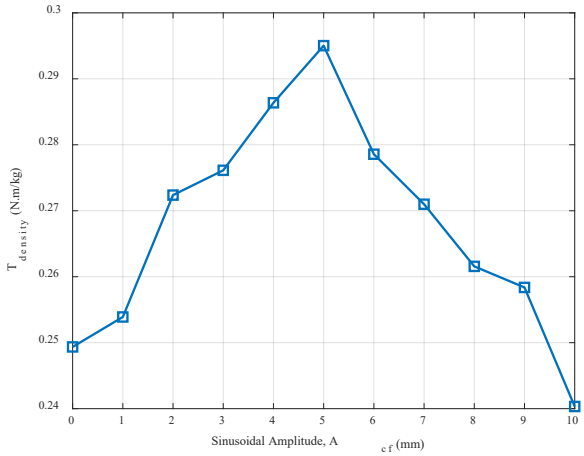


Figure 3.10. Torque density variation as a function of varying contour amplitude.

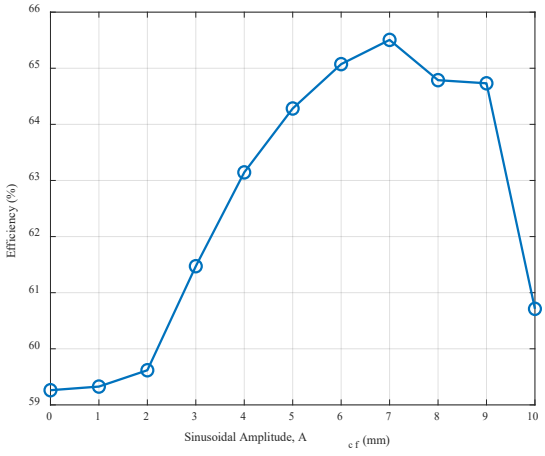


Figure 3.11. Efficiency variation as a function of varying contour amplitude.

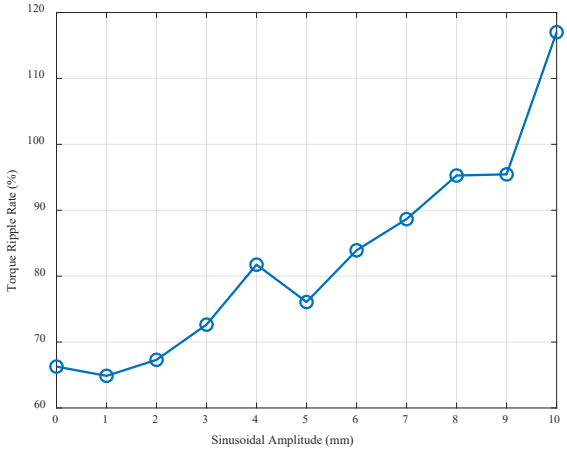


Figure 3.12. Variation in torque ripple rate as a function of varying contour amplitude.

Table 3.3. Output Characteristics of Benchmark and Optimal Design.

Parameters	**Units**	**Benchmark Design**	**Optimal Design**	**Percentage Variation**
Amplitude of the contour (A_{cf})	mm	0	5	-
Average Torque (T_{av})	Nm	0.229	0.286	+ 24.7
Torque Ripple Rate (T_{RR})	%	66.27	76.07	+14.7
Torque Density ($T_{density}$)	Nm/kg	0.249	0.295	+ 18.4
Efficiency	%	59.2	64.2	+ 8.44

3.3.2 Practical Validation through Static Torque Measurements

To practically validate the performance gains from implementing a contoured airgap topology, static torque measurements were performed. This practical validation provided a crucial confirmation of the theoretically and numerically predicted improvements in electromagnetic performance parameters, particularly output torque comparison against the identical input coil current for planar and contoured airgap topology. Simplified and reduced two-pole setup of the benchmark and optimal design from the previous analysis were prototyped to effectively represent and validate the essential characteristics of the contoured airgap configuration.

3.3.2.1 Prototype Design and Manufacturing

A reduced-scale mock-up setup was designed to enable direct comparison between planar (straight) and contoured airgap topologies. This simplified prototype consisted of two stator teeth and two rotors with two poles each, effectively forming a two-pole configuration that adequately represents the airgap geometry and flux paths of a full-scale machine. The design illustrations for the stator-rotor components of the reduced-scale setup are presented in Figure 3.13.

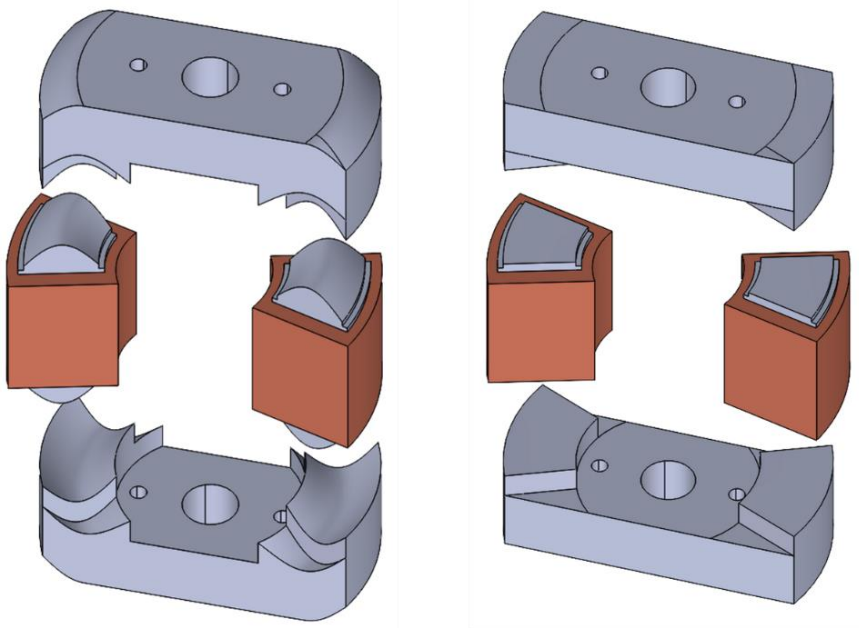


Figure 3.13. Illustration of the stator and rotor components for reduced-scale setup.

These main components, two stator teeth and two rotor structures each, were fabricated using metal-AM. Due to the static nature of the intended torque measurements, solid metallic structures were chosen rather than traditional laminated cores, as the absence of alternating fields eliminates concerns regarding eddy current losses.

The magnetic core components were fabricated with SLM Solutions GmbH Realizer SLM-280 LPBF 3D printer. As illustrated in Figure 3.14 (a), the L-PBF process entails melting thin layers of metal powder with a laser beam. After each layer is scanned, the build platform is lowered, and a fresh powder layer is applied. After printing, the prototype core was cut off from the base plate, cleaned, and annealed. The subsequent thermal treatment for grain recrystallization was conducted in a graphite chamber Webb-107 vacuum furnace. The Fe-Si powder used for the printing process was supplied by the Sandvik Group. It consisted of nearly spherical particles with a median diameter of 38µm (d50). This high-purity powder had a chemical composition of 3.7% silicon, trace elements, and iron.

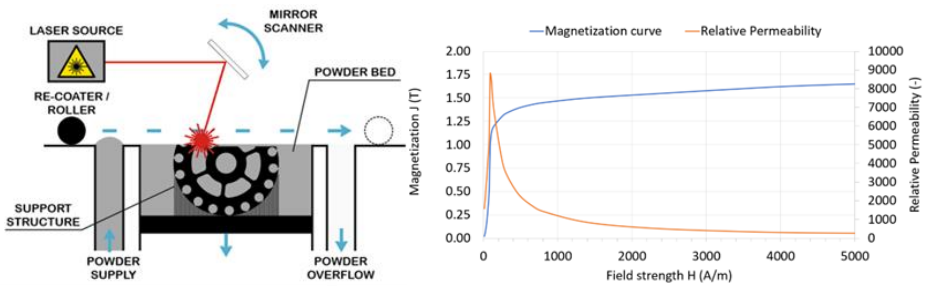


Figure 3.14. Laser powder bed fusion of soft magnetic materials, (a) printing process schematic [30], (b) DC magnetization curve of the printed heat-treated material [61].

The complete workflow on which the processing parameters selection is based upon is outlined in detail in [61], exploring the considerations before, during, and after printing to facilitate the 3D printing of cores with desirable magnetic properties. The empirical DC material magnetization curve used for the numerical simulations is outlined in Figure 3.14 (b). The optimized printing and annealing parameters are summarized in Table 3.4.

Table 3.4. Prototype printing and heat treatment parameters [61].

Printing Parameters	**Units**	**Values**
Laser power	W	350
Scanning velocity	mm/s	750
Energy density	J/mm3	77
Layer thickness	µm	50
Hatch distance	µm	120
Laser spot size	µm	~120
Scan strategy	-	Stripes
Environment	-	Nitrogen
Preheating	-	No
Remelting	-	No
Chamber oxygen	%	~0.1
Annealing Parameters	**Units**	**Values**
Temperature	° C	1200
Hold time	min	60
Heating rate	° C/min	5
Vacuum level	mBar	~0.1

Post-processing steps included careful removal of support structures, surface finishing to achieve the desired airgap accuracy, and manual winding of the stator teeth with insulated copper wire according to the specified winding configuration.

The assembly procedure involved precise alignment of rotor and stator components, ensuring consistent airgap dimensions and mechanical robustness. The assembled prototypes were then mounted on a suitable mechanical fixture to facilitate accurate static torque measurement. Due to practical limitations, the achieved airgap dimensions were 0.5mm instead of the theoretical value of 0.25mm. Figures 3.15 and 3.16 present the workflow of the prototyping and practical measurement process along with the pictorial illustration of the additively manufactured components and the assembled reduced-scale mock-up setup, clearly illustrating both planar and contoured airgap prototypes in the measurement setting.

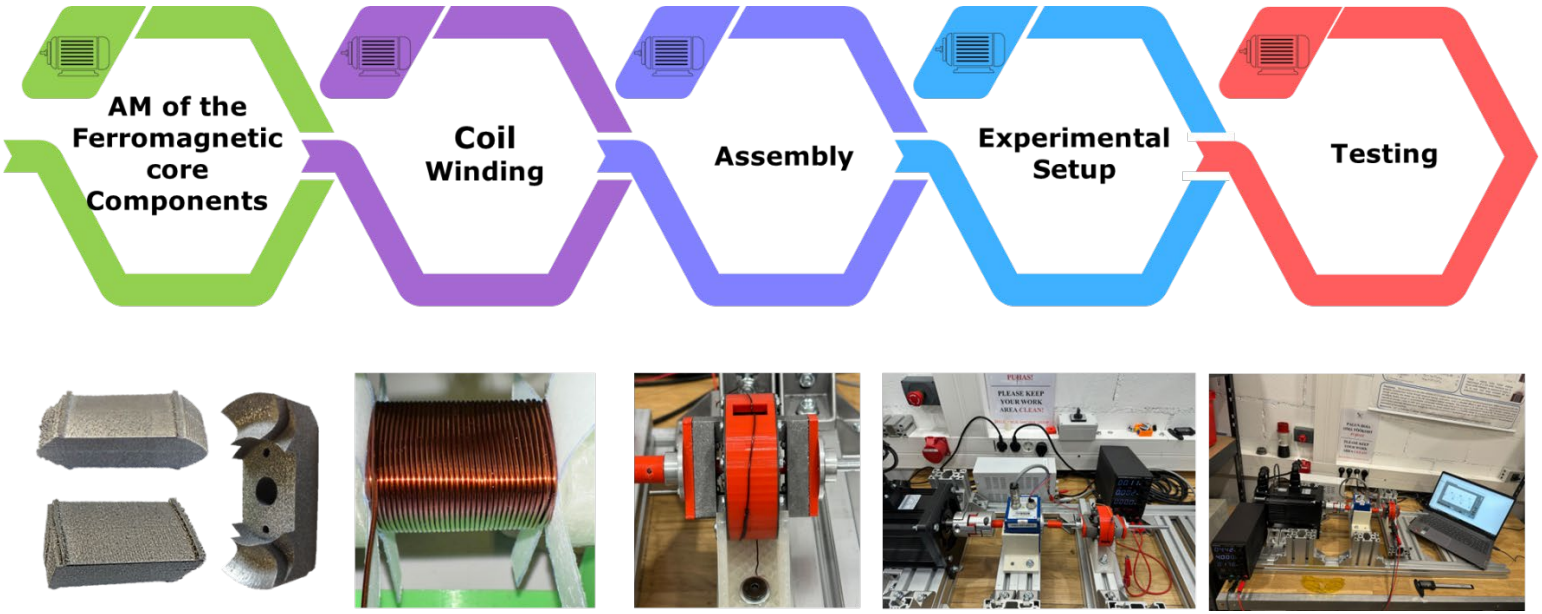


Figure 3.15. Schematic workflow of the prototyping and practical measurement process.

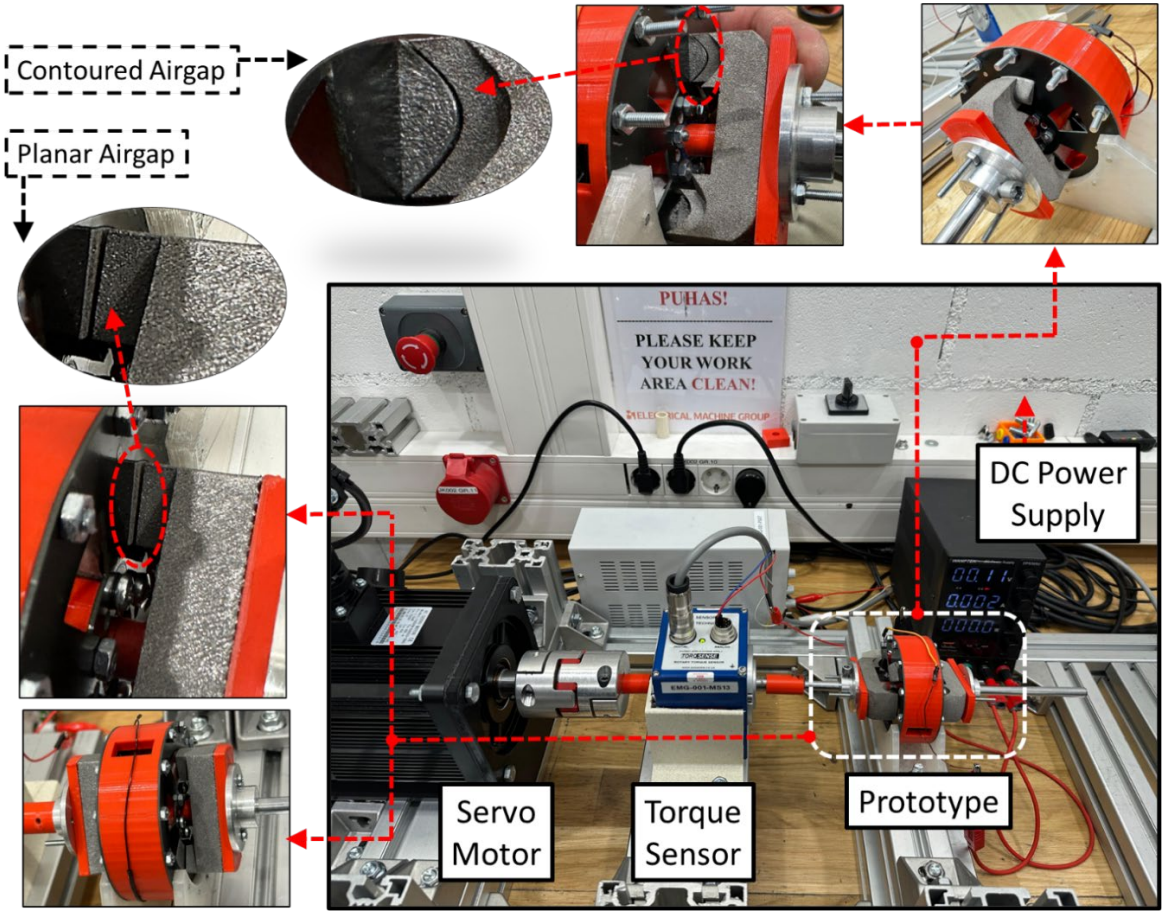


Figure 3.16. Machine assembly and practical measurement setup.

3.3.2.2 Experimental Static Torque Measurement Setup

The experimental validation of static torque was performed using a dedicated measurement setup, shown in Figure 3.16, designed to precisely assess the torque characteristics of the planar and contoured airgap topologies. The reduced-scale mock-up prototypes were mechanically coupled to a servo motor operating at a very low rotational speed (≤ 1 rpm). This very low and controlled rotational speed allowed accurate replication of static rotor positioning, facilitating the measurement of torque at defined angular steps.

Torque was measured using an ST (Sensor Technology) torque sensor (model RWT421-DE-KG), selected for its accuracy and suitability for low-magnitude torque measurements. During the experiments, the stator coils were powered using a regulated DC power supply, and the excitation current was systematically varied from 2.5A to 5A in increments of 0.5 A to evaluate torque performance across different excitation levels.

The measurement data was acquired and logged using a DEWETRON data acquisition recorder, providing reliable and high-resolution recording capabilities. Torque data was collected for both planar (benchmark) and contoured (optimal) airgap topologies under identical measurement conditions, enabling direct comparative analysis.

The measured static torque values facilitated the comparison against those obtained through FEA. The evaluation involved calculating mean torque values and quantifying the percentage improvement achieved by the contoured airgap design relative to the planar airgap design, thus providing experimental validation for the theoretical performance enhancements predicted by numerical simulations.

3.3.2.3 Results and Comparative Analysis

The static torque characteristics obtained through practical measurements and finite element analysis (FEA) simulations are presented in Figure 3.17 and Table 3.5. The torque profiles illustrate the comparative behavior of the planar and contoured airgap topologies across excitation current levels ranging from 2.5 A to 5 A. It was observed that the contoured airgap consistently exhibits higher torque values compared to the planar airgap across all current levels, verifying the theoretical prediction that airgap contouring reduces reluctance and consequently increases torque output.

Table 3.5 summarizes the mean torque values and the corresponding percentage increases calculated from both practical measurements and numerical simulations. The percentage improvement provided by the contoured topology, compared to the planar airgap topology, is clearly evident and consistent across both FEA and practical measurements. Small discrepancies between the practical and FEA values are observed, primarily due to differences in material properties and practical experimental factors.

Due to the absence of accurate magnetic properties of the material, utilized for AM production of stator-rotor components in the FEA software's database, numerical simulations were performed using the M400-50A magnetic steel model. In contrast, practical prototypes utilized a slightly different magnetic material (3.5% FeSi) as documented in [61]. This discrepancy in materials accounts for the lower torque values observed in practical measurements compared to simulation results. Nevertheless, the consistency in the percentage increase of static torque between straight and contoured topologies, as observed experimentally, closely aligns with simulation predictions.

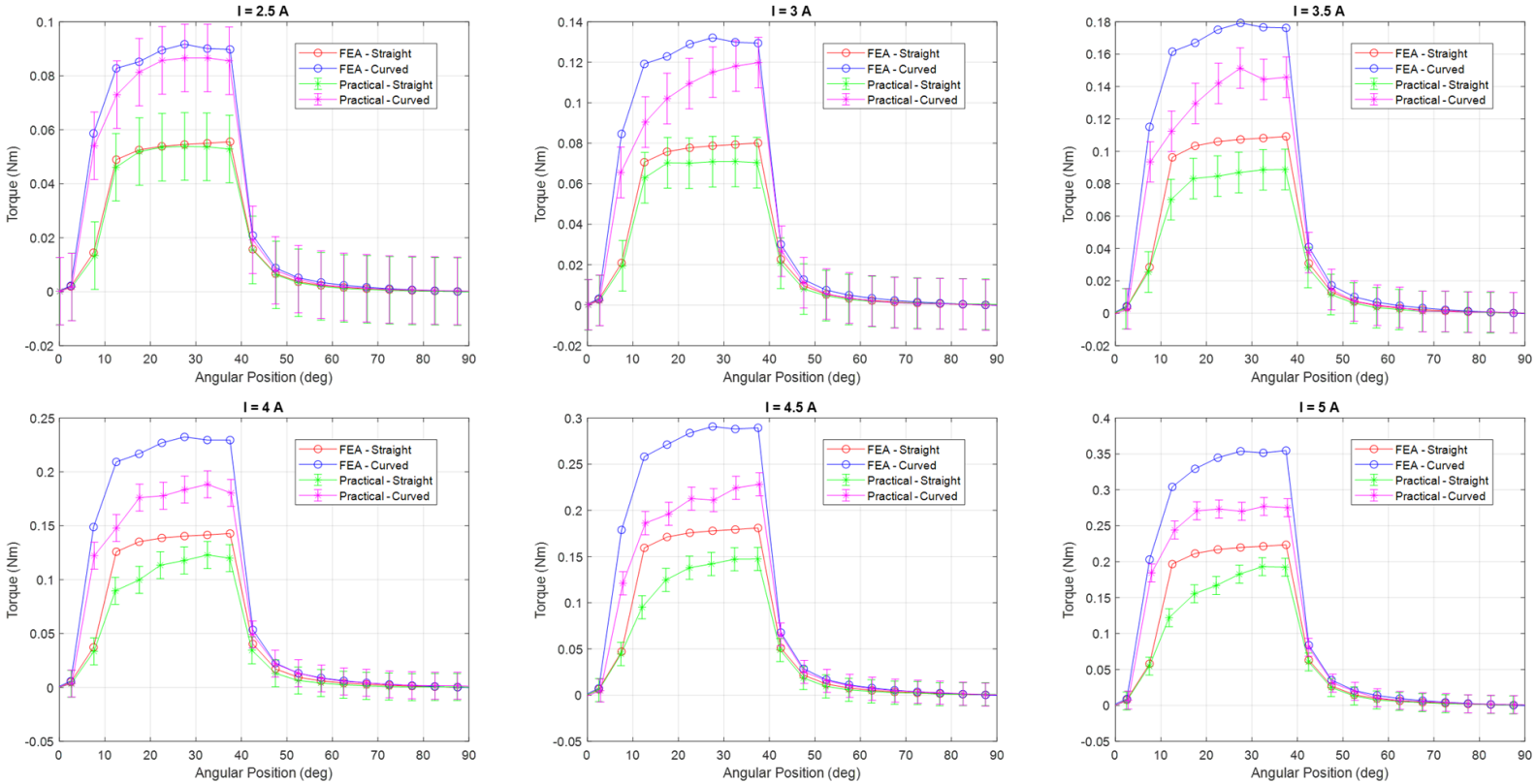


Figure 3.17. Torque profile analysis, FEA vs. practical measurements for planar and contoured airgap topology (I = 2.5A to 5A).

Table 3.5. Comparison of Mean Torque and Percentage Increase (FEA vs. Practical) for I = 2.5A to 5A.

Coil Current (A)	Airgap Topology	Mean Torque, FEA (Nm)	Mean Torque, Practical (Nm)	% Increase (FEA)	% Increase (Practical)
2.5	**Planar**	0.02054	0.0188	71.56	66.38
	Contoured	0.03524	0.03128		
3.0	**Planar**	0.02963	0.02527	71.48	61.45
	Contoured	0.05081	0.0408		
3.5	**Planar**	0.0404	0.03257	70.89	69.51
	Contoured	0.06904	0.05521		
4.0	**Planar**	0.05282	0.04247	69.67	68.82
	Contoured	0.08962	0.0717		
4.5	**Planar**	0.0669	0.05215	67.11	62.01
	Contoured	0.1118	0.08449		
5.0	**Planar**	0.08262	0.06638	63.27	64.50
	Contoured	0.1349	0.1092		

Additional practical factors contributing to deviations include minor inaccuracies in component alignment and dimensional tolerances introduced during laboratory-scale prototyping. Furthermore, inherent accuracy limitations of the torque measurement sensor (ST RWT421-DE-KG) may introduce minor variations in measured results.

Despite these influencing factors, the relative percentage improvement in torque from planar to contoured airgap topologies remained highly consistent across simulations and practical measurements. This consistency reinforces and validates the fundamental hypothesis that airgap contouring significantly enhances the electromagnetic performance parameters of electrical machines and provides a foundation for future optimization and scaling efforts.

3.4 Implementation of Contoured Airgap in Radial Flux SynRM

From the comparative analysis of results from previous section, the effectiveness of contoured airgap topology for axial-flux SRM's electromagnetic performance parameter enhancement is established. To showcase potential of the principle for diverse machine types and flux-orientations, this section presents the implementation and numerical modeling-based validation of contoured airgap topology in radial-flux SynRM. The results from this case study will also serve as the benchmark for the validation of enhance modeling technique presented in the next chapter.

The radial flux SynRM of [62], initially designed with the state-of-the-art presented in [54], [63], [Publication-V] was further improved to have fluid flux-barriers in the rotor design [64]. This improved design as illustrated in Figure 3.18, with design parameters presented in Table 3.6 was selected as the benchmark machine design to evaluate the effects of implementing a contoured airgap topology.

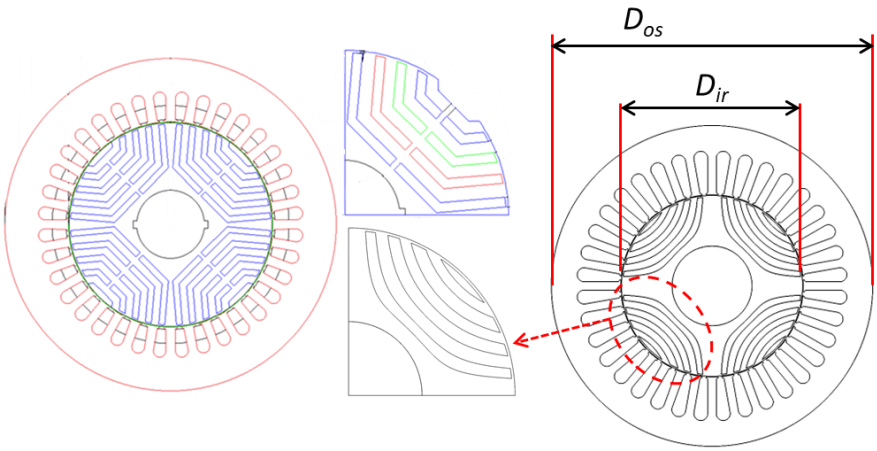


Figure 3.18. Machine geometry, 2D layout of conventional stator and rotor design from [62] and the improved rotor design.

The finite element analysis of the benchmark machine, conducted at varying levels of machine's operating point i.e. at *1/3* I_{rated}*, 2/3* I_{rated} *and* I_{rated}, along-with the respective load angles for maximum-torque-per-ampere (MTPA), confirms the output performance parameters wherein, the respective torque profiles are presented in Figure 3.19 and the main output characteristics validated through FEA are presented in Table 3.7. The next subsection will detail the design criteria employed while implementing the contoured airgap topology and simulated iteratively for the incremental increase in contour amplitude.

Table 3.6. Design Parameters of the Benchmark Radial-flux SynRM.

Parameters	**Units**	**Values**
Rated Power	kW	13
Rated Voltage	V	230
Rated Phase Current (RMS)	A	22.27
Rated Speed	rpm	1500
Number of Phases	-	3
Number of Rotor Poles	-	4
Number of Stator Slots	-	36
No. of Turns/coil	-	132
Electric Loading	kA/m	42.77
RMS Current Density	A/mm^2	3.89
Airgap Length	mm	0.5
Airgap Diameter	mm	131
Machine Stack Length	mm	150
Stator Outer Diameter (D_{os})	mm	231
Rotor Inner Diameter (D_{ir})	mm	57.5
Stator-tooth Width	mm	6
Stator Yoke Width	mm	18.2
Phase Resistance	ohm	0.6
Load angle for MTPA @ rated load	deg	60
Average Flux Density for Core	T	1.5
Rotor Flux-barrier to Guide ratio	-	0.5

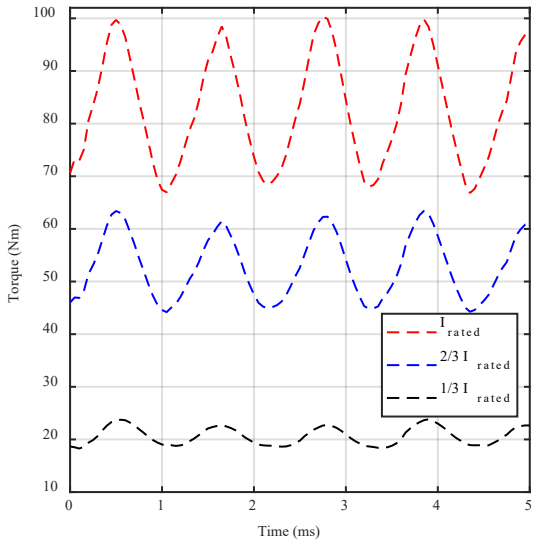


Figure 3.19. Torque profiles for varying operating points of the benchmark machine under MTPA strategy.

Table 3.7. Output Characteristics of Benchmark Radial-flux SynRM Design.

Parameters		**Units**	**Values**
Mean Torque	*1/3 I_{rated}*	Nm	20.64
	2/3 I_{rated}		52.91
	I_{rated}		82.71
Torque Density		Nm/kg	1.97
Efficiency		%	~92
Torque Ripple Rate @ rated load		%	40.5

3.4.1 Implementation and Evaluation of Airgap contour

The major imposed criteria for this study are described below and illustrated with the help of Figure 3.20. Sinusoidal airgap contours with varying amplitudes (A_c) from 0mm (benchmark) to 45 mm, in increments of 5 mm were systematically evaluated using FEA. The contoured rotor surface was generated by axial variation of rotor radius, maintaining a consistent airgap clearance, while the stator geometry was adapted accordingly.

- The stator back iron thickness is kept constant, i.e. the outer perimeter of the stator follows the contoured profile of the airgap.
- The stator slot area is kept constant throughout the machine length, to accommodate the same number of winding conductors throughout the machine's stack length.
- The stator tooth width is also kept constant, resulting in the decreased slot height when increasing the contour amplitude.
- The airgap thickness is also kept constant throughout the machine length.
- For the rotor design, while increasing the mid-plane diameter, the flux-barrier and the flux-guide width was kept constant.

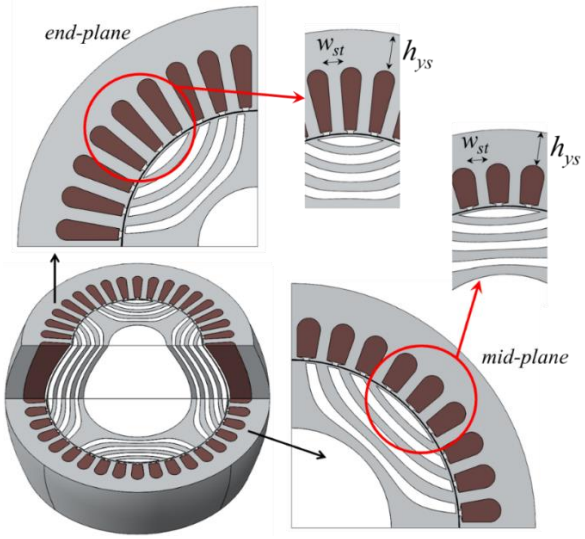


Figure 3.20. Cross-sectional views of the end-plane and mid-plane geometry.

The effects of contoured airgap topologies were evaluated through comprehensive FEA simulations. Torque characteristics at three distinct operating points of the machine (1/3, 2/3, and full-rated current) were analyzed. Figures 3.21, 3.22 and 3.23 present the variation in machine's main performance parameters with varying amplitude of the contour. It is evident that the contoured airgap consistently improved mean torque output at each investigated operating point of the machine, compared to the benchmark planar airgap configuration. This confirms the validity of the concept efficacy in the case of radial-flux SynRM too. Analysis of the other performance parameters such as torque density and efficiency also yield the same conclusions as established from Chapter 2 where the fundamentals of airgap contour implementation in practical, non-linear magnetic materials were discussed. That is to say, the torque density does show an increasing trend with an increasing amplitude of the contour until at an optimal point beyond which the degrading effects of localized saturation dominates. Another observation, in line with the conclusions drawn in the previous chapter, is the relatively higher gains at lower applied MMF and vice versa. The torque ripple also shows increased value as the applied MMF and /or contour amplitude increases. The specific numerical and percentage values for the performance parameter variations are presented in Table 3.8.

3.5 Conclusion

In conclusion, this chapter has successfully demonstrated the practical feasibility and effectiveness of implementing contoured airgap topologies in rotating electrical machines, validating the hypotheses set out at the beginning of this thesis report. The comprehensive analyses conducted through both numerical simulations and practical experimental validation clearly establish that airgap contouring significantly enhances electromagnetic performance parameters. Specifically, the implementation of sinusoidal contouring led to notable increases in torque production, torque density, and machine efficiency across varying operational conditions. This supports the first hypothesis, confirming that contoured airgap topology enabled by additive manufacturing effectively reduces airgap reluctance and enhances electromagnetic performance.

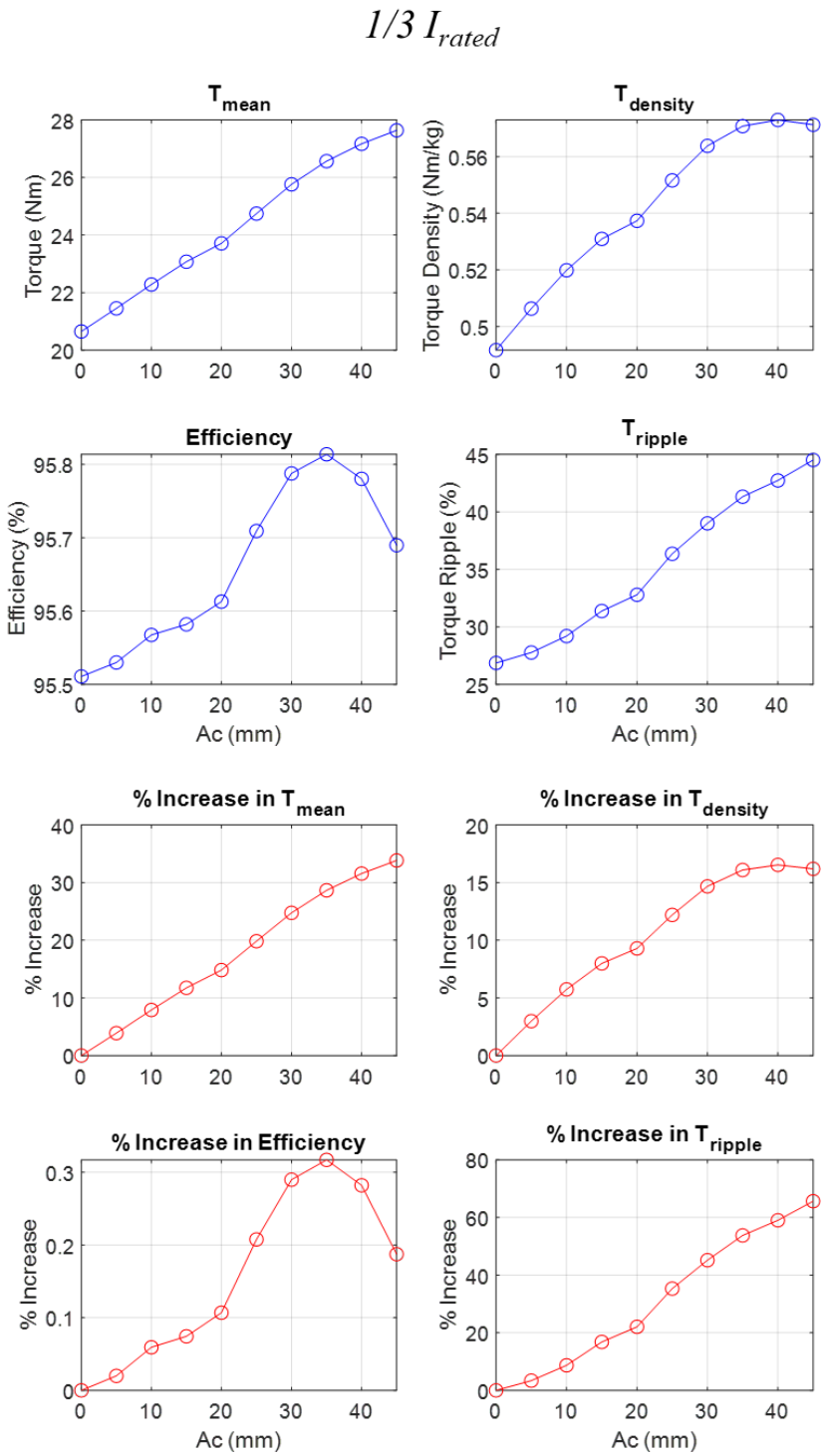


Figure 3.21. Performance characteristics of Radial-Flux SynRM against varying Contour Amplitude in terms of Magnitude (bled) and Percent (red) variation, for operating point of 1/3 I_{rated} at the corresponding load angle of MTPA for each contour amplitude.

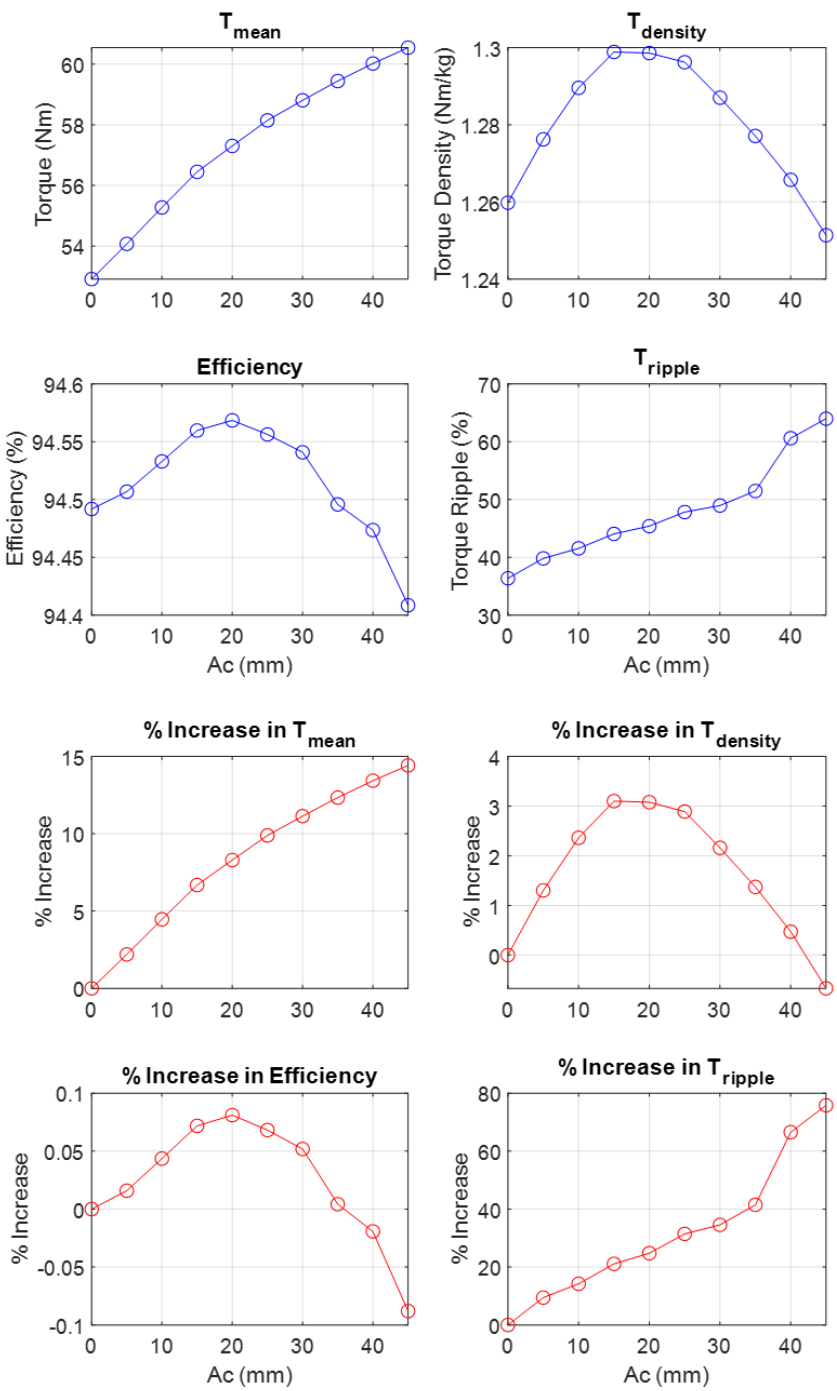


Figure 3.22. Performance characteristics of Radial-Flux SynRM against varying Contour Amplitude in terms of Magnitude (bled) and Percent (red) variation, for operating point of 2/3 I_{rated} at the load angle of MTPA for each contour amplitude.

I_{rated}

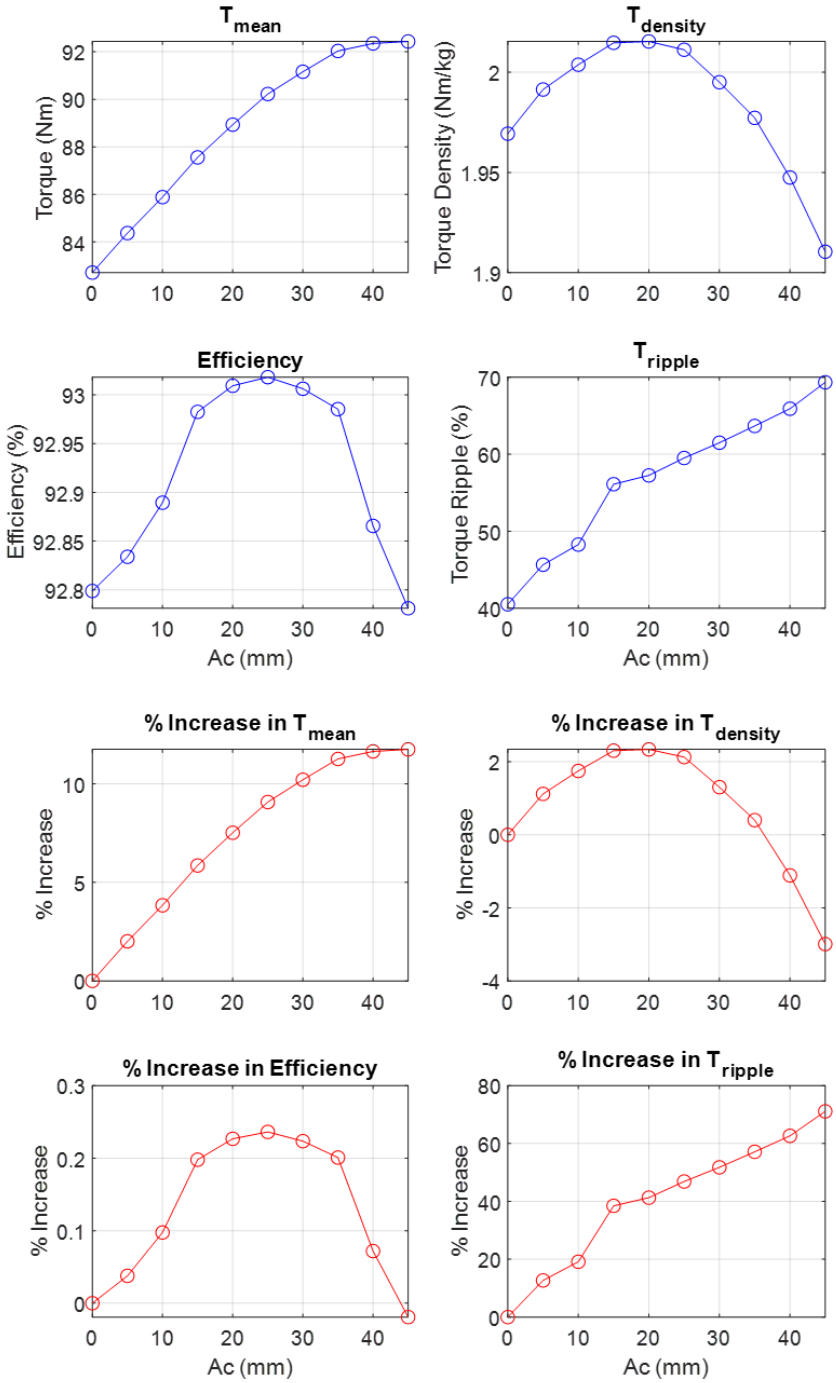


Figure 3.23. Performance characteristics of Radial-Flux SynRM against varying Contour Amplitude in terms of Magnitude (bled) and Percent (red) variation, for operating point of I_{rated} at the load angle of MTPA for each contour amplitude.

Table 3.8. Performance Parameters for Varying Contour Amplitude in SynRM.

Analysis	Parameter	Units	Operating Condition	Contour Amplitude (mm)									
				0	**5**	**10**	**15**	**20**	**25**	**30**	**35**	**40**	**45**
Magnitude	Mean Torque	Nm	*1/3* I_{rated}	20.65	21.45	22.28	23.07	23.71	24.75	25.76	26.57	27.17	27.64
			2/3 I_{rated}	52.91	54.07	55.27	56.45	57.30	58.15	58.81	59.44	60.02	60.55
			I_{rated}	82.71	84.38	85.89	87.56	88.93	90.22	91.16	92.03	92.35	92.43
	Torque Density	Nm/kg	*1/3* I_{rated}	0.49	0.51	0.52	0.53	0.54	0.55	0.56	0.57	0.57	0.57
			2/3 I_{rated}	1.26	1.28	1.29	1.30	1.30	1.30	1.29	1.28	1.27	1.25
			I_{rated}	1.97	1.99	2.00	2.01	2.02	2.01	2.00	1.98	1.95	1.91
	Efficiency	%	*1/3* I_{rated}	95.51	95.53	95.57	95.58	95.61	95.71	95.79	95.81	95.78	95.69
			2/3 I_{rated}	94.49	94.49	94.52	94.57	94.57	94.56	94.54	94.50	94.47	94.41
			I_{rated}	92.80	92.83	92.89	92.98	93.01	93.02	93.01	92.99	92.87	92.78
	Torque Ripple Rate	%	*1/3* I_{rated}	26.87	27.77	29.20	31.38	32.79	36.35	39.00	41.31	42.73	44.50
			2/3 I_{rated}	36.38	39.82	41.55	44.06	45.40	47.83	48.96	51.47	60.60	63.97
			I_{rated}	40.52	45.65	48.27	56.10	57.25	59.51	61.49	63.67	65.91	69.33
% Variation from Benchmark Machine Parameters	Mean Torque	%	*1/3* I_{rated}	-	3.89	7.91	11.75	14.83	19.84	24.76	28.67	31.58	33.86
			2/3 I_{rated}	-	2.19	4.46	6.68	8.30	9.90	11.14	12.35	13.44	14.43
			I_{rated}	-	2.01	3.84	5.86	7.52	9.08	10.21	11.27	11.65	11.75
	Torque Density		*1/3* I_{rated}	-	2.99	5.74	7.99	9.29	12.20	14.68	16.10	16.54	16.20
			2/3 I_{rated}	-	1.30	2.36	3.10	3.08	2.89	2.16	1.37	0.47	-0.67
			I_{rated}	-	1.12	1.75	2.30	2.34	2.13	1.31	0.40	-1.11	-2.99
	Efficiency		*1/3* I_{rated}	-	0.02	0.06	0.07	0.11	0.21	0.29	0.32	0.28	0.19
			2/3 I_{rated}	-	-0.01	0.03	0.08	0.08	0.07	0.05	0.00	-0.02	-0.09
			I_{rated}	-	0.04	0.10	0.20	0.23	0.24	0.22	0.20	0.07	-0.02
	Torque Ripple Rate		*1/3* I_{rated}	-	3.38	8.69	16.81	22.06	35.32	45.17	53.78	59.03	65.65
			2/3 I_{rated}	-	9.45	14.21	21.09	24.77	31.45	34.56	41.47	66.55	75.81
			I_{rated}	-	12.67	19.12	38.46	41.28	46.87	51.76	57.13	62.65	71.11

4 Modified Winding Function Analysis for Iterative Design Process Optimization

The advent of AM has introduced new possibilities for electrical machine design, allowing for the realization of relatively complex three-dimensional geometries that were previously unfeasible with conventional manufacturing techniques. This essential expansion of the design space to 3D, presents new challenges in modeling and simulation. The reliance on three-dimensional FEA increases as traditional analytical models lack in incorporating the complexities of three-dimensional machine designs. Without advancing the analytical modeling approaches, the reliance on full three-dimensional FEA based iterative design process will become a bottleneck in the AM-enabled ecosystem of rapidly producible application-specific electrical machines. In the context of AM-enabled ecosystem of electrical machine production, the design process itself must also evolve to accommodate more rapid iterations. This shift necessitates the development of improved analytical models capable of better approximating performance parameters and handling three-dimensional design features while maintaining computational efficiency.

Among analytical approaches, the modified winding function analysis has emerged as a valuable tool for electrical machine performance evaluation, particularly in early-stage design iterations. Compared to traditional magnetic equivalent circuit (MEC) and d–q models, its primary advantage lies in its direct inductance-based formulation, which is well-suited for analyzing the influence of spatial airgap variations due to slot openings and/or salient pole geometries on stator or rotor sides and, different winding configurations with a higher degree of computational efficiency. MWFA extends classical winding function analysis (WFA) by incorporating the physical stator and rotor geometry instead of considering the airgap throughout the machine periphery, a constant or approximated by series functions. However, despite its advantages, MWFA has traditionally been developed for two-dimensional design space, where the third dimension is assumed to be uniformly stacked and non-skewed. This assumption limits its applicability to electrical machines with three-dimensional design features, including those enabled by additive manufacturing. Additionally, MWFA does not incorporate material non-linearities, making it less effective for analyses at operating points where saturation effects become prominent.

By improving the accuracy and scope of design features that MWFA can incorporate, the dependence on intensive three-dimensional FEA simulations in design iterations can be reduced. This will allow MWFA to remain a viable, computationally efficient tool for evaluating machine performance, particularly in the context of AM-enabled designs. The advances presented in this chapter aim to bridge the gap between rapid analytical modeling and high-precision numerical validation, ultimately streamlining the iterative design process for rapidly produceable, mass-personalized modern electrical machines.

In this chapter, the focus is on extending and refining the MWFA methodology specifically to address these emerging requirements. The enhancements discussed include strategies to incorporate the electromagnetic characteristics of machine's core materials, allowing for accurate modeling under nonlinear operating conditions in a computationally efficient manner. Additionally, a comprehensive formulation is introduced to effectively handle the three-dimensional design features, particularly the incorporation of contoured airgap topologies and slot skewing, both critical to modern machine designs.

Subsequent sections of this chapter will comprehensively review the state-of-the-art in MWFA, propose and validate a hybrid FEA-Analytical approach to account for nonlinear magnetic behavior, and present a novel strategy to incorporate three-dimensional design features in MWFA. The proposed modifications ensure that MWFA not only retains its inherent advantages of computational efficiency and applicability in iterative design process but also aligns closely with the practical realities and challenges posed by advanced machine designs enabled through additive manufacturing.

4.1 State-of-the-art and Fundamental Principles Of MWFA

MWFA is an analytical modeling approach primarily utilized for early-stage electromagnetic evaluation of electrical machines. MWFA enhances classical winding function analysis by integrating precise winding configurations and physical stator-rotor geometries, such as slot openings and salient poles, directly into inductance calculations. Consequently, inductance becomes a rotor position-dependent parameter, providing more accurate torque profile estimations. Despite its effectiveness, MWFA has a traditionally limited role in the iterative design process owing to its simplifying assumptions such as linear magnetic properties, planar airgaps and non-skewed geometric structures, posing challenges for three-dimensional designs for modern machines specifically enabled by AM.

The generic MWFA based modeling procedure involves two main phases: an offline calculation of inductances for a complete mechanical rotation using MATLAB scripts, and an online SIMULINK-based performance evaluation that utilizes the rotor-position based precomputed inductances. The overall modeling framework is depicted in Figure 4.1.

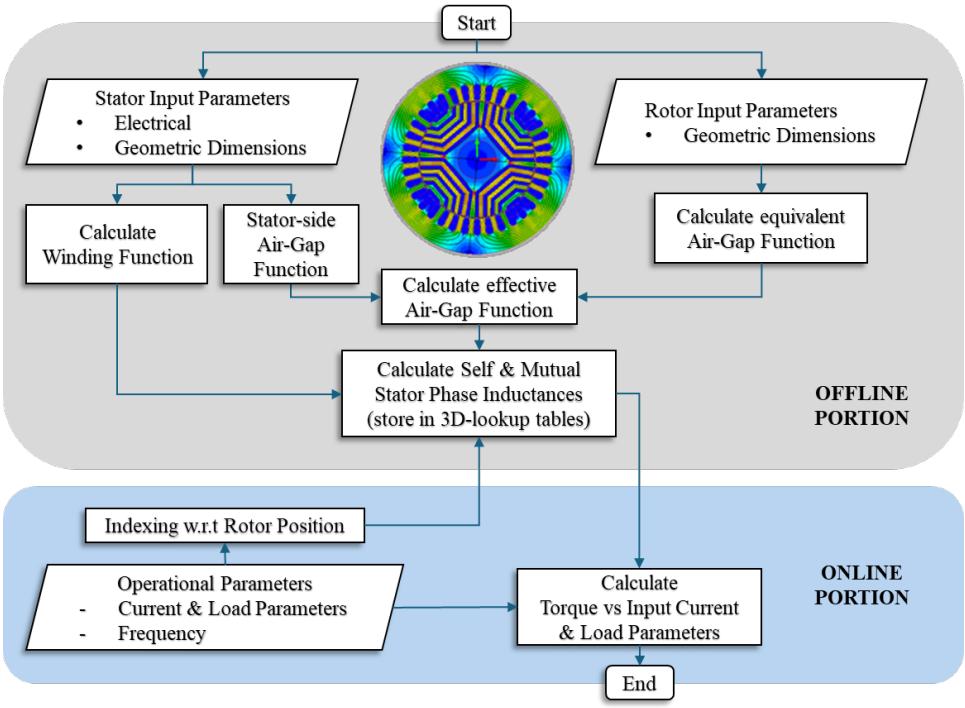


Figure 4.1. Block diagram for MWFA based modeling procedure.

The following subsections provide detailed formulations of MWFA's fundamental principles, illustrated through a reference SynRM [62], [Publication-VI], [Publication-VII]. Key parameters of this reference machine are presented in Figure 4.2 and Table 4.1.

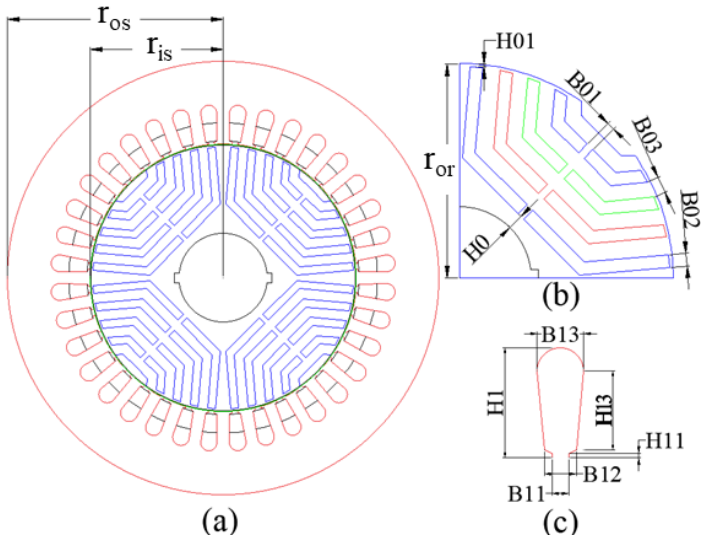


Figure 4.2. Machine geometry (a) 2D-layout of stator and rotor, (b) Rotor flux-barrier dimensions, (c) Stator slot dimensions.

Table 4.1. Design Parameters of SynRM.

PARAMETERS	VALUE	PARAMETERS	VALUE
Rated Power	13426 VA	**H0**	5 mm
Rated Current	20.3 A	**H01**	1 mm
Stator Inner Diameter	135.95 mm	**H1**	20 mm
Rotor Outer Diameter	135 mm	**H11**	0.85 mm
Air-Gap Length	0.95 mm	**H13**	14.3 mm
Stack Length	200 mm	**B01**	2.5 mm
Number of Poles	04	**B02**	4 mm
Number of Stator Slots	36	**B03**	5 mm
Core Material	M400-50A	**B11**	3 mm
Number of Winding Turns per-Slot	23	**B12**	5.85 mm
Number of Winding Layers	02	**B13**	8.5 mm

4.1.1 Inductance Calculation

In MWFA, the inductances, self and mutual, as a function of rotor position (θ) are calculated using the following fundamental formulation

$$L_{xy}(\theta) = \mu_o r l \int_0^{2\pi} \mathrm{P}(\theta,\beta) N_x(\theta,\beta) n_y(\theta,\beta) d\theta \qquad (4.1)$$

where r, μ_o, l, $P(\theta,\beta)$, $N_x(\theta,\beta)$ and $n_y(\theta,\beta)$ represent the average airgap radius, permeability of free space, stack length, airgap permeance function, winding function,

and turn function, respectively. These terms are the function of stator and rotor relative position with β measured from a fixed reference point and θ relative to the stator frame of reference.

To reduce the complexity of solution, the inductance calculation equation can be reduced to a mean value function as follows, giving its discrete implementation.

$$L_{xy}(\theta) = \frac{\mu_0 2\pi r l}{n} \sum_{k=1}^{n} \Big(P(\theta,\beta).N_x(\theta,\beta).n_y(\theta,\beta) \Big)_k \tag{4.2}$$

In practical computations, inductances are determined at discrete rotor positions spanning one full mechanical rotation (0 to 2π). Therefore, rotor position-dependent functions are represented as vectors with "n" discrete elements. The mean inductance at any given rotor position θ is then obtained through element-wise multiplication of these vectors, followed by averaging the elements of the resultant vector over all discrete steps. This discretized approach significantly simplifies the complexity inherent in continuous integral formulations of equation (4.1), especially as the number of rotor position-dependent variables increases.

4.1.2 Turn Function and Winding Function

The stator winding function, $N_x(\theta)$, is defined as

$$N_x(\theta) = n_x(\theta) - \langle P n_x \rangle / \langle P \rangle \tag{4.3}$$

where $n_x(\theta)$ is the turn function and $\langle P \rangle$ is the mean airgap permeance. In multi-layer windings, shifts between winding layers help achieve better sinusoidal flux distributions. To incorporate this characteristic, the per-layer turn functions are shifted relative to each other, before adding to yield a resultant turn function. The machine under consideration has a double-layer winding with a short-pitch value of one stator-slot.

The per-layer turn function for the phase-A winding is shown in Figure 4.3 (a)**.** For each layer, a stator slot houses 23 number of windings turns. The resultant winding function per phase and for all three phases is presented in Figure 4.3(b) and Figure 4.4.

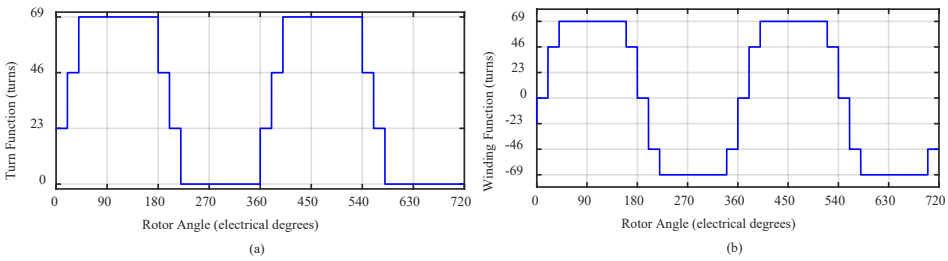


Figure 4.3. Phase-A (a) per-layer turn function, (b) resultant winding function for two-layers.

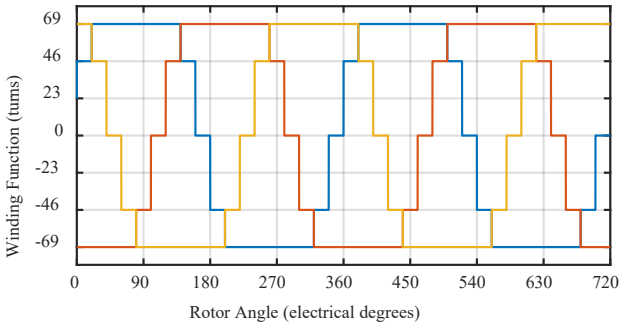


Figure 4.4. Winding Function of three-phase stator.

4.1.3 Airgap Permeance Function

The airgap permeance function considers stator and rotor geometrical influences. The overall permeance function is then given by,

$$P(\theta, \beta) = \frac{1}{g_s(\theta) + g_r(\theta, \beta)} \tag{4.4}$$

The stator side airgap function, $g_s(\theta)$, incorporating the stator slot opening is defined by,

$$g_s(\theta) = \begin{cases} g_{avg} & B_{11} \le \theta \le B_{11} + B_{tt} \\ g_{avg} + H_{11} & 0 \le \theta \le B_{11} \end{cases} \tag{4.5}$$

$$g_{avg} = \frac{r_{is} - r_{or}}{2} \tag{4.6}$$

where H_{11}, B_{11} and B_{tt} are the thickness of the empty portion from the stator slot, the width of stator slot opening and stator tooth-tip, respectively. r_{is} and r_{or} are the inner radius of the stator and outer radius of the rotor, respectively. The machine's geometry is illustrated in Figure 4.2. The rotor-associated airgap remains constant at g_{avg}, as the rotor has a uniform surface. The stator and rotor air-gap functions as a function of rotor position θ are shown in Figure 4.5.

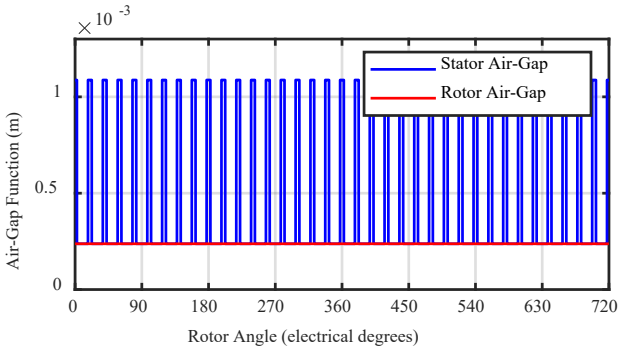


Figure 4.5. Stator and rotor associated air-gap function.

4.1.4 Rotor Flux-Barrier Translation

The operating principle of SynRM relies on the insertion of flux barriers into the rotor structure. These flux barriers introduce anisotropy into the rotor's magnetic path, creating distinct difference in reluctance along the direct-axis (d-axis) and quadrature-axis (q-axis). This reluctance differential is fundamental for torque generation, as torque arises from the rotor's tendency to align itself with the stator's rotating magnetic field, thus seeking the path of minimum magnetic reluctance.

The reluctance of a magnetic path is directly proportional to its length and inversely proportional to the cross-sectional area available for magnetic flux transmission. To analytically model this effect within the MWFA framework, the flux barriers' reluctance is translated into an equivalent increase in the rotor-associated air-gap length. To achieve this translation, the rotor is segmented into subsections, each corresponding to a specific flux barrier. The ratio between the rotor subsection's surface area without flux barriers A_1 and the area with flux barriers A_2, along with the bridge area A_{RB} that connects adjacent flux paths, determines the equivalent extension of the air-gap length. This relationship is mathematically expressed as follows,

$$l_{fb} = \left[\left(\frac{A_1}{A_2 + kA_{RB}}\right) - 1\right] l_{ag} \tag{4.7}$$

where l_{fb} and l_{ag} are the equivalent air-gap length for flux barrier and the actual air-gap length respectively. Since this surface area bridges two individual flux paths, the value of scaling factor for bridge area k, in this case is chosen to be ½. The air-gap function for rotor flux-barrier translation by (7), for one rotor pole is presented in Figure 4.6.

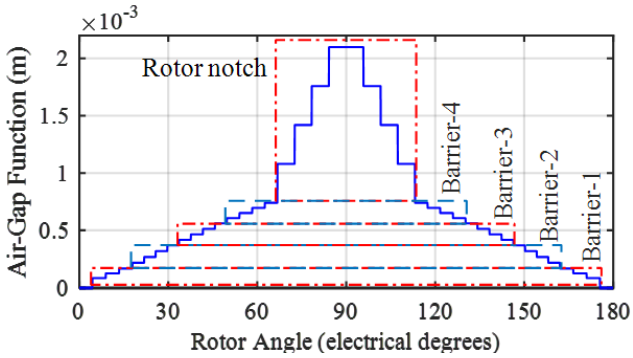


Figure 4.6. Rotor flux-barrier translation towards airgap, with a stepped transition between flux barriers.

4.1.5 Torque Calculation

Torque in MWFA is computed using co-energy analysis, dependent on inductance variations with rotor position, θ.

$$T_e = \frac{p}{2}[I]^T \left[\frac{\partial}{\partial\theta}[L(\theta)]\right][I] \tag{4.8}$$

where p is the number of pole pairs, $[I]$ is the input current matrix and $\partial[L(\theta)]/\partial\theta$ is the inductance matrix derivative at the respective rotor angular position θ. For the case of SynRM, the load angle δ is introduced towards the input current in the form of following equations

$$I = \begin{bmatrix} I_{pk}Sin(\omega t + \delta) \\ I_{pk}Sin(\omega t - 2\pi/3 + \delta) \\ I_{pk}Sin(\omega t + 2\pi/3 + \delta) \end{bmatrix} \quad (4.9)$$

4.1.6 Results And Analysis

The self and mutual inductances for stator phases are calculated by (2). For illustration purposes, the self-inductance of phase A and mutual inductance between phase A and B are presented in Figure 4.7 (a) and (b). The self and mutual inductance profiles for other phases are like those illustrated in Figure 4.7 but displaced 120˚ apart. The electromagnetic torque waveforms for the machine under consideration, for peak input currents of 10A and 18A at δ = 10˚ mechanical, are presented in Figure 4.8.

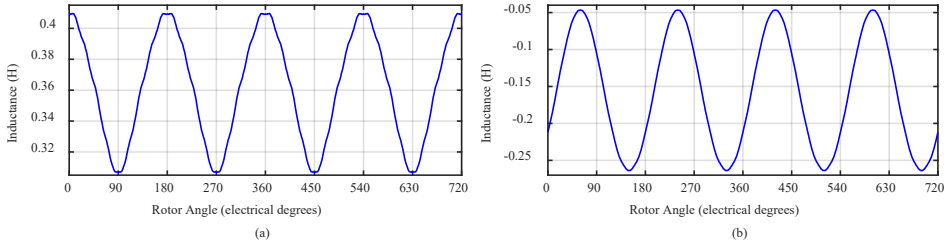


Figure 4.7. (a) Self-inductance of one phase, (b) Mutual inductance between two phases.

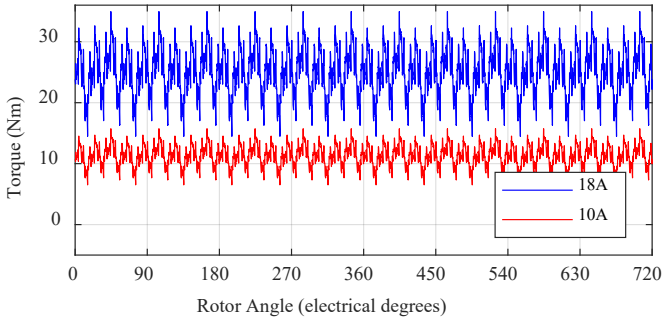


Figure 4.8. Electromagnetic torque waveform for input current of 10A and 18A, at $\delta = 10^{\circ}$.

The analytical MWFA model presented is evaluated based on its ability to reflect the sensitivity of output performance parameters to various machine design parameters. The parameters considered include stator slot count, winding configuration, layered windings, stator-teeth dimensions, air-gap length, and rotor geometric characteristics such as pole-arc to pole-pitch ratio and flux barrier dimensions.

Figure 4.9 (a) and (b) illustrate the air-gap function and corresponding torque profiles for two different pole-arc to pole-pitch ratios, holding all other parameters constant with an input current of 15 A and a load angle δ of $10°$. These results illustrate the influence of minor geometric variations on the machine performance, demonstrating an increase in mean torque from 20.5 Nm to 22.6 Nm and a ripple percentage rise from 33.1% to 36.7% upon decreasing the pole-arc.

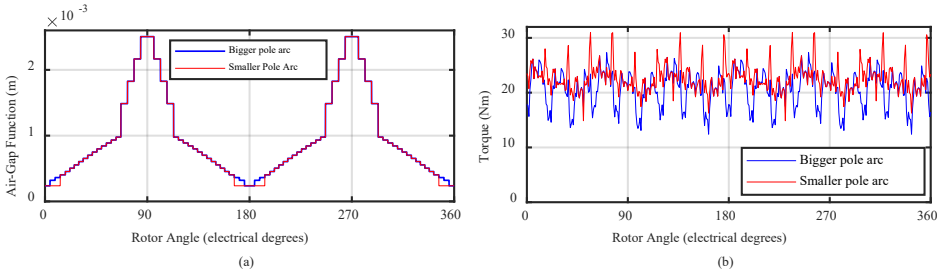


Figure 4.9. (a) Air-gap function for design variation in pole arc (b) Associated torque profile for respective design variation.

Similarly, adjustments in flux-barrier width directly impact the available area for d-axis flux. As depicted in Figure 4.10, a 1 mm increase in flux-barrier width reduces the mean torque from 20.5 Nm to 19.6 Nm, while the torque ripple decreases slightly from 33.18% to 31.4%, given the same input conditions (15 A, δ = 10°).

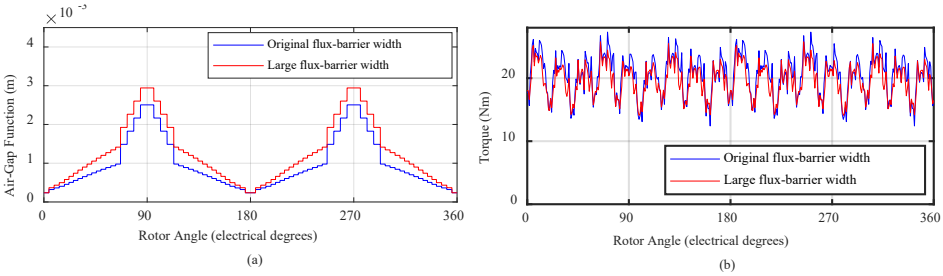


Figure 4.10. (a) Air-gap function for design variation in flux-barrier width (b) Associated torque profile for respective design variation.

To assess the accuracy and practical applicability of the MWFA model in the design iteration process, a comparison with an FEA model is conducted. Torque profiles calculated using MWFA and FEA for different load angles at a 10 A input current are shown in Figure 4.11. The mean torque obtained through FEA was 11.29 Nm, whereas MWFA yielded 12.13 Nm at a load angle of 10°, representing a deviation of approximately 7.4%. This discrepancy, though minor, is primarily attributable to localized saturation effects inherent in complex machine structures and the lower temporal resolution of FEA simulations. Notably, increasing the temporal resolution of FEA significantly escalates computational time, highlighting MWFA's computational advantage.

In context of torque profile estimation, the MWFA model also demonstrates conformity with the torque profiles observed in FEA simulations. The shape and phase of the MWFA-predicted torque profiles align closely with their numerically simulated counterparts. This consistency confirms that MWFA can not only approximate the mean torque values but also accurately capture the dynamic electromagnetic behavior of the machine.

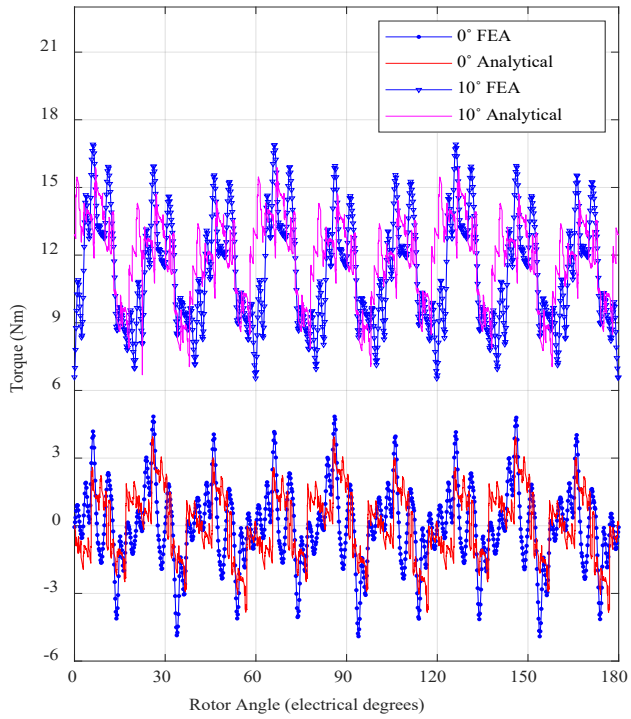


Figure 4.11. Torque profile comparison between MWFA and FEA for different load angle δ and I = 10 A.

Further analysis over the entire input current range, i.e. from no load to rated conditions, reveals limitation of the conventional MWFA approach, especially when utilizing it in the machine design process where near-rated or rated operating conditions push the magnetic characteristics of the material in the non-linear region. As illustrated in Figure 4.12, deviations from FEA predictions become pronounced near rated currents due to magnetic saturation of the ferromagnetic core material. With the assumption of linear magnetic material in the mathematical formulation of MWFA, the squared value of I in torque calculation of (8) renders its behavior to follow the same squared trend versus the input current.

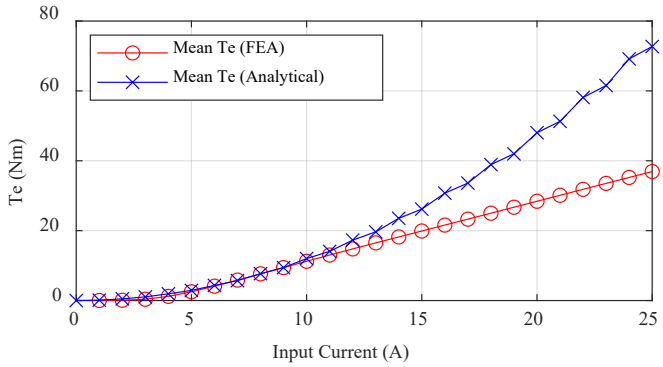


Figure 4.12. Comparison of mean torque calculation by the analytical model without the inclusion of non-linearity in magnetic permeability and FEA.

Despite these limitations, the MWFA method significantly outperforms traditional numerical methods regarding computational efficiency, with simulation runtimes of approximately 15 seconds per iteration compared to multiple hours required by equivalent FEA simulations. This characteristic makes MWFA particularly suited for initial rapid iterative evaluations, facilitating early-stage design optimizations before more detailed numerical analyses.

4.1.7 Characteristics of MWFA

Although the MWFA-based approach offers computational efficiency and rapid assessment in early-stage design iterations, its overall applicability in the design process of modern electrical machines and viability for design process optimization is constrained by several fundamental assumptions. These limitations often necessitate extensive use of numerical modeling techniques, such as three-dimensional FEA, to achieve design accuracy in diverse operating conditions and more complex geometries. The key limiting assumptions of conventional MWFA can be summarized as follows.

4.1.7.1 Linear Magnetic Characteristics

In the derivation of flux linkages and inductances for classic winding function analysis (WFA) which formulates the foundation of MWFA, the magnetic permeability of the core material is considered infinite, rendering the magnetomotive-force (MMF) drop across the core material to be non-existent. This assumption leads to an overestimation of the airgap MMF and the relationship between applied MMF and the airgap MMF to be linear. Whereas in reality neither is the MMF drop in the machine's ferromagnetic core negligible, nor does it follow the applied MMF in a linear relationship. The MMF drop in the core is proportional to the magnetic path reluctance offered by the core which depends on two main factors: the core's geometry and material's magnetic permeability.

4.1.7.2 Planar Airgap Topology

MWFA usually assumes a uniform (planar) airgap topology, which disregards any axial or radial variations in airgap length. Modern designs, especially those facilitated by AM, incorporate contoured or non-uniform airgaps to enhance performance parameters. Conventional MWFA formulations lack the mechanisms to account for such three-dimensional complexities in the machine structure, limiting their effectiveness when considered for these newer design possibilities.

4.1.7.3 Non-Skewed Structure

Another simplifying assumption in MWFA is the treatment of the machine as having a perfectly symmetric, non-skewed structure along the direction normal to the flow of flux. In practice, slot skewing is a common design technique employed to mitigate torque ripples and reduce harmonic content in electrical machines. Since MWFA inherently assumes a non-skewed structure, it fails to estimate the performance enhancements and ripple reduction effects introduced by skewed configurations. This further limits its accuracy and viability for the iterative design process.

4.1.7.4 Implications for The Design Process

Although MWFA offers rapid performance parameter estimation, the inherent simplifying assumptions limit its use to early design iterations. As design complexity increases, particularly with the integration of non-linear core material behavior, contoured airgaps, and skewed machine structures, the dependence on more detailed numerical modeling methods increases. Addressing these limitations is essential for

reducing the dependency on computationally intensive numerical methods in the design process. The modifications proposed in subsequent sections aim to extend MWFA's accuracy and applicability by incorporating correction factors and hybrid strategies that account for the non-linear, three-dimensional characteristics of modern electrical machines.

4.2 Incorporation of Core Material's Electromagnetic Characteristics

This section details a hybrid approach [Publication-VI], [Publication-VII] to overcome that limitation by introducing an airgap MMF reduction factor, namely permeability factor, into the fundamental MWFA equations. The key objective is to map how the effective permeability of the core material changes with the operating current, then incorporate that permeability factor into the winding function formulation to achieve more realistic performance estimate.

4.2.1 The Proposed Strategy

The standard formulations for airgap MMF, flux linkage and Inductance calculation for WFA are presented as follows,

$$\mathcal{F}_x(\theta) = N_x(\theta).\, i_x \tag{4.10}$$

$$\lambda_{xy} = \frac{\mu_o r l}{g} \int_0^{2\pi} \mathcal{F}_x(\theta)\, n_y(\theta) d\theta \tag{4.11}$$

$$L_{xy} = \frac{\lambda_{xy}}{i_x} = \frac{\mu_o r l}{g} \int_0^{2\pi} N_x(\theta)\, n_y(\theta) d\theta \tag{4.12}$$

where (13) lays the foundation of the MWFA approach. These formulations assume that the ferromagnetic core has negligible reluctance. In other words, the analytical derivation treats magnetic permeability as infinite, resulting in all thew applied MMF to appear across the airgap alone. Consequently, analytical predictions while ignoring the MMF-drop in the core can overestimate inductances and torque values at higher excitation.

In reality, however, the MMF drop within the core is non-negligible. Its value is dictated by the magnetic path reluctance of the core, which in turn depends on both its geometry and the material's magnetic permeability. As a consequence, the effective airgap MMF, and hence the computed flux linkages and inductances, are lower than the calculated values of (10)-(12). To incorporate this effect of reduced airgap MMF a permeability factor, k_p, is introduced into the MWFA formulations. The modified expressions become,

$$\mathcal{F}_x(\theta) = k_p N_x(\theta).\, i_x \tag{4.13}$$

$$\lambda_{xy} = k_p \frac{\mu_o r l}{g} \int_0^{2\pi} \mathcal{F}_x(\theta)\, n_y(\theta) d\theta \tag{4.14}$$

$$L_{xy} = k_p \frac{\lambda_{xy}}{i_x} = \frac{\mu_o r l}{g} \int_0^{2\pi} N_x(\theta)\, n_y(\theta) d\theta \tag{4.15}$$

The specific value of permeability factor is defined by the ratio of the airgap magnetic reluctance ($\mathcal{R}_{ag}$) to the total reluctance ($\mathcal{R}_{ag} + \mathcal{R}_c$), where $\mathcal{R}_c$ represents the core's reluctance. It can be expressed as,

$$k_p = \frac{\mathcal{R}_{ag}}{\mathcal{R}_{ag} + \mathcal{R}_c} = \frac{l_g}{l_g + l_c/\mu_r} \tag{4.16}$$

where, l_g and l_c denote the effective magnetic path lengths of the airgap and the core, respectively, while μ_r is the relative permeability of the core material. While the magnetic path lengths in airgap and the core can be estimated analytically with a fair degree of accuracy, the relative permeability of the material depends on the specific operating point of the machine core on the BH-curve of the material.

4.2.2 Determination of Machine Core's Operating Point on the BH-Curve

To accurately integrate material's electromagnetic characteristics into MWFA, it is essential to determine the precise operating point of the machine's ferromagnetic core on the material's BH-curve. The operating point depends primarily upon the magnetic field intensity (H) experienced by the core material under different input current conditions. Correct identification of this operating point ensures that the permeability factor, k_p, introduced in the previous subsection reflects realistic magnetic conditions, thereby enhancing the analytical model's predictive accuracy in all the operation regions of the machine.

The magnetic field intensity (H) within a simplistic core structure is mathematically defined as,

$$H = \frac{NI}{l} \tag{4.17}$$

where N represents the number of winding-turns, I is the input current, and l denotes the mean magnetic path length within the core. For a given electrical machine geometry and winding configuration, the magnetic field intensity can be directly related to the input current through a geometry-dependent proportionality constant Δ, as expressed in the simplified form,

$$H = \Delta\, I \tag{4.18}$$

where Δ controls the proportionality of the magnetic field intensity relative to the input current, as illustrated conceptually in Figure 4.13 (a)-(d). Determining the appropriate value of Δ is crucial, as it directly affects the accuracy of mapping the machine's operating zone onto the BH-curve and subsequently impacts the calculated permeability factor.

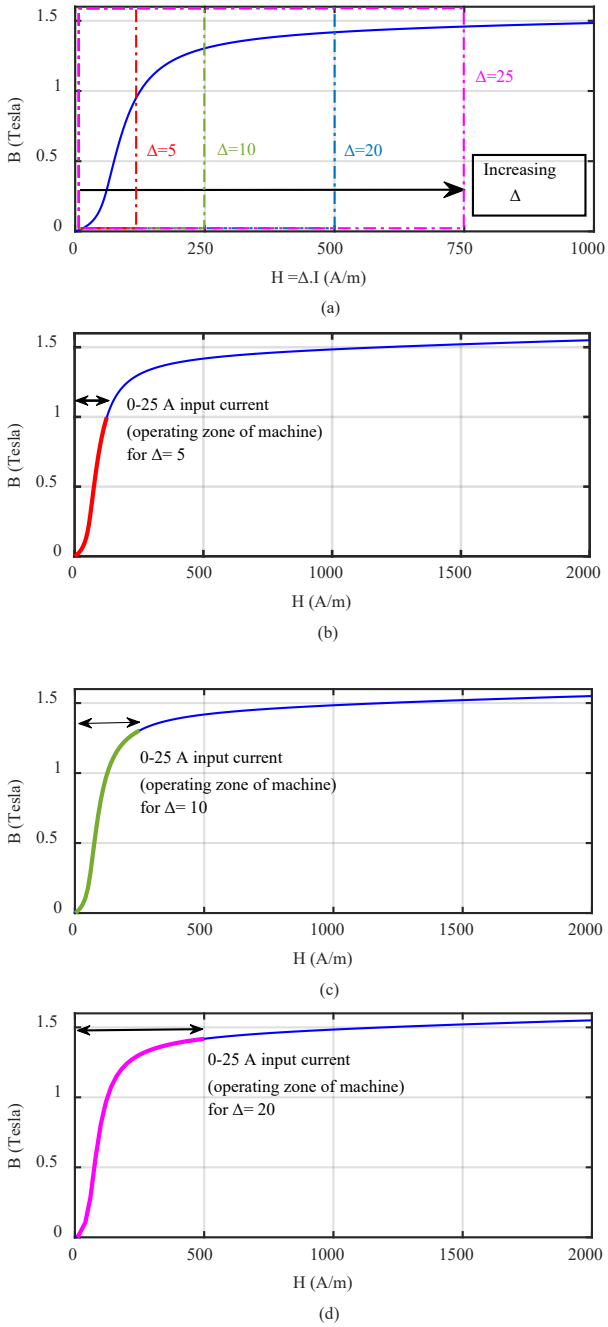


Figure 4.13. (a) BH-curve mapping against input current for (b) Δ = 5, (c) Δ = 10, (d) Δ = 20.

The specific value of Δ is established through an iterative hybrid FEA-Analytical calibration process, illustrated by the algorithmic block diagram in Figure 4.14. This hybrid approach systematically combines numerical accuracy with analytical efficiency and involves the following key steps.

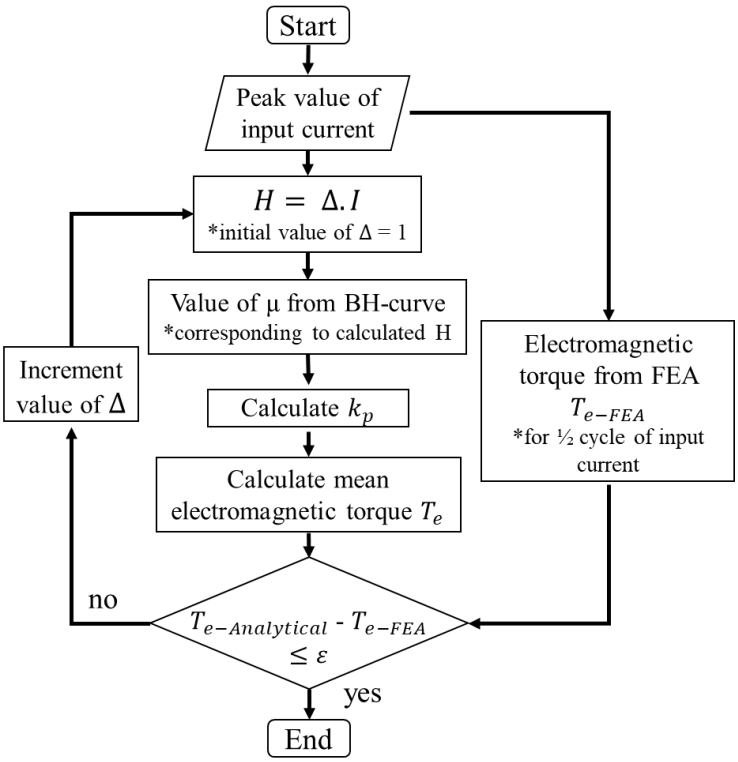


Figure 4.14. Block-diagram of the iterative procedure for determination of machine's operating point on BH-curve and subsequent calculation of saturation factor k_p as a function of input current.

4.2.2.1 FEA Benchmarking

The reference or benchmark value of torque is obtained from 2D-FEA for a half cycle of rated input current applied to the fundamental symmetrical section of machine geometry. The value of ε decides the error limit or accuracy of mapping.

4.2.2.2 Analytical Torque Estimation and Iterative Calibration

For the benchmark input current, an initial guess of the proportionality constant Δ is made. Using this value, the magnetic field intensity is calculated. The corresponding magnetic flux density (B) and relative permeability values are then extracted from the known BH-curve of the selected core material. Using these values, the permeability factor is computed based on equation (16) from the previous subsection. Incorporating this computed k_p value into the MWF, a corrected analytical torque is calculated. This analytical torque value is then directly compared with the corresponding FEA benchmark value.

4.2.2.3 Convergence and accuracy criterion

If the difference between the analytical torque and the benchmark FEA torque exceeds the pre-defined tolerance ε, the value of Δ is adjusted iteratively. This iterative calibration continues until the analytical and benchmark torque values converge within the acceptable tolerance, establishing the final optimized value of Δ. Figure 4.14(b)–(d) visually demonstrates this iterative procedure, showing BH-curves mapped against a representative input current range (0–25 A) for various values of Δ. Upon convergence

to the desired accuracy ε, the value of Δ is finalized, accurately defining the machine's operational mapping onto the BH-curve.

Once optimized, the determined proportionality constant (Δ) enables straightforward estimation of the core's operating point on the material BH-curve for any input current level. For computational efficiency, the corresponding relative permeability (μ_r) values for the complete operating current range are precomputed and stored in lookup tables. During the online simulation phase, MWFA rapidly retrieves the appropriate permeability factor from these tables, facilitating fast yet precise analytical performance evaluation.

As an illustrative example, the machine under investigation in this chapter utilizes M400-50A as the core material. The iterative hybrid calibration procedure described above yields an optimal Δ value of approximately 13.5 for this specific geometry and material. Consequently, the relative permeability for M400-50A, ranging from zero up to a maximum of approximately 64,868.9, leads to calculated permeability factor values within a realistic range, typically $0 < k_p < 1$.

4.2.3 Results and Validation

The iterative hybrid FEA-analytical mapping procedure outlined in the previous subsection was implemented to determine the optimized proportionality constant for the reference SynRM. After iterative calibration, the optimal value of Δ was identified to be approximately 13.5. This optimized value enabled precise mapping of the core's operational points onto the BH-curve for the input current range of 0–25 A. Although this range exceeds the machine's rated current of 20.3 A, it was deliberately selected to evaluate the MWFA model's accuracy and robustness under overload conditions, thus ensuring comprehensive validation.

Figure 4.15 illustrates the machine's calculated operational zone. Specifically, Figure 4.15(a) depicts the mapped BH-curve corresponding to the determined value of Δ, clearly indicating the operating points at different input currents. The associated variation in relative permeability is shown in Figure 4.15(b), while Figure 4.15(c) presents the computed permeability factor across the entire evaluated input current range. The computed k_p values logically remain within realistic boundaries ($0 < k_p \leq 1$), demonstrating the analytical model's effectiveness in capturing the effect of material's non-linear magnetic characteristics.

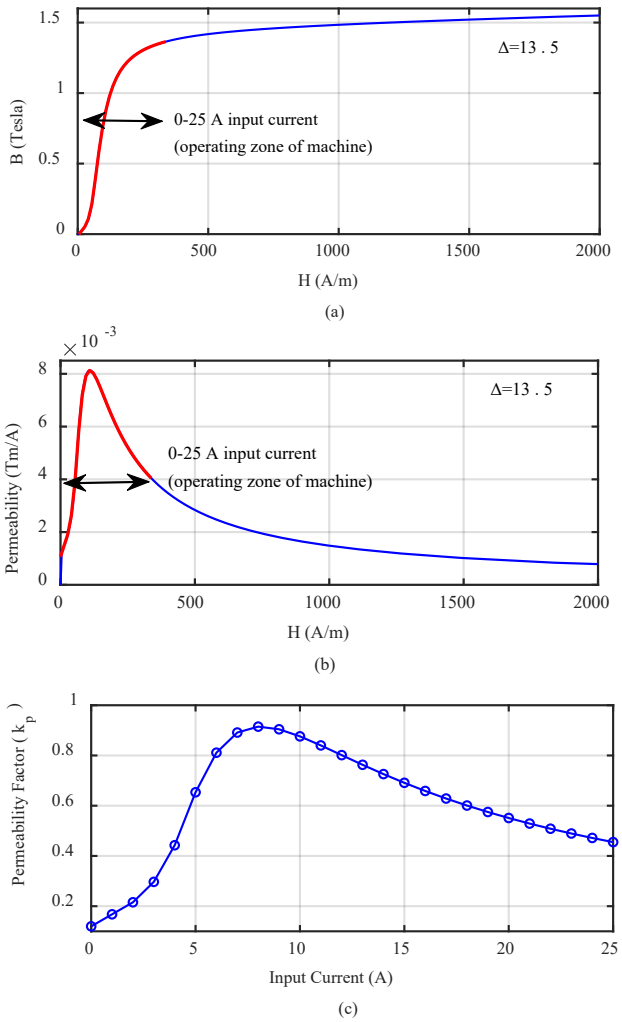


Figure 4.15. Operating zone of the machine under consideration on (a) BH-curve, (b) Permeability curve, (c) Value of k_p versus input current.

To further evaluate the impact of incorporating core material's electromagnetic characteristics, airgap MMF distributions calculated analytically, both without and with the inclusion of the permeability factor, are compared for two distinct current levels (10A and15A peak) at a mechanical load angle of $\delta = 10°$. As shown in Figure 4.16(a) and (b), neglecting core material's characteristics overestimates the airgap MMF significantly. Conversely, when the permeability factor is employed, the calculated airgap MMF is effectively reduced reflecting the consideration of MMF-drop in the machine core.

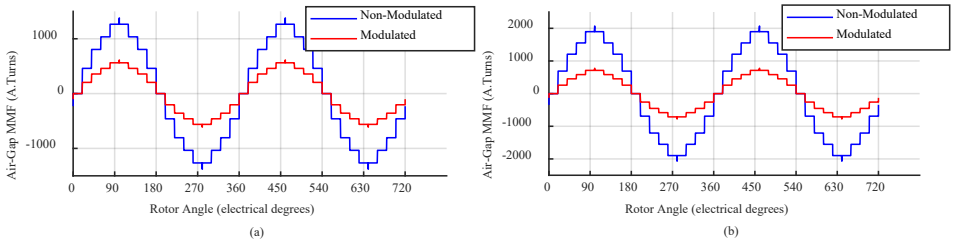


Figure 4.17. Airgap MMF with and without the inclusion of saturation factor k_p, for input current of (a) 10A, (b) 15A.

These material-characteristic dependent corrections in airgap MMF directly influence electromagnetic torque calculations. Figure 4.17(a) and (b) illustrate torque waveform comparisons between MWFA predictions (with and without permeability factor correction) and corresponding FEA results at input currents of 10 A and 15 A respectively, maintaining the same mechanical load angle i.e. $\delta = 10°$. The inclusion of the permeability factor evidently improves analytical torque predictions, aligning closely with FEA-derived torque waveforms and thereby validating the enhanced MWFA formulation's accuracy.

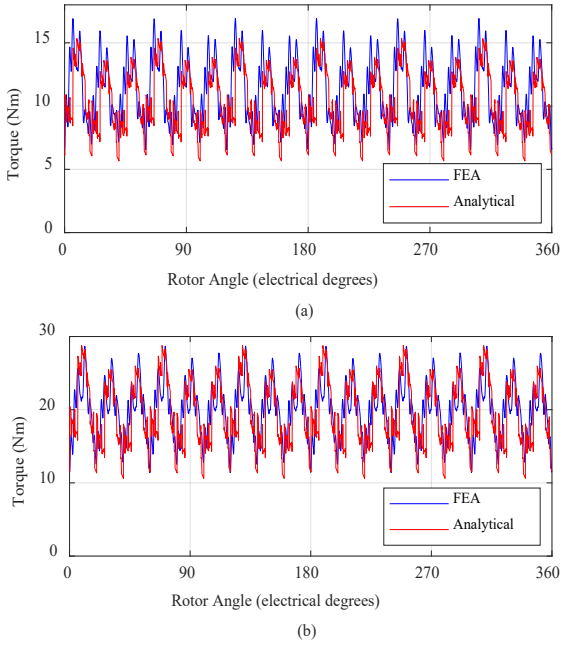


Figure 4.17. Torque waveform comparison with FEA results, δ =10˚ mechanical (a) 10A, (b) 15A.

For additional validation over the complete range of input current, Figure 4.18 presents a comparison between the mean electromagnetic torque calculated by the analytical MWFA model without incorporating core material non-linearity and corresponding FEA results across the evaluated input current range. As expected, the linear MWFA predictions exhibit a purely quadratic relationship with input current, significantly diverging from numerical FEA results, particularly at higher input currents where magnetic saturation becomes prominent.

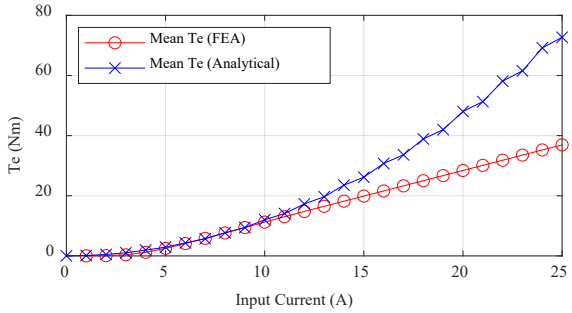


Figure 4.18. Comparison of mean torque calculation by the analytical model without the inclusion of core material's electromagnetic characteristics and FEA.

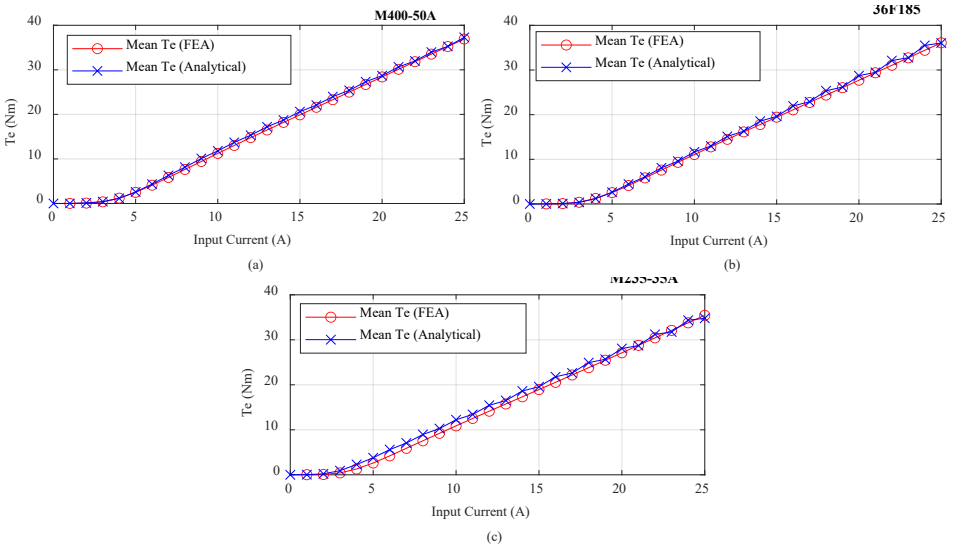


Figure 4.19. Comparison of mean torque calculation by the proposed analytical model (under non-linear magnetic condition) and FEA for different materials (a) M400-50A, (b) 36F185, (c) M235-35A.

On the contrary, after integrating the permeability factor into the analytical MWFA formulation, the analytical torque estimations closely align with FEA results across the full input current range, as depicted in Figure 4.19(a), for core material M400-50A. To further illustrate the accuracy and general applicability of this modeling strategy, additional validations using alternative core materials, 36F185 and M235-35A, are presented in Figure 4.19(b) and (c). In each case, the proposed modification in the analytical model maintains good agreement with the corresponding FEA results, reinforcing its effectiveness and diverse utility across varying material properties.

The comparative evaluation of simulation runtimes, benchmarked on the identical computational resource of a 12-core modern CPU, further reinforces the practical utility and computational efficiency of the proposed hybrid MWFA methodology. As summarized in Table 4.2, the initial hybrid calibration procedure, performed only once per machine geometry and core material, typically requires approximately 15–20 minutes. After this calibration, subsequent iterative analyses leveraging the MWFA approach are completed in roughly 15 seconds per iteration.

Table 4.2. Simulation runtime comparison for same temporal resolution and machine runtime (4 sec), FEA vs Analytical.

Type of Modeling	Simulation Runtime	
Analytical MWFA	tuning via hybrid FEA-Analytical procedure *(one-time procedure)	15–20 minutes
	each subsequent iteration	15 seconds
FEA	each individual iteration	Approx. 50 Hrs.

Conversely, achieving similar precision and temporal resolution via full-scale three-dimensional FEA demands approximately 50 hours per iteration. This stark contrast in computational times validates the fundamental hypothesis that improving the accuracy and applicability of MWFA enables the analytical method to significantly alleviate computational burdens traditionally associated with iterative numerical simulations. Consequently, the refined MWFA framework not only accurately accounts for core saturation effects but also fundamentally enhances the iterative design workflow – shifting the majority of iterative computational burden from resource-intensive FEA simulations to rapid and efficient analytical evaluations. This transition is particularly advantageous in the context of additive manufacturing-enabled electrical machines, where rapid, precise, and computationally efficient design iterations are critical for achieving optimal, customized machine performance.

Following this detailed analysis, it is evident that by far, the second hypothesis has indeed been proved. The hybrid FEA-Analytical approach not only reduces the computational time and complexity associated with machine design analysis but also substantively enhances its suitability for iterative design processes. This streamlined approach allows for quicker iterative refinements in design.

4.3 Incorporation of Three-Dimensional Design Features

As previously outlined, conventional MWFA inherently assumes a three-dimensionally uniform machine geometry, neglecting critical three-dimensional variations such as contoured airgaps and skewed stator or rotor configurations. Addressing this limitation is essential for MWFA to effectively support the iterative design optimization process, especially in the context of advanced machine geometries enabled by AM. Although the proposed strategy presented here is applicable to various flux topologies, i.e. radial or axial, all subsequent modifications and explanations are provided in the context of the machine topology currently under consideration i.e. radial flux SynRM. The following subsections propose specific strategies and associated formulations to extend MWFA for incorporating these complex three-dimensional design features.

4.3.1 The Proposed Strategy

To effectively incorporate three-dimensional design features within the MWFA-based modeling framework, the proposed strategy [Publication-VIII] involves segmenting the machine geometry into discrete sections in axial direction. Each segment independently captures local variations in critical design parameters, including the airgap radius, airgap permeance function, winding functions, and turn functions. By discretizing the geometry into m segments, each with its own distinct characteristics, the inductance formulation can accurately represent the cumulative impact of axial variations.

Referring to the fundamental inductance formulation (2), all involved parameters are inherently functions of stator and rotor relative positions, expressed through the angles θ and β. For each axial segment *j* (j = 1, 2, ..., m), the inductance calculation is conducted separately as follows

$$L_{xy-j}(\theta_j) = \frac{\mu_0 2\pi}{n} r_j l_j \sum_{k=1}^{n} \left(P_j(\theta_j, \beta). N_{xj}(\theta_j, \beta). n_{yj}(\theta_j, \beta) \right)_k \tag{4.19}$$

where, r_j and I_j denote the mean airgap radius and axial length of the j-th segment, respectively. Similarly, $P_j(\theta_j, \beta)$, $N_{xj}(\theta_j, \beta)$ and $n_{yj}(\theta_j, \beta)$ represent the permeance, winding, and turn functions specific to segment θ. θ_j indicates the rotor angular position within the stator reference frame for the $j - th$ segment, allowing the model to reflect localized rotational asymmetries.

The total inductance of the machine, accounting for axial variations, is then obtained by summation of the inductances of individual segments as follows.

$$L_{xy}(\theta) = \sum_{j=1}^{m} L_{xy-j}(\theta_j) \tag{4.20}$$

$$\begin{aligned} L_{xy}(\theta) = \frac{\mu_0 2\pi}{n} \Bigg[& r_1 l_1 \sum_{k=1}^{n} \left(P_1(\theta_1, \beta). N_{x1}(\theta_1, \beta). n_{y1}(\theta_1, \beta) \right)_k \\ & + r_2 l_2 \sum_{k=1}^{n} \left(P_2(\theta_2, \beta). N_{x2}(\theta_2, \beta). n_{y2}(\theta_2, \beta) \right)_k + \cdots \\ & + r_m l_m \sum_{k=1}^{n} \left(P_m(\theta_m, \beta). N_{xm}(\theta_m, \beta). n_{ym}(\theta_m, \beta) \right)_k \Bigg] \end{aligned} \tag{4.21}$$

Through this segmented approach, MWFA effectively handles the complexity associated with three-dimensional geometric features, significantly enhancing its predictive accuracy while maintaining computational efficiency suitable for iterative design processes.

4.3.2 Formulation for Contoured Airgap Topology

As previously discussed, conventional MWFA inherently assumes a planar (uniform) airgap, neglecting axial variations introduced by contoured topologies. While the complexity of implementing these topologies in MWFA varies based on specific design constraints, the fundamental modification framework remains consistent. In the context of the radial flux SynRM under consideration, constraints implemented for airgap contouring specifically impact the effective airgap dimensions, whereas other machine parameters and material properties remain unchanged. The effect of specific design constraints on the formulation of MWFA under proposed strategy is discussed in the next subsection.

4.3.2.1 Effect of Design Constraints for Contoured Airgap Topology on MWFA Formulation

Considering the inductance formulation of MWFA (21), the terms contributing to inductance include the turn function, winding function, airgap permeance function, material permeability, and airgap surface area. The effects of airgap contouring on these terms, under previously described constraints of contoured airgap topology for radial

flux SynRM, are discussed as follows. Additionally, since the rotational symmetry along the axial direction is not altered under the currently discussed constraints of airgap contouring, $\theta_1 \dots \theta_m = \theta$.

1. **Turn Function and Winding Function**

   The winding parameters, including the number of winding-turns per slot, coil arrangement, and their spatial distribution around the stator periphery, remain unaffected by airgap contouring. Consequently, the turn and winding functions remain identical for each axial segment.

2. **Airgap Permeance Function**

   The airgap permeance function considers spatial variations in airgap thickness associated with stator and rotor design. Given that the constraints defining contoured airgap topology maintain uniform airgap thickness and unchanged stator slot layout, including slot openings, the permeance function remains identical for each axial segment.

3. **Airgap Surface Area**

   The most significant impact of airgap contouring arises from the increased airgap surface area. This increase, depicted in Figure 4.20, directly influences inductance calculations. Under the current constraints, the inductance formulation (21) reduces to,

$$L_{xy}(\theta) = \frac{\mu_0 2\pi}{n} [r_1 l_1 + r_2 l_2 + \cdots + r_m l_m] \sum_{k=1}^{n} \left(P(\theta,\beta).N_x(\theta,\beta).n_y(\theta,\beta) \right)_k \quad (4.22)$$

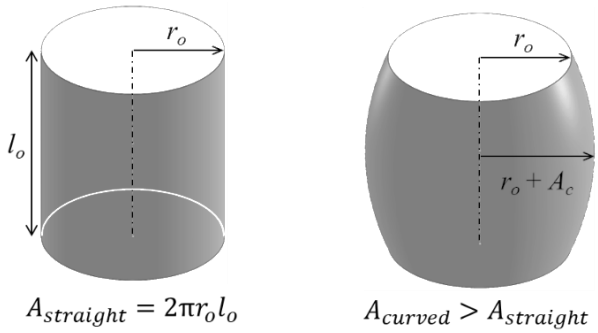


Figure 4.20. Change in airgap surface area due to contouring.

The increased airgap surface area is dependent on the contour shape and amplitude. Since the contour utilized in this current example is sinusoidal, instead of segmenting the machine, it can be accounted for by incorporation of a proportionality factor k_c in inductance formulation of MWFA. The value of k_c is directly proportional to increased airgap surface area due to the contour and is given by

$$k_c = A_{curved}/A_{straight} \quad (4.23)$$

The contour equation (as defined in **2.18**) becomes

$$r(x) = r_o + A_c \sin\left(\frac{\pi x}{l_o}\right) \qquad 0 \le x \le l_o \tag{4.24}$$

The surface area for the contoured airgap is calculated by

$$A_{curved} = 2\pi \int_0^{l_0} \left[r_0 + A_c \sin\left(\frac{\pi x}{l_o}\right)\right] \sqrt{1 + \left(\frac{\pi A_c}{l_o} \cos\left(\frac{\pi x}{l_o}\right)\right)^2}\, dx \tag{4.25}$$

where the surface area of the straight airgap surface is simply calculated by $2\pi r_0 l_0$.

4. Magnetic Path Reluctance

Under the specific constraints of contouring, individual dimensions, i.e. the thickness of the stator-rotor components remain unchanged. This makes the machine's operating point on the BH-curve largely unaffected. However, contouring increases the magnetic path length around the periphery of the machine, consequently increasing magnetic path reluctance. To incorporate this effect, the permeability factor formulation is adjusted by introducing the proportionality factor k_c.

$$k_p = \frac{\mathcal{R}_{ag}}{\mathcal{R}_{ag} + \mathcal{R}_c} = \frac{l_g}{l_g + k_c l_c/\mu_r} \tag{4.26}$$

The Inductance formulation of (21), with incorporated effect of contoured airgap topology, essentially becomes,

$$L_{xy}(\theta) = \frac{\mu_0 k_p k_c 2\pi r_o l_o}{n} \sum_{k=1}^{n} \Big(P(\theta,\beta).N_x(\theta,\beta).n_y(\theta,\beta)\Big)_k \tag{4.27}$$

4.3.2.2 Results and Analysis

The proposed analytical methodology incorporating the proportionality factor k_c and permeability correction factor k_p has been validated through comparative analysis against FEA results. A parametric sweep of the contour amplitude A_c, varying in consecutive increments of 5 mm, was performed on the benchmark radial-flux SynRM.

Figure 4.21(a) illustrates the proportionality factor as a function of contour amplitude. As the contour amplitude increases, k_c exhibits a nonlinear relationship, underscoring that the effective increase in airgap surface area does not follow a linear trend, but instead depends specifically on the contour's geometry. Figure 4.21(b) shows the corresponding variation of the permeability correction factor as a function of input current for different contour amplitudes. This factor demonstrates a decreasing trend with increasing contour amplitude, reflecting the higher magnetic reluctance due to the extended magnetic path length imposed by the contouring, thus offsetting some of the benefits gained by increased airgap surface area.

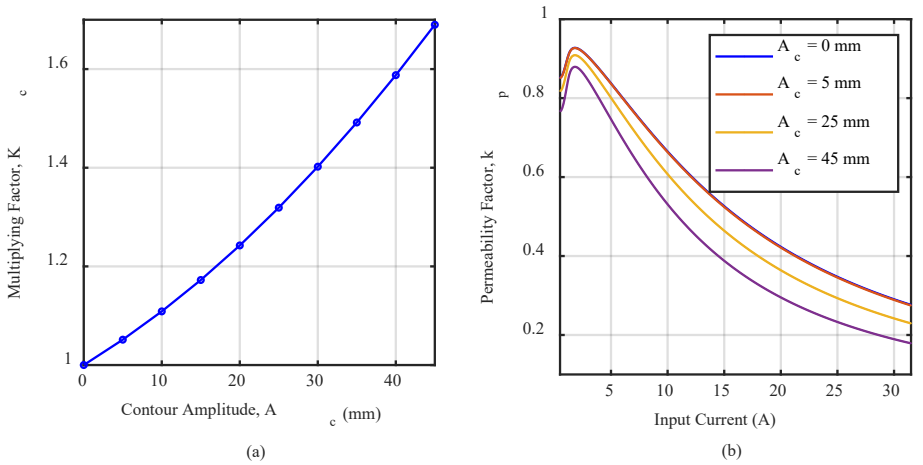


Figure 4.21. (a) Values of proportionality factor k_c vs. the contour amplitude, and (b) Values of permeability factor k_p vs. the input current, for different values of contour amplitude A_c.

To determine the validity of the proposed MWFA strategy, comparisons of torque waveforms under various operational scenarios were conducted. Figure 4.22 illustrates torque estimation for a machine with a planar airgap (i.e. $\boldsymbol{A_c}$ = 0 mm) at a loading angle δ = 10° and an input current of 10A-peak. The MWFA model, after incorporating the correction factors, accurately aligns with the FEA-calculated values, in terms of torque profile and the mean torque (T_{e-MWFA}= 5.0775 Nm versus T_{e-FEA} = 5.2729 Nm). Excluding these correction factors results in significant deviation i.e. T_{e-MWFA}= 7.5687 Nm, as illustrated in the figure, establishing the validity and efficacy of the proposed strategy.

Figure 4.23 extends this analysis to a contoured airgap machine ($\boldsymbol{A_c}$ = 5mm) under the same operating conditions. The MWFA model, without correction factors, predicts a significantly higher torque (T_{e-MWFA} = 7.5687 Nm), whereas the corrected MWFA closely aligns with the FEA result (T_{e-MWFA} = 5.4385 Nm compared to T_{e-FEA} = 5.6534 Nm).

Figure 4.24 illustrates torque profiles for an airgap contour amplitude of 25mm under different operational conditions (δ = 20°, input current of 20A-peak). Without correction factors, the overestimated mean torque value through MWFA comes out to be 56.8850 Nm. Whereas, incorporating the proposed correction factors notably lowers the deviation, aligning closely with the FEA-derived torque (T_{e-MWFA} = 26.4262 Nm versus T_{e-FEA} = 25.0032 Nm). Table 4.3 summarizes the quantified percentage deviations between MWFA-predicted torque and corresponding FEA results for the above presented results.

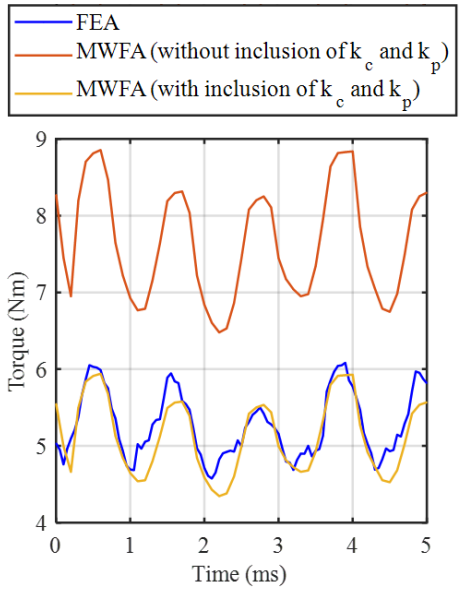


Figure 4.22. The generated torque in case of a planar airgap machine ($\boldsymbol{A_c}$= 0), under loading angle (δ = 10°), stator current (I_{in} = 10A-peak).

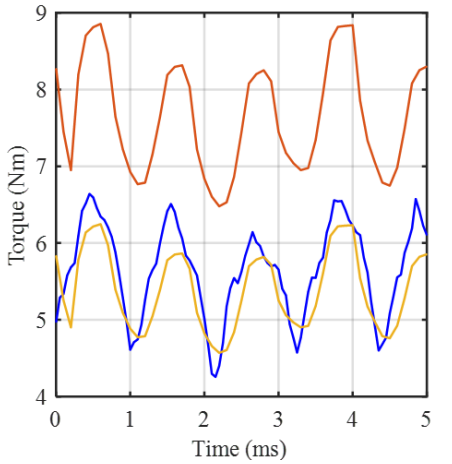


Figure 4.23. The generated torque in case of a contoured airgap machine ($\boldsymbol{A_c}$= 5mm), under loading angle (δ = 10°), stator current (I_{in} = 10A-peak).

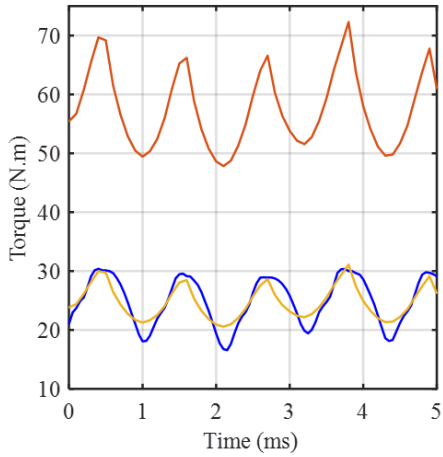


Figure 4.24. The generated torque in case of a contoured airgap machine (A_c= 25mm), under loading angle (δ = 20°), stator current (I_{in} = 20 A-pk), while the mean torque using FEA is (T_{e-FEA} = 25.0032N-m), and through MWFA (T_{e-MWFA} = 56.8850N-m without proposed strategy) and (T_{e-MWFA}= 26.4262N-m with proposed strategy).

Table 4.3. Summary of MWFA-Calculated Torque Deviations from FEA.

Airgap Contour Amplitude, A_c (mm)	Load Angle, δ (°)	Input Current (A)	T_{e-FEA} (Nm)	T_{e-MWFA} without correction (Nm)	Deviation without correction (%)	T_{e-MWFA} with correction (Nm)	Deviation with correction (%)
0	10	10	5.27	7.95	+ 50.8 %	5.0775	- 3.7 %
5	10	10	5.65	7.56	+33.9 %	5.4385	-3.8 %
25	20	20	25.00	56.88	+ 127.5 %	26.4262	+ 5.7 %

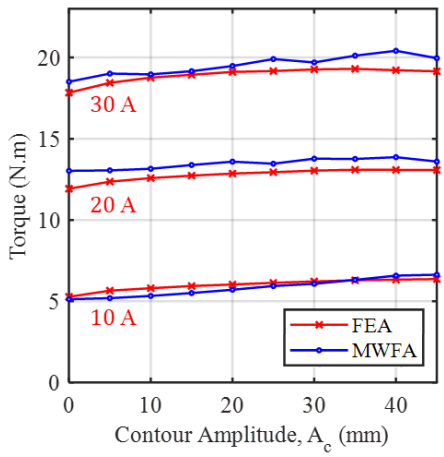


Figure 4.25. The comparison of generated torque calculated using FEA (blue) and proposed MWFA (red) under loading angle (δ = 10°), stator current (I_{in} = 10, 20 and 30A_{peak}).

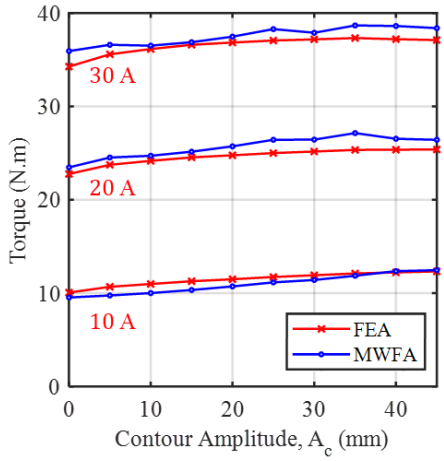


Figure 4.26. The comparison of generated torque calculated using FEA (blue) and proposed MWFA (red) under loading angle (δ = 20°), stator current (I_{in} =10, 20 and 30A_{peak}).

These results and analyses conclusively demonstrate that the proposed MWFA modifications effectively capture the complex relationship between geometric and magnetic factors in machines with contoured airgaps. Consequently, this enhanced analytical model proves reliable for accurate, computationally efficient performance prediction and iterative design optimization in advanced machine designs enabled by additive manufacturing.

4.3.3 Formulation for Slot Skewing

Skewing in electrical machine structures is utilized to mitigate torque ripple and reduce spatial harmonics, particularly the slotting harmonics (SH). Incorporating slot skewing within the MWFA framework enhances its capability to accurately represent practical machine behaviors, broadening its application to more realistic machine designs. Due to its extensive use in induction motors, the implementation and validation of slot skewing in MWFA is illustrated through an induction motor.

Incorporating slot skewing into MWFA necessitates the introduction of angular displacement parameter, termed as the skew angle (α_{sk}), into the fundamental formulation of the proposed strategy of (4.19)–(4.21). The machine geometry is divided into m segments axially, each displaced by an incremental skew angle from the previous segment. Each segment independently captures local variations in critical design parameters, including airgap permeance, winding, and turn functions, reflecting the skewed configuration.

For a total skew angle α_{sk} divided uniformly across m axial segments, each segment experiences an incremental angular shift, denoted as $\Delta\alpha$, illustrated in Figure 4.27 and calculated by

$$\Delta\alpha = \alpha_{sk}/m \tag{4.28}$$

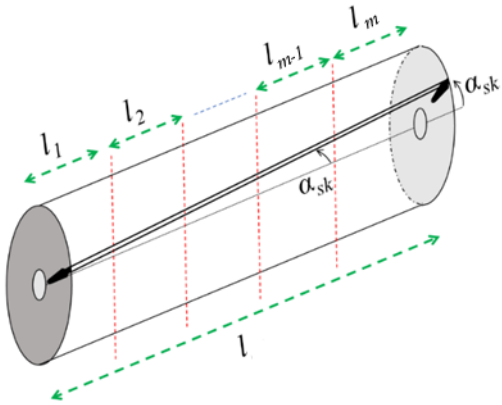


Figure 4.27. The illustration of rotor segmentation and skew angle.

In each axial segment j (j = 1, 2, …, m), the rotor's angular position θ_j relative to the stator frame is adjusted to reflect the cumulative skew, formulated as

$$\theta_j = \theta + (j-1)\,\Delta\alpha \tag{4.29}$$

Utilizing these modified rotor positions, the inductance calculation per axial segment follows the generalized form established previously in (19)-(21), capturing segment-specific winding and airgap functions affected by skew.

$$L_{xy-j}(\theta_j) = \frac{\mu_0 2\pi}{n} r_j l_j \sum_{k=1}^{n} \left(P_j(\theta_j,\beta).N_{xj}(\theta_j,\beta).n_{yj}(\theta_j,\beta) \right)_k \tag{4.30}$$

The total inductance, considering skewing, is obtained by aggregating the individual inductance of each segment along the axial direction.

$$L_{xy}(\theta) = \sum_{j=1}^{m} L_{xy-j}(\theta_j) \tag{4.31}$$

This segmented skewing approach effectively incorporates the spatially distributed angular displacement into MWFA, significantly enhancing the analytical method's capability to accurately represent torque ripple reductions and harmonic attenuation associated with skewed structures.

4.3.3.1 Results and Analysis

The proposed slot skew formulation within MWFA was validated through an induction motor whose key specifications are summarized in Table 4.4. The validation employs numerical simulations and experimental data, confirming the efficacy of MWFA in estimating reductions in SH components and the attenuation of torque ripple, thereby extending MWFA's practicality to skewed machine topologies.

Table 4.4. Design Parameters of Induction Motor.

Parameter	Symbol	Value	Parameter	Symbol	Value
Rated speed	N_r	1400 rpm@50 Hz	**Number of poles**	P	4
Rated power	P_r	18 kW@50 Hz	**Number of rotor bars skewed**	N_{rb}	40
Connection	Y, Δ	Star (Y)	**Number of stator slots**	Ns	48
Power factor	cosϕ	0.860			

The proposed MWFA approach employed to compute stator-rotor mutual inductance profiles essential for calculating machine performance parameters is illustrated in Figure 4.28 (a). The inductances are calculated by dividing the rotor axially into four equal segments, each shifted with incremental angular shift for equivalent skew angle of one stator slot pitch. Summation of these segmented inductances smooths the overall inductance profile, effectively attenuating slot-related ripples, as illustrated in Figure 4.28 (b).

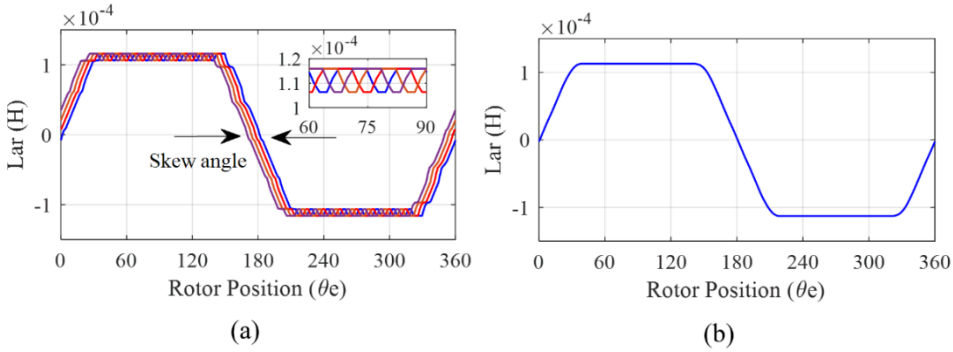


Figure 4.28. The stator-rotor mutual inductance, (a) for each segment (4 segments), (b) the overall inductance profile.

Figure 4.29 demonstrates that rotor slot skewing not only smoothens stator-rotor mutual inductances but also significantly reduces ripple magnitudes in stator-stator self (L_{aa}), stator-stator mutual (L_{ab}), stator-rotor (L_{ar}), and rotor-rotor (L_{rr}) inductances. Comparative analysis of the plots clearly highlights the reduction in peak-to-peak ripple magnitude when rotor slot skew is considered.

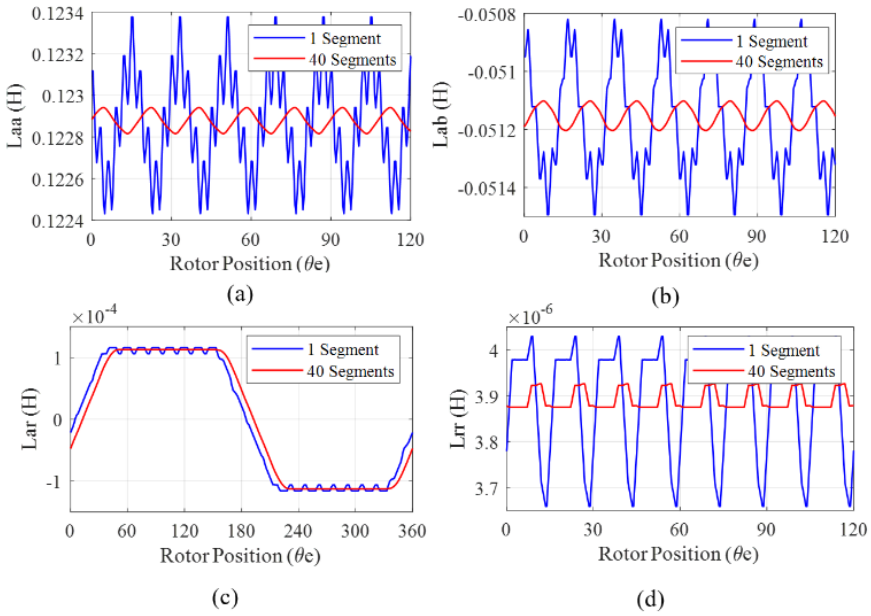


Figure 4.29. The calculated inductances with (red) and without (blue) rotor slots skew, (a) stator to stator self (L_{aa}), (b) stator to stator mutual (L_{ab}), (c) stator to the rotor (L_{ar}), and (d) rotor to rotor (L_{rr}) concerning the rotor position.

Similarly, the inductance derivatives concerning rotor position also exhibit significant reduction in ripples upon rotor skew inclusion, as shown in Figure 4.30. These reduced ripples directly correlate with reduced torque ripple and smoother current waveforms, significantly improving the machine's operational characteristics.

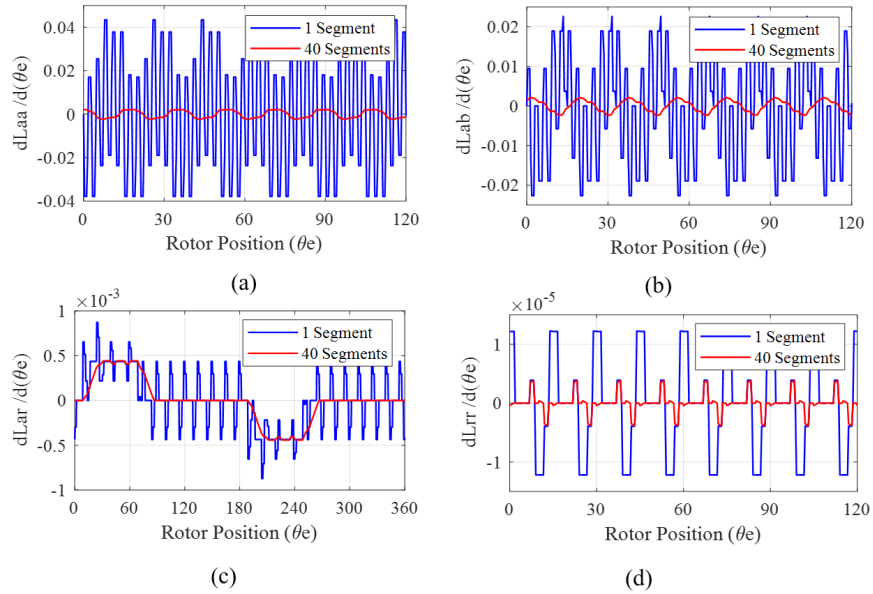


Figure 4.30. The derivative of the inductances with (red) and without (blue) rotor slot skews (a) stator to stator self (L_{aa}), (b) stator to stator mutual (L_{ab}), (c) stator to the rotor (L_{ar}), and (d) rotor to rotor (L_{rr}) with respect to the rotor position.

The comparative simulation results of phase currents and torque waveforms for both skewed and non-skewed rotor conditions are presented in Figure 4.31. The currents with rotor slot skew (Figure 4.31(b)) exhibit reduced harmonic distortion compared to the non-skewed rotor (Figure 4.31(a)). Torque profiles further highlight this improvement, with reduced ripple amplitudes clearly observable in Figure 4.31 (c) and (d). As stated earlier too, slot skewing predominantly targets attenuation of slotting harmonics (SH). Figure 4.32 depicts how rotor skew significantly reduces the principal slotting harmonics, SH1 and SH2. Theoretically predicted frequencies of these harmonics were calculated using (31).

$$f_{sh} = \left[(kn_b \pm n_d)\left(\frac{1-s}{P}\right) \pm v \right] fs \tag{4.32}$$

where slip (s), number of rotor bars (n_b), and pole pairs (P) directly influence harmonic frequencies. For the machine under test (40 rotor bars, two pole pairs, at 0.0067 slip), SH1 and SH2 theoretically appear at 883 Hz and 983 Hz, respectively. With skew, these harmonics attenuate from 0.04922 A and 0.0617 A to 0.00398 A and 0.00914 A.

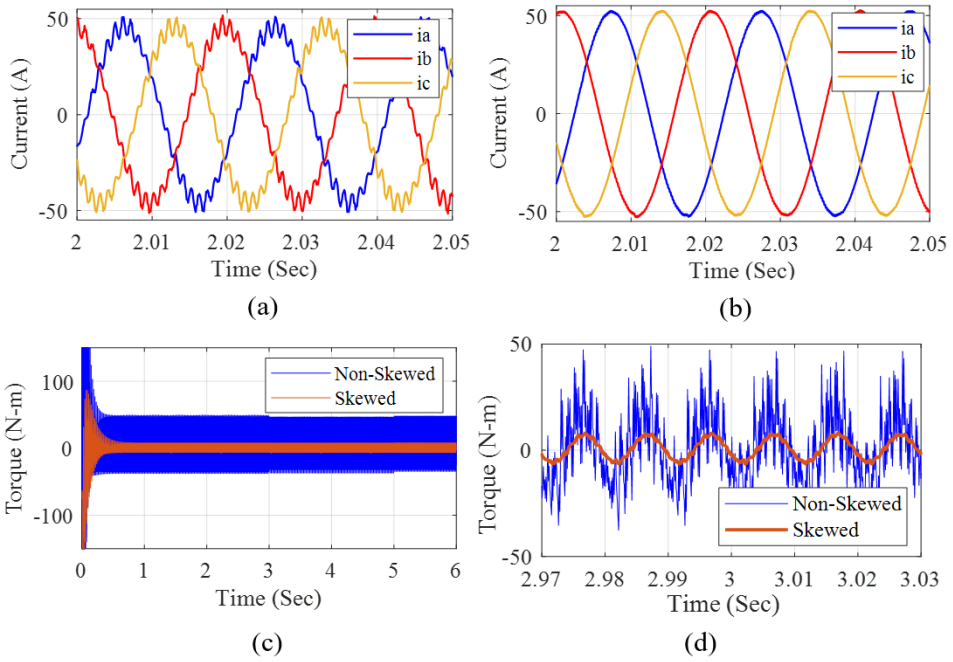


Figure 4.31. The stator currents with the rotor in (a) 2D without slot skew, (b) 3D with slot skew equal to one stator slot pitch, (c) the comparison of torque profile with and without rotor slot skews, (d) the zoomed comparison of torque profile with and without skews.

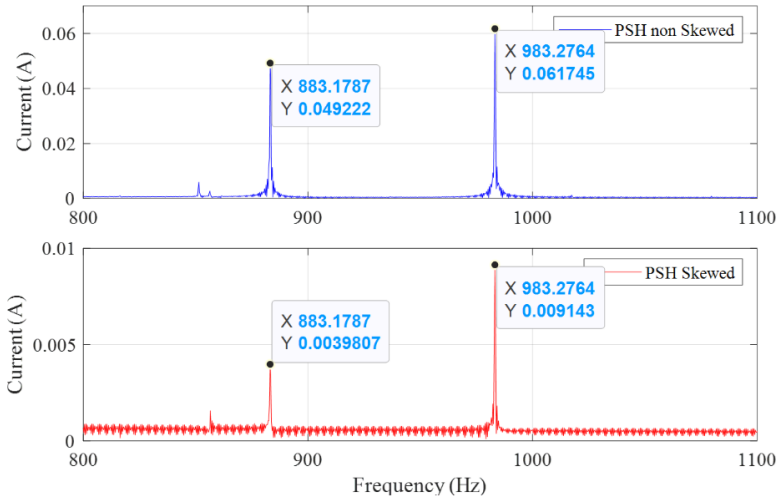


Figure 4.32. The development of PSH1 and PSH2 with and without slot skew in phase current.

Further analysis summarized in Table 4.5 and illustrated in Figure 4.33 illustrates slotting harmonics variations with slip, confirming the method's robustness under various load conditions.

Table 4.5. The Development of PSH with Skewed Rotor.

Simulation slip (s)	**RSH1**		**RSH2**	
	(Hz)	**(A)**	**(Hz)**	**(A)**
0.0030	946.96	0.00047	1047	0.0005
0.035	914.90	0.00231	1015	0.0048
0.05	899.90	0.00332	1000	0.0068
0.0667	883.17	0.00454	983.27	0.0075

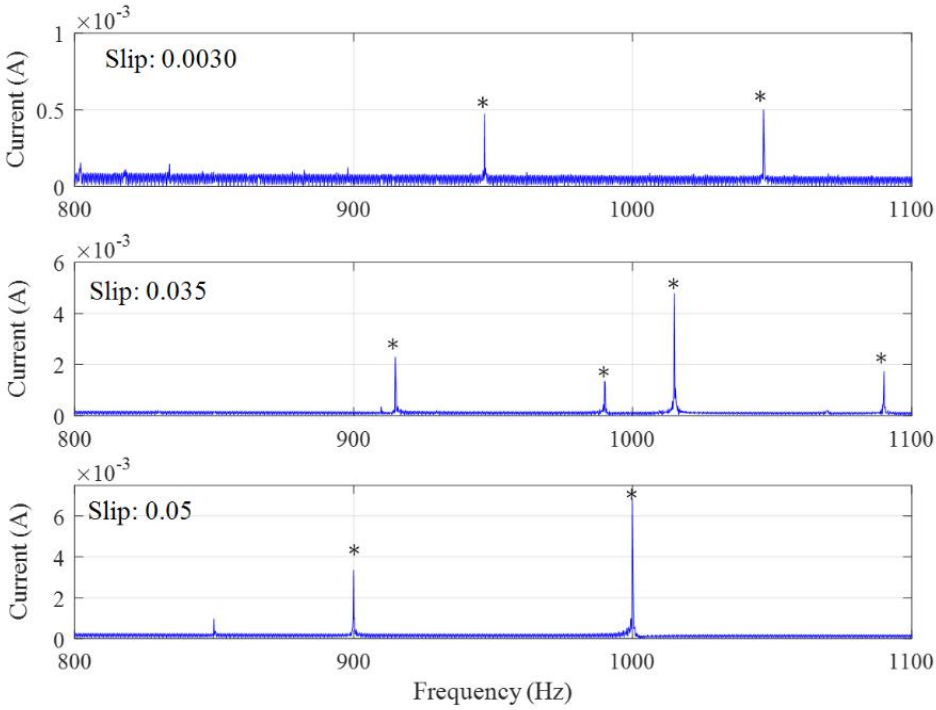


Figure 4.33. The development of PSH1 and PSH2 with skewed rotor bars while PSH2 is present because the phase-current is taken into consideration here.

For experimental validation, a dedicated test rig comprising two identical motors coupled back-to-back was utilized (Figure 4.34). Practical measurements of stator currents, using a DEWETRON transient recorder with 10 kHz sampling frequency over 70 seconds, facilitated high-resolution frequency spectrum analysis.

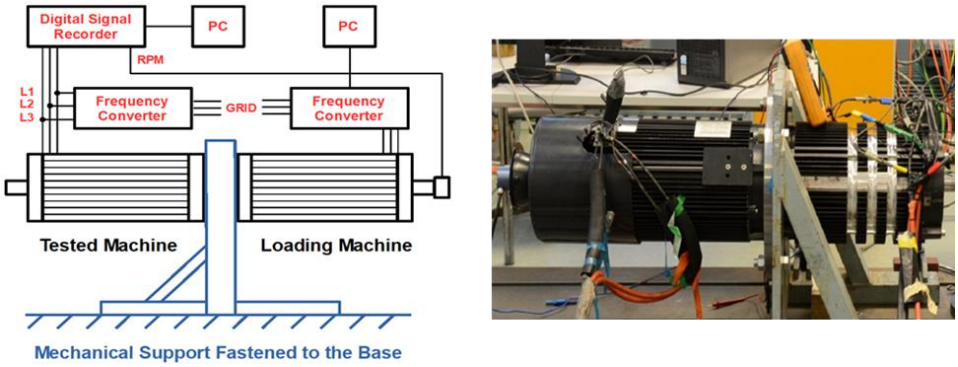


Figure 4.34. The experimental setup, block diagram (left), test rig (right).

Measured results (Figure 4.35 and Table 4.6) demonstrate excellent agreement with simulated data (Figure 4.34 and Table 4.5), particularly for the SH1 component. The validated MWFA approach incorporating slot skew effectively predicts operational behavior, providing significant computational advantages while ensuring analytical accuracy, suitable for rapid iterative design processes. Minor discrepancies in SH2 result

accuracy, suitable for rapid iterative design processes. Minor discrepancies in SH2 result primarily from neglected magnetic nonlinearities and localized saturation effects. These factors could be accounted for by integrating the earlier proposed strategy for incorporation of material B-H curves.

Table 4.6. The Development of PSH with Skewed Rotor in Practical Measurement.

Slip	RSH1		RSH2	
	(Hz)	(A)	(Hz)	(A)
0.0030	945.40	0.00042	1045.20	0.0005
0.035	914.76	0.00189	1014.76	0.0008
0.05	899.23	0.00233	999.21	0.0007

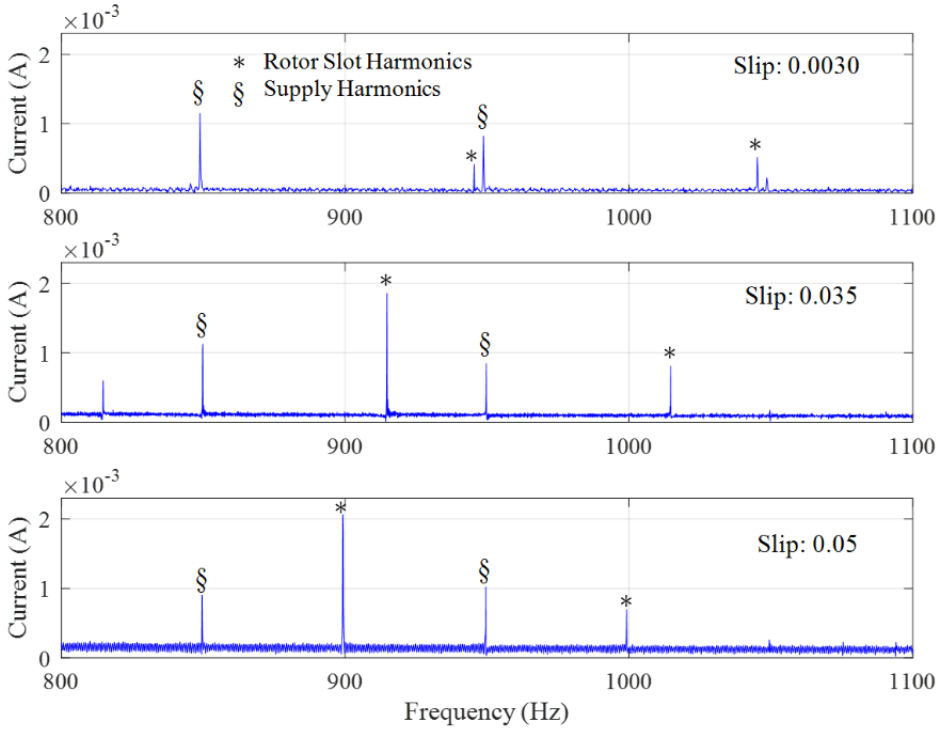


Figure 4.35 The PSH1 and PSH2 in practical measurements.

5 Conclusions and Future Work

This doctoral thesis has established a comprehensive framework for designing and modeling contoured airgap topologies in additively manufactured electrical machines, aiming at enhancing their electromagnetic performance. The investigations highlight the critical role of airgap design in optimizing machine performance. Leveraging additive manufacturing (AM) technologies, this work successfully demonstrates the feasibility of integrating complex airgap contours which were previously impractical with traditional manufacturing methods.

The findings from analytical and simulation studies provided significant insights into the behavior of these machines under various operational conditions. The implementation of sinusoidal and other airgap contours, as validated through both theoretical modeling and experimental validation, resulted in improved flux linkage and reduced magnetic reluctance, thus leading to enhanced torque production and overall machine efficiency. The research also highlighted the trade-offs between increased airgap surface area and the onset of magnetic saturation, which were crucial for determining the optimal contour designs.

This doctoral thesis has successfully established a detailed framework for the design and modeling of contoured airgap topologies in additively manufactured electrical machines, significantly enhancing their electromagnetic performance. Through analytical and simulation studies, the thesis demonstrates how advanced airgap designs optimize machine efficiency and performance, particularly through the strategic use of additive manufacturing (AM) technologies.

Equally critical to realizing the full potential of AM, however, is the need to overcome the computational inefficiencies that limit iterative design workflows -especially for low-volume, application-specific machines. This brings focus to the second major research gap, the lack of a computationally efficient yet sufficiently accurate modeling framework that can handle non-linear magnetic properties and complex 3D geometries. It is within this context that the optimization of the design process became central to the broader contribution of this work. The enhancement of the Modified Winding Function Analysis (MWFA) played a crucial role in reducing the reliance on computationally expensive finite element methods (FEA). By refining the MWFA to accurately account for complex geometries and saturation effects within the machine core, the thesis offers a potent tool for rapid, iterative design processes. This optimization is particularly beneficial in the context of AM, where the overall production efficiency demands for the design process to be rapid and optimized for computational efficiency.

Moreover, the thesis lays groundwork for further integration of design process optimization by suggesting segmented modeling approach for analytical models that could incorporate hybrid flux topologies and complex volume calculations. This would not only enhance the analytical accuracy in predicting machine losses but also fosters a more agile design framework capable of adapting to diverse manufacturing settings and operational demands.

In conclusion, the research presented in this thesis marks a substantial step forward in the electromechanical design field, especially in the utilization of AM for electrical machines. It opens up new possibilities for future research, particularly in extending the capabilities of analytical models to fully leverage the design freedom offered by AM technologies, ultimately leading to smarter, more efficient, and cost-effective machine designs. These advancements emphasize the transformative potential of integrating

detailed design process optimization strategies into the core of electrical machine development, promising a new era of innovation and efficiency in electromechanical manufacturing.

5.1 Future Works

Building upon the foundation established in this doctoral thesis, future research can further enhance the design and analysis of electrical machines with the following advanced studies:

1. **Investigation of More Complex Geometrical Shapes for Airgap**: Expanding the scope of airgap geometries could explore the effects of more complex shapes, such as non-periodic or asymmetric contours. This exploration aims to optimize flux linkage and torque production beyond traditional sinusoidal and circular contours, potentially uncovering new pathways to efficiency improvements.
2. **Saturation Mitigation Techniques**: Developing shapes or configurations specifically aimed at mitigating saturation effects in the core, especially near the contoured airgaps, is critical. Research could focus on geometric modifications or the introduction of composite materials within the core to distribute flux densities more evenly, thereby reducing local saturation and enhancing performance.
3. **Application and Case Study for PM Machines**: Conducting case studies on the implementation of contoured airgap topology in permanent magnet (PM) machines could reveal opportunities to reduce the mass of rare-earth magnets used. This research could contribute to cost savings and resource efficiency in PM machine production, aligning with sustainable manufacturing practices.
4. **Extending Modified Winding Function Analysis (MWFA)**: Enhancing the MWFA to better account for localized saturations and complex geometrical impacts on electromagnetic and thermal performance. This extension would involve integrating more refined core material characteristics and loss modeling into the analytical framework, thus providing more accurate predictions of machine behavior under varied operating conditions.
5. **Incorporation of Complex Geometry in MWFA**: Extending the MWFA to include more detailed volume and geometry calculations could improve its capability in estimating losses, such as iron and copper losses, especially for machines with complex geometries. This would enhance the model's utility in the design process by providing more accurate loss profiles and helping in thermal management optimization.
6. **Incorporation of Hybrid Flux Topologies in MWFA**: Advancing the MWFA to incorporate hybrid flux topologies, such as those found in machines combining characteristics of both radial and axial flux machines, could broaden the applicability of the analytical approach. This expansion would allow for the exploration of innovative machine designs that could offer superior performance characteristics.
7. **Utilization of Developed Algorithms for Data-Driven Insights**: Leveraging the refined algorithms and models to generate extensive datasets detailing the effects of various design parameters on machine performance. This data could be used to train machine learning models, providing predictive insights and optimizing design processes through AI-driven tools. Such applications could drastically reduce design cycles and enhance the adaptability of machines to specific applications.

8. **Integration of Thermal and Mechanical Considerations into Design and Prototyping Workflow** Focus on enhancing the practical prototyping process by incorporating thermal management solutions and mechanical design constraints directly into the early-stage electromagnetic design workflow. This would involve co-optimizing thermal dissipation pathways, mechanical robustness (e.g., vibration tolerance, structural stresses), and electromagnetic performance – particularly for AM-fabricated components. Developing such models and prototyping strategies would ensure more reliable, application-ready machines while reducing post-design iterations and enabling a more holistic, performance-driven design approach.

These proposed directions not only aim to deepen the understanding of contoured airgap technologies but also seek to integrate advanced computational tools and manufacturing techniques, setting a robust platform for the next generation of high-performance electrical machines.

References

[1] P. Murmu, H. Fielder, and M. McCurdy, “Technology Scan of Electric Motors application,” 2024. Accessed: Apr. 09, 2025. [Online]. Available: https://www.eeca.govt.nz/assets/EECA-Resources/Research-papers-guides/Technology-Scan-of-Electric-Motor-Applications_EECA.pdf

[2] F. Del Pero, L. Berzi, C. Antonia Dattilo, and M. Delogu, “Environmental sustainability analysis of Formula-E electric motor,” *Proceedings of the Institution of Mechanical Engineers, Part D: Journal of Automobile Engineering*, vol. 235, no. 2–3, 2021, doi: 10.1177/0954407020971246.

[3] W. Cai, X. Wu, M. Zhou, Y. Liang, and Y. Wang, “Review and Development of Electric Motor Systems and Electric Powertrains for New Energy Vehicles,” *Automotive Innovation*, vol. 4, no. 1, 2021, doi: 10.1007/s42154-021-00139-z.

[4] E. Agamloh, A. von Jouanne, and A. Yokochi, “An overview of electric machine trends in modern electric vehicles,” 2020. doi: 10.3390/MACHINES8020020.

[5] Z. Ahmad, A. Kallaste, T. Vaimann, M. U. Naseer, S. Hussain, and A. Rassolkin, “Review of Design Freedom Offered by Additive Manufacturing for Performance Enhancement of Electrical Machine,” *IEEE Open Journal of the Industrial Electronics Society*, 2024, doi: 10.1109/OJIES.2024.3509547.

[6] G. Burnand, A. Thabuis, D. M. Araujo, and Y. Perriard, “Novel Optimized Shape and Topology for Slotless Windings in BLDC Machines,” *IEEE Trans Ind Appl*, vol. 56, no. 2, 2020, doi: 10.1109/TIA.2019.2956717.

[7] A. Thabuis, X. Ren, and Y. Perriard, “Enhanced Electric Motors Using Multi-Functional 3D Printed Winding With Integrated Heat Sinks,” *IEEE Transactions on Energy Conversion*, vol. 38, no. 2, 2023, doi: 10.1109/TEC.2022.3221189.

[8] F. Nishanth, A. D. Goodall, I. Todd, and E. L. Severson, “Characterization of an Axial Flux Machine with an Additively Manufactured Stator,” *IEEE Transactions on Energy Conversion*, 2023, doi: 10.1109/TEC.2023.3285539.

[9] F. Wu, A. El-Refaie, and A. Al-Qarni, “Additively Manufactured Hollow Conductors Integrated with Heat Pipes: Design Tradeoffs and Hardware Demonstration,” *IEEE Trans Ind Appl*, vol. 57, no. 4, 2021, doi: 10.1109/TIA.2021.3076423.

[10] C. Jenkins *et al.*, “Innovations in Axial Flux Permanent Magnet Motor Thermal Management for High Power Density Applications,” *IEEE Transactions on Transportation Electrification*, vol. 9, no. 3, 2023, doi: 10.1109/TTE.2023.3242698.

[11] N. Simpson, G. Yiannakou, H. Felton, J. Robinson, A. Arjunan, and P. H. Mellor, “Direct Thermal Management of Windings Enabled by Additive Manufacturing,” *IEEE Trans Ind Appl*, vol. 59, no. 2, pp. 1319–1327, Mar. 2023, doi: 10.1109/TIA.2022.3209171.

[12] Z. Ahmad, A. Kallaste, T. Vaimann, M. U. Naseer, S. Hussain, and A. Rassolkin, “Review of Design Freedom Offered by Additive Manufacturing for Performance Enhancement of Electrical Machine,” 2024, *Institute of Electrical and Electronics Engineers Inc.* doi: 10.1109/OJIES.2024.3509547.

[13] M. U. Naseer, A. Kallaste, B. Asad, T. Vaimann, and A. Rassõlkin, “A Review on Additive Manufacturing Possibilities for Electrical Machines,” *Energies (Basel)*, vol. 14, no. 7, p. 1940, Mar. 2021, doi: 10.3390/en14071940.

[14] F. Wu and A. M. El-Refaie, “Toward Additively Manufactured Electrical Machines: Opportunities and Challenges,” *IEEE Trans Ind Appl*, vol. 56, no. 2, 2020, doi: 10.1109/TIA.2019.2960250.

[15] H. Parmar, T. Khan, F. Tucci, R. Umer, and P. Carlone, “Advanced robotics and additive manufacturing of composites: towards a new era in Industry 4.0,” 2022. doi: 10.1080/10426914.2020.1866195.

[16] R. Wrobel and B. Mecrow, “A Comprehensive Review of Additive Manufacturing in Construction of Electrical Machines,” 2020. doi: 10.1109/TEC.2020.2964942.

[17] T. C. Dzogbewu and D. de Beer, “Powder Bed Fusion of Multimaterials,” 2023. doi: 10.3390/jmmp7010015.

[18] T. N. Lamichhane, L. Sethuraman, A. Dalagan, H. Wang, J. Keller, and M. P. Paranthaman, “Additive manufacturing of soft magnets for electrical machines—a review,” 2020. doi: 10.1016/j.mtphys.2020.100255.

[19] D. G. Ahn, “Directed Energy Deposition (DED) Process: State of the Art,” 2021. doi: 10.1007/s40684-020-00302-7.

[20] B. Aydogan, A. O’Neil, and H. Sahasrabudhe, “Microstructural and mechanical characterization of stainless steel 420 and Inconel 718 multi-material structures fabricated using laser directed energy deposition,” *J Manuf Process*, vol. 68, 2021, doi: 10.1016/j.jmapro.2021.06.031.

[21] M. P. Paranthaman *et al.*, “Binder Jetting: A Novel NdFeB Bonded Magnet Fabrication Process,” *JOM*, vol. 68, no. 7, 2016, doi: 10.1007/s11837-016-1883-4.

[22] I. Gibson, D. Rosen, B. Stucker, and M. Khorasani, “Additive Manufacturing Technologies.”

[23] A. Alammar, J. C. Kois, M. Revilla-León, and W. Att, “Additive Manufacturing Technologies: Current Status and Future Perspectives,” 2022. doi: 10.1111/jopr.13477.

[24] A. Selema, M. N. Ibrahim, and P. Sergeant, “Metal Additive Manufacturing for Electrical Machines: Technology Review and Latest Advancements,” 2022. doi: 10.3390/en15031076.

[25] F. Wu, A. M. El-Refaie, and A. Al-Qarni, “Additively Manufactured Hollow Conductors for High Specific Power Electrical Machines: Aluminum vs Copper,” in *2021 IEEE Energy Conversion Congress and Exposition, ECCE 2021 - Proceedings*, 2021. doi: 10.1109/ECCE47101.2021.9595470.

[26] T. Pham, P. Kwon, and S. Foster, “Additive manufacturing and topology optimization of magnetic materials for electrical machines—a review,” 2021. doi: 10.3390/en14020283.

[27] M. Sarap, A. Kallaste, P. S. Ghahfarokhi, H. Tiismus, and T. Vaimann, “Utilization of Additive Manufacturing in the Thermal Design of Electrical Machines: A Review,” *Machines*, vol. 10, no. 4, 2022, doi: 10.3390/machines10040251.

[28] H. Wang, T. N. Lamichhane, and M. P. Paranthaman, “Review of additive manufacturing of permanent magnets for electrical machines: A prospective on wind turbine,” 2022. doi: 10.1016/j.mtphys.2022.100675.

[29] N. Simpson, D. J. North, S. M. Collins, and P. H. Mellor, “Additive Manufacturing of Shaped Profile Windings for Minimal AC Loss in Electrical Machines,” *IEEE Trans Ind Appl*, vol. 56, no. 3, 2020, doi: 10.1109/TIA.2020.2975763.

[30] H. Tiismus, A. Kallaste, T. Vaimann, and A. Rassõlkin, “State of the art of additively manufactured electromagnetic materials for topology optimized electrical machines,” *Addit Manuf*, vol. 55, Jul. 2022, doi: 10.1016/J.ADDMA.2022.102778.

[31] F. Wu, A. M. El-Refaie, and A. Al-Qarni, “Minimization of Winding AC Losses Using Inhomogeneous Electrical Conductivity Enabled by Additive Manufacturing,” in *IEEE Transactions on Industry Applications*, 2022. doi: 10.1109/TIA.2022.3152457.

[32] N. Simpson, S. P. Munagala, A. Catania, F. Derguti, and P. H. Mellor, “Functionally Graded Electrical Windings Enabled by Additive Manufacturing,” in *2022 International Conference on Electrical Machines, ICEM 2022*, 2022. doi: 10.1109/ICEM51905.2022.9910912.

[33] R. Wrobel and B. Mecrow, “A Comprehensive Review of Additive Manufacturing in Construction of Electrical Machines,” Jun. 01, 2020, *Institute of Electrical and Electronics Engineers Inc.* doi: 10.1109/TEC.2020.2964942.

[34] F. Wu and A. M. El-Refaie, “Towards fully additively-manufactured permanent magnet synchronous machines: Opportunities and challenges,” in *2019 IEEE International Electric Machines and Drives Conference, IEMDC 2019*, Institute of Electrical and Electronics Engineers Inc., May 2019, pp. 2225–2232. doi: 10.1109/IEMDC.2019.8785210.

[35] S. Jung, L. B. Kara, Z. Nie, T. W. Simpson, and K. S. Whitefoot, “Is Additive Manufacturing an Environmentally and Economically Preferred Alternative for Mass Production?,” 2023. doi: 10.1021/acs.est.2c04927.

[36] A. Nazir *et al.*, “Multi-material additive manufacturing: A systematic review of design, properties, applications, challenges, and 3D printing of materials and cellular metamaterials,” 2023. doi: 10.1016/j.matdes.2023.111661.

[37] Y. Chen, C. Xiong, and Y. Li, “Additive Manufacturing of Rare Earth Permanent Magnetic Materials: Research Status and Prospects,” Apr. 01, 2024, *Multidisciplinary Digital Publishing Institute (MDPI)*. doi: 10.3390/met14040446.

[38] M. Oel *et al.*, “Multi-material laser powder bed fusion additive manufacturing of concentrated wound stator teeth,” *Additive Manufacturing Letters*, vol. 7, 2023, doi: 10.1016/j.addlet.2023.100165.

[39] A. Selema *et al.*, “Evaluation of 3D-Printed Magnetic Materials For Additively-Manufactured Electrical Machines,” *J Magn Magn Mater*, vol. 569, Mar. 2023, doi: 10.1016/j.jmmm.2023.170426.

[40] N. Simpson, G. Yiannakou, H. Felton, J. Robinson, A. Arjunan, and P. H. Mellor, “Direct Thermal Management of Windings Enabled by Additive Manufacturing,” *IEEE Trans Ind Appl*, vol. 59, no. 2, 2023, doi: 10.1109/TIA.2022.3209171.

[41] A. Selema, M. N. Ibrahim, and P. Sergeant, “Development of Novel Semi-Stranded Windings for High Speed Electrical Machines Enabled by Additive Manufacturing,” *Applied Sciences (Switzerland)*, vol. 13, no. 3, 2023, doi: 10.3390/app13031653.

[42] A. Selema, M. N. Ibrahim, and P. Sergeant, “Additively Manufactured Ultralight Shaped-Profile Windings for HF Electrical Machines and Weight-Sensitive Applications,” *IEEE Transactions on Transportation Electrification*, vol. 8, no. 4, 2022, doi: 10.1109/TTE.2022.3173126.

[43] S. Hussain, A. Kallaste, M. U. Naseer, M. Sarap, H. Tiismus, and T. Vaimann, “Preliminary Design Analysis of an Axial Flux Yokeless Stator Switched Reluctance Machine,” in *2023 IEEE 64th Annual International Scientific Conference on Power and Electrical Engineering of Riga Technical University, RTUCON 2023 - Proceedings*, Institute of Electrical and Electronics Engineers Inc., 2023. doi: 10.1109/RTUCON60080.2023.10413130.

[44] M. U. Naseer, A. Kallaste, B. Asad, T. Vaimann, and A. Rassõlkin, “A review on additive manufacturing possibilities for electrical machines,” 2021. doi: 10.3390/en14071940.

[45] H. Li, X. Hu, and L. Cui, “Magnetic Field Analysis for the Permanent Magnet Spherical Motor With SMC Core,” *IEEE Trans Magn*, vol. 59, no. 6, 2023, doi: 10.1109/TMAG.2023.3244617.

[46] R. Huang, Z. Song, H. Zhao, and C. Liu, “Overview of Axial-Flux Machines and Modeling Methods,” *IEEE Transactions on Transportation Electrification*, vol. 8, no. 2, 2022, doi: 10.1109/TTE.2022.3144594.

[47] B. Kaiser and N. Parspour, “Transverse Flux Machine-A Review,” 2022. doi: 10.1109/ACCESS.2022.3150905.

[48] J. H. Woo, C. W. Kim, T. K. Bang, S. H. Lee, K. S. Lee, and J. Y. Choi, “Experimental Verification and Electromagnetic Characteristic Analysis of Permanent Magnet Linear Oscillating Actuator Using Semi 3D Analysis Technique with Corrected Stacking Factor,” *IEEE Transactions on Applied Superconductivity*, vol. 30, no. 4, 2020, doi: 10.1109/TASC.2020.2986737.

[49] R. Omri, A. Ibala, and A. Masmoudi, “3D Rotor Position-Dependant MEC Modeling of Different Claw Pole Machine Topologies,” *IEEE Access*, vol. 10, 2022, doi: 10.1109/ACCESS.2022.3157629.

[50] R. P. Magisetty and N. S. Cheekuramelli, “Additive manufacturing technology empowered complex electromechanical energy conversion devices and transformers,” 2019. doi: 10.1016/j.apmt.2018.11.004.

[51] R. Wrobel, B. Scholes, A. Hussein, R. Law, A. Mustaffar, and D. Reay, “A metal additively manufactured (MAM) heat exchanger for electric motor thermal control on a high-altitude solar aircraft – Experimental characterisation,” *Thermal Science and Engineering Progress*, vol. 19, 2020, doi: 10.1016/j.tsep.2020.100629.

[52] J. Krishnasamy and M. Hosek, “Spray-Formed Hybrid-Field Traction Motor,” in *SAE Technical Papers*, SAE International, Mar. 2017. doi: 10.4271/2017-01-1225.

[53] M. Hosek, J. Krishnasamy, S. Sah, and T. Bashaw, “Spray-formed hybrid-field electric motor,” in *Proceedings of the ASME Design Engineering Technical Conference*, American Society of Mechanical Engineers (ASME), Dec. 2016. doi: 10.1115/DETC2016-59339.

[54] J. Pyrhönen, T. Jokinen, and V. Hrabovcová, *Design of Rotating Electrical Machines*. John Wiley and Sons, 2008. doi: 10.1002/9780470740095.

[55] A. E. Fitzgerald, “Electric Machinery. A.E. Fitzgerald, Charles Kingsley, JR., Stephen D. Umans”.

[56] M. U. Naseer, A. Kallaste, B. Asad, T. Vaimann, and A. Rassolkin, “Axially Asymmetric Design for Additive Manufacturing of Synchronous Reluctance Machines,” *2023 IEEE International Electric Machines and Drives Conference, IEMDC 2023*, 2023, doi: 10.1109/IEMDC55163.2023.10238995.

[57] M. U. Naseer, A. Kallaste, B. Asad, T. Vaimann, and A. Rassõlkin, “Design Procedure and Preliminary Analysis for the Introduction of Axial Asymmetry in the Synchronous Reluctance Machines,” *Proceedings - 2023 IEEE Workshop on Electrical Machines Design, Control and Diagnosis, WEMDCD 2023*, 2023, doi: 10.1109/WEMDCD55819.2023.10110903.

[58] M. U. Naseer, A. Kallaste, T. Vaimann, and B. Asad, “Curved Airgap Topology: A Promising Strategy for Enhancing Axial- Flux Machine Performance Metrics,” in *25th International Conference on the Computation of Electromagnetic Fields*, Naples, Italy: IEEE, Jun. 2025.

[59] S. Hussain, A. Kallaste, M. U. Naseer, M. Sarap, H. Tiismus, and T. Vaimann, “Preliminary Design Analysis of an Axial Flux Yokeless Stator Switched Reluctance Machine,” pp. 1–6, Jan. 2024, doi: 10.1109/RTUCON60080.2023.10413130.

[60] S. Hussain, A. Kallaste, M. U. Naseer, H. Tiismus, and T. Vaimann, “Development of an Axial Flux SRM Through Additive Manufacturing,” *2024 International Conference on Electrical Machines, ICEM 2024*, 2024, doi: 10.1109/ICEM60801.2024.10700569.

[61] H. Tiismus *et al.*, “Laser Additively Manufactured Magnetic Core Design and Process for Electrical Machine Applications,” *Energies 2022, Vol. 15, Page 3665*, vol. 15, no. 10, p. 3665, May 2022, doi: 10.3390/EN15103665.

[62] S. Orlova, V. Pugachov, A. Rassnlkin, A. Kallaste, and T. Vaimann, “Design of rotors for synchronous reluctance motor: Analytical treatment and optimization,” *2019 21st European Conference on Power Electronics and Applications, EPE 2019 ECCE Europe*, Sep. 2019, doi: 10.23919/EPE.2019.8914760.

[63] M. U. Naseer, A. Kallaste, B. Asad, T. Vaimann, and A. Rassolkin, “Initial Design Estimation of Synchronous Machines,” *2022 29th International Workshop on Electric Drives: Advances in Power Electronics for Electric Drives (IWED)*, pp. 1–7, Jan. 2022, doi: 10.1109/IWED54598.2022.9722585.

[64] S. Yammine, C. Henaux, M. Fadel, S. Desharnais, and L. Calégari, “Synchronous reluctance machine flux barrier design based on the flux line patterns in a solid rotor,” *Proceedings - 2014 International Conference on Electrical Machines, ICEM 2014*, pp. 297–302, Nov. 2014, doi: 10.1109/ICELMACH.2014.6960196.

Acknowledgements

I would like to express my deepest gratitude to my supervisor, **Professor Ants Kallaste**, and co-supervisor, **Dr. Toomas Vaimann**, for their invaluable guidance, continuous support, and encouragement throughout the course of this doctoral research. Their expertise, constructive feedback, and unwavering commitment have played a pivotal role in shaping the direction and quality of this work.

I am sincerely thankful to **Dr. Bilal Asad** and my colleagues at the Department of Electrical Power Engineering and Mechatronics, Tallinn University of Technology, for providing a supportive and collaborative research environment. Special thanks to my fellow researchers and friends who contributed insightful discussions and shared the journey with me during challenging and rewarding times alike.

I extend heartfelt appreciation to my family for their unconditional love, patience, and belief in me. Their support has been my greatest strength and motivation throughout this challenging academic pursuit.

This research was financially supported by the Estonian Research Council through the research grant PRG-1827, and I gratefully acknowledge this funding, which made the completion of this work possible.

Abstract

Design and Modeling of Contoured Airgap Topology for Additively Manufactured Electrical Machines

This doctoral thesis presents a comprehensive framework for the electromagnetic design and modeling of contoured airgap topologies in electrical machines, enabled by additive manufacturing (AM). The research is motivated by the need to overcome the geometric constraints imposed by conventional manufacturing, which traditionally limit electrical machine topologies to planar, two-dimensional designs. While additive manufacturing has already proven beneficial for structural integration and thermal management in electrical machines, its full potential for electromagnetic design innovation, especially in three-dimensional topology, remains largely unexploited.

To address this gap, the work introduces and systematically validates contoured airgap surfaces as a novel approach to reduce magnetic reluctance and enhance flux linkage within compact machine geometries. A range of contour shapes, including sinusoidal, triangular, and circular profiles, were analyzed through finite element simulations and compared against benchmark planar topology. The performance improvements, particularly in flux linkage, torque production, and torque density, were evaluated under both linear and non-linear magnetic material conditions. Experimental validation using additively manufactured prototypes confirmed that contoured geometries yield consistent and significant improvements in output torque across a range of operating currents, validating the first hypothesis of this thesis.

In parallel, this work addresses a second critical research challenge: the computational inefficiency of the iterative machine design process when using three-dimensional finite element analysis (FEA). To avoid this limiting characteristic, this work enhances the Modified Winding Function Analysis (MWFA) to support the rapid and accurate modeling of machines in nonlinear region of material characteristics and three-dimensional features, including contoured airgaps and slot skewing. A hybrid FEA-analytical approach is developed, enabling accurate estimation of saturation effects in the core material through a one-time FEA-supported correction that significantly reduces the computational load of subsequent iterations. Benchmarked against FEA, the enhanced MWFA reduces iteration time from several hours to under 20 seconds without compromising accuracy, thereby validating the second hypothesis concerning computational efficiency.

Furthermore, the thesis proposes an extended MWFA formulation using a segmented modeling approach that incorporates three-dimensional variations in machine design, thus enabling the analytical modeling of complex 3D machines with a high degree of flexibility. These advancements enable the extended use of MWFA in iterative design workflows and lay foundation for future utilization for machine learning-based optimization possibilities, enabling smarter, faster, and more application-specific machine development in the AM context.

In conclusion, this thesis not only demonstrates the performance potential of contoured airgap topologies enabled by additive manufacturing but also provides the analytical tools necessary to exploit this design-freedom efficiently. By bridging the gap between design innovation and computational modeling, the work lays the foundation for a new generation of electrical machines – compact, efficient, and customized for high-performance applications through AM-driven design workflows.

Lühikokkuvõte

Kõverdatud õhupilu topoloogiaga kihtlisandusmeetodil valmistatud elektrimasinate projekteerimine ja modelleerimine

Käesolev doktoritöö keskendub elektrimasinate projekteerimisele ja modelleerimisele, kasutades kihtlisandustehnoloogia võimalusi, eelkõige uudse kõverdatud õhupilu topoloogia rakendamist. Uurimistöö lähtepunktiks on vajadus ületada traditsioonilise tasapinnalise disainiga elektrimasinate geomeetrilised piirangud ning uurida võimalusi, mida pakub kihtlisandustehnoloogia kolmemõõtmelise geomeetria vabaduseks.

Töö esimeseks eesmärgiks oli välja töötada ja katseliselt valideerida kõverdatud õhupiluga geomeetriaid, mis võimaldavad vähendada magnetahela magnetilist takistust ja suurendada aheldusvoogu. Uurimuses analüüsiti lõplike elementide meetodil mitmeid erinevaid õhupilu kuju – sealhulgas siinuselised, kolmnurksed ja ringikujulised profiilid – ning võrreldi neid klassikalise tasapinnalise topoloogiaga. Analüüsi tulemusena tuvastati, et kõverdatud õhupilu geomeetriad võimaldavad märkimisväärselt tõsta aheldusvoogu, pöördemomenti ja momenditihedust nii lineaarsete kui ka mitte-lineaarsete materjalide korral. Katsekehadega läbiviidud katsed kinnitasid neid tulemusi, tõestades, et selliste topoloogiate rakendamine suurendab elektrimasinate väljundmomenti erinevatel koormustel, toetades esitatud hüpoteesi.

Teise olulise uurimissuundana käsitletakse lõplike elementide meetodi (FEA) põhise iteratiivse projekteerimise arvutuslikku ebaefektiivsust. Selle lahendamiseks täiustati modifitseeritud mähisefunktsiooni analüüsi meetodit (MWFA), et see toetaks kiiret ja täpset elektrimasinate arvutust mitte-lineaarsetes tööpiirkondades ning võimaldaks arvestada kõverdatud õhupilu ja ruumilise geomeetria eripäradega. Töö käigus töötati välja hübriidarvutusmetoodika, mis kombineerib analüütilise ja FEA-põhise lähenemise, võimaldades üheainsa FEA-arvutusega täpselt hinnata südamiku küllastusmõjusid ning oluliselt vähendada iteratsioonide arvutuskoormust. Parendatud MWFA meetod vähendab arvutusaja mitmelt tunnilt alla 20 sekundi, säilitades kõrge täpsuse, ja kinnitab teist hüpoteesi arvutustõhususe kohta.

Lisaks pakub töö välja edasiarendatud MWFA valemi, mis tugineb segmenteeritud modelleerimise lähenemisele ja võimaldab integreerida kolmemõõtmelisi geomeetrilisi muutujaid masina konstruktsiooni. Selline lähenemine suurendab analüütilise modelleerimise paindlikkust, toetab MWFA laiemat rakendamist iteratiivses projekteerimisprotsessis ning loob aluse tulevikusuunalistele tehisintellektil põhinevatele optimeerimisvõimalustele, eriti seoses kihtlisandustehnoloogia rakendustega.

Kokkuvõttes demonstreerib doktoritöö, et kõverdatud õhupilu geomeetria kasutamine kihtlisandustehnoloogias võimaldab oluliselt parandada elektrimasinate elektromagnetilist jõudlust. Uurimistulemused ning välja töötatud arvutusvahendid pakuvad tugeva aluse uue põlvkonna elektrimasinate loomiseks – masinatele, mis on kompaktsemad, efektiivsemad ning paremini kohandatavad erinevatele rakendustele, kasutades ära kihtlisandustehnoloogia geomeetrilist vabadust ja innovatsioonipotentsiaali.

Author's Publications

Publication I

M. U. Naseer, A. Kallaste, B. Asad, T. Vaimann, and A. Rassõlkin, "A Review on Additive Manufacturing Possibilities for Electrical Machines," Energies (Basel), vol. 14, no. 7, p. 1940, Mar. 2021, doi: 10.3390/en14071940.

energies

MDPI

Review

A Review on Additive Manufacturing Possibilities for Electrical Machines

Muhammad Usman Naseer [1,*], Ants Kallaste [1], Bilal Asad [1,2], Toomas Vaimann [1] and Anton Rassõlkin [1]

[1] Institute of Electrical Power Engineering and Mechatronics, Tallinn University of Technology, 19086 Tallinn, Estonia; ants.kallaste@taltech.ee (A.K.); bilal.asad@taltech.ee (B.A.); toomas.vaimann@taltech.ee (T.V.); anton.rassolkin@taltech.ee (A.R.)

[2] Department of Electrical Engineering and Automation, Aalto University, 02150 Espoo, Finland

* Correspondence: mnasee@taltech.ee

Abstract: This paper presents current research trends and prospects of utilizing additive manufacturing (AM) techniques to manufacture electrical machines. Modern-day machine applications require extraordinary performance parameters such as high power-density, integrated functionalities, improved thermal, mechanical & electromagnetic properties. AM offers a higher degree of design flexibility to achieve these performance parameters, which is impossible to realize through conventional manufacturing techniques. AM has a lot to offer in every aspect of machine fabrication, such that from size/weight reduction to the realization of complex geometric designs. However, some practical limitations of existing AM techniques restrict their utilization in large scale production industry. The introduction of three-dimensional asymmetry in machine design is an aspect that can be exploited most with the prevalent level of research in AM. In order to take one step further towards the enablement of large-scale production of AM-built electrical machines, this paper also discusses some machine types which can best utilize existing developments in the field of AM.

Keywords: additive manufacturing; conventional electrical machines; non-conventional electrical machines; asymmetry in machines; metal 3D-printing; future electrical machines; electrical machine design

check for updates

Citation: Naseer, M.U.; Kallaste, A.; Asad, B.; Vaimann, T.; Rassõlkin, A. A Review on Additive Manufacturing Possibilities for Electrical Machines. *Energies* **2021**, *14*, 1940. https://doi.org/10.3390/en14071940

Academic Editor: Carlos Platero

Received: 17 March 2021
Accepted: 30 March 2021
Published: 31 March 2021

Publisher's Note: MDPI stays neutral with regard to jurisdictional claims in published maps and institutional affiliations.

Copyright: © 2021 by the authors. Licensee MDPI, Basel, Switzerland. This article is an open access article distributed under the terms and conditions of the Creative Commons Attribution (CC BY) license (https://creativecommons.org/licenses/by/4.0/).

1. Introduction

Additive manufacturing (AM) or 3D-printing is an all-encompassing terminology used for the processes where the manufacturing is done in layers, rendered from the digital model of a specific item or assembly. Recently, there has been a growing interest in the field of AM as it has emerged as an alternative manufacturing process, offering virtually unlimited potential for a wide range of industrial and special-purpose applications [1]. The AM offers various benefits over other conventional manufacturing processes, such as realizing complex/special purpose geometries, a wide range of multi-material usage possibilities, and rapid prototyping. There is also a potential for large in-volume production of complex mechanisms using AM, which is also evident from the fact that few aerospace companies have already announced the employment of AM in their manufacturing processes [2–6].

Due to the promising aspects of what it has to offer, AM has also attracted interest from the electrical machines' manufacturing point of view. For electrical machines, as compared to the conventional manufacturing processes, the AM process has not yet progressed to an advanced stage. With the ongoing advances in the field of AM, it would soon find its place as the better alternative for electrical machines' manufacturing. This is due to the fact that flexibility in design possibilities offered by employing AM, such as integration of structural and thermal management components with the active parts, make it the best solution for a wide range of applications such as special-purpose machines for aerospace, medical, robotics and automotive industry where high power-density, ruggedness, and

compact structure is required. With the forecasted improvements in the field of AM, the manufacturability and performance of electrical machines could be significantly improved.

At present, research work has been done majorly on the AM of individual working parts for various electrical machines, like mechanical and thermal management assemblies, coils/windings, permanent magnets (PM), and stator/rotor packs, etc., but a complete AM-built and user-ready electrical machine, for large scale production and industrial applications, is a feat which is yet to be accomplished owing to a few challenges regarding slow manufacturing speed, internal constructional defects, limited multi-material printing capability and the need for post-processing of printed parts [7]. The flexibility in employing AM process for the manufacturing of electrical machines is dependent on the individual machine design, AM technique, post processing technique and its effects on machine properties. Another front for integration of AM into electrical machines' manufacturing industry is the automation or minimization of post-processing procedures. Although it is currently on its initial stages of development, but it is another step forward towards the integration of AM in large-scale production industry [8].

This study investigates the current level of research and development, regarding employment of AM in manufacturing individual working parts of electrical machines and the potential of its employment for a completely AM-built electrical machine. This article also presents some candidates for AM-built electrical machines for the possibility of exploiting maximum benefits offered by AM at present stage, while keeping in view the limitations of currently available AM techniques.

2. Trends of AM in Construction of Electrical Machines

When considering AM for electrical machines, it offers virtually unlimited possibilities from prototyping to mass-personalized production. Employment of AM in production of electrical machines is a promising aspect offering various benefits over conventional manufacturing techniques, such as; realization of 3D-designs (including electrical, magnetic, mechanical and thermal considerations) [9], recyclable constructions [10] and optimal material utilization. Basic and standardized AM techniques for manufacturing processes have been described in [11,12] almost all of which have been used in manufacturing electrical machines or its parts, at various instances [13–15]. Among all the AM processes, selective laser melting (SLM), fused deposition modeling (FDM) and binder jet printing (BJP) technology are the ones shown to be most promising for the manufacturing of electrical machines [16].

2.1. Part-Wise Approach

From design and manufacturing point of view, any electrical machine can be subdivided into two basic subassemblies; active parts like core, coils/windings, PMs and the passive parts like thermal management components, mechanical assemblies. The research and development is progressing with a significant pace on both fronts with industrial implementations actually ahead of what is reflected in the research literature [13,17,18].

2.1.1. Active Parts

Active parts in electrical machines mainly comprise of core, windings/coils and PMs; responsible for the main functionality of the machine.

Core

Core in an electrical machine is the body with high magnetic permeability, used to confine and guide magnetic field. When considering its design and construction, magnetic properties such as, magnetic saturation, permeability, hysteresis losses, eddy current losses and mechanical properties are needed to be considered. Soft magnetic composite (SMC) and intermetallic alloys possess best of electromagnetic properties. Existing conventional methods employ these materials by molding, stacking or sintering them to achieve required geometry and electromagnetic properties [19]. But these materials are usually tricky to

process using conventional methods, due to poor mechanical properties and limitation on the realization of complex geometries.

AM offers flexibility in various aspects; from selection of material composition and complex geometric shape realization to structural topology optimization. This gives a better control over electromagnetic and mechanical properties. Many researches have showcased promising results, highlighting the potential of AM utilization in manufacturing electrical machines. In addition to the flexibility in geometrical shape realization, [20,21] report high magnetic permeability of up-to 31,000, low hysteresis losses i.e., low coercivity of minimum 16 A/m and up-to 50% weight reduction in AM-built machine core. However increase in eddy currents, due to non-laminated dense structure was also reported [22,23], but this can be decreased significantly with the help of layered structure of different electrical resistivity. The layer-based manufacturing process of AM can also introduce a degree of anisotropy i.e., difference in electromagnetic properties, in build direction compared to other direction. This is a challenge that research in machine design and topology optimization has to address or account for, collectively [24]. Another issue associated with AM is the introduction of macroscopic faults in structure, which is also shown to decrease by using preheated print-bed [21]. In [25] the authors have shown that conventionally brittle Fe–Co and Fe–Si intermetallic alloys, at almost ideal compositions for electromagnetic applications, can be processed in bulk form by employing AM techniques without consequential macroscopic defects.

AM's ability to realize different topology optimizations could be the means to produce high mechanical strength-low density, special purpose core geometries to optimally guide magnetic energy in electrical machines [20,26–32]. This also comes with the additional advantage of increased ductility due to enablement of multiscale microstructures. For major applications ranging from automotive to aerospace industries, the cores for rotating electrical machines need to have high torque-to weight ratio while keeping the structural integrity intact in conjunction with high permeability and low hysteresis and eddy current losses. Virtually, AM provides possibility for achieving maximum limits for this by providing opportunity to utilize topology optimizations in order to have appropriate geometry for electromagnetic energy guidance, optimal geometry for reduction in eddy current losses and cogging torque, optimal material composition for reduction in hysteresis losses and weight reduction due to low material usage while keeping the structural integrity. Figure 1 presents some of such examples for AM-built core structures.

Coils/Windings

The winding assembly consisting of coils/windings, electrical insulation material and the holding assembly; is responsible to produce magnetic field in the electrical machine. From design and construction point-of-view, for electrical machines; the power losses are needed to be kept at minimum. Low electrical resistivity and high conductor fill-factor produces less power losses and indicates a good winding design. However, for modern machine applications requiring high speed and high frequency operation, the losses associated to skin and proximity effect dominate and hence complicate the design of winding assembly. With conventional design and manufacturing techniques, the balance between these important factors gets compromised.

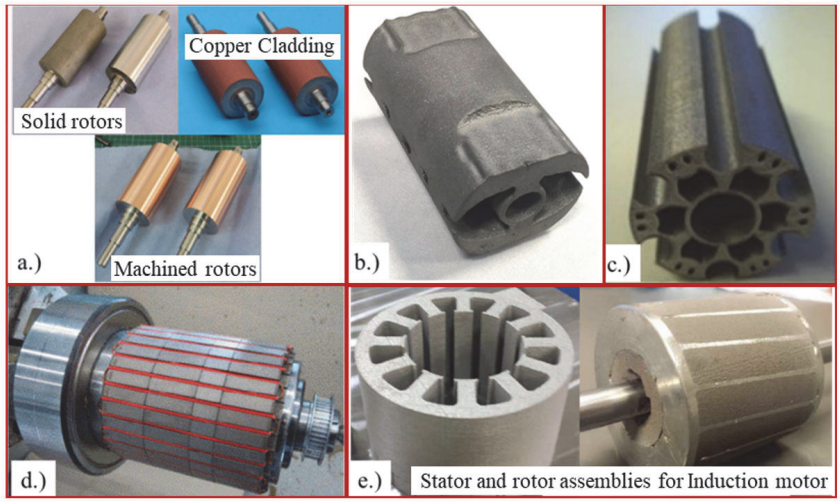


Figure 1. Examples of AM-built cores (**a**) solid steel rotor with copper cladding for usage in electric vehicles-Rolls Royce Central Technology [33] (**b**) PM rotor with optimized torque density [34] (**c**) prototype rotor for switched reluctance machine [16,26] (**d**) lightweight rotor utilizing lattice structure topology, for PM synchronous machine [35] (**e**) stator and rotor assemblies of an induction machine for automotive applications [36].

AM-built copper-alloy based coil, showed varied electrical properties for different heat treatments i.e., electrical conductivity from 51 to 75% international annealed copper standard-pure copper 100% (IACS) for the $CuCr_1Zr$ alloy [37,38]. Furthermore, it has been shown that specific profiling of the winding conductors, as shown in Figure 2a not only improved the slot area utilization (fill-factor) but also minimized the AC losses. Experimental results showed 20% improvement in continuous operation output [39].

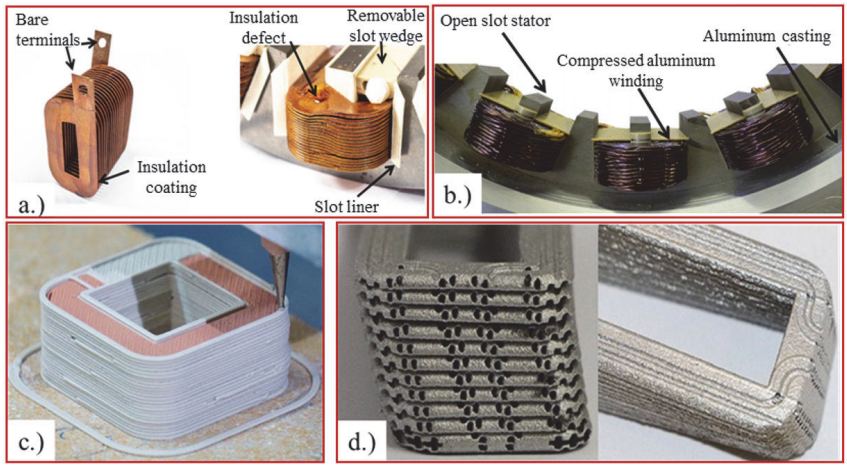


Figure 2. Examples of AM-built windings (**a**,**b**) AM-built shaped-profile, electrically insulated winding [39] (**c**) MM-AM built winding assembly with integrated ceramic insulation [13] (**d**) AM-built tooth-coil winding with integrated liquid-cooling channels [40].

Furthermore, processing of the coils/windings such as electrical insulation or coating can be done via Multi-Material (MM)-AM, rather than the conventional insulation technique such as enameling with resin, as illustrated in Figure 2b,c. This effectively eliminates the need for post processing of the AM produced part. The winding assembly along with insulation was tested thermally, by heating it 20 times up-to 300 °C, without showing any structural defects in insulation or change in electrical parameters of the coil.

Also, compared to conventional resin based insulation, good thermal characteristics of the resin based insulation from MM-AM provides for the attainability of higher current density in printed coil structures [13]. With the advent of AM in electrical machines, there's a potential possibility for unique/novel/application-specific winding design with improved manufacturability and material utilization without compromising on the vital design factors. This shows the prospective improvements in electrical machine performance with the utilization of AM techniques.

Permanent Magnets

Machines having efficiency, compactness and high torque-to-weight ratio as primary concerns, utilize permanent magnets (PMs) and therefore the manufacturing and consequent properties of PMs have significant importance. For such applications, PMs need to possess good functional magnetic, thermal and mechanical properties. For common applications, low energy-density PMs/soft magnets like Ferrites or MnAlC are used. But, for high energy-density/high specific-output applications, hard magnetic and high energy-product permanent magnets of materials like NdFeB/AlNiCo/SmCo are essential. Conventionally, PMs are either made by sintering or bonding which involve a large number of lengthy mechanical steps including pressing/molding and subsequent machining. This causes increase in production time and cost with the limitation on realization of complex/application-specific design possibilities.

In [24] the authors have presented a comparison about effects of various AM techniques on the mechanical and magnetic properties of PMs. The PMs produced by SLM have shown to produce magnets with 90% density [41] but significant cracks and residual stresses are introduced in magnet which negatively impact its mechanical and magnetic properties. But this issue, as discussed earlier, can be suppressed to a large extent by pre & post-AM heat treatment [21]. The material extrusion and Binder Jet printing (BJP) produced NdFeB PMs have similar properties to that of fused deposition modelling (FDM) based PMs [42,43]. The challenge with BJP manufactured PMs is that the volume content needs to be increased which would in-turn increase the magnet density and residual flux density. This is shown to be done with the help of eutectic alloy infiltration with BJP technique [44]. Big area additive manufacturing (BAAM) is a special technology, NdFeB magnets manufactured through this technique have shown significantly enhanced performance as compared to other AM techniques. With material density and residual flux density being 20% higher and energy product (indicating of magnetic energy density) being 40% higher than that of other AM-PMs, BAAM magnet reflects competitiveness in terms of intrinsic coercive force and residual flux density. Thermal degradation performance of AM magnets is also better than its counterparts as also illustrated in Figure 3 [45–47].

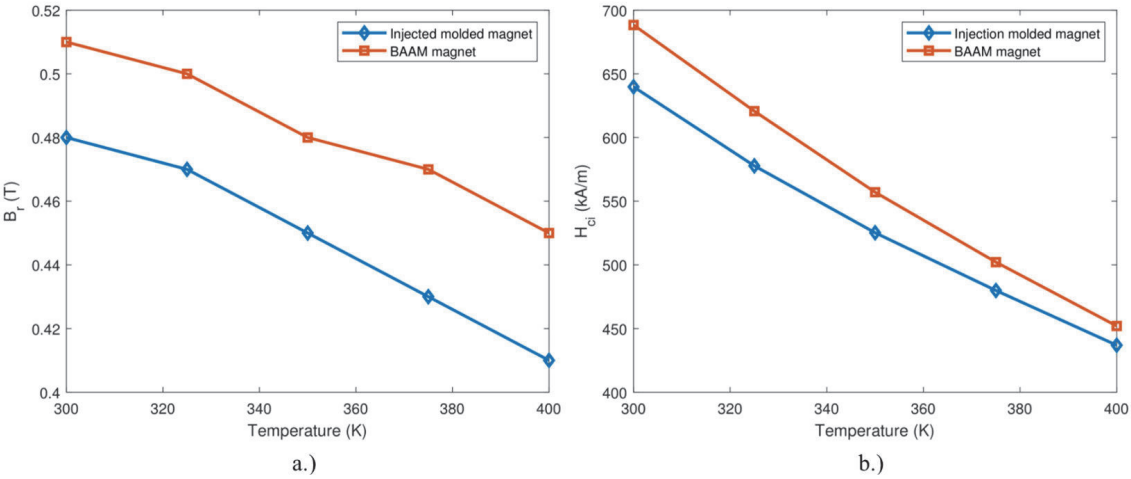


Figure 3. Comparison regarding the effect of thermal degradation on performance of conventional and AM-manufactured magnets (**a**) Remnant flux density as function of ambient temperature (**b**) Intrinsic coercive force as function of ambient temperature [24,45].

Furthermore, topology optimization (TO) enablement with almost all the AM techniques makes it easier to shape the PM geometry with relatively less analytical modelling. TO gives optimal distribution of multi-material within a specific, more complex or application-specific design space compared to conventional optimization techniques. This gives better magnetic energy delivery with the least of material waste [48–50]. Figure 4 presents various design concept realizations by utilizing AM.

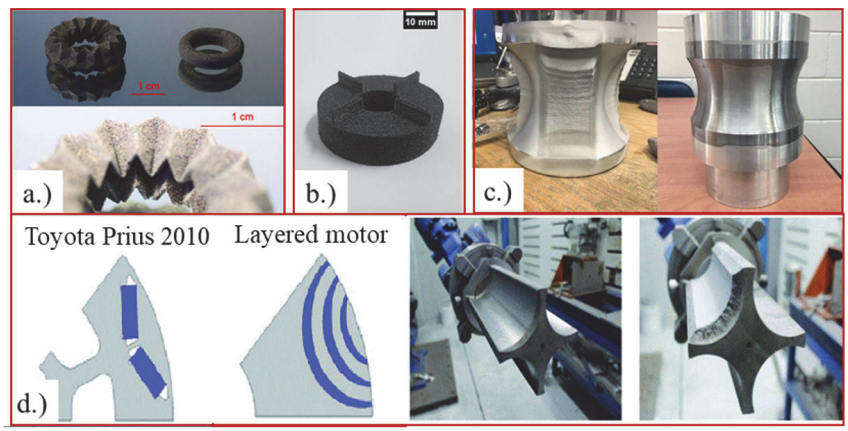


Figure 4. Examples of AM-built PMs (**a**) complex shaped PM realization [51] (**b**) NdFeB magnet produced by Selective Lase Sintering (SLS) [52] (**c**) bi-material hollow shape for electrical engines, with base material as iron and having NdFeB-Al composite at 0°,90°,180°,270° [53] (**d**) Enhanced interior PM motor for hybrid electric vehicle, with layered PM (left) design concept (right) fabrication process utilizing cold-spray AM [54].

Introduction of rare-earth elements in material composition is also used to enhance the magnetic properties such as intrinsic coercive force of the subject PM, even at high operating temperatures of 180 °C and higher. But this usually increases the cost of production which is less desirable in many applications [55,56]. Decreasing the use of rare-earth elements in

magnet production has a positive effect on the cost and production diversity [57]. Through AM, isotropic or anisotropic properties can be modified/created by controlling the grain structure [15,58,59]. This yields better control over magnetic properties without relying much on rare-earth materials like Dy, Tb, Pr etc.

2.1.2. Passive Parts

Passive parts in electrical machines include mechanical and thermal management assemblies comprising of machine frame, shaft, cooling structures and bearings, etc. These assemblies must have integrated functionalities in order to achieve compactness and improvement in performance parameters, vital for modern machine applications. Realizing the concept of integrated functionality is somewhat hindered due to limitations of conventional manufacturing techniques.

AM allows the machine designer/manufacturer to rethink the design of these assemblies by offering a wide range of material selection, reduction in the size/weight of structural parts due to enablement of various lattice structures and integration of various functionalities together, which cannot be realized with conventional manufacturing techniques. This means more compact, high power density and low-inertia electrical machines in an application-specific design space without compromising the operational performance. Figures below showcase some of the examples regarding employment of AM in mechanical and thermal management assemblies for electrical machines. In these examples [35,60–64] as shown in Figure 5, uniquely designed heat exchangers and various potential options for structural topologies have been presented. These include liquid and air-cooled rotor and stator assemblies, lattice structure assemblies, heat exchangers utilizing alternative plastics and ceramics, heat guides and rolling bearings etc. The integration of different functionalities, together in a structure, resulted in higher total mass flow for the heat exchange with consequent increase in cooling efficiency and reduction in overall weight. Due to increased mass flow for heat exchange, rapid cooling of peak loads also allowed for longer operation at peak loads.

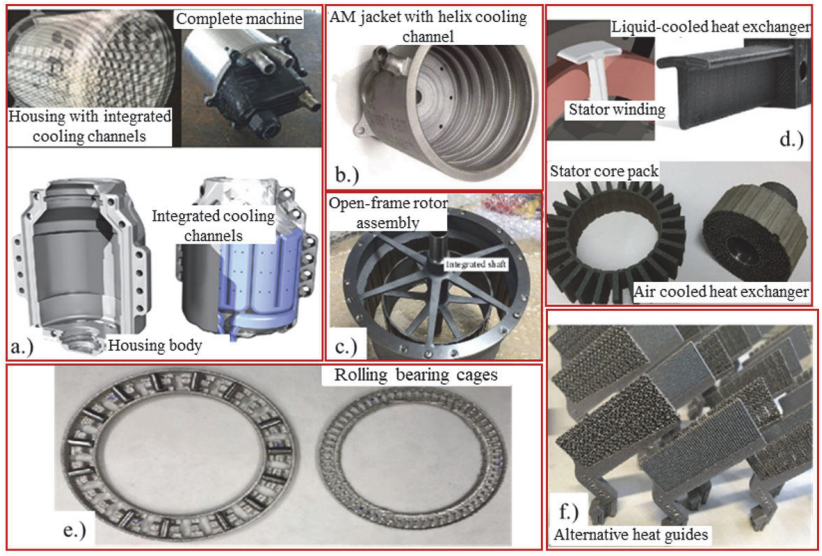


Figure 5. AM-built electrical machine parts (**a**) [60,61], (**b**) [65], (**d**) [62] integrated liquid cooled assemblies (**c**) air cooled rotor and stator assembly [66] (**e**) rolling bearing cages [63] (**f**) heat exchangers [67].

Research and development in this area of AM manufacturing is relatively on advanced stage with results comparable to the conventional techniques, as demonstrated by the comparison of mechanical properties for various conventional methods (wrought annealed, forging and casting) vs. AM techniques, as shown in Figure 6 [68–71].

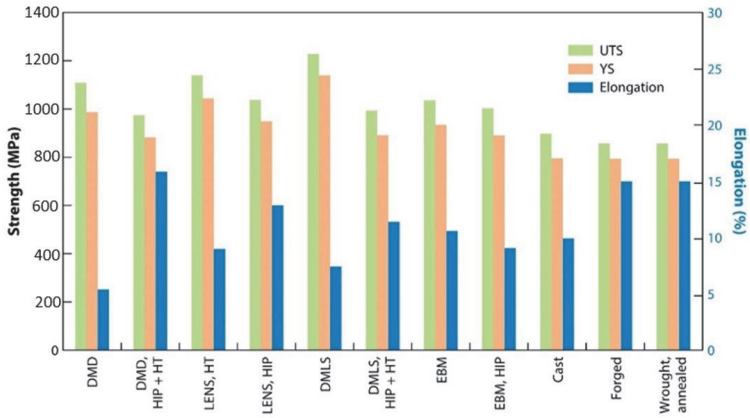


Figure 6. Comparison of mechanical properties for AM-built and Conventional built metallic material Ti-6Al-4V (UTS-ultimate tensile strength, YS-yield stress, DMD-direct metal deposition, LENS-laser engineered net shaping, DMLS-direct metal laser sintering, EBM-electron beam melting; HT-heat treated, HIP-hot isostatic pressing) [69].

In conclusion, AM has a lot to offer in almost every aspect of manufacturing process for electrical machines, such as:

- reduction in time and cost of production
- reduction in weight due to enablement of structural topology optimization
- better control over magnetic properties owing to the opportunity of varying the material composition
- less dependency on rare-earth elements due to control over isotropic/anisotropic properties through modification of grain structure
- enablement of complex/application-specific design realizations, by eliminating a lot of mechanical steps as well as the need of molds for almost any desired geometrical shape
- increase in power density, due to the opportunity of integrated functionalities within individual assemblies

2.2. Holistic Approach

It is only very recently that there has been emphasis on AM of electrical machines. That is why the technological developments and achievements in this field are relatively immature, however, research is progressing at a significant pace regarding the employment of AM in manufacturing electrical machines. Scientific research is a step-wise process so naturally, as a rule of thumb; research efforts were initially focused on the application of AM to produce individual machine components.

Various approaches by researchers are being adapted for the realization of completely AM built, self-replicating electrical machines; Figure 7a shows a simple brushless, Halbach array DC electric motor in which only the mechanical assembly is made using AM (from PLA plastic material), that houses its active parts like permanent magnets and coils/windings etc. This motor showcased efficiency of approximately 68% [72].

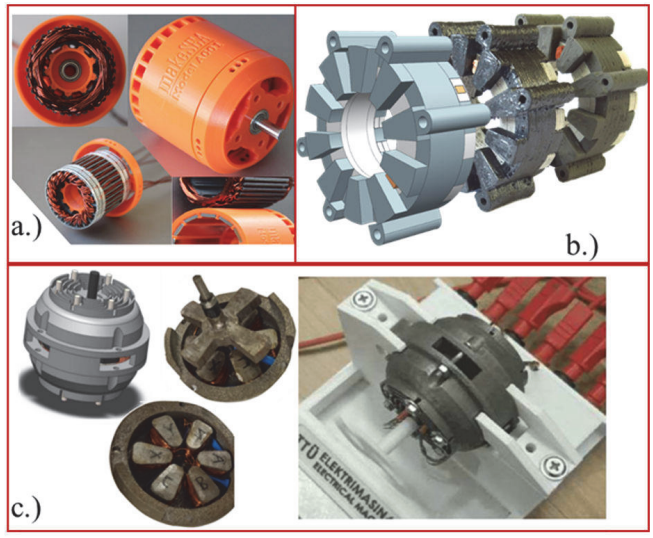


Figure 7. Examples of AM-built electrical machines (**a**) halbach array DC motor [72] (**b**) stator of end-winding reluctance machine [17] (**c**) Prototype Axial-Flux SRM [73].

Researchers from Chemnitz University of Technology claimed to have produced a completely MM-AM built end-winding reluctance machine, functional machine using high viscosity metallic/ceramic pastes (Figure 7b). The machine is reported to have withstood operating temperatures of 300 °C due to the use of ceramic insulation which has high thermal conductivity but it needs extensive post-processing [17]. Figure 7c showcases an SLM printed prototype, fully functional axial-flux switched reluctance machine (SRM) but this prototype-production too, involved significant amount of post-processing [73].

In [74,75] the authors have presented a prototype of an advanced electric motor design with hybrid field topology for automotive traction (Figure 8). The theoretical modelling shows promising performance characteristics of continuous power density at 2.8 kW/Kg or 8.6 kW/L and an above 90% efficiency in a broad operating region on torque-speed characteristics plot. This is a lot high relative to the commercially available traction motors. The authors report that the motor is currently under construction and after completion, results on the performance characteristics will be presented after third-party testing/validation.

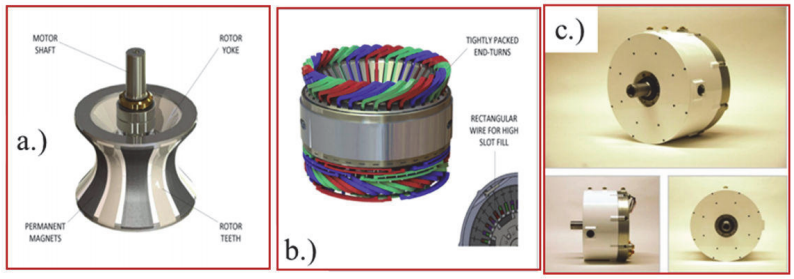


Figure 8. Hybrid-field Traction Motor (**a**) rotor (**b**) stator with integrated cooling (**c**) Partially assembled motor [74,75].

Another aspect in realization of complete additively manufactured electrical machine is the integration of power electronics, research in which has also been initiated. Efforts

in micro-scale laser based AM to produce structures below 100 µm resolution may enable integration of power electronics with the electrical machines, that will enable production of integrated motor drives resulting in compact electrical machines for high performance demanding applications like in automotive and aerospace industry [76,77].

3. Future Prospects of Holistic Approach

As presented in previous sections, efforts have resulted in varied level of progress towards production of additively manufactured machine parts; with development in production/integration of thermal management and mechanical assemblies ahead from the production of active parts (core, coils/windings and the permanent magnets). However, to manufacture a fully additively manufactured electrical machine, very little has been done. It is now that the researchers are entertaining the idea of holistic manufacturing of electrical machines through AM and the most natural step forward seems to direct the efforts towards a comprehensive design approach, keeping in view the current state-of-the-art in this field.

3.1. Conventional/Symmetrical Electrical Machines

Conventional machines such as induction and synchronous machines have a widespread use for bulk energy conversion. Usually, they are simple/symmetrical in design and large in size. Industrial manufacturing of such machines, at present, is most feasible with conventional methods owing to the fact that resultant performance parameters obtained are very much mature and offer best results corresponding to operational requirement, cost and time for in-volume production. Employment of AM in industrial production of such machines is hindered, due to the following factors;

- limitation on the overall size which can be realized with AM at present i.e., relatively small print-bed size
- relatively less maturity regarding electromagnetic properties of AM materials
- associated production cost and time

Efforts are being put into these aspects, by researchers and various industries. Until this gap is filled-in, employment of AM in industrial manufacturing of conventional/symmetrical electrical machines is limited mostly to;

- rapid prototyping
- production of individual machine parts having application specific complex geometries which are impossible to manufacture otherwise

References [2–6,33,78–81] showcase various examples where renowned automotive, aerospace and satellite companies have utilized AM for production of complex machine parts. Despite the limitations and challenges associated with current state-of-the-art in AM, asymmetry in machine design is an area where benefits of AM can be exploited the most. In the next section, this aspect will be discussed in detail while exploring for machine types best suitable to be manufactured using current state-of-the-art in AM.

3.2. Non-Conventional/Asymmetrical Electrical Machines

Symmetry in design is a characteristic that has imposed major limitations on exploiting the full potential of electrical machines. Basically, the aim has been to reduce complexity and manufacturing costs in order to cater for the limitations of conventional manufacturing techniques. Since the advent of AM, this limitation is virtually no longer relevant. With the degree of freedom in design offered by AM, more stringent requirements of operating environment, power-density, reliability, compactness and performance parameters can be met easily.

Research work to exploit alternative asymmetrical/non-conventional machine designs is under process by various researchers. Design examples such as those presented in [82–91] highlight the benefits of introducing asymmetry based on; unity motor asymmetry concept, repositioning of slot openings per-pole-per-phase, altering position of embedded bars on adjacent rotor poles and asymmetrical rotor configuration. Figure 9 presents pictorial

representation for such examples and Table 1 showcases various benefits achieved from introduction of asymmetry in design. The associated disadvantages include unbalanced magnetic-pull and increased complexity in design which are needed to be considered during the design process.

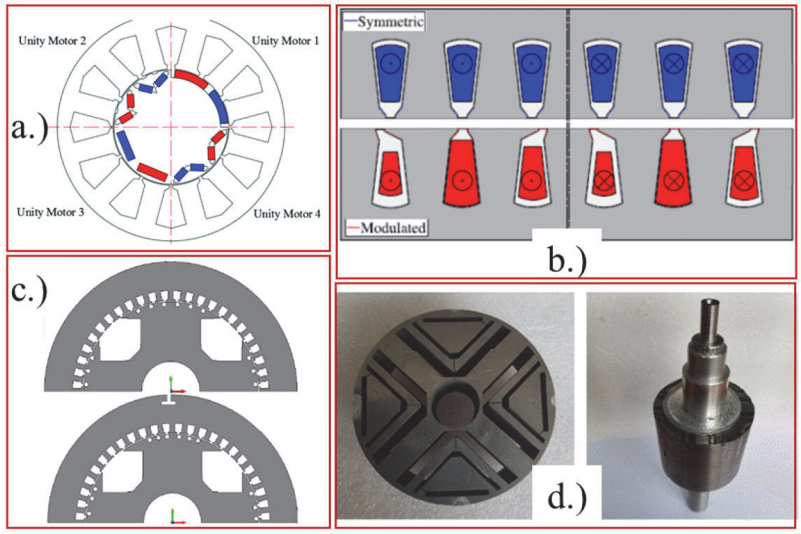


Figure 9. Concept of; (**a**) unity-motor asymmetry in rotor [83] (**b**) asymmetric slot-opening pattern (induction motor) [89] (**c**) asymmetric damper-cage topology (synchronous generator) [89] (**d**) hybrid-pole IPM machine with an asymmetrical magnet configuration in rotor [91].

Table 1. Introduction of asymmetry in machine design with corresponding benefits.

Type of Asymmetry	Machine type	References	Investigated Performance-Parameter of Interest	Improvement in Performance Parameter
Unity-motor asymmetry	PM motor	[83]	• Torque Ripple • Cogging Torque • Sensor-less Control	39.8% reduction 56.6% reduction 81.1% reduction in position error
Asymmetric slot-opening pattern	Induction Motor	[89]	• Torque Ripple	63% reduction
Asymmetric damper cage	Synchronous Generator	[89]	• Total Harmonic • Distortion	54% improvement
Asymmetric flux-barriers configuration in rotor	Synchronous Reluctance Machine	[90]	• Torque • Power Factor • Efficiency	9.6% increase 22.4% increase 2.3% increase
Asymmetrical magnet arrangement in rotor	Hybrid Pole Interior-PM Machine	[91]	• Torque Ripple • Torque	40.9% reduction 28.9 % increase

Selective variation in electrical conductivity (EC) of coils/windings, enabled by AM, can contribute in managing winding losses. In [92] authors demonstrate this by employing

conductors near slot opening with low EC to reduce winding AC losses and conductors near slot bottom with high EC to reduce DC losses. These results showcase the potential of improvement in performance parameters of various machines by employing targeted asymmetry in design. It equips the designers with more freedom to optimize machine performance.

4. Potential Candidate Machines for AM

In majority of examples and reference cited above, design asymmetry in order to improve performance characteristics of electrical machines, was introduced in 2-D (to remain within the limitations of conventional analysis and manufacturing techniques). With AM, the ability to introduce design asymmetry in 3-D enables a lot of flexibility in design and manufacturing of special purpose electrical machines. By special purpose electrical machine, it is meant for the machines which may be small in size, compact, application-specific and offering high energy density; having relatively complex design and manufacturing topology than the conventional Induction or Synchronous machines. The aim of this section is to investigate the candidate electrical machines from the standpoint of AM possibility and benefits of AM-utilization such as:

- Reduction in weight due to enablement of topology optimization
- Complex shape realization for optimal electromagnetic energy guidance
- High winding fill-factor for increased power density, etc.
- The target machine categories may include;
- Reluctance machines
- Hysteresis machines
- Brushless DC machines

These machines can be further classified into various types depending upon individual construction, application/utilization, performance characteristics and the control schemes involved. A no. of such machines with respect to their design, working principle, performance parameters and utilization will be discussed, in order to narrow down the machine selection for intended design of AM-built electrical machine. The selection of candidate machine types for AM is made while keeping in view following baselines:

- Least involvement of multi-material utilization
- Machine topology and design parameters falling within the constraints of present stage AM-capabilities
- Have the maximum chance of exploiting present stage AM capability to realize complex geometries, which is not possible otherwise.

Another classification that offers potential benefits of AM-utilization is the axial flux topology in electrical machines. Axial flux machines have a few pros over radial flux machines, due to which they deliver significantly high power-density. First is the fact that in axial flux machines, the PMs are located relatively further from the central axis. This provides larger lever resulting in increased torque. Secondly, in radial flux machines, major portion of the winding in the form of coil overhang remains inactive i.e., it doesn't serve any function other than just making loops. In addition to that, it causes electrical losses in the form of heat dissipation across electrical resistance that it offers. This effectively lowers the power/weight ratio and cooling efficiency. While in axial flux machines, there is less coil overhang and thus it provides high power/weight ratio and higher efficiency due to effective cooling as compared to the radial flux machines. Furthermore, in dual rotor topology of axial flux machines, the magnetic flux path is considerably short than in radial flux machines [93].

4.1. Switched Reluctance Machines (SRM)

These machines offer attractive qualities of high torque and a wide range of operating speed. By controlling switching sequence together with an appropriate electromagnetic design, the torque-speed characteristics of the SRMs can be made suitable for various

traction applications in automotive industry. Furthermore, by simply changing the control parameter selection with torque and speed, a given machine design can offer different characteristics. On the other side, the complex control scheme due to on-line parameter variation, noise and vibration are some of its associated issues [94,95].

The readiness of metal AM for manufacturing of soft magnetic rotor for SRMs is demonstrated in [96] by comparing an additively manufactured rotor (Fe-5.0% w.t. Si) with that of a conventional laminated, non-oriented silicon steel rotor. Due to the absence of laminations, eddy current losses were significant; but at the rated speed, the output power was comparable to that of benchmark machine. The ratio of output power improved further, with increase in operating speed as presented Figure 10 and Table 2.

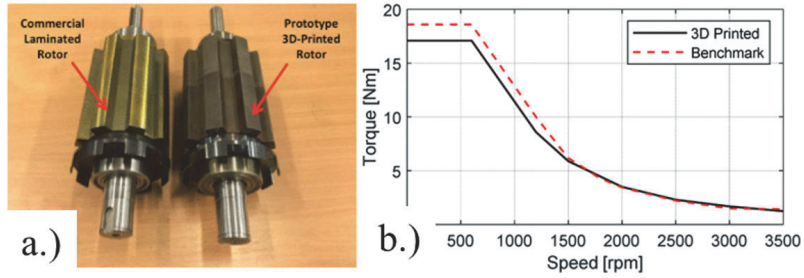


Figure 10. (**a**) Benchmark and Prototype AM-Built SRM-rotor (**b**) Torque –Speed characteristics of Benchmark and AM-built-rotor SRM [96,97].

Table 2. Variation in measured quantities of AM-built SRM from benchmark machine [96].

Measured Quantities *Percentage Increase/Decrease From Benchmark SRM	**AM-Built-Rotor SRM (At Rated Speed)**	**AM-Built-Rotor SRM (At 2.5 Times Rated Speed)**
Output Mechanical Power	12.8% less	3.6% less
Input Electrical Power	6.7% high	23.5% high
Average Phase Current	1.2% high	1.7% high
RMS Phase Current	1.4% high	14.5% high

Another SLM fabricated asymmetric rotor for SRM is presented in Figure 11. This rotor is designed with skew and honeycomb structure, which is difficult to fabricate otherwise by conventional method. With this design, the reduction in torque ripple was analyzed by FEA simulation and then validated experimentally, giving approximately 45% reduced torque ripple [98].

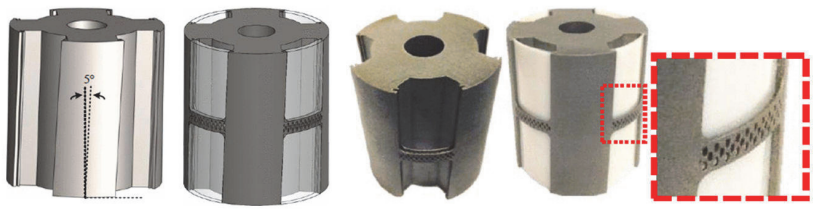


Figure 11. AM-built, Novel SRM-Rotor [98].

AM also enables application of topology optimization on machine design, Application of topology optimization on SRM design [99,100] and subsequent analysis, shows

achievement of optimization goals i.e., high average torque and low torque ripple with low mass.

4.2. Synchronous Reluctance Machine (SynRM)

The synchronous reluctance machine (SynRM) has the advantage of relatively simple construction and low moment of inertia of rotor which gives fast response characteristic and high torque density but as the name suggests, it is essentially a constant-speed machine dependent on supply frequency. The speed control can be achieved over a wide range by employing frequency control scheme. These types of machines are widely used in proportioning devices, synthetic-fibre manufacturing industries, wrapping and folding machines, positioning of control rods in nuclear industries, industrial drive systems requiring synchronized and continuous processes. Potential use of such machines for traction purposes is also reported [101–103].

Considering the design prospects from AM point of view, the SynRM-rotor has three basic topologies namely; salient pole (SP), axially laminated anisotropy (ALA) structure and transversally laminated anisotropy (TLA) with ALA having the highest saliency ratio and maximum reported power factor of 0.8 [104]. ALA rotor has a complex structure and is relatively difficult to manufacture by conventional techniques. This is where AM comes-in. With the employment of AM, the SynRM rotor can be easily realized with the additional improvement and optimization of performance parameters by exploring new design topologies. In [105–108] the authors have presented different design topologies (as shown in Figure 12) for AM-built rotors with integration/enhancement of various functionalities.

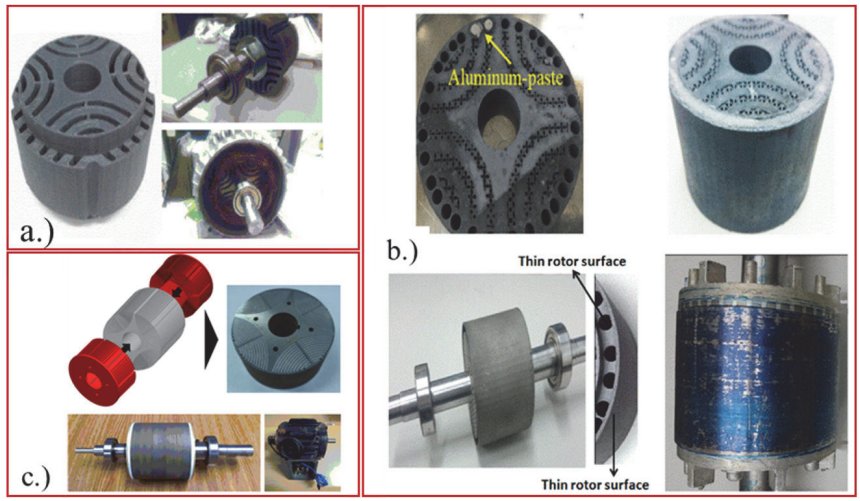


Figure 12. AM-built rotors for SynRM (**a**) 3D printed prototype [106] (**b**) Prototype Line Start-SynRM (LS-SynRM) with 3d-Net structure in rotor [107] (**c**) Prototype rotor design, assembled rotor and SynRM [108].

In [105] significant reduction in torque ripple i.e., one-fourth and 1.4% higher average torque, attributed to elimination of rotor bridges and center-posts (not possible with conventional manufacturing techniques), was achieved. The comparison of torque characteristics is shown in Figure 13.

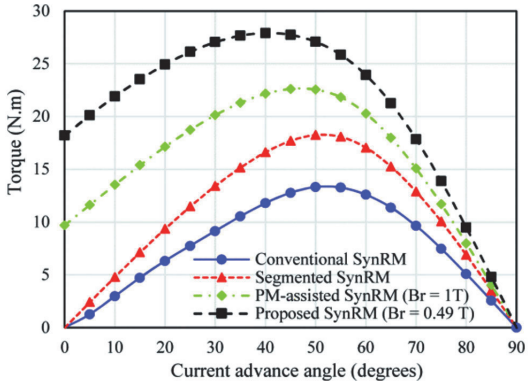


Figure 13. Comparison of torque characteristics [105].

In [106] the authors focused on efficiency and the starting ability of SynRM, by designing a 1-HP LS-SynRM and subsequently manufacturing it using AM. For the same design topology, the authors also presented a LS-SynRM [107] having flux barriers with 3D-net structure (only realizable with AM). The control over silicon content and machine's geometry optimization permitted lower iron losses and higher efficiency for same operating conditions. For another example of AM-built Syn-RM [108] the reduction of eddy-currents, while retaining the mechanical integrity, was achieved by addressing the multi-material printing limitation of metal-AM in an innovative way. A polycarbonate resin-based, separately printed insulation structure was assembled with the metal-AM produced rotor core. The performance analysis at rated-speed showed 6% increase in output density and 1% increase in efficiency as compared to existing model being applied in industry. In [109], the authors showcase potential degree of freedom offered by AM in terms of parameter selection for FEM basedshape optimization. The paper presents substantial improvement in performance parameters such as torque ripple and average torque output by the means of optimizing the reluctance motor's rotor shape. These results, how small in terms of improvement they may be, prove the case for potential of utilizing AM in manufacturing SynRMs.

4.3. Claw-Pole Machines

Claw-pole machines (CPM) having electrically excited claw-pole DC fields, yield higher torque density of up-to three times higher than conventional machines. This is mainly due to their ability to produce 3D-hetropolar magnetic field from single-coil excitation within claw-pole halves. The benefit of higher torque density, makes CPM an ideal candidate for a wide range of applications requiring size compactness like in automobile alternators, medium-sized household appliances etc. These machines have a complex design that is not easily realizable using conventional electrical-steel lamination construction and the use of SMCs has shown to be most advantageous regarding the manufacturing purposes [110,111].

Various topologies for rotor/stator-claw construction have been proposed over-time for industrial applications. A prototype CPM is shown in Figure 14a for illustration purpose. This machine was designed, manufactured with SMC-core of low mass density, analyzed and successfully tested for key performance and production parameters against a benchmark induction motor which is bulk-produced in industry for medium-sized household applications [112].

The torque coefficient of a CPM is dependent on the number of pole pairs but with increase in pole number, leakage flux also increases resulting in decreased power factor and efficiency. This necessitates for an optimization of pole pair quantity. Then comes the issue of cogging torque which is best dealt with magnet skewing, claw pole shape optimization, stator tooth notching, magnet axial pairing and magnet shift. The authors of [113,114]

investigated these design topologies for a CPM, against the performance parameters. The basic design model consists of claw-pole stator cores encapsulating a global winding and a rotor core mounted with magnets. Figure 14b–e illustrate these topologies. With these design changes and optimizations, the CPM achieves higher output torque density but the design gets extremely complex. This complexity in design limits the usage of conventional manufacturing techniques but with the flexibility in design realization offered by AM, CPM becomes a strong candidate for AM-built electrical machine of future.

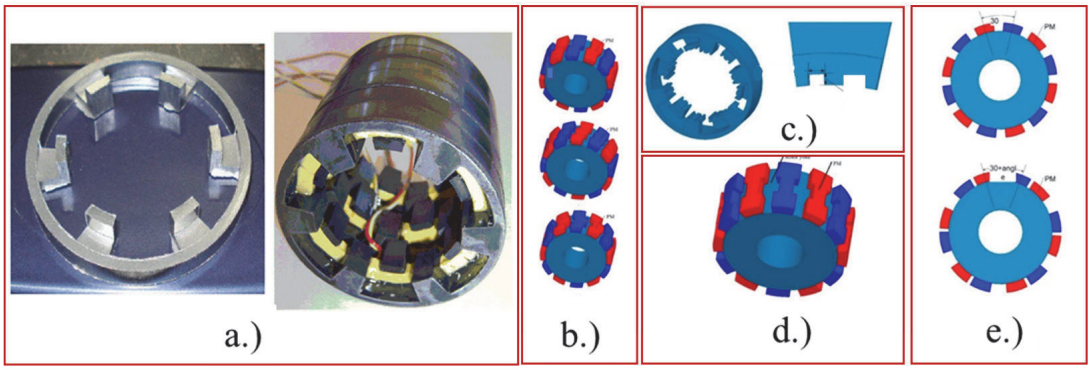


Figure 14. (**a**) Molded stator of three phase CPM [112] (**b**) Magnet Skewing [115] (**c**) Claw-pole shaping & stator tooth notching [113] (**d**) Magnet axial pairing [113] (**e**) Magnet Shifting [113].

4.4. Hysteresis Motors

A hysteresis motor is essentially a synchronous motor without the DC excitation. The interaction of rotating stator flux with that of remnant flux (due to hysteresis effect which is normally not desirable in other machines), produces torque. These machines offer constant torque from initial to synchronous speed with the ability to accelerate and synchronize high-inertia loads. However, due to its operation being mainly based on the hysteresis losses, its power factor and torque/volume ratio is low [115]. Still, these machines are useful in low power applications where constant speed and low torque ripple are the main required characteristics such as; precision equipment, clocks, hard disks and gyroscopes etc. [116]. Their construction is relatively simple with a solid rotor of hard-magnetic material. The stator is of slotted construction; to house single or poly-phase windings that produce rotating flux. Figure 15 illustrates the hysteresis motor construction concept [117].

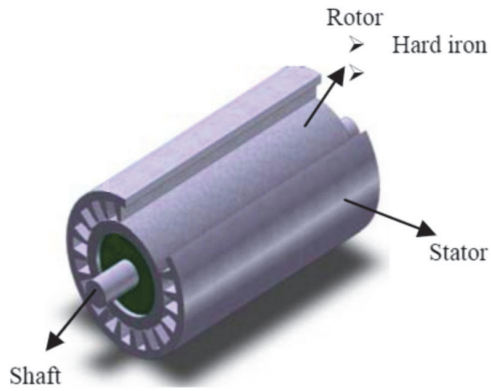


Figure 15. Illustration of hysteresis motor construction [117].

With the rising demand of high speed and low torque-ripple machines for special-purpose and precision demanding applications; hysteresis motors with solid rotor have a promising utilization scenario, over other electrical machines with sintered PMs or laminated sheet configurations. This is due to a number of factors, such as:

- Mechanical strength is affected with laminated sheet configuration of conventional motors, which limits the maximum attainable speed.
- Solid rotor of hysteresis motor provides high stiffness during critical speed transitions
- Thermal behavior of conventional induction motors, where eddy currents cause overheating of rotor and in the case of synchronous PM motors, where excessive heating can cause demagnetization
- Hysteresis motor's ability to improve its torque performance due to magnetization of rotor in response to impulsive electrical over-excitation [115,118–120]

Recent research works such as in [118,119,121] have showcased potential of various design topologies for hysteresis motors, regarding their application in high-speed context.

The authors of [51,122] also presented the attributes in terms of density and coercivity for magnetic material with various compositions, manufactured through cold spray (CS) and fused filament fabrication (FFF) techniques. The magnetic material was manufactured from readily available commercial powders. Table 3 provides attributes for hard magnetic materials from various techniques and different printing parameters.

Table 3. Attributes of various AM produced magnetic materials [51,123,124].

Powder Mix Composition	Density(g/cm^3)	Coercivity(kA/m)	AM Technique
52% (vol.) MQP-S-11-9; 48% H15	4.43	676	CS
52% (vol.) MQFP-B; 48% H15	4.32	715	CS
77% (vol.) MQFP-B; 23% H15	5.05	706	CS
77% (vol.) MQFP-B; 23% H3	6.15	693	CS
38.5% (vol.) MQP-S-11-9, 38.5% MQFP-B (23% H15)	5.01	694	CS
65% (vol.) isotropic NdFeB; 35% polyamide	5.2	688.4	BAAM
$Nd_2Fe_{14}B$	7	695	SLM (printed grain size 1 μm)
$Nd_2Fe_{14}B$	–	20	SLM (laser velocity 0.025 m/s)
$Nd_2Fe_{14}B$	–	10	SLM (laser velocity 0.036 m/s)

MQP-S-11-9 (NdFeB with grain size 40 μm); MQFP-B (NdFeB with grain size 10 μm); H15 (Al binder with grain size 20 μm); H3 (Al binder with grain size 4 μm).

A wide range of variation in coercivity value with various AM-techniques and associated printing parameters, establishes the prospect of utilizing AM in manufacturing hysteresis motor with magnetic characteristics optimized for application-specific requirements. Other than the section where AM of permanent magnets was discussed, this article was mostly aimed at finding and highlighting the techniques to mitigate the generic issues of hysteresis and eddy current losses in printed machine parts. Manufacturing of hysteresis motor can significantly utilize the benefits offered by AM in the form of efficient mechanical and thermal management assemblies, without investing much effort in avoiding the associated hysteresis and eddy current losses.

5. Conclusions

Existing research and the future potential of utilizing AM in the fabrication of electrical machines are investigated in this paper. Prevalent studies show that the efforts have been majorly focused on utilizing AM to produce individual machine parts or subassemblies. In that respect too, a varied level of progress is observed. The research level is relatively

mature for passive parts such as mechanical and thermal management assemblies compared to active parts such as coils/windings, cores, and PMs. Due to this varied level of progress and minimal effort towards producing complete electrical machines, AM has not yet progressed to a level where it can replace conventional manufacturing techniques for large-scale production.

Virtually, AM offers a broad range of benefits over conventional manufacturing techniques such as:

- Optimal material utilization
- Structural topology optimization resulting in improved thermal and mechanical performance
- Optimal electromagnetic energy guidance through complex geometric shape realization
- Size and weight reduction due to enablement of integrated functionalities
- Control over material composition and hence its physical properties

With this much to offer, AM virtually has the potential to replace conventional manufacturing techniques completely. However, in reality, it lacks in some aspects such as the maximum size of print-bed, associated time & cost of production, the need for post-processing, and a relatively lesser level of research maturity in electromagnetic properties of printed parts. Due to these reasons, the utilization of AM in the industry is currently hindered.

With AM being utilized at its full potential, the production of mass-personalized or application-specific electrical machines will be enabled. With efforts in the right direction, it is just a matter of time before AM will be equivalent/competitive to conventional manufacturing techniques. The most natural step forward is to explore application-specific/complex machine designs which are not realizable otherwise. These may include customized machines for various industries like robotics, automotive, aerospace and medium-sized appliances, etc. These applications require compact and high power-density electrical machines. The candidate machines presented in this text offer such qualities with a lot of potential for improvement in their performance parameters by introducing asymmetry in their design. Asymmetry in design is a feature that is most difficult to realize using conventional manufacturing methods and that is where AM comes-in, as the only potential enabling technique for this feature.

Another thing evident from the examples cited in this article is that a number of many industries like General Electric (GE), Boeing and Rolls Royce are already utilizing AM in producing high-performance parts for applications ranging from vehicle traction to satellite and aerospace purposes. All of this necessitates the direction of research efforts towards the upcoming future of entirely AM-built electrical machines, and the most natural step-forward is the development of a comprehensive design scheme, keeping in view the latest state-of-the-art.

Author Contributions: Conceptualization, M.U.N., and A.K.; methodology, M.U.N. and A.K.; validation, A.K., and B.A.; Writing—Original draft preparation, M.U.N.; Writing—Review and editing, M.U.N., A.K., T.V. and A.R.; visualization, A.K., M.U.N.; supervision, A.K. All authors have read and agreed to the published version of the manuscript.

Funding: This work was supported by the Estonian Research Council grant (PSG-137).

Institutional Review Board Statement: Not Applicable.

Informed Consent Statement: Not Applicable.

Data Availability Statement: Data is contained within the article.

Conflicts of Interest: The authors declare no conflict of interest.

References

1. Dilberoglu, U.M.; Gharehpapagh, B.; Yaman, U.; Dolen, M. The Role of Additive Manufacturing in the Era of Industry 4.0. *Procedia Manuf.* **2017**, *11*, 545–554. [CrossRef]
2. Metal Additive Manufacturing. *GE to Install First Metal Additively Manufactured Part on GEnx Commercial Airline Engines*; Metal Additive Manufacturing: Shrewsbury, UK, 2018; Volume 4, p. 10.
3. Ridge, O. GE Research Launches Project to Develop Metal Additively Manufactured Heat Exchanger. 2019. Available online: https://www.metal-am.com/ge-research-launches-project-to-develop-metal-additively-manufactured-heat-exchanger/ (accessed on 25 January 2021).
4. Metal, A.M. Boeing 777X Takes Flight with Reported 300 Additively Manufactured Parts in each GE9X Engine. 2020. Available online: https://www.metal-am.com/boeing-777x-takes-flight-with-reported-300-additively-manufactured-parts-in-each-ge9x-engine/ (accessed on 25 January 2021).
5. ESA Awards Dawn Aerospace €385K Contract for Additively Manufactured Rocket Engines. Available online: https://www.metal-am.com/esa-awards-dawn-aerospace-e385k-contract-for-additively-manufactured-rocket-engines/ (accessed on 25 January 2021).
6. Metal Additive Manufacturing. *Airbus Helicopters Begins Large-Scale Metal Additive Manufacturing of A350 Components*; Metal Additive Manufacturing: Shrewsbury, UK, 2018; Volume 4, p. 36.
7. Tiismus, H.; Kallaste, A.; Belahcen, A.; Rassolkin, A.; Vaimann, T. Challenges of Additive Manufacturing of Electrical Machines. In Proceedings of the 2019 IEEE 12th International Symposium on Diagnostics for Electrical Machines, Power Electronics and Drives (SDEMPED), Toulouse, France, 27–30 August 2019; pp. 44–48. [CrossRef]
8. Project to Automate Post-Processing of Additively Manufactured Parts. Available online: https://www.metal-am.com/project-to-automate-post-processing-of-additively-manufactured-parts/ (accessed on 25 January 2021).
9. Aguilera, E.; Ramos, J.; Espalin, D.; Cedillos, F.; Muse, D.; Wicker, R.; MacDonald, E. 3D Printing of Electro Mechanical Systems. In Proceedings of the Solid Freeform Fabrication Symposium, Austin, TX, USA, 12–14 August 2013.
10. Hiller, J.D.; Lipson, H. Fully Recyclable Multi-Material Printing. In Proceedings of the Solid Freeform Fabrication, Austin, TX, USA, 3–5 August 2009.
11. Wrobel, R.; Mecrow, B.C. A Comprehensive Review of Additive Manufacturing in Construction of Electrical Machines. *IEEE Trans. Energy Convers.* **2020**, *35*, 1054–1064. [CrossRef]
12. Tiismus, H.; Kallaste, A.; Vaimann, T.; Rassolkin, A.; Belahcen, A. Technologies for Additive Manufacturing of Electrical Machines. In Proceedings of the 2019 20th International Conference of Young Specialists on Micro/Nanotechnologies and Electron Devices (EDM), Erlagol, Russia, 29 June–3 July 2019; Volume 2019, pp. 651–655. [CrossRef]
13. Lorenz, F.; Rudolph, J.; Wemer, R. Design of 3D Printed High Performance Windings for Switched Reluctance Machines. In Proceedings of the 2018 23rd International Conference on Electrical Machines (ICEM), Alexandroupoli, Greece, 3–6 September 2018; pp. 2451–2457. [CrossRef]
14. Wu, F.; El-Refaie, A.M. toward Additively Manufactured Electrical Machines: Opportunities and Challenges. *IEEE Trans. Ind. Appl.* **2020**, *56*, 1306–1320. [CrossRef]
15. Paranthaman, M.P.; Yildirim, V.; Lamichhane, T.N.; Begley, B.A.; Post, B.K.; Hassen, A.A.; Sales, B.C.; Gandha, K.; Nlebedim, I.C. Additive Manufacturing of Isotropic NdFeB PPS Bonded Permanent Magnets. *Materials* **2020**, *13*, 3319. [CrossRef]
16. Lamichhane, T.N.; Sethuraman, L.; Dalagan, A.; Wang, H.; Keller, J.; Paranthaman, M.P. Additive manufacturing of soft magnets for electrical machines—A review. *Mater. Today Phys.* **2020**, *15*, 100255. [CrossRef]
17. 3D-Multimaterialdruck | Professur Elektrische Energiewandlungssystem und Antriebe | Fakultät für Elektrotechnik und I . . . | TU Chemnitz. Available online: https://www.tu-chemnitz.de/etit/ema/AMMM/ (accessed on 25 January 2021).
18. Silbernagel, C. Submitted: Investigation of the Design, Manufacture and Testing of Additively Manufactured Coils for Electric Motor Applications. 2019. Available online: https://www.researchgate.net/publication/336922428_Investigation_of_the_design_manufacture_and_testing_of_additively_manufactured_coils_for_electric_motor_applications (accessed on 25 January 2021).
19. Shokrollahi, H.; Janghorban, K. Soft magnetic composite materials (SMCs). *J. Mater. Process. Technol.* **2007**, *189*, 1–12. [CrossRef]
20. Garibaldi, M. Laser Additive Manufacturing of Soft Magnetic Cores for Rotating Electrical Machinery: Materials Development and Part Design. 2018. Available online: https://www.researchgate.net/publication/329610071_Laser_additive_manufacturing_of_soft_magnetic_cores_for_rotating_electrical_machinery_materials_development_and_part_design#fullTextFileContent (accessed on 25 January 2021).
21. Goll, D.; Schuller, D.; Martinek, G.; Kunert, T.; Schurr, J.; Sinz, C.; Schubert, T.; Bernthaler, T.; Riegel, H.; Schneider, G. Additive manufacturing of soft magnetic materials and components. *Addit. Manuf.* **2019**, *27*, 428–439. [CrossRef]
22. Tiismus, H.; Kallaste, A.; Belahcen, A.; Rassolkin, A.; Vaimann, T. Hysteresis Loss Evaluation of Additively Manufactured Soft Magnetic Core. In Proceedings of the 2020 International Conference on Electrical Machines (ICEM), Gothenburg, Sweden, 23–26 August 2020; pp. 1657–1661. [CrossRef]
23. Tiismus, H.; Kallaste, A.; Belahcen, A.; Vaimann, T.; Rassõlkin, A.; Lukichev, D. Hysteresis Measurements and Numerical Losses Segregation of Additively Manufactured Silicon Steel for 3D Printing Electrical Machines. *Appl. Sci.* **2020**, *10*, 6515. [CrossRef]
24. Pham, T.; Kwon, P.; Foster, S. Additive Manufacturing and Topology Optimization of Magnetic Materials for Electrical Machines—A Review. *Energies* **2021**, *14*, 283. [CrossRef]

25. Babuska, T.F.; Wilson, M.A.; Johnson, K.L.; Whetten, S.R.; Curry, J.F.; Rodelas, J.M.; Atkinson, C.; Lu, P.; Chandross, M.; Krick, B.A.; et al. Achieving high strength and ductility in traditionally brittle soft magnetic intermetallics via additive manufacturing. *Acta Mater.* **2019**, *180*, 149–157. [CrossRef]
26. Metsä-Kortelainen, S.; Lindroos, T.; Savolainen, M.; Jokinen, A.; Revuelta, A.; Pasanen, A.; Ruusuvuori, K.; Pippuri, J. Manufacturing of Topology Optimized Soft Magnetic Core through 3D Printing. 2016. Available online: https://cris.vtt.fi/en/publications/manufacturing-of-topology-optimized-soft-magnetic-core-through-3d (accessed on 26 January 2021).
27. Freeman, F.S.; Lincoln, A.; Sharp, J.; Lambourne, A.; Todd, I. Exploiting thermal strain to achieve an in-situ magnetically graded material. *Mater. Des.* **2019**, *161*, 14–21. [CrossRef]
28. Zhang, Z.-Y.; Jhong, K.J.; Cheng, C.-W.; Huang, P.-W.; Tsai, M.-C.; Lee, W.-H. Metal 3D printing of synchronous reluctance motor. In Proceedings of the 2016 IEEE International Conference on Industrial Technology (ICIT), Taipei, Taiwan, 14–17 March 2016; Volume 2016, pp. 1125–1128. [CrossRef]
29. Yan, Y.; Lu, G.-Q.; Ngo, K.D.T.; Guido, L.J.; Aning, A.O.; Reynolds, W.T. *Design Methodology and Materials for Additive Manufacturing of Magnetic Components*; Virginia Tech: Blacksburg, VA, USA, April 2017. Available online: https://vtechworks.lib.vt.edu/handle/10919/77394 (accessed on 26 January 2021).
30. Yan, Y.; Ding, C.; Ngo, K.D.T.; Mei, Y.; Lu, G.-Q. Additive manufacturing of planar inductor for Power Electronics applications. In Proceedings of the 2016 International Symposium on 3D Power Electronics Integration and Manufacturing (3D-PEIM), Raleigh, NC, USA, 13–15 June 2016. [CrossRef]
31. Mikler, C.V.; Chaudhary, V.; Borkar, T.; Soni, V.; Jaeger, D.; Chen, X.; Contieri, R.; Ramanujan, R.V.; Banerjee, R. Laser Additive Manufacturing of Magnetic Materials. *JOM* **2017**, *69*, 532–543. [CrossRef]
32. Benack, N.C.; Wang, T.; Matthews, K.; Taheri, M.L. Additive Manufacturing Methods for Soft Magnetic Composites (SMCs). *Microsc. Microanal.* **2018**, *24*, 1066–1067. [CrossRef]
33. Lambourne, A. Opportunities and Challenges of ALM in Electrical Machines. In Proceedings of the Advanced Propulsion Centre UK Seminar, Birmingham, UK, 11–12 November 2019; Institute of Electrical and Electronics Engineers Inc.: Piscataway, NJ, USA, 2019; Volume 35.
34. Garibaldi, M.; Gerada, C.; Ashcroft, I.A.; Hague, R.J. Free-Form Design of Electrical Machine Rotor Cores for Production Using Additive Manufacturing. *J. Mech. Des. Trans.* **2019**, *141*, 1–27. [CrossRef]
35. Lammers, S.; Adam, G.; Schmid, H.J.; Mrozek, R.; Oberacker, R.; Hoffmann, M.J.; Quattrone, F.; Ponick, B. Additive Manufacturing of a lightweight rotor for a permanent magnet synchronous machine. In Proceedings of the 2016 6th International Electric Drives Production Conference (EDPC), Nuremberg, Germany, 30 November–1 December 2016; pp. 41–45. [CrossRef]
36. Chinthavali, M. 3D printing technology for automotive applications. In Proceedings of the 2016 International Symposium on 3D Power Electronics Integration and Manufacturing (3D-PEIM), Raleigh, NC, USA, 13–15 June 2016; pp. 1–13. [CrossRef]
37. Simpson, N.; Mellor, P.H. Additive manufacturing of shaped profile windings for minimal AC loss in gapped inductors. In Proceedings of the 2017 IEEE International Electric Machines and Drives Conference (IEMDC), Miami, FL, USA, 21–24 May 2017. [CrossRef]
38. Simpson, N.; Mellor, P.H. Additive Manufacturing of Shaped Profile Windings for Minimal AC Loss in Electrical Machines. In Proceedings of the 2018 IEEE Energy Conversion Congress and Exposition (ECCE), Portland, OR, USA, 23–27 September 2018; pp. 5765–5772. [CrossRef]
39. Simpson, N.; North, D.J.; Collins, S.M.; Mellor, P.H. Additive Manufacturing of Shaped Profile Windings for Minimal AC Loss in Electrical Machines. *IEEE Trans. Ind. Appl.* **2020**, *56*, 2510–2519. [CrossRef]
40. Wohlers, C.; Juris, P.; Kabelac, S.; Ponick, B. Design and direct liquid cooling of tooth-coil windings. *Electr. Eng.* **2018**, *100*, 2299–2308. [CrossRef]
41. Urban, N.; Huber, F.; Franke, J. Influences of process parameters on rare earth magnets produced by laser beam melting. In Proceedings of the 2017 7th International Electric Drives Production Conference (EDPC), Wuerzburg, Germany, 5–6 December 2017; Volume 2017, pp. 1–5. [CrossRef]
42. Compton, B.G.; Kemp, J.W.; Novikov, T.V.; Pack, R.C.; Nlebedim, C.I.; Duty, C.E.; Rios, O.; Paranthaman, M.P. Direct-write 3D printing of NdFeB bonded magnets. *Mater. Manuf. Process.* **2018**, *33*, 109–113. [CrossRef]
43. Paranthaman, M.P.; Shafer, C.S.; Elliott, A.M.; Siddel, D.H.; McGuire, M.A.; Springfield, R.M.; Martin, J.; Fredette, R.; Ormerod, J. Binder Jetting: A Novel NdFeB Bonded Magnet Fabrication Process. *JOM* **2016**, *68*, 1978–1982. [CrossRef]
44. Li, L.; Tirado, A.; Conner, B.; Chi, M.; Elliott, A.M.; Rios, O.; Zhou, H.; Paranthaman, M.P. A novel method combining additive manufacturing and alloy infiltration for NdFeB bonded magnet fabrication. *J. Magn. Magn. Mater.* **2017**, *438*, 163–167. [CrossRef]
45. Li, L.; Tirado, A.; Nlebedim, I.C.; Rios, O.; Post, B.; Kunc, V.; Lowden, R.R.; Lara-Curzio, E.; Fredette, R.; Ormerod, J.; et al. Big Area Additive Manufacturing of High Performance Bonded NdFeB Magnets. *Sci. Rep.* **2016**, *6*, 1–7. [CrossRef]
46. Li, L.; Post, B.; Kunc, V.; Elliott, A.M.; Paranthaman, M.P. Additive manufacturing of near-net-shape bonded magnets: Prospects and challenges. *Scr. Mater.* **2017**, *135*, 100–104. [CrossRef]
47. Li, L.; Jones, K.; Sales, B.; Pries, J.L.; Nlebedim, I.; Jin, K.; Bei, H.; Post, B.K.; Kesler, M.S.; Rios, O.; et al. Fabrication of highly dense isotropic Nd-Fe-B nylon bonded magnets via extrusion-based additive manufacturing. *Addit. Manuf.* **2018**, *21*, 495–500. [CrossRef]
48. Wang, S.; Kang, J. Topology optimization of nonlinear magnetostatics. *IEEE Trans. Magn.* **2002**, *38*, 1029–1032. [CrossRef]

49. Huber, C.; Abert, C.; Bruckner, F.; Pfaff, C.; Kriwet, J.; Groenefeld, M.; Teliban, I.; Vogler, C.; Suess, D. Topology optimized and 3D printed polymer-bonded permanent magnets for a predefined external field. *J. Appl. Phys.* **2017**, *122*, 053904. [CrossRef]
50. Wu, F.; El-Refaie, A.M. Towards Fully Additively-Manufactured Permanent Magnet Synchronous Machines: Opportunities and Challenges. In Proceedings of the 2019 IEEE International Electric Machines & Drives Conference (IEMDC), San Diego, CA, USA, 12–15 May 2019; pp. 2225–2232. [CrossRef]
51. Jaćimović, J.; Binda, F.; Herrmann, L.G.; Greuter, F.; Genta, J.; Calvo, M.; Tomše, T.; Simon, R.A. Net Shape 3D Printed NdFeB Permanent Magnet. *Adv. Eng. Mater.* **2017**, *19*, 1700098. [CrossRef]
52. Mapley, M.; Pauls, J.P.; Tansley, G.; Busch, A.; Gregory, S.D. Selective laser sintering of bonded magnets from flake and spherical powders. *Scr. Mater.* **2019**, *172*, 154–158. [CrossRef]
53. Lamarre, J.-M.; Bernier, F. Permanent Magnets Produced by Cold Spray Additive Manufacturing for Electric Engines. *J. Therm. Spray Technol.* **2019**, *28*, 1709–1717. [CrossRef]
54. Ibrahim, M.; Bernier, F.; Lamarre, J.-M. Novel Multi-layer Design and Additive Manufacturing Fabrication of a High Power Density and Efficiency Interior PM Motor. In Proceedings of the 2020 IEEE Energy Conversion Congress and Exposition (ECCE), Detroit, MI, USA, 11–15 October 2020; pp. 3601–3606. [CrossRef]
55. Sagawa, M.; Fujimura, S.; Yamamoto, H.; Matsuura, Y.; Hiraga, K. Permanent magnet materials based on the rare earth-iron-boron tetragonal compounds. *IEEE Trans. Magn.* **1984**, *20*, 1584–1589. [CrossRef]
56. Tenaud, P.; Vial, F.; Sagawa, M. Improved corrosion and temperature behaviour of modified Nd-Fe-B magnets. *IEEE Trans. Magn.* **1990**, *26*, 1930–1932. [CrossRef]
57. Kramer, M.J.; McCallum, R.W.; Anderson, I.A.; Constantinides, S. Prospects for Non-Rare Earth Permanent Magnets for Traction Motors and Generators. *JOM* **2012**, *64*, 752–763. [CrossRef]
58. Paranthaman, M.P.; Sridharan, N.; List, F.A.; Babu, S.S.; Dehoff, R.R.; Constantinides, S. *Additive Manufacturing of Near-net Shaped Permanent Magnets*; Oak Ridge National Laboratory: Oak Ridge, TN, USA, 2016. [CrossRef]
59. Sridharan, N.; Cakmak, E.; List, F.A.; Uçar, H.; Constantinides, S.; Babu, S.S.; McCall, S.K.; Paranthaman, M.P. Rationalization of solidification mechanism of Nd–Fe–B magnets during laser directed-energy deposition. *J. Mater. Sci.* **2018**, *53*, 8619–8626. [CrossRef]
60. Additive Manufacturing Moves TUfast. Available online: https://additivenews.com/additive-manufacturing-moves-tufast/ (accessed on 28 January 2021).
61. Nottingham PhD Student Wins Additive World Design Challenge Award. Available online: https://exchange.nottingham.ac.uk/blog/phd-student-wins-additive-world-design-challenge-award/ (accessed on 28 January 2021).
62. Sixel, W.; Liu, M.; Nellis, G.; Sarlioglu, B. Cooling of Windings in Electric Machines via 3D Printed Heat Exchanger. In Proceedings of the 2018 IEEE Energy Conversion Congress and Exposition (ECCE), Portland, OR, USA, 23–27 September 2018; pp. 229–235. [CrossRef]
63. Tate, J.G.; Richardson, B.S.; Love, L.J. *Additive Manufacturing for Low Volume Bearings*; Oak Ridge National Laboratory: Oak Ridge, TN, USA, 2017. [CrossRef]
64. Carriero, A.; Locatelli, M.; Ramakrishnan, K.; Mastinu, G.; Gobbi, M. A Review of the State of the Art of Electric Traction Motors Cooling Techniques. *SAE Tech. Pap. Ser.* **2018**. [CrossRef]
65. European Powder Metallurgy Association (EPMA)—Cooling Jacket with Internal Helix Structure. Available online: https://www.epma.com/spotlight-on-pm/cooling-jacket-with-internal-helix-structure (accessed on 27 March 2021).
66. Wrobel, R.; Mecrow, B. Additive Manufacturing in Construction of Electrical Machines—A Review. In Proceedings of the 2019 IEEE Workshop on Electrical Machines Design, Control and Diagnosis (WEMDCD), Athens, Greece, 22–23 April 2019; pp. 15–22. [CrossRef]
67. Wrobel, R.; Hussein, A. Design Considerations of Heat Guides Fabricated Using Additive Manufacturing for Enhanced Heat Transfer in Electrical Machines. In Proceedings of the 2018 IEEE Energy Conversion Congress and Exposition (ECCE), Portland, OR, USA, 23–27 September 2018; pp. 6506–6513. [CrossRef]
68. Isaza, J.F.; Aumund-Kopp, C. Additive Manufacturing with metal powders: Design for manufacture evolves into design for function. *Powder Metall. Rev.* **2014**, *3*, 41–50.
69. Lewandowski, J.J.; Seifi, M. Metal Additive Manufacturing: A Review of Mechanical Properties. *Annu. Rev. Mater. Res.* **2016**, *46*, 151–186. [CrossRef]
70. Mower, T.M.; Long, M.J. Mechanical behavior of additive manufactured, powder-bed laser-fused materials. *Mater. Sci. Eng. A* **2016**, *651*, 198–213. [CrossRef]
71. Dutta, B.; Froes, F.H. The additive manufacturing (AM) of titanium alloys. In *Titanium Powder Metallurgy: Science, Technology and Applications*; Elsevier: Amsterdam, The Netherlands, 2015; pp. 447–468.
72. Laimer, C. Brushless Motor—makeSEA. Available online: https://www.makesea.com/web/claimer/brushless-motor (accessed on 28 January 2021).
73. Tiismus, H.; Kallaste, A.; Vaimann, T.; Rassolkin, A.; Belahcen, A. Additive Manufacturing of Prototype Axial Flux Switched Reluctance Electrical Machine. In Proceedings of the 2021 28th International Workshop on Electric Drives: Improving Reliability of Electric Drives (IWED), Moscow, Russia, 27–29 January 2021.
74. Hošek, M.; Krishnasamy, J.; Sah, S.; Bashaw, T. Spray-Formed Hybrid-Field Electric Motor. In Proceedings of the 2016 ASME Design Engineering Technical Conference, Vancouver, BC, Canada, 17–21 July 2016; Volume 3. [CrossRef]

75. Krishnasamy, J.; Hosek, M. Spray-Formed Hybrid-Field Traction Motor. *SAE Tech. Pap. Ser.* **2017**, *1*. [CrossRef]
76. Schniedenharn, M.; Belting, M.; Batista, R.J.S.; Meiners, W.; Weisheit, A. Micro scale laser based additive manufacturing for metals. In Proceedings of the ICALEO 2013—32nd International Congress on Applications of Lasers & Electro-Optics, Miami, FL, USA, 6–10 October 2013; Volume 2013, pp. 661–666. [CrossRef]
77. Conrad, M.; De Doncker, R.W.; Schniedenharn, M.; Diatlov, A. Packaging for power semiconductors based on the 3D printing technology Selective Laser Melting. In Proceedings of the 2014 16th European Conference on Power Electronics and Applications, Lappeenranta, Finland, 26–28 August 2014. [CrossRef]
78. Why Companies Steadily Embrace Additive Manufacturing | IE. Available online: https://interestingengineering.com/why-companies-steadily-embrace-additive-manufacturing (accessed on 1 February 2021).
79. Formatec—Ceramic Injection Moulding. Available online: https://formateceurope.com/ceramic-injection-moulding (accessed on 22 February 2021).
80. Australian Army Successfully Conducts Field Test of SPEE3D Metal 3D Printer—3D Printing Industry. Available online: https://3dprintingindustry.com/news/australian-army-successfully-conducts-field-test-of-spee3d-metal-3d-printer-172941/ (accessed on 22 February 2021).
81. Marshall Aerospace Soars with 3D Printing | Stratasys. Available online: https://www.stratasys.com/explore/case-study/marshall-aerospace-and-defence-group (accessed on 20 February 2021).
82. Nemec, M.; Makuc, D.; Ambrozic, V.; Fiser, R. Simplified model of induction machine with electrical rotor asymmetry. In Proceedings of the XIX International Conference on Electrical Machines—ICEM 2010, Rome, Italy, 6–8 September 2010. [CrossRef]
83. Sun, X.; Sizov, G.; Melfi, M. Asymmetrical Design in Electrical Machines. In Proceedings of the 2019 IEEE Energy Conversion Congress and Exposition (ECCE), Baltimore, MD, USA, 29 September–3 October 2019; pp. 3786–3792. [CrossRef]
84. Chen, Q.; Shi, X.; Xu, G.; Zhao, W. Torque calculation of five-phase synchronous reluctance motors with shifted-asymmetrical-salient-poles under saturation condition. *China Electrotech. Soc. Trans. Electr. Mach. Syst.* **2020**, *4*, 105–113. [CrossRef]
85. Caruso, M.; Cecconi, V.; Di Tommaso, A.O.; Miceli, R.; Nevoloso, C. Performance Comparison of Electrical Motors equipped with slightly Asymmetrical Windings. In Proceedings of the 2019 AEIT International Conference of Electrical and Electronic Technologies for Automotive (AEIT AUTOMOTIVE), Torino, Italy, 2–4 July 2019. [CrossRef]
86. Ren, W.; Xu, Q.; Li, Q. Asymmetrical V-Shape Rotor Configuration of an Interior Permanent Magnet Machine for Improving Torque Characteristics. *IEEE Trans. Magn.* **2015**, *51*, 1–4. [CrossRef]
87. Sanada, M.; Hiramoto, K.; Morimoto, S.; Takeda, Y. Torque Ripple Improvement for Synchronous Reluctance Motor Using an Asymmetric Flux Barrier Arrangement. *IEEE Trans. Ind. Appl.* **2004**, *40*, 1076–1082. [CrossRef]
88. Wanjiku, J.; Khan, M.A.; Barendse, P.S.; Pillay, P. Influence of Slot Openings and Tooth Profile on Cogging Torque in Axial-Flux PM Machines. *IEEE Trans. Ind. Electron.* **2015**, *62*, 7578–7589. [CrossRef]
89. Nuzzo, S.; Marfoli, A.; Papini, L.; Bolognesi, P.; Gerada, C.; Galea, M. The potential of exploiting non-symmetric structures in electrical machines. In Proceedings of the IECON 2019 45th Annual Conference of the IEEE Industrial Electronics Society, Lisbon, Portugal, 14–17 October 2019; Volume 2019, pp. 1393–1398. [CrossRef]
90. Zhao, W.; Chen, D.; Lipo, T.A.; Kwon, B.-I. Performance Improvement of Ferrite-Assisted Synchronous Reluctance Machines Using Asymmetrical Rotor Configurations. *IEEE Trans. Magn.* **2015**, *51*, 1–4. [CrossRef]
91. Yang, H.; Wang, W.; Lin, H.; Zhu, Z.Q.; Lyu, S.; Niu, S. A Novel Hybrid-Pole Interior PM Machine with Magnet-Axis-Shifting Effect. In Proceedings of the 2019 IEEE International Electric Machines & Drives Conference (IEMDC), San Diego, CA, USA, 12–15 May 2019; pp. 273–279. [CrossRef]
92. Wu, F.; El-Refaie, A.M. Minimization of Winding AC Losses Using Inhomogeneous Electrical Conductivity Enabled by Additive Manufacturing. In Proceedings of the 2020 IEEE Energy Conversion Congress and Exposition (ECCE), Detroit, MI, USA, 11–15 October 2020; pp. 3607–3614. [CrossRef]
93. Moreels, D.; Axial Flux vs. Radial Flux Machines. 31 January 2018. Available online: https://www.magnax.com/magnax-blog/axial-flux-vs-radial-flux.-4-reasons-why-does-axial-flux-machines-deliver-a-higher-power-density (accessed on 3 February 2021).
94. Krishnamurthy, M.; Edrington, C.; Emadi, A.; Asadi, P.; Ehsani, M.; Fahimi, B. Making the case for applications of switched reluctance motor technology in automotive products. *IEEE Trans. Power Electron.* **2006**, *21*, 659–675. [CrossRef]
95. Edvarrd. Characteristics and Work Principles of Switched Reluctance (SR) Motor. 8 December 2014. Available online: https://electrical-engineering-portal.com/characteristics-and-work-principles-of-switched-reluctance-sr-motor (accessed on 3 February 2021).
96. Gargalis, L.; Madonna, V.; Giangrande, P.; Rocca, R.; Hardy, M.; Ashcroft, I.; Galea, M.; Hague, R. Additive Manufacturing and Testing of a Soft Magnetic Rotor for a Switched Reluctance Motor. *IEEE Access* **2020**, *8*, 206982–206991. [CrossRef]
97. Gargalis, L.; Madonna, V.; Giangrande, P.; Rocca, R.; Ashcroft, I.; Hague, R.; Galea, M. Development and Testing of Soft Magnetic Rotor for a Switched Reluctance Motor Built Through Additive Manufacturing Technology. In Proceedings of the 2020 23rd International Conference on Electrical Machines and Systems (ICEMS), Hamamatsu, Japan, 24–27 November 2020; pp. 263–268. [CrossRef]

98. Tseng, G.; Jhong, K.; Tsai, M.; Huang, P.; Lee, L. Application of Additive Manufacturing for Low Torque Ripple of 6/4 Switched Reluctance Motor—IEEE Conference Publication. In Proceedings of the 19th International Conference on Electrical Machines and Systems (ICEMS), Chiba, Japan, 13–26 November 2016. Available online: https://ieeexplore.ieee.org/document/7837094 (accessed on 3 February 2021).
99. Manninen, A.; Keranen, J.; Pippuri-Makelainen, J.; Riipinen, T.; Metsa-Kortelainen, S.; Lindroos, T. Impact of Topology Optimization Problem Setup on Switched Reluctance Machine Design. In Proceedings of the 2019 22nd International Conference on the Computation of Electromagnetic Fields (COMPUMAG), Paris, France, 15–19 July 2019. [CrossRef]
100. Lee, J.; Seo, J.H.; Kikuchi, N. Topology optimization of switched reluctance motors for the desired torque profile. *Struct. Multidiscip. Optim.* **2010**, *42*, 783–796. [CrossRef]
101. Ban, B.; Stipetic, S.; Klanac, M. Synchronous Reluctance Machines: Theory, Design and the Potential Use in Traction Applications. In Proceedings of the 2019 International Conference on Electrical Drives & Power Electronics (EDPE), The High Tatras, Slovakia, 24–26 September 2019; Volume 2019, pp. 177–188. [CrossRef]
102. Bianchi, N.; Bolognani, S.; Carraro, E.; Castiello, M.; Fornasiero, E. Electric Vehicle Traction Based on Synchronous Reluctance Motors. *IEEE Trans. Ind. Appl.* **2016**, *52*, 4762–4769. [CrossRef]
103. Jurca, F.N.; Mircea, R.; Martis, C.; Martis, R.; Florin, P.P. Synchronous reluctance motors for small electric traction vehicle. In Proceedings of the 2014 International Conference and Exposition on Electrical and Power Engineering (EPE), Brno, Czech Republic, 12–14 May 2014; pp. 317–321. [CrossRef]
104. Cai, S.; Shen, J.; Hao, H.; Jin, M. Design methods of transversally laminated synchronous reluctance machines. *China Electrotech. Soc. Trans. Electr. Mach. Syst.* **2017**, *1*, 164–173. [CrossRef]
105. Ibrahim, M.; Bernier, F.; Lamarre, J.-M. Design of a PM-Assisted Synchronous Reluctance Motor Utilizing Additive Manufacturing of Magnetic Materials. In Proceedings of the 2019 IEEE Energy Conversion Congress and Exposition (ECCE), Baltimore, MD, USA, 29 September–3 October 2019; pp. 1663–1668. [CrossRef]
106. Zhang, Z.-Y.; Tsai, M.-C.; Huang, P.-W.; Cheng, C.-W.; Huang, J.-M. Characteristic comparison of transversally laminated anisotropic synchronous reluctance motor fabrication based on 2D lamination and 3D printing. In Proceedings of the 2015 18th International Conference on Electrical Machines and Systems (ICEMS), Pattaya, Thailand, 25–28 October 2015; pp. 894–897. [CrossRef]
107. Huang, P.; Tsai, M.; Jiang, I. 3D Structure Line Start Synchronous Reluctance Motor Design Based on Selective Laser Melting of 3D Printing. In Proceedings of the 2018 IEEE International Magnetics Conference (INTERMAG), Singapore, 23–27 April 2018. [CrossRef]
108. Hong, H.-S.; Liu, H.-C.; Cho, S.-Y.; Lee, J.; Jin, C.-S. Design of High-End Synchronous Reluctance Motor Using 3-D Printing Technology. *IEEE Trans. Magn.* **2017**, *53*, 1–5. [CrossRef]
109. Kaska, J.; Orosz, T.; Karban, P.; Dolezel, I.; Pechanek, R.; Panek, D. Optimization of Reluctance Motor with Printed Rotor. In Proceedings of the 2019 22nd International Conference on the Computation of Electromagnetic Fields (COMPUMAG), Paris, France, 15–19 July 2019. [CrossRef]
110. Jack, A.; Mecrow, B.; Maddison, C.; Wahab, N. Claw pole armature permanent magnet machines exploiting soft iron powder metallurgy. In Proceedings of the 1997 IEEE International Electric Machines and Drives Conference Record, Milwaukee, WI, USA, 18–21 May 2002. [CrossRef]
111. Guo, Y.; Zhu, J.G.; Watterson, P.; Wu, W. Comparative study of 3-D flux electrical machines with soft magnetic composite cores. *IEEE Trans. Ind. Appl.* **2003**, *39*, 1696–1703. [CrossRef]
112. Guo, Y.; Zhu, J.; Dorrell, D. Design and Analysis of a Claw Pole Permanent Magnet Motor With Molded Soft Magnetic Composite Core. *IEEE Trans. Magn.* **2009**, *45*, 4582–4585. [CrossRef]
113. Liu, C.; Lu, J.; Wang, Y.; Lei, G.; Zhu, J.; Guo, Y. Techniques for Reduction of the Cogging Torque in Claw Pole Machines with SMC Cores. *Energies* **2017**, *10*, 1541. [CrossRef]
114. Liu, C.; Lu, J.; Wang, Y.; Lei, G.; Zhu, J.; Guo, Y. Design Issues for Claw Pole Machines with Soft Magnetic Composite Cores. *Energies* **2018**, *11*, 1998. [CrossRef]
115. Galluzzi, R.; Amati, N.; Tonoli, A. Modeling, Design, and Validation of Magnetic Hysteresis Motors. *IEEE Trans. Ind. Electron.* **2020**, *67*, 1171–1179. [CrossRef]
116. Rajagopal, K. Design of a compact hysteresis motor used in a gyroscope. *IEEE Trans. Magn.* **2003**, *39*, 3013–3015. [CrossRef]
117. Inácio, D.; Inácio, S.; Pina, J.M.; Gonçalves, A.; Neves, M.V.; Rodrigues, A.L.; Pronto, A. Numerical and experimental comparison of electromechanical properties and efficiency of HTS and ferromagnetic hysteresis motors. *J. Phys. Conf. Ser.* **2008**, *97*. [CrossRef]
118. Galluzzi, R.; Tonoli, A.; Amati, N. Magnetic hysteresis machines for next-generation electric turbochargers. In Proceedings of the 2017 International Conference of Electrical and Electronic Technologies for Automotive, Torino, Italy, 15–16 June 2017. [CrossRef]
119. Jagieła, M.; Bumby, J.; Spooner, E. Time-domain and frequency-domain finite element models of a solid-rotor induction/hysteresis motor. *IET Electr. Power Appl.* **2010**, *4*, 185. [CrossRef]
120. O'Kelly, D. Hysteresis motor with overexcitation and solid-state control. *Proc. Inst. Electr. Eng.* **1978**, *125*, 288. [CrossRef]
121. Jagiela, M.; Garbiec, T.; Kowol, M. Design of High-Speed Hybrid Hysteresis Motor Rotor Using Finite Element Model and Decision Process. *IEEE Trans. Magn.* **2014**, *50*, 861–864. [CrossRef]
122. Goll, D.; Schurr, J.; Trauter, F.; Schanz, J.; Bernthaler, T.; Riegel, H.; Schneider, G. Additive manufacturing of soft and hard magnetic materials. *Procedia CIRP* **2020**, *94*, 248–253. [CrossRef]

123. Bernier, F.; Ibrahim, M.; Mihai, M.; Thomas, Y.; Lamarre, J.-M. Additive manufacturing of soft and hard magnetic materials used in electrical machines. *Met. Powder Rep.* **2020**, *75*, 334–343. [CrossRef]
124. Popov, V.; Koptyug, A.; Radulov, I.; Maccari, F.; Muller, G. Prospects of additive manufacturing of rare-earth and non-rare-earth permanent magnets. *Procedia Manuf.* **2018**, *21*, 100–108. [CrossRef]

Publication II

M. U. Naseer, A. Kallaste, and T. Vaimann, “A method for contouring an airgap profile in an electromagnetic device,” Estonian Patent Office, P202500004, 2025.

A method for contouring an airgap profile in an electromagnetic device

TECHNICAL FIELD

Present invention relates to a method for contouring an airgap profile in an electromagnetic device comprising an airgap in a magnetic path to reduce airgap reluctance.

BACKGROUND ART

International patent application WO2021/083631A1 discloses solution relating to a varying the cross-sections of airgap-forming electromagnetic parts to mitigate rotor temperature imbalances and prevent local overheating. While it introduces modifications to the airgap geometry, it lacks specificity in the shape of these variations. Electromagnetic performance aspects are not addressed, and the stator outer diameter remains constant. This design choice can lead to significant localized magnetic saturation, increasing the overall reluctance and potentially decreasing the device's output performance.

United States patent application US2014/0021822A1 proposes a use of rectangular projections and recesses in the airgap-forming parts to increase the airgap surface area. While it acknowledges the effect of increased airgap surface area on electromagnetic performance, it limits the geometric variations to simple rectangular shapes. The solution emphasizes manufacturability through sectionalized sintered cores but does not provide a comprehensive strategy for optimizing electromagnetic performance across different size and types of devices.

United States patent US8653713B2 includes a solution, where one, two, and three-step protrusions are used to modify the airgap profile, maintaining the airgap constant only in the radial direction. However, it lacks a shaping strategy for triangular or V-shaped contours. The increased airgap length in directions other than the radial causes the magnetic flux to concentrate radially, which may reduce the utilization of the increased airgap surface area. Additionally, the patent suggests that step protrusions can solve saturation issues at high magnetomotive forces, a claim not substantiated with comprehensive analysis applicable to various electromagnetic devices.

United States patents US6066908, US6034462 and US5777421 disclose serrated faces and sawtooth or conical shapes on the airgap-forming surfaces to reduce reluctance by increasing the airgap surface area. However, they do not define a precise contouring strategy or provide mathematical formulations for the shapes. The focus is on specific machine types and does not extend the applicability to devices like linear actuators or air-gapped transformers and inductors.

European patent applications EP2555389A1 and EP0944158A2 and French patent FR3109249B1 relate to concepts such as staggered (zigzag) airgap profiles, sinusoidal shapes, and increased rotor surface areas through varying cross-sections. While they aim to reduce airgap reluctance and enhance electromagnetic performance, they often lack detailed contouring strategies and do not address the implications of core saturation, or the optimization of contour amplitude based on operating conditions applicable to a broad range of electromagnetic devices.

The design and optimization of airgap profiles in electrical machines have been the subject of numerous studies and patents, aiming to improve electromagnetic performance, thermal management, and mechanical integrity. Various approaches have been proposed to modify the airgap geometry, primarily focusing on radial flux machines with inner rotors. However, these prior art solutions exhibit limitations that the present invention addresses through a novel contoured airgap topology applied to axial flux machines.

The prior art in the field of airgap design has primarily focused on specific machine types or limited geometrical modifications, often without a comprehensive strategy applicable to a broad range of electromagnetic devices. The present invention advances the state of the art by providing a universally applicable contoured airgap topology supported by mathematical formulations and thorough electromagnetic evaluations.

SUMMARY OF INVENTION

Present invention provides a method for contouring an airgap profile in an electromagnetic device comprising an airgap in a magnetic path to reduce airgap reluctance.

In the present invention, the airgap is profiled such that the airgap profile

corresponds to a contour of the guide profile line between the opposite faces forming the airgap between them at the midpoint of the airgap thickness taken perpendicular to said guide profile line, where said guide profile line lies in plane containing x- and y-axes, where said x-, y- and z-axes represent the first, second and third dimension, where x-axis is perpendicular to the general direction of flux flow in the magnetic path in the vicinity of said airgap, y-axis is in the general direction of the flux flow in said magnetic path and z-axis perpendicular both with x and y-axes.

This means that in a stationary electromagnetic device, x- and z-axes lie in the cross-section plane of the magnetic path core in the vicinity of the airgap and y-axis is perpendicular with said plane.

This means that in a rotating electromagnetic device in the case of an axial flux motor, the y-axis is parallel with the axis of rotation of motor, where the x-axis is perpendicular to said axis of rotation of motor. Said guide profile line and axis of rotation of motor both lie in the plane of longitudinal cut of said motor.

This means that in a rotating electromagnetic device in the case of a radial flux motor, the x-axis is parallel with the axis of rotation of motor, where the y-axis is perpendicular to said axis of rotation of motor. Said guide profile line and axis of rotation of motor both lie in the plane of longitudinal cut of said motor.

The airgap-facing surface profiles of the core components are offset by half the airgap thickness (g/2) perpendicular to said guide profile line on both sides of said guide profile line to define the airgap-facing surfaces of the core components such that the normal distance between the airgap-facing components remains uniform and a distribution of flux lines throughout the airgap profile are both uniform, and a shape of said airgap guide profile line is triangular, sinusoidal or circular.

In an embodiment, where the shape of said airgap guide profile line is triangular, said triangular airgap contour corresponds to the following conditions

$$\begin{cases} y = y_o + \frac{g}{2} + \frac{2A_c}{(x_2 - x_1)}(x - x_1) & x_1 < x < \frac{(x_1 + x_2)}{2} \\ y = y_o + \frac{g}{2} + 2A_c - \frac{2A_c}{(x_2 - x_1)}(x - x_1) & \frac{(x_1 + x_2)}{2} < x < x_2 \end{cases}$$

where

x_1 is the starting point of the core component, defining the starting point of airgap

in first axis,

x_2 is the edge-point of the core component defining the end point of the airgap in the first axis,

y_o is the midpoint of airgap thickness in the second axis,

A_c is the amplitude of the central-guide contour profile.

In an embodiment, where the shape of said airgap guide profile line is sinusoidal, said sinusoidal airgap contour corresponds to the following conditions

$$\begin{cases} y = y_o + \frac{g}{2} + A_c \sin\frac{\pi(x - x_1)}{(x_2 - x_1)} \end{cases} \qquad 0.01 < A_c < \frac{y_o}{2}$$

where

x_1 is the starting point of the core component, defining the starting point of airgap in first axis,

x_2 is the edge-point of the core component defining the end point of the airgap in the first axis,

y_o is the midpoint of airgap thickness in the second axis,

A_c is the amplitude of the central-guide contour profile.

In an embodiment, where the shape of said airgap guide profile line is circular, said circular airgap contour corresponds to the following conditions

$$\begin{cases} r = \left| \frac{\left(\frac{x_2 - x_1}{2}\right)^2 + {A_c}^2}{2A_c} \right| \\ \left(x - \frac{x_1 + x_2}{2}\right)^2 + \left(y - \frac{g}{2} + \sqrt{r^2 - \left(\frac{x_1 - x_2}{2}\right)^2} - y_o\right)^2 = r^2 \qquad for\ 0.01 < |A_c| < \frac{x_2 - x_1}{2} \\ \left(x - \frac{x_1 + x_2}{2}\right)^2 + \left(y - \frac{g}{2} - \sqrt{r^2 - \left(\frac{x_1 - x_2}{2}\right)^2} - y_o\right)^2 = r^2 \qquad for\ \frac{x_2 - x_1}{2} < |A_c| < \frac{y_o}{2} \end{cases}$$

where

x_1 is the starting point of the core component, defining the starting point of airgap in first axis,

x_2 is the edge-point of the core component defining the end point of the airgap in the first axis,

y_o is the midpoint of airgap thickness in the second axis,

A_c is the amplitude of the central-guide contour profile,

r is the radius of the circular contour profile.

Though the novel contoured airgap topology showcased here is unequivocally applicable to a wide range of electromagnetic devices involving airgap in their magnetic path. These include radial flux electrical machines (outer and inner rotor topologies), axial flux electrical machines (single stator-single rotor to multi stator-multi rotor configurations, air-gapped transformers/inductors, linear actuators and/or linear electrical machines).

The present invention introduces a novel method of reducing airgap reluctance and increasing power density without increasing the machine's mass/volume. This is achieved by contouring the faces of the machine components adjacent to the airgap, effectively modifying the airgap profile to increase its surface area. By introducing contours to the airgap-facing surfaces, the electromagnetic performance is enhanced without the need for larger machine components. This design innovation leads to a reduction in airgap reluctance, thereby improving the magnetic flux production against a given MMF (MMF = magnetomotive force), enhancing energy conversion efficiency, and increasing the power density of the machine.

Electrical machines, including motors and generators of various types, fundamentally rely on magnetic circuits that incorporate an airgap to facilitate mechanical movement. The presence of this airgap is essential for the operational functionality of these devices. However, the airgap introduces a significant challenge, that is, due to its low magnetic permeability compared to ferromagnetic core materials, the airgap's magnetic reluctance dominates the overall reluctance of the magnetic circuit. This high reluctance impedes the production of magnetic flux against an applied magnetomotive force (MMF), consequently affecting the efficiency of energy conversion and the power density of the machine. Enhancing these parameters is a primary objective in the design and optimization of electrical machines, as they are highly desired characteristics that determine the effectiveness and competitiveness of the machines in various applications.

In conventional designs, the reluctance of the magnetic circuit is lowered by enhancing the permeability of the core material on one side, and by reducing the airgap reluctance either through reduced airgap thickness or increased cross-sectional area of the airgap on the other side. While improving core material permeability is beneficial, it reaches a practical limit due to material properties and

cost considerations. The thickness of the airgap is constrained by mechanical manufacturing tolerances and thermal expansion considerations during operation. As such, there is a lower limit to how much the airgap thickness can be reduced without compromising mechanical integrity and operational reliability. Therefore, the primary possibility for further reducing airgap reluctance lies in increasing the airgap's surface area.

Traditionally, the airgap surface area is uniform and straight, a design choice driven by conventional manufacturing technologies such as the use of laminated steel sheets. These manufacturing constraints limit the ability to modify the airgap surface without significantly altering the machine's overall dimensions. In conventional design topology, increased cross-sectional area of the airgap can be achieved by increasing the cross-sectional area of the airgap facing components of the electrical machine such as the rotor, and stator surface areas. This leads to an increase in the overall volume of the machine components. This trade-off improves energy conversion efficiency but adversely affects the power density, which is a critical parameter in many applications.

By addressing both the design and practical implementation aspects, the invention achieves significant enhancements in energy conversion efficiency and power density without increasing the device's external dimensions. This innovative approach not only overcomes the limitations of prior art but also offers a versatile solution that can be adapted to various electromagnetic devices, including rotating machines (both radial and axial flux), linear actuators, transformers, and inductors.

The invention's universal applicability and optimization strategies provide a significant opportunity to develop more efficient and power-dense electromagnetic devices, meeting the ever-increasing demands for higher performance in diverse applications.

BRIEF DESCRIPTION OF DRAWINGS

Present invention is described below with reference to the accompanying schematic illustrations, in which:

Figure 1a and 1b depict respectively a magnetic circuit with airgap on Figure 1a and its schematic representation on Figure 1b.

Figures 2a to 2d illustrate straight and contoured magnetic circuit profiles, where respectively:

Figure 2a depicts straight airgap profile,

Figure 2b depicts triangular airgap profile with triangular guide profile line,

Figure 2c depicts sinusoidal airgap profile with sinusoidal guide profile line,

Figure 2d depicts circular airgap profile with circular guide profile line.

Figure 3 illustrates a benchmark magnetic circuit with straight air gap topology.

Figures 4a to 4c depict coil flux linkage versus input coil current for core material with constant magnetic permeability in comparison respectively triangular, sinusoidal and circular airgap profile, where respectively:

Figure 4a depicts a comparison straight airgap profile versus triangular airgap profile,

Figure 4b depicts a comparison straight airgap profile versus sinusoidal airgap profile,

Figure 4c depicts a comparison straight airgap profile versus circular airgap profile.

Figure 5 illustrates a decreasing cross-sectional area of the core in the vicinity of the contoured air gap.

Figure 6 illustrates a central contour defining the airgap.

Figure 7 depicts an implemented contour profiles for various magnitudes of contour amplitudes according to the defined contouring strategy and the respective FEA (= Finite Element Analysis) plots for flux lines in the core material and the airgap.

Figures 8a to 8c depict coil flux linkage versus input coil current for M400-50A core material with non-linear magnetic permeability in comparison respectively triangular, sinusoidal and circular airgap profile, where respectively:

Figure 8a depicts a comparison straight airgap profile versus triangular airgap profile,

Figure 8b depicts a comparison straight airgap profile versus sinusoidal airgap profile,

Figure 8c depicts a comparison straight airgap profile versus circular airgap profile.

Figures 9a to 9d depict a structure for an axial flux motor with straight/conventional airgap profile, where respectively:

Figure 9a is an exploded view of components assembly with one coil-side cut-away to expose the stator tooth-side (forming the airgap),

Figure 9b a cross-sectional view on the motor components assembly at the line B-B, Figure 9c a bottom view of the rotor at the line C-C shown in figure 9b and

Figure 9d a top view of stator assembly at the line D-D shown in figure 9b.

Figures 10a and 10b depict respectively a structure for an axial flux motor with contoured airgap profile, where Figure 10a contains an exploded view of components assembly and figure 10b a cross-sectional view on the motor components assembly at the line E-E shown in figure 10a.

Figure 11a depicts a cross-section of the radial flux motor.

Figures 11b and 11c depict respectively a radial flux motor with straight and contoured airgap profile in a cross-sectional view at the line F-F shown on Figure 11a.

DESCRIPTION OF EMBODIMENTS

ANALYTICAL AND SIMULATION EVIDENCE

To substantiate the effectiveness of the contoured airgap design, analytical calculations and finite element analysis (FEA) simulations can be employed using a basic gapped core magnetic circuit with a coil of N turns. In this setup, the magnetic circuit's performance is evaluated based on the flux linkage of the coil under a fixed applied MMF, represented by a current i flowing through the coil.

Reluctance ($\mathcal{R}$) of a magnetic circuit component is given by the analytical approximation formula:

$$\mathcal{R} = \frac{l}{\mu A}$$

where l is the length of the magnetic path, μ is the magnetic permeability of the material, and A is the cross-sectional area of the magnetic flux path. A basic magnetic circuit illustrating these terms is presented in Figure 1.

The magnetomotive force (MMF) is given by

$$MMF = Ni$$

and the flux in the magnetic circuit is then given by:

$$\phi = \frac{MMF}{\mathcal{R}_{total}}$$

$$\mathcal{R}_{total} = \mathcal{R}_c + \mathcal{R}_g$$

$$\mathcal{R}_c = \frac{l_c}{\mu A_{core}}$$

$$\mathcal{R}_g = \frac{g}{\mu_o A_g}$$

where l_c is the length of the magnetic path in core, μ is the magnetic permeability of the material, and A_{core} is the cross-sectional area of the magnetic path in the core. g is the airgap length and A_g is the cross-sectional area of the air gap.

Flux Linkage: A Key Performance Indicator of Magnetic Circuits

To measure and evaluate the performance of electromagnetic systems, flux linkage is often used as a key indicator. Flux linkage (λ) combines the magnetic flux (ϕ) with the number of turns (N) in a coil.

$$\lambda = N\phi$$

Substituting for the term of flux (ϕ) in above equation gives:

$$\lambda = \frac{N \times MMF}{\mathcal{R}_{total}} \qquad \text{(A)}$$

This shows that for a given number of turns in a coil and the applied MMF, the flux linkage depends on the reluctance of the magnetic path. Another representation of flux linkage is deduced by expanding the term MMF in previous equation

$$\lambda = \frac{N \times N \times i}{\mathcal{R}_{total}}$$

Whereas

$$L = \frac{N^2}{\mathcal{R}_{total}}$$

So, the alternate formulation for flux linkage becomes

$$\lambda = Li \qquad \text{(B)}$$

where L is the inductance of the coil.

In circuits with airgaps, since the airgap reluctance dominates, the flux linkage is mainly influenced by the airgap reluctance. A lower airgap reluctance leads to a higher flux production and consequently higher flux linkage. Both representations of flux linkage give the same results and the choice among them depends on how you are measuring it. For simulations using numerical methods, equation (A) is utilized and for practical measurements, equation (B) is utilized.

Focusing on the airgap section of the core 1, the basic concept of contouring the airgap 2 is illustrated in Figure 2. Figure 2 shows the front view of the area of interest (marked with dotted line in Figure 3), that is, the airgap 2 portion and is uniform in the third dimension. For reference purposes, the airgap 2 length g is given a value of 0.5mm here and is kept same for all the contour illustrations of triangular, sinusoidal and circular airgap profile.

Analytically, it is evident that while the reluctance of the core remains largely unchanged, the introduction of a contoured airgap results in a decreased airgap reluctance due to the increased surface area. This reduction in reluctance leads to a higher flux linkage in the coil for the same applied MMF, indicating an improvement in the magnetic circuit's performance.

FEA simulations can be utilized to further validate this effect by comparing the flux linkage in circuits with straight and contoured airgap profiles for various values of contour amplitude and the coil current.

The magnetic circuit utilized for the current FEA analysis is shown in Figure 3. The shape and dimensioning of the magnetic circuit is done to uniformly distribute the flux in the airgap 2 and the magnetic core 1 components adjacent to the airgap 2.

Figure 4 presents the coil flux linkage versus input coil current for core material with constant magnetic permeability, for straight airgap profile in comparison with the varying amplitudes of triangular, sinusoidal and circular airgap profiles. The simulations demonstrate that the contoured design enhances the magnetic flux path's permeability, leading to improved performance indicator, that is, flux linkage without necessitating an increase in the magnetic circuit's overall size.

DETAILED ANALYSIS OF THE CONTOURED AIRGAP TOPOLOGY

Limitations of Contour Amplitude in Circular Profiles

The effectiveness of contoured airgap profiles in reducing magnetic reluctance and enhancing the performance of electrical machines depends on several interrelated factors. Concerning the shape of the contour profile, one significant observation is the limitation on the amplitude of the contour, particularly in circular profiles. In these profiles, the amplitude, defined by the radius of the circular shape, cannot be increased beyond half the width of the core limb.

On Figure 3 the width of the core limb in the reference region of interest is 5mm leading to the constraint that the amplitude of the circular profile cannot be increased beyond half the length of this, that is in this reference example, 2.5mm.

This geometric constraint inherently limits the potential increase in airgap surface area achievable through contouring. Designers must consider this limitation when selecting the contour amplitude to optimize performance.

Non-proportional Relationship Between Airgap Surface Area and Flux Linkage

Furthermore, when examining the results closely, even with core materials exhibiting very high and constant magnetic permeability against the applied magnetomotive force (MMF), the gains in flux linkage are not directly proportional to the increase in airgap surface area. For instance, an increase of 20% in airgap surface area does not necessarily translate to a 20% increase in flux linkage; the actual gain is somewhat lower.

This discrepancy arises because, although the overall reluctance of the core remains largely unchanged, the cross-sectional area of the core decreases in the

immediate vicinity of the contour due to the shaping of the core faces. This fact is illustrated in Figure 5.

This reduction increases the local core reluctance, partially offsetting the potential gains from the increased airgap surface area. The impact of this effect is a function of the contour amplitude. The amplitude of the contour significantly affects the core's reluctance. As the contour amplitude increases, the reduction in the core's cross-sectional area near the airgap becomes more pronounced. This reduction leads to an increase in local core reluctance, especially in the immediate vicinity of the contoured airgap.

Thus, while a higher contour amplitude can decrease airgap reluctance by increasing surface area, it can simultaneously increase core reluctance due to the decreased cross-sectional area of the magnetic path inside the core components. This trade-off must be carefully balanced to optimize the overall performance of the magnetic circuit, which has been ignored in a prior art.

Impact of Contouring Strategy on Airgap Thickness

The geometrical shape of the core faces adjacent to the airgap is crucial in determining the performance gains from contoured airgap profiles. It is essential to maintain a consistent airgap thickness in the direction of the magnetic flux flow, to achieve the best and most uniform airgap reluctance distribution. This uniformity ensures that the magnetic field is evenly distributed across the airgap, minimizing localized flux density peaks that could lead to saturation or increased losses.

Achieving a uniform airgap thickness necessitates a specific contouring strategy. Starting from a straight airgap profile, a guide profile line is established at the midpoint of the airgap thickness. This line is then offset by half the airgap thickness ($g/2$) on both sides to define the airgap-facing surfaces of the core components. This method ensures that the direct, or normal distance between the airgap-facing components remains uniform in the direction of the magnetic flux flow in the airgap.

Contouring Strategy

Defining the contour mathematically is essential for precise implementation. Mathematical equations representing the contour shapes, such as triangular,

sinusoidal and circular profiles are given below along with the implementation strategy.

The contour in the airgap profile will be introduced in the general direction of flow of flux in the adjacent core components. As part of the air gap contouring strategy, a central contour guideline is established at the mid-height of the air gap based on specified geometrical equations that follow. To maintain uniformity, the contour is offset by $g/2$ on either side, ensuring a consistent direct/normal distance between the offset lines. These offset lines subsequently define the surfaces of the core components adjacent to the air gap.

The conditional geometric equations defining the central airgap contour are as follows and are illustrated in Figure 6. The illustration of Figure 6 is relative and shows the cross-sectional view of the airgap forming component in a magnetic circuit, where x, y and z axes represent the first, second and third dimension and can be modified/interchanged according to the specific design plane.

In the equations below,

x_1 is the starting point of the core component, defining the starting point of airgap in first axis,

x_2 is the edge-point of the core component defining the end point of the airgap in the first axis,

y_o is the midpoint of airgap thickness in the second axis,

A_c is the amplitude of the central-guide contour profile,

r is the radius of the circular contour profile.

The equations are presented in x and y axis parameters where the contour is introduced in the direction of flow of flux i.e. perpendicular/normal to the direction of flow of flux.

Whereas, the third dimension, i.e. z-axis can be uniformly straight or curved, according to the electromagnetic device's specific topology.

Triangular airgap contour

$$\begin{cases} y = y_o + \dfrac{g}{2} + \dfrac{2A_c}{(x_2 - x_1)}(x - x_1) & x_1 < x < \dfrac{(x_1 + x_2)}{2} \\ y = y_o + \dfrac{g}{2} + 2A_c - \dfrac{2A_c}{(x_2 - x_1)}(x - x_1) & \dfrac{(x_1 + x_2)}{2} < x < x_2 \end{cases}$$

Sinusoidal airgap contour

$$\begin{cases} y = y_o + \dfrac{g}{2} + A_c \sin\dfrac{\pi(x - x_1)}{(x_2 - x_1)} & 0.01 < A_c < \dfrac{y_o}{2} \end{cases}$$

Circular airgap contour

$$\begin{cases} r = \left| \dfrac{\left(\frac{x_2 - x_1}{2}\right)^2 + {A_c}^2}{2A_c} \right| & \\ \left(x - \dfrac{x_1 + x_2}{2}\right)^2 + \left(y - \dfrac{g}{2} + \sqrt{r^2 - \left(\frac{x_1 - x_2}{2}\right)^2} - y_o\right)^2 = r^2 & for\ 0.01 < |A_c| < \dfrac{x_2 - x_1}{2} \\ \left(x - \dfrac{x_1 + x_2}{2}\right)^2 + \left(y - \dfrac{g}{2} - \sqrt{r^2 - \left(\frac{x_1 - x_2}{2}\right)^2} - y_o\right)^2 = r^2 & for\ \dfrac{x_2 - x_1}{2} < |A_c| < \dfrac{y_o}{2} \end{cases}$$

Figure 7 presents the implemented contour profiles for various magnitudes of contour amplitudes according to the previously defined contouring strategy, the respective FEA simulation results for the flux flow in the core material and the airgap.

The flux lines shown in individual FEA plots demonstrate the efficacy of the current contouring strategy in ensuring the uniform airgap thickness, through the uniform distribution of flux lines throughout the airgap profile.

Influence of Magnetic Material Properties

Up to this point, the analysis has considered core materials with constant magnetic permeability. However, practical magnetic core materials exhibit non-linear magnetic permeability that varies with the applied MMF. At higher MMFs, the magnetic core material begins to saturate, leading to an increase in core reluctance.

This effect is particularly pronounced in regions near the contoured airgap, where the core cross-sectional area is reduced due to the contouring. The localized saturation in these areas increases the core reluctance, which can significantly limit the gains from the decreased airgap reluctance, especially at higher contour amplitudes.

Finite element analysis (FEA) simulations can be utilized to demonstrate this effect by comparing the flux linkage in circuits with straight and contoured airgap profiles for different values of coil current using practical core materials, such as M400-50A. The coil flux linkage versus input coil current for M400-50A core material with non-linear magnetic permeability, for straight airgap profile in comparison with the

varying amplitudes of triangular, sinusoidal and circular airgap profiles is presented in Figure 8.

The simulations show that at higher levels of applied MMF, the core saturation in the immediate vicinity of the contoured airgap becomes more significant. This increased core reluctance in these regions partially offsets the benefits gained from the increased airgap surface area, reducing the overall performance gains from contouring.

This observation underscores that the gains from any contour shape and its respective amplitude are a function of the magnetic circuit's operating point. At lower values of applied MMF, the gains are more substantial, while at higher MMFs, the benefits diminish.

This dependency on the operating point implies that the contour shape and amplitude need to be optimized according to the specific operating conditions of the magnetic circuit or electrical machine. The proposed design strategy involves iteratively increasing the contour amplitude from a minimal value to an optimal one, assessing the performance gains at each increment. This iterative process continues until the maximum gains in flux linkage are achieved at the selected operating point without causing excessive core saturation.

In conclusion, the implementation of contoured airgap profiles requires a comprehensive strategy that includes defining the contour mathematically, ensuring a uniform airgap thickness through precise offsetting, and optimizing the contour amplitude based on the magnetic circuit's operating point. Only by balancing these factors, it is possible to enhance the energy conversion efficiency and increasing power density without increasing the electrical machine’s mass/volume.

The practical realization of these contoured airgap profiles is facilitated by advanced manufacturing technologies, such as additive manufacturing (3D printing). This technology allows for the precise fabrication of complex geometries required for the contoured profiles, overcoming the limitations imposed by conventional manufacturing methods, which might involve increased complexity and cost when producing such shapes. While it is possible to achieve these profiles with traditional manufacturing techniques, additive manufacturing offers greater flexibility and precision, making it a more efficient and practical solution.

By adopting this innovative approach, electrical machine designers can effectively reduce airgap reluctance, improve magnetic flux production against a given MMF, and enhance the overall performance of the machine. This advancement provides a significant opportunity to develop more efficient and power dense electrical machines, meeting the ever-increasing demands for higher performance in various applications.

APPLICATION OF CONTOURED AIRGAP TOPOLOGY TO AXIAL FLUX ELECTRICAL MACHINES

The magnetic circuit structure developed based on the analytical and simulation results described earlier is applied to a dual-rotor axial flux electrical machine, as detailed below.

An example of the present invention is an axial flux motor, though the contoured airgap topology is equally applicable to the generators and other electromagnetic devices requiring an airgap, be it an axial flux or a radial flux electrical machine, including, among other things, a single stator-single rotor, a multi stator-multi rotor and an outer rotor or an inner rotor configuration.

The axial flux motor comprises a rotor and a stator arranged along a common rotational axis. The rotor is configured to rotate about the axis, while the stator remains stationary.

Next references are made to Figures 9a, 9b and 9c illustrating the structure of a conventionally designed dual rotor, single stator axial flux motor. The rotor consists of a series of rotor-side magnetic poles (these magnetic poles could be made from permanent magnets (PM) for PM machines and from magnetic core material, for reluctance machines or wound rotor machines) distributed circumferentially around the axis. Similarly, the stator features stator-side magnetic poles aligned with the rotor poles across the airgap.

The rotor and stator are constructed from soft magnetic composite materials or laminated steel to minimize eddy current losses, depending on manufacturing preferences. The magnetic poles could be made from permanent magnets (PM) for PM machines and from magnetic core material, for reluctance machines or wound rotor machines.

Implementation of the Contoured Airgap

As illustrated in Figures 10a and 10b, the facing surfaces of the rotor-side magnetic poles 4 and stator-side magnetic poles 5 are contoured according to the strategies outlined previously. The contours are introduced axially, increasing the effective airgap surface area and increasing power density without increasing the electrical machine's mass/volume.

Figure 10b provides a cross-sectional view along line B-B′ in Figure 10a, showing the alignment of the rotor and stator poles with the contoured airgap between them. The airgap thickness g remains constant across the contour due to the precise offsetting method described earlier, ensuring uniform magnetic flux distribution.

Figure 11a depicts a cross-section of the radial flux motor, where on Figures 11b and 11c are depicted respectively a radial flux motor with straight airgap 2 and contoured airgap 2 profile in a cross-sectional view at the line F-F shown on Figure 11a. In figure 11c, the airgap 2 thickness g remains constant across the contour due to the precise offsetting method described earlier, ensuring uniform magnetic flux distribution.

Design Considerations and Variations

The contours applied to the airgap-facing surfaces can adopt various mathematical profiles, such as sinusoidal, triangular, or circular shapes, as defined in the earlier mathematical expressions. The selection of the contour shape and amplitude depends on the desired performance characteristics and operating conditions.

In the embodiment shown, a sinusoidal contour is utilized with an amplitude optimized based on the motor's operating point. The optimization process involves iteratively adjusting the contour amplitude and assessing the performance gains through simulation and experimental validation.

Manufacturing and Material Considerations

The rotor and stator can be fabricated using additive manufacturing techniques, such as 3D printing, to accurately produce complex contoured geometries. Alternatively, conventional manufacturing methods can be adapted, though they

may involve increased complexity.

Materials with suitable magnetic properties, such as soft magnetic composites or high-permeability steel laminations, are selected to complement the contoured design. These materials help mitigate core saturation effects, particularly in regions where the cross-sectional area is reduced due to contouring.

Applicability to Other Devices

While the example provided focuses on an axial flux motor, the contoured airgap topology is equally applicable to other electromagnetic devices, including axial flux generators and transformers. The principles of increasing the airgap surface area to reduce reluctance and enhance performance remain consistent across radial flux topology in electrical machines too.

REFERENCE SIGNS LIST

1	core
2	airgap
3	coil
4	rotor-side magnetic pole
5	stator-side magnetic pole
6	stator winding
7	shaft
8	rotor back iron
9	rotor
10	stator

CLAIMS

1. A method for contouring an airgap profile in an electromagnetic device comprising an airgap in a magnetic path to reduce airgap reluctance,

characterized in that

the airgap is profiled such that the airgap profile corresponds to a contour of the guide profile line between the opposite faces forming the airgap between them at the midpoint of the airgap thickness taken perpendicular to said guide profile line, where said guide profile line lies in plane containing x and y axes,

where x, y and z axes represent the first, second and third dimension, where x-axis is perpendicular to the general direction of flux flow in the magnetic path in the vicinity of said airgap, y-axis is in the general direction of the flux flow in said magnetic path and z-axis perpendicular both with x and y-axes,

where the airgap-facing surface profiles of the core components are offset by half the airgap thickness (g/2) perpendicular to said guide profile line on both sides of said guide profile line to define the airgap-facing surfaces of the core components such that the normal distance between the airgap-facing components remains uniform and a distribution of flux lines throughout the airgap profile are both uniform, and a shape of said airgap guide profile line is triangular, sinusoidal or circular.

2. The method according to claim 1, **characterized in that**, a shape of said airgap guide profile line is triangular, where said triangular airgap contour corresponds to the following conditions

$$\begin{cases} y = y_o + \frac{g}{2} + \frac{2A_c}{(x_2 - x_1)}(x - x_1) & x_1 < x < \frac{(x_1 + x_2)}{2} \\ y = y_o + \frac{g}{2} + 2A_c - \frac{2A_c}{(x_2 - x_1)}(x - x_1) & \frac{(x_1 + x_2)}{2} < x < x_2 \end{cases}$$

where

x_1 is the starting point of the core component, defining the starting point of airgap in first axis,

x_2 is the edge-point of the core component defining the end point of the airgap in the first axis,

y_o is the midpoint of airgap thickness in the second axis,

A_c is the amplitude of the central-guide contour profile.

3. The method according to claim 1, **characterized in that**, a shape of said airgap guide profile line is sinusoidal, where said sinusoidal airgap contour corresponds to the following conditions

$$\begin{cases} y = y_o + \frac{g}{2} + A_c \sin\frac{\pi(x - x_1)}{(x_2 - x_1)} & 0.01 < A_c < \frac{y_o}{2} \end{cases}$$

where

x_1 is the starting point of the core component, defining the starting point of airgap in first axis,

x_2 is the edge-point of the core component defining the end point of the airgap in the first axis,

y_o is the midpoint of airgap thickness in the second axis,

A_c is the amplitude of the central-guide contour profile.

4. The method according to claim 1, **characterized in that**, a shape of said airgap guide profile line is circular, where said circular airgap contour corresponds to the following conditions

$$\begin{cases} r = \left| \frac{\left(\frac{x_2 - x_1}{2}\right)^2 + {A_c}^2}{2A_c} \right| \\ \left(x - \frac{x_1 + x_2}{2}\right)^2 + \left(y - \frac{g}{2} + \sqrt{r^2 - \left(\frac{x_1 - x_2}{2}\right)^2} - y_o\right)^2 = r^2 & for\ 0.01 < |A_c| < \frac{x_2 - x_1}{2} \\ \left(x - \frac{x_1 + x_2}{2}\right)^2 + \left(y - \frac{g}{2} - \sqrt{r^2 - \left(\frac{x_1 - x_2}{2}\right)^2} - y_o\right)^2 = r^2 & for\ \frac{x_2 - x_1}{2} < |A_c| < \frac{y_o}{2} \end{cases}$$

where

x_1 is the starting point of the core component, defining the starting point of airgap in first axis,

x_2 is the edge-point of the core component defining the end point of the airgap in the first axis,

y_o is the midpoint of airgap thickness in the second axis,

A_c is the amplitude of the central-guide contour profile,

r is the radius of the circular contour profile.

5. The method according to any previous claim, **characterized in that**, said electromagnetic device is an axial flux electrical machine.

6. The method according to any previous claim 1 to 4, **characterized in that**, said electromagnetic device is a radial flux electrical machine.

7. The method according to any previous claim 1 to 4, **characterized in that**, said electromagnetic device is a linear electrical machine.

8. The method according to any previous claim 1 to 4, **characterized in that**, said electromagnetic device is an air-gapped transformer or inductor.

ABSTRACT

The invention relates to a method for contouring an airgap 2 profile in an electromagnetic device comprising an airgap in a magnetic path to reduce airgap reluctance. In the present invention, the airgap 2 is profiled such that the airgap profile corresponds to a contour of the guide profile line between the opposite faces forming the airgap between them at the midpoint of the airgap 2 thickness taken perpendicular to said guide profile line.

(Figure 2c)

FIG. 1a

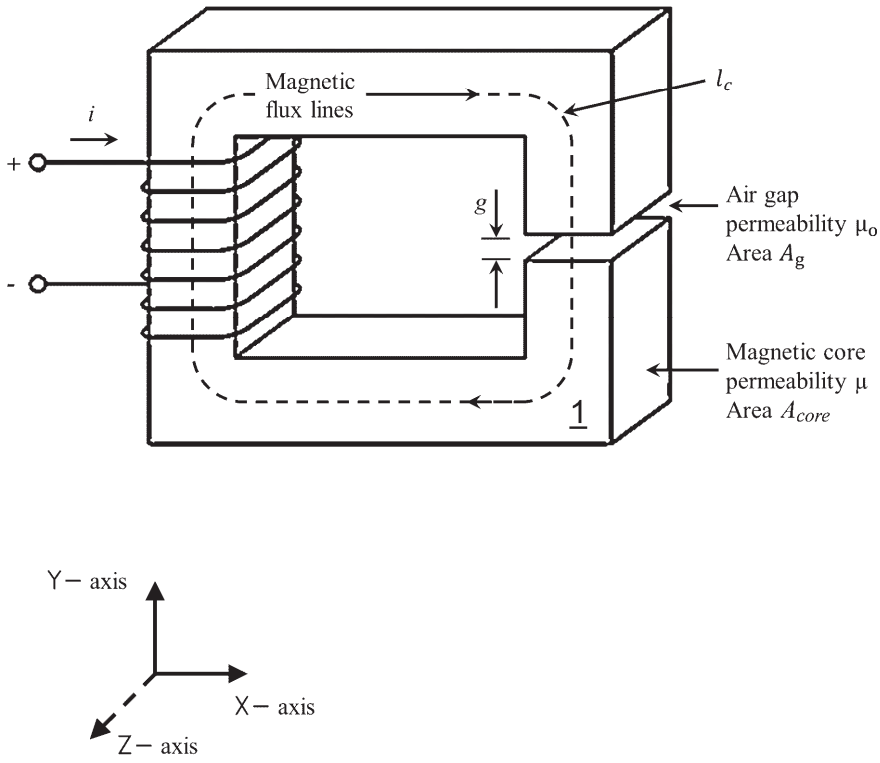
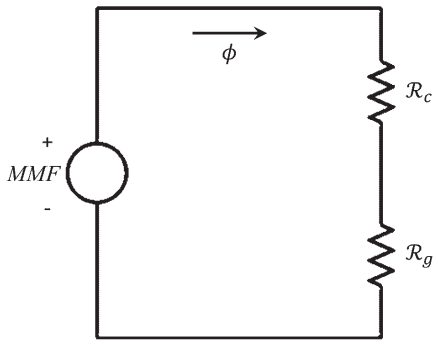

Magnetic
flux lines
l_c
i
+
-
g
Air gap
permeability μ_o
Area A_g
Magnetic core
permeability μ
Area A_{core}
1
Y – axis
X – axis
Z – axis

FIG. 1b


ϕ
$\mathcal{R}_c$
+
MMF
-
$\mathcal{R}_g$

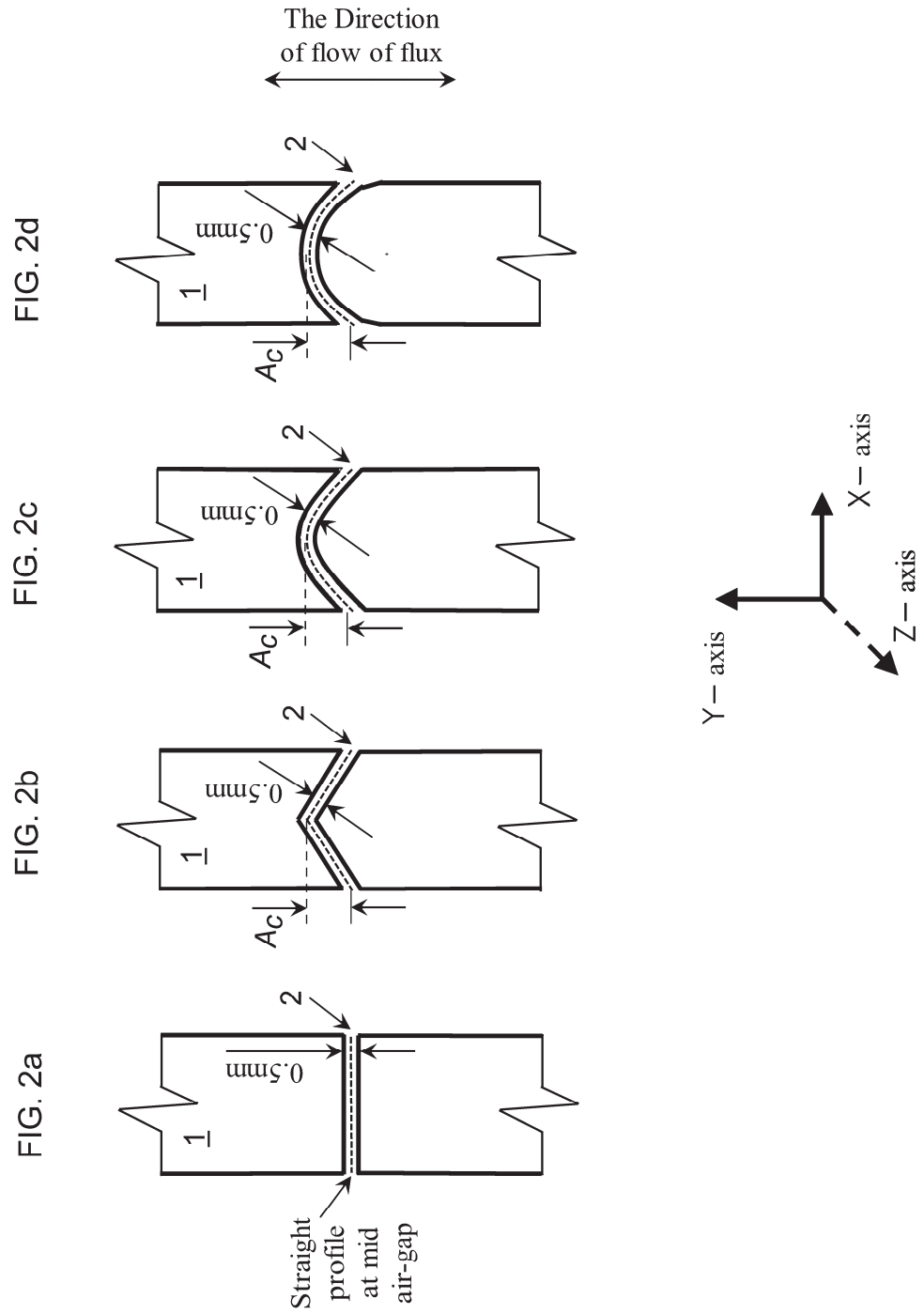

FIG. 2a
FIG. 2b
FIG. 2c
FIG. 2d
The Direction
of flow of flux
0.5mm
1
2
Ac
Straight
profile
at mid
air-gap
X – axis
Y – axis
Z – axis

FIG. 3a

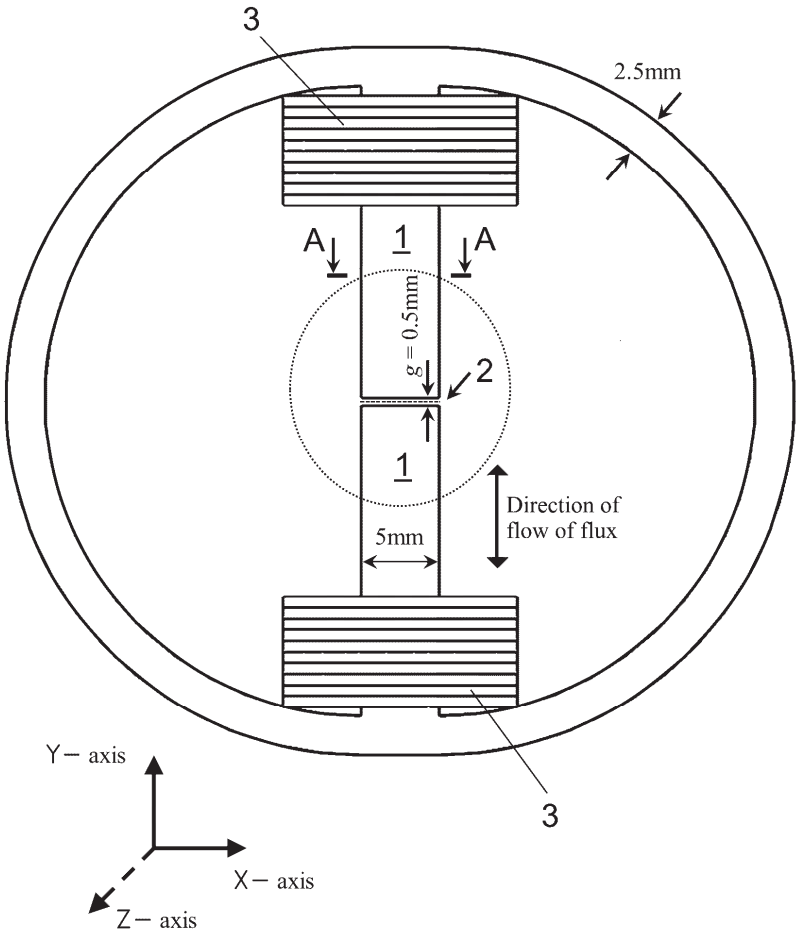

3
2.5mm
A
1
A
g = 0.5mm
2
1
Direction of
flow of flux
5mm
3
Y− axis
X− axis
Z− axis

FIG. 3c

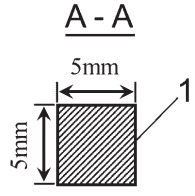

A - A
5mm
1
5mm

FIG. 4a

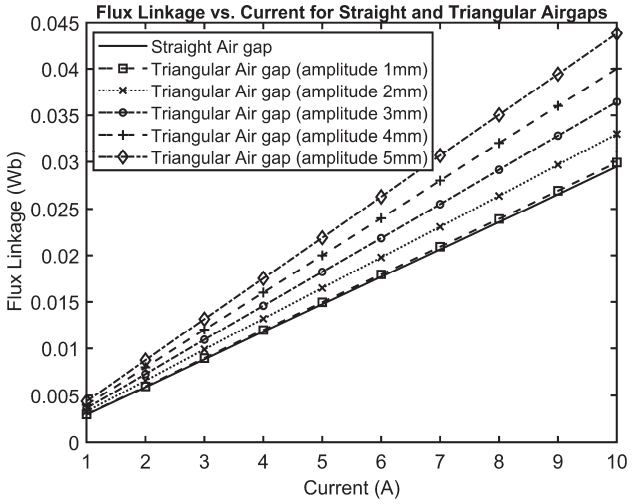


FIG. 4b

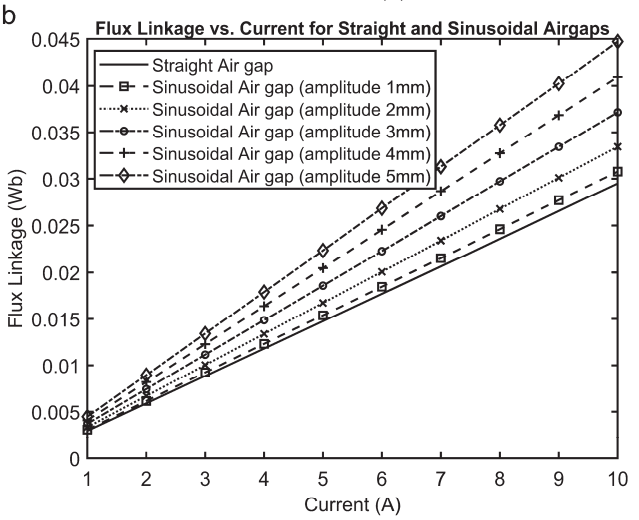


FIG. 4c

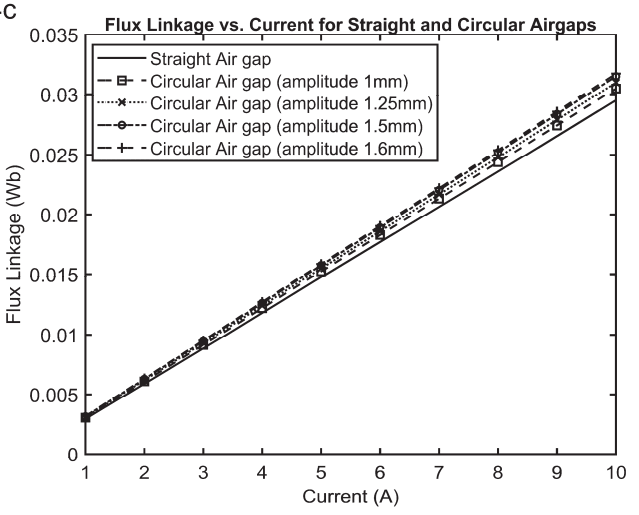


FIG. 5

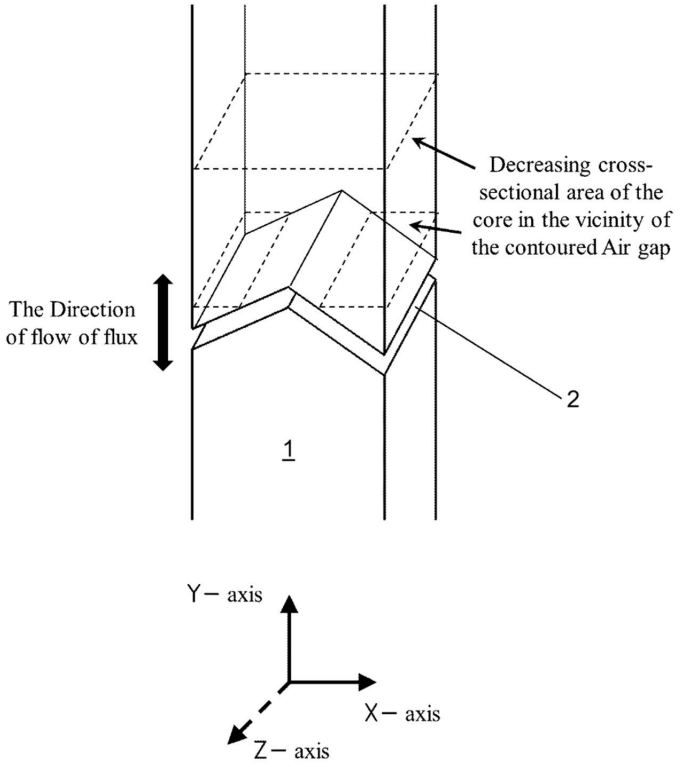
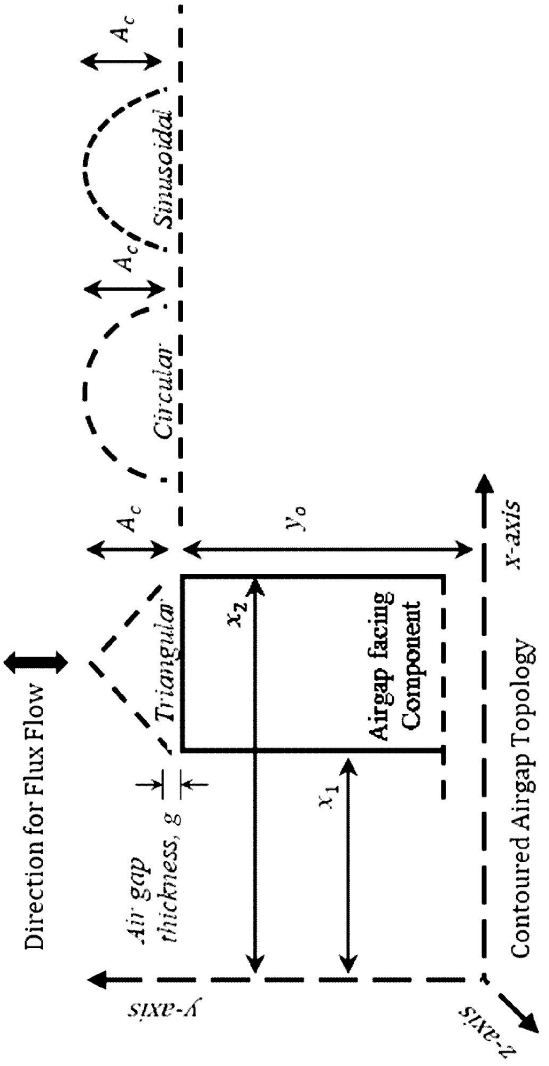

Decreasing cross-sectional area of the core in the vicinity of the contoured Air gap
The Direction of flow of flux
2
1
Y– axis
X– axis
Z– axis

FIG. 6


Direction for Flux Flow
Air gap thickness, g
Triangular
Circular
Sinusoidal
A_c
A_c
A_c
y_o
x_2
x_1
Airgap facing Component
Contoured Airgap Topology
x-axis
y-axis
z-axis

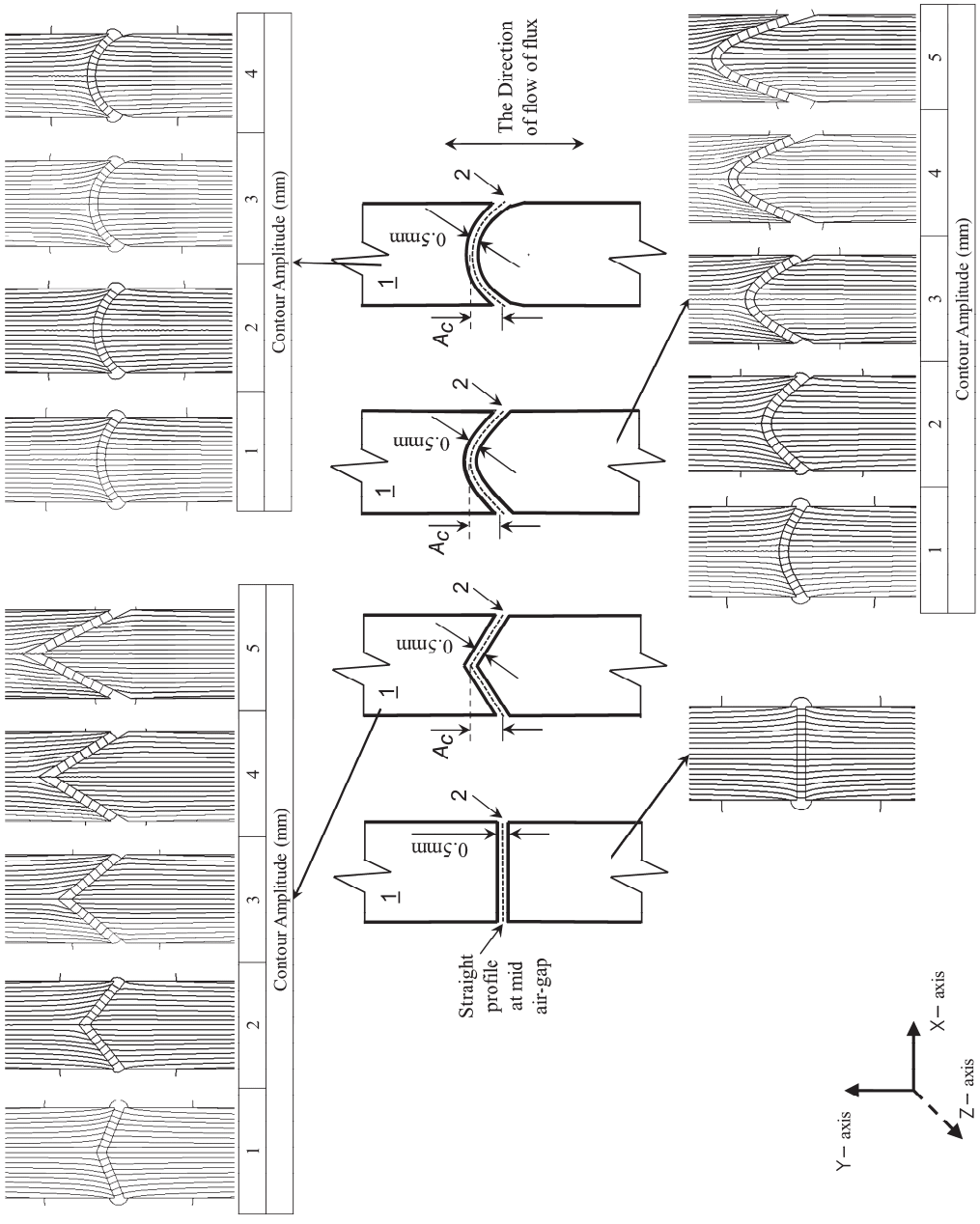

Contour Amplitude (mm)
1
2
3
4
5
0.5mm
Ac
The Direction of flow of flux
Straight profile at mid air-gap
Y – axis
X – axis
Z – axis

FIG. 7

FIG. 8a

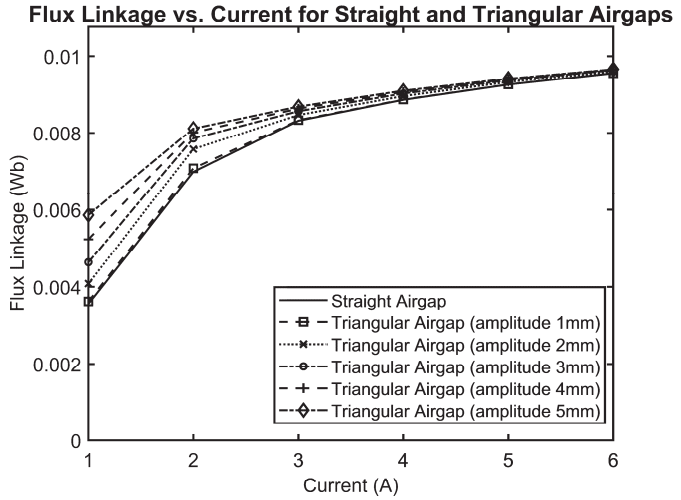


FIG. 8b

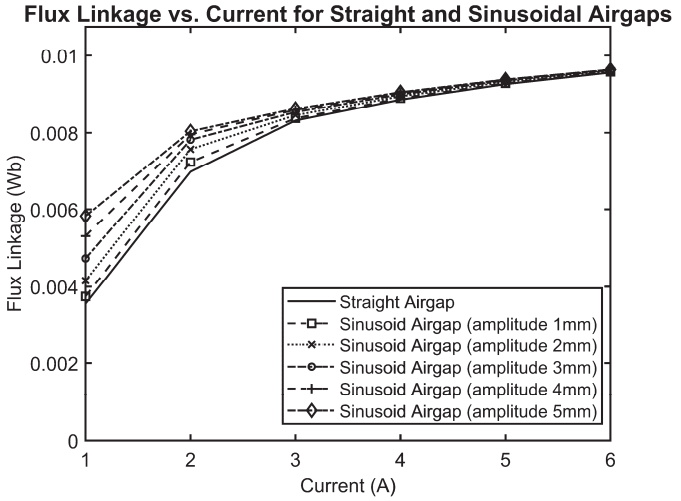


FIG. 8c

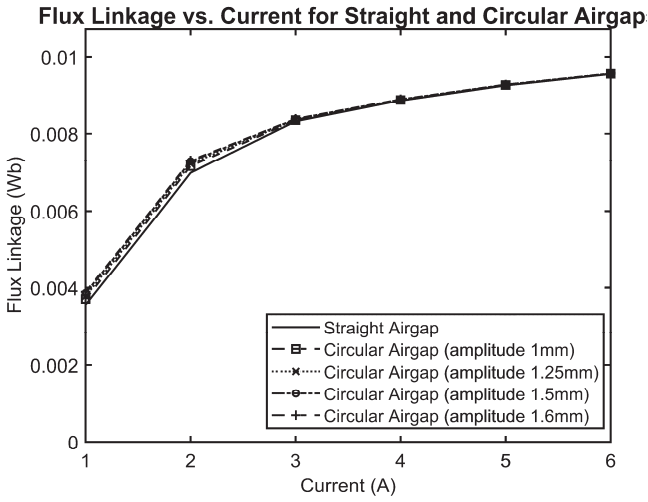


FIG. 9a

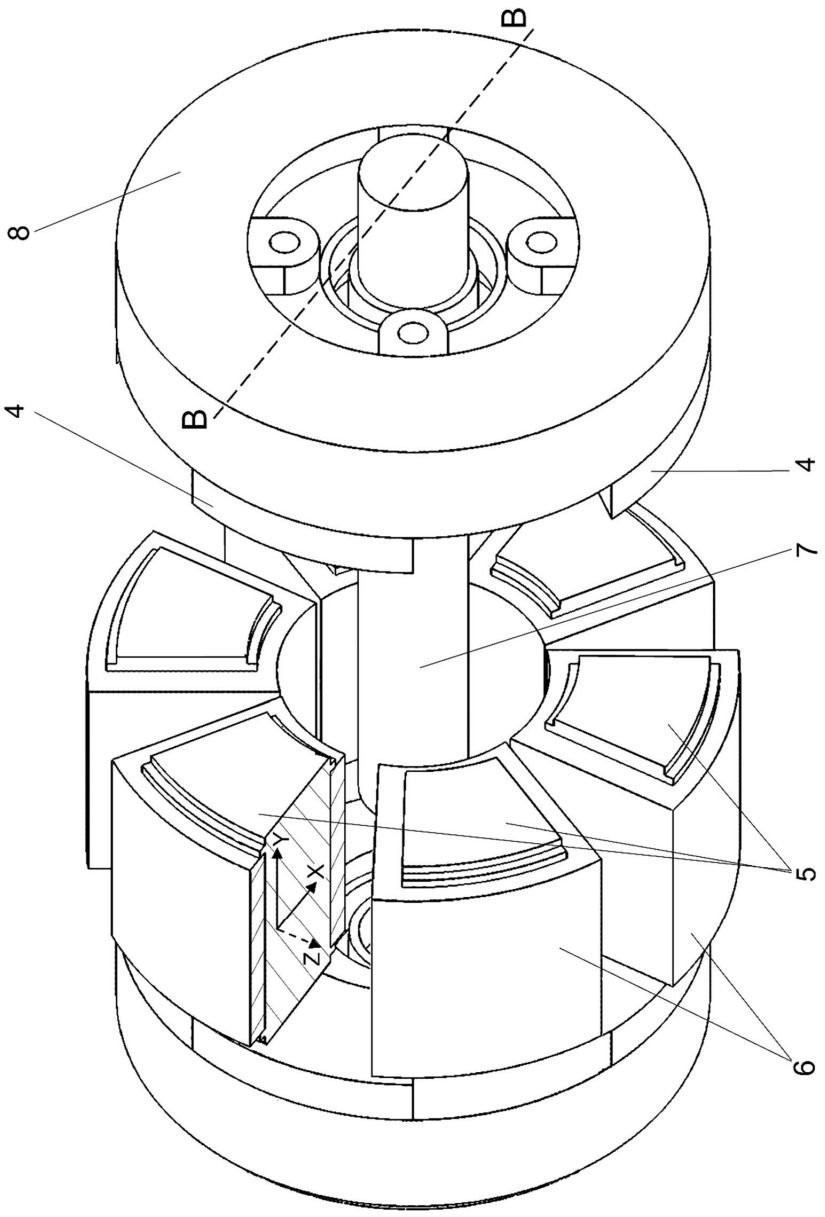


FIG. 9b

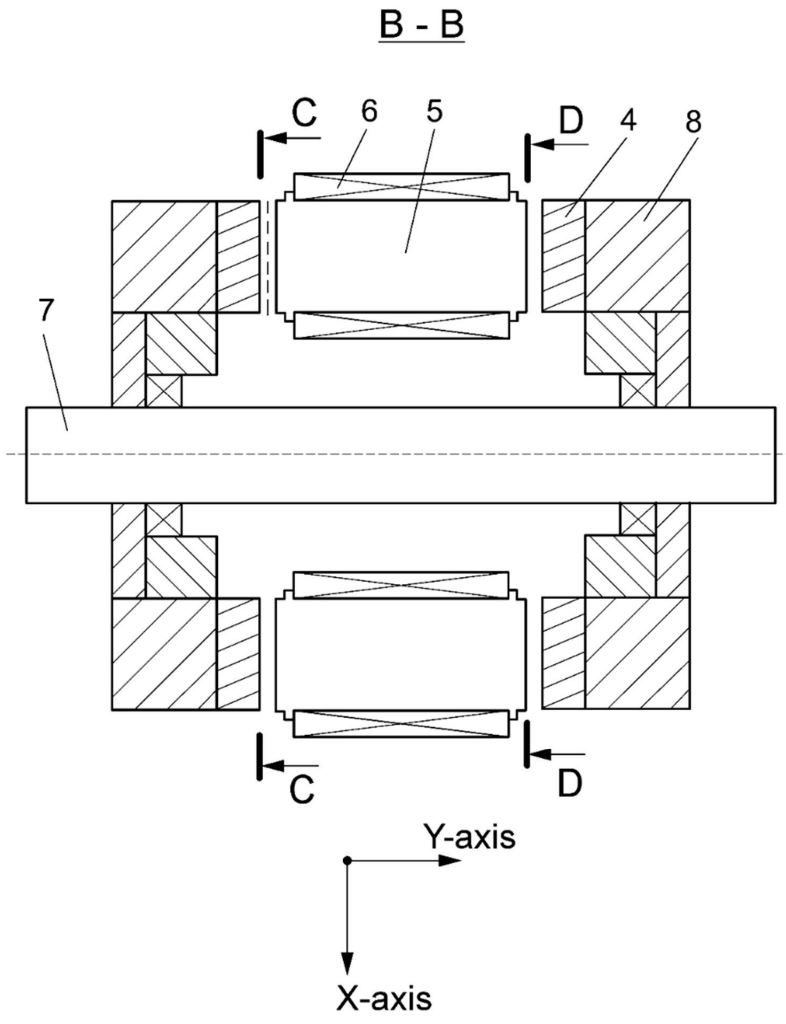


FIG. 9d D - D

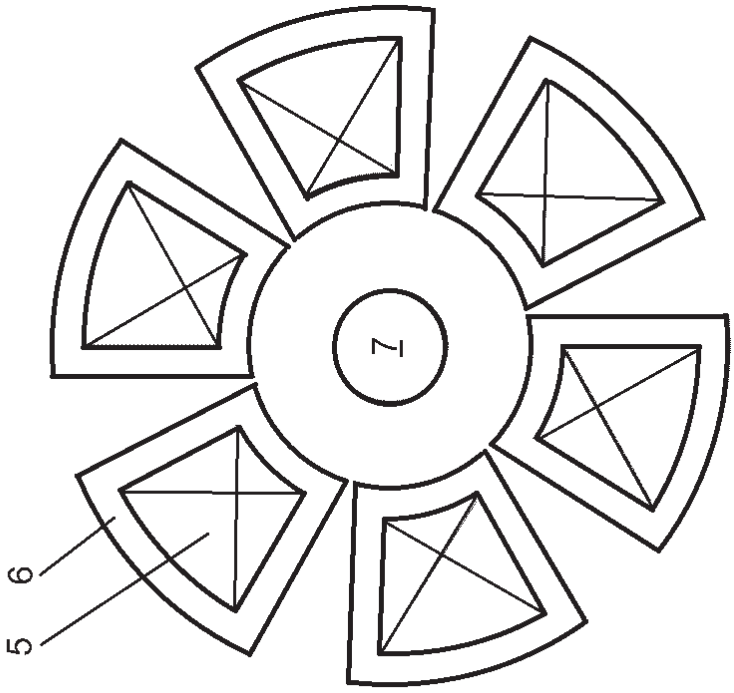


FIG. 9c C - C

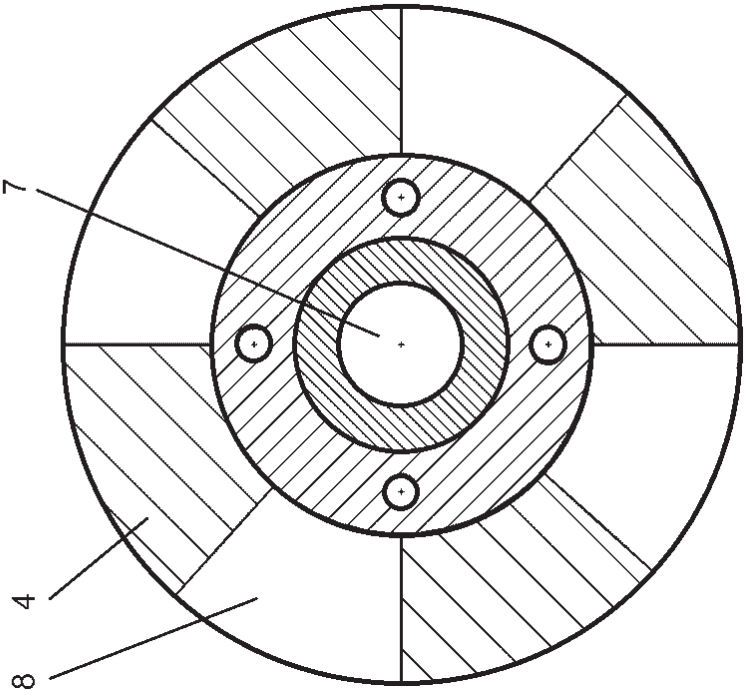


FIG. 10a

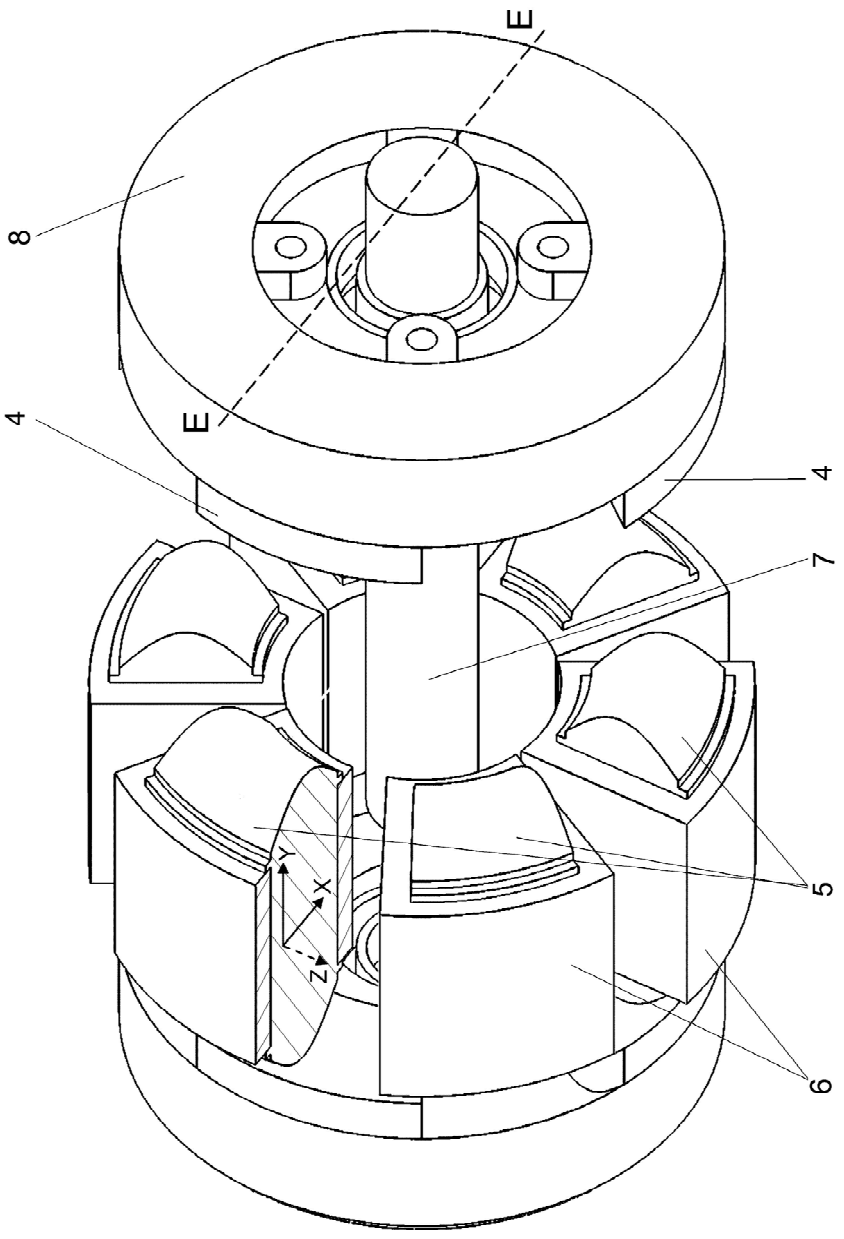


FIG. 10b

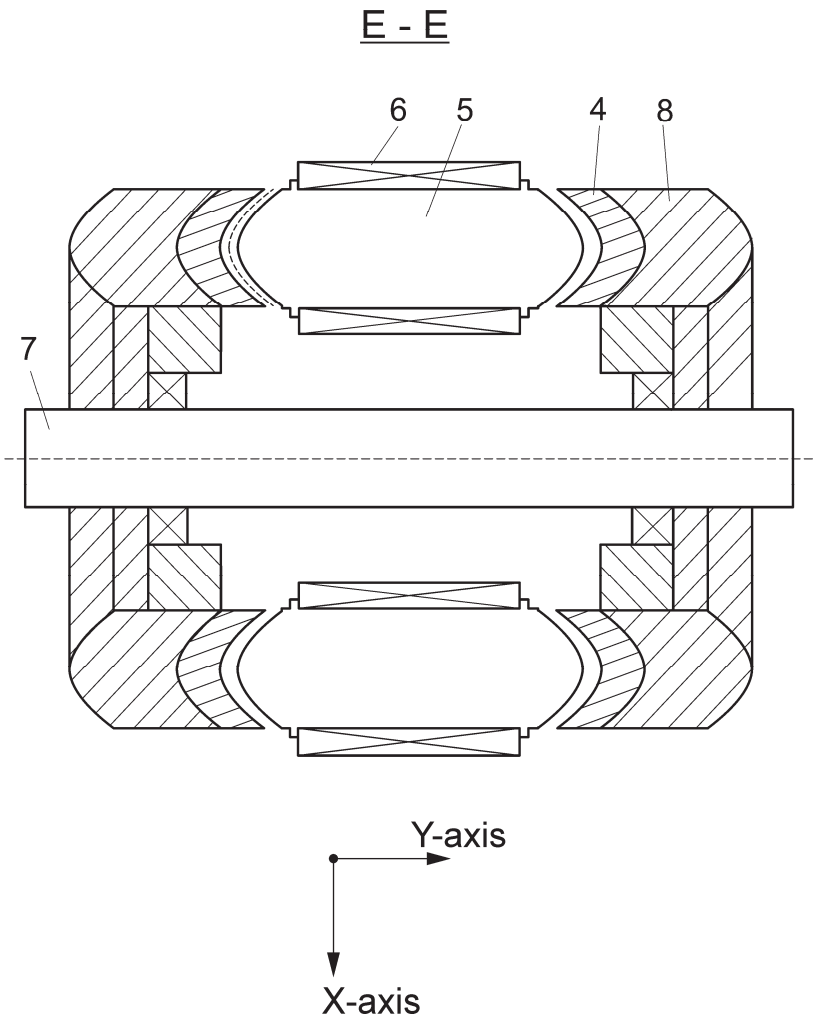


FIG. 11a

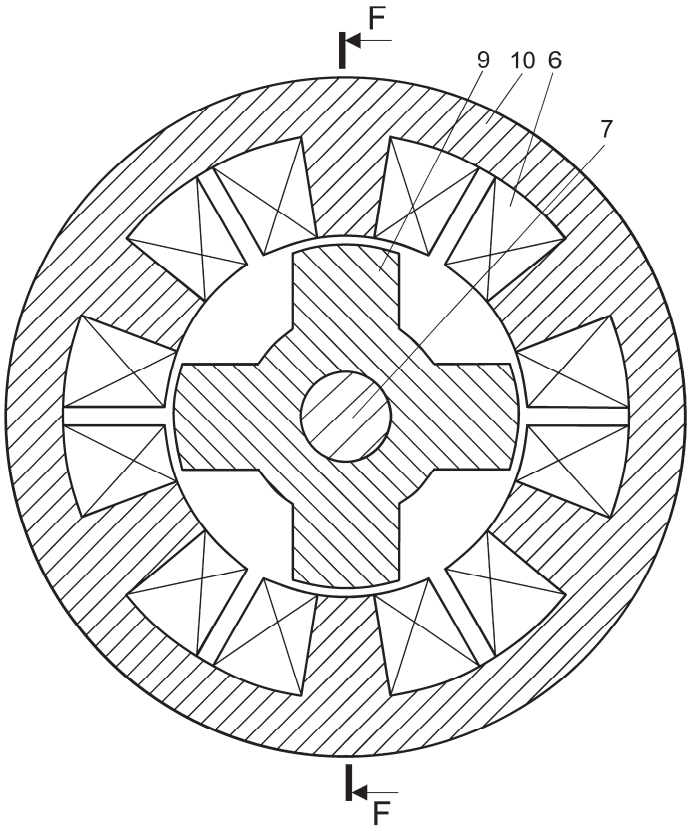


FIG. 11c

F - F

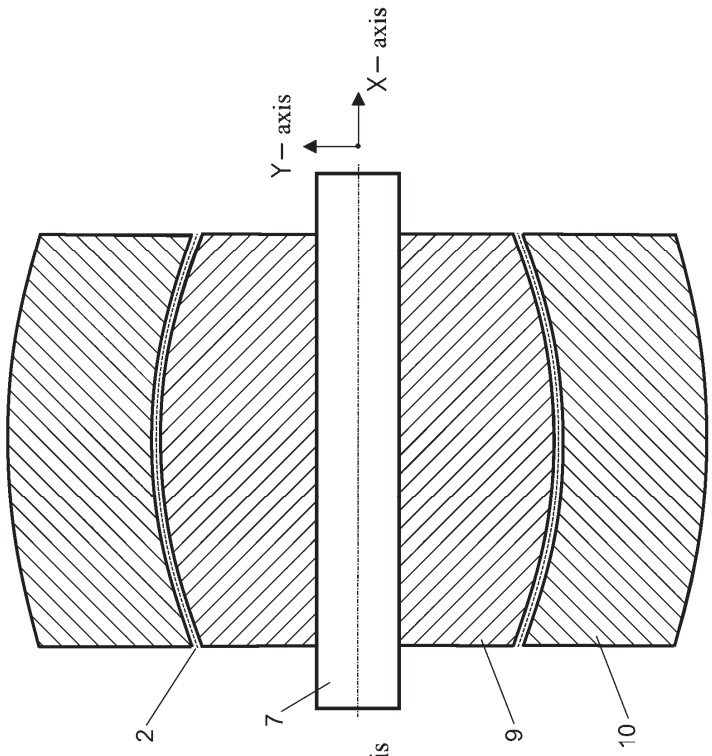
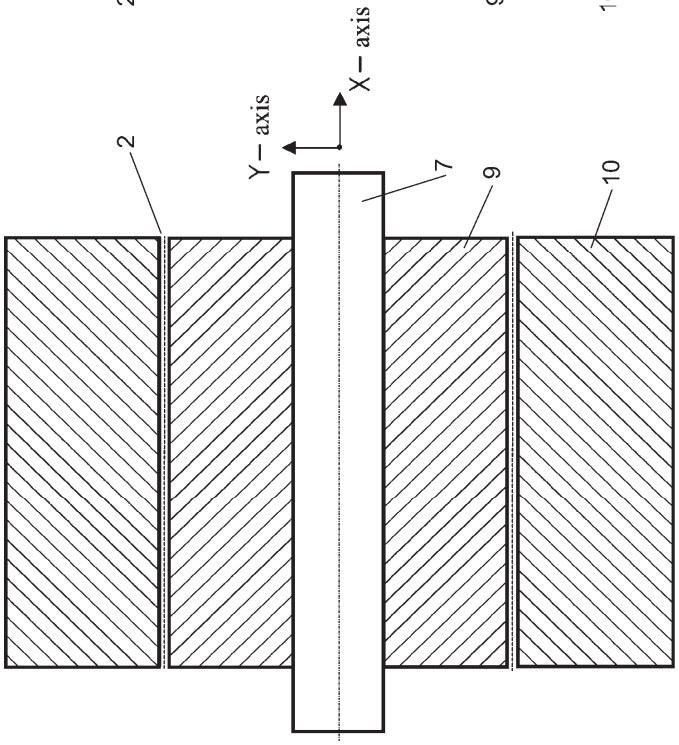


FIG. 11b

F - F



Publication III

M. U. Naseer, A. Kallaste, T. Vaimann, and B. Asad, “Curved Airgap Topology: A Promising Strategy for Enhancing Axial- Flux Machine Performance Metrics,” Accepted for Publication in 25th International Conference on the Computation of Electromagnetic Fields, Naples, Italy: IEEE, Jun. 2025.

Curved Airgap Topology: A Promising Strategy for Enhancing Axial-Flux Machine Performance Metrics

Muhammad Usman Naseer[1], Ants Kallaste[1], Toomas Vaimann[1], Bilal Asad[1]

[1]Dept. of Electrical Power Engineering and Mechatronics, Tallinn University of Technology, Tallinn 19086 Estonia, mnasee@taltech.ee

This study highlights the impact of non-uniform airgap design on the performance of axial flux machines. Increased curvature of the airgap profile enhances the flux linkage between stator and rotor, yielding higher torque-production capability, while maintaining constant electric loading and outer dimensions. The results indicate an optimal point where the compromise between net flux and overall flux density in the airgap is minimized. The analysis also shows fluctuations in torque profile with higher airgap curvature, suggesting potential for improvement through control strategies.

***Index Terms*— AC machines, machine design, design tools, additive manufacturing, three-dimensional printing, rotating machines**

I. Introduction

THE interest in enhanced and customized performance parameters and integrated functionalities in electrical machine design has intensified in response to the ever-changing demands across various application sectors such as electric vehicles, renewable energy systems, aviation and space sector, as well as industrial and domestic applications [1], [2], [3]. Traditionally, design possibilities for electrical machines have been largely confined to two dimensions, with limited possibility to look for design optimization in the third dimension. However, with the advent of the latest manufacturing techniques such as Additive Manufacturing (AM), and with the rapid integration of such technologies in the production of electrical machine parts, these limitations on design possibilities are rapidly diminishing [2].

Despite the extensive exploration of AM in electrical machine production, a significant research gap persists: the independent investigation of asymmetry or non-uniformity in the third dimension, particularly in the context of axial flux machines. While some studies have explored non-uniform design topologies, the state-of-the-art lacks systemic investigation. This paper aims to bridge this gap by establishing a systematic framework for integrating non-uniformity into the airgap of electrical machines, specifically focusing on curved airgap topology for axial flux machines.

II. Description of Curved Airgap Topology

A. Dynamics of macro design variables

Performance parameters of most electrical machines are heavily reliant on the effective manipulation of their macro design variables. Foremost among them are the fundamentals, such as electric loading and flux density, which interact in the airgap of the machine to produce torque. The effective airgap area between the stator and rotor is responsible for the efficient flux linkage between the stator and rotor and plays a pivotal role in determining the machine's performance parameters.

Influencing any of the above-mentioned parameters directly affects the machine's power or torque production capability. To further supplement this statement, and under the scope of this study, the analytical sizing equation of an axial-flux SRM [3] is presented in (1).

$$P_o = \frac{\pi^2}{480} k_e k_d k_1 B_{av} A_s D_{avg} \left(D_o^2 - D_i^2\right) n_{rpm} \tag{1}$$

$$k_1 = \left(1 - \frac{1}{\sigma_s \sigma_u}\right) \tag{2}$$

$$l_{perimeter} = \pi D_{avg} \tag{3}$$

$$A_{ag} = \frac{\pi}{4}\left(D_o^2 - D_i^2\right) \tag{4}$$

$$P_o = \kappa \left(A_{ag} B_{av}\right) \left(l_{perimeter} A_s\right) n_{rpm} \tag{5}$$

$$\kappa = \frac{\pi^2}{480} k_e k_d k_1 \tag{6}$$

where k_e stands for efficiency, k_d is the duty cycle, k_1 incorporates the saturated; aligned to unaligned inductance ratio σ_s, and the unsaturated; aligned to unaligned inductance ratio σ_u. B_{av} is the average airgap flux-density, A_s is the electric loading on the mid-plane perimeter of the machine airgap, D_o and D_i are the outer and inner diameters of the machine respectively, D_{avg} is the average diameter, and n_{rpm} is the machine's rated operating speed in revolutions-per-minute. Equations (3) and (4) present the rearrangement of the geometrical parameters from the machine sizing equation (1) in the form of the machine's airgap surface area (A_{ag}) and the length of mid-airgap perimeter ($l_{perimeter}$). Fig. 1 illustrates the geometry of the axial-flux machine in the context of conventional airgap SRM topology.

Equation (5) presents an alternate representation of the same equation, analytically elaborating the previously stated concepts. It effectively showcases the set of macro variables, effective manipulation of which could result in enhanced performance parameters such as higher torque or power density.

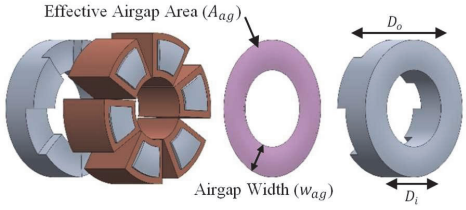


Fig. 1. Conventional Airgap Topology for Axial-Flux Machine

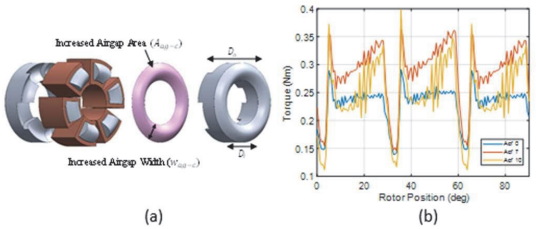


Fig. 2. (a) Curved-Airgap Topology for Axial Flux Machine, (b) Machine's Torque Profile with varying A_{cf}

B. Proposed Enhancement Strategy

The proposed enhancement strategy is targeted at altering the magnetic circuit of the machine to achieve higher torque density.

For this purpose, the electrical loading is kept constant, i.e. the machine's mid-airgap perimeter and the ampere-turns on the perimeter are not altered. The other term in the sizing equation is the product of airgap surface area i.e. the effective area where stator and rotor interact electromagnetically, and the average flux density on the same surface area. While keeping the inner and outer diameter of the machine intact, a curvature with amplitude A_{cf}, to the stator and rotor teeth faces is introduced to modify the geometric configuration of the airgap. This yields an increase in effective airgap surface area, as shown in Fig. 2(a).

III. Simulation Results

The generated torque profile as a function of rotor position, for various values of A_{cf} is shown in Fig. 2(b). The torque profile analysis shows that from the rotor position of unaligned to aligned, initially, the generated torque drops. That is because of the higher local magnetic saturation at sharp teeth edges of rotor poles. This increased local saturation will hinder the increase in the current when the stator and rotor teeth just start aligning with each other. This effect will control the generated torque and makes the torque profile rise when the rotor starts aligning with the energized stator phase.

The generated mean torque as a function of varying A_{cf} from 1 to 10 mm is shown in Fig. 3(a). The effect of different values of A_{cf} on torque ripples is depicted in Fig. 3(d). The results indicate that the mean generated torque increases with increasing A_{cf}, untill an optimized value and then starts decreasing due to increase in magnetic saturation at the rotor pole edges. This increase in the mean torque is at the cost of slightly increased torque ripples because the inductance profile is rapidly changing due to the rapid change in the effective overlapping airgap in comparison with the benchmark machine with the uniform air gap.

Fig. 3(b) and (c) present the comparative analysis of torque density (considering the active part weights only) and efficiency, as a function of varying A_{cf}. The trend here is similar, and the reason for increase in torque density and efficiency is that with comparatively smaller increase in stator volume (curved stator teeth face), a larger gain in torque generation occurs. On the other hand, the small added volume of material in the stator core causes only iron losses and these losses are a very small portion of the total losses in the machine i.e. iron losses and copper losses. Table-I presents the gain in output characteristics of the optimal design i.e. at $A_{cf} = 5mm$, in comparison with the benchmark design.

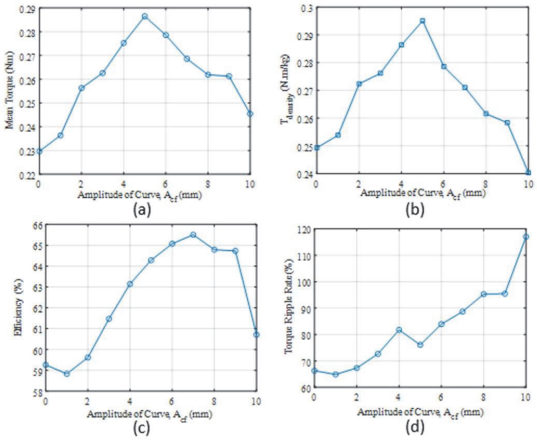


Fig. 3. (a)Mean torque production of machine at rate voltage, as a function of varying A_{cf}, (b) Torque Density variation as a function of varying curve amplitude, (c) Efficiency variation as a function of varying curve amplitude, (d) Torque Ripple Rate with varying amplitude of curve

TABLE I. Output Characteristics of Optimal Design

Parameters	Units	Benchmark Design	Optimal Design	%age Increase
Amplitude of the Sinusoid (A_{cf})	mm	0	5	-
Average Torque (T_{av})	N.m	0.229	0.286	+ 24.7
Torque Ripple Rate (T_{RR})	%	66.27	76.07	+14.7
Torque Density ($T_{density}$)	N.m/kg	0.249	0.295	+ 18.4
Efficiency	%	59.2	64.2	+ 8.44

IV. Conclusion

In summary, the results of the study indicate that the curved airgap topology enhances torque production until an optimal value is reached, beyond which diminishing returns occur due to magnetic saturation. Despite slight increases in torque ripples, this underscores the effectiveness of our design. Comparative analysis confirms significant improvements in torque density and efficiency at A_{cf} = 5mm, demonstrating the potential of non-uniform air gap designs to optimize axial flux machine performance.

References

[1] X. Zhang et al. "High-specific-power electric machines for electrified transportation applications-technology options," *ECCE 2016 - IEEE Energy Conversion Congress and Exposition, Proceedings*, 2016.

[2] Z. Ahmad, et al. "Review of Design Freedom Offered by Additive Manufacturing for Performance Enhancement of Electrical Machine," *IEEE Open Journal of the Industrial Electronics Society*, 2024.

[3] S. Hussain, et al., "Recent Trends in Additive Manufacturing and Topology Optimization of Reluctance Machines," *Energies 2023, Vol. 16, Page 3840*, vol. 16, no. 9, p. 3840, Apr. 2023.

Publication IV

M. U. Naseer, A. Kallaste, B. Asad, T. Vaimann, and A. Rassõlkin, “Design Procedure and Preliminary Analysis for the Introduction of Axial Asymmetry in the Synchronous Reluctance Machines,” Proceedings - 2023 IEEE Workshop on Electrical Machines Design, Control and Diagnosis, WEMDCD 2023, 2023, doi: 10.1109/WEMDCD55819.2023.10110903.

Design Procedure and Preliminary Analysis for the Introduction of Axial Asymmetry in the Synchronous Reluctance Machines

Muhammad Usman Naseer
Dept. of Electrical Power Engineering and Mechatronics
Tallinn University of Technology
Tallinn, Estonia
https://orcid.org/0000-0002-1682-9169

Ants Kallaste
Dept. of Electrical Power Engineering and Mechatronics
Tallinn University of Technology
Tallinn, Estonia
ants.kallaste@taltech.ee

Bilal Asad
Dept. of Electrical Power Engineering and Mechatronics
Tallinn University of Technology
Tallinn, Estonia
bilal.asad@taltech.ee

Toomas Vaimann
Dept. of Electrical Power Engineering and Mechatronics
Tallinn University of Technology
Tallinn, Estonia
toomas.vaimann@taltech.ee

Anton Rassõlkin
Dept. of Electrical Power Engineering and Mechatronics
Tallinn University of Technology
Tallinn, Estonia
anton.rassolkin@taltech.ee

2023 IEEE Workshop on Electrical Machines Design, Control and Diagnosis (WEMDCD) | 978-1-6654-8693-4/23/$31.00 ©2023 IEEE | DOI: 10.1109/WEMDCD55819.2023.10110903

***Abstract*—This article presents a MATLAB-based iterative design strategy, aimed at the investigation of axially asymmetric design possibilities for electrical machines. The developed tool for this strategy has modifiable individual portions and the capability of selecting various design criteria. The current study showcases the interdependence of various design parameters on the output performance parameters of a synchronous reluctance machine, for a selected set of design constraints. A brief analysis of the interrelated variables is presented and an approach to study and establish better control over compromising parameters is proposed for future work.**

Keywords— AC machines, design tools, additive manufacturing, three-dimensional printing, rotating machines

I. Introduction

The increasing demand for application-specific performance parameters in modern electrical machines, such as improved electromagnetics, low torque ripple and higher power density etc. is pushing the limits of design and manufacturing techniques. Conventional methods typically limit design possibilities to two dimensions, whereas the geometry remains uniform in the third dimension. Additive manufacturing (AM) offers the possibility to introduce non-uniformity in the third dimension which is difficult or impossible to achieve otherwise. AM also enables the integration of multiple functionalities within a single component, reducing the overall size and weight of the machine. This means significant improvements in their overall performance i.e. in the context of electromagnetic, thermal and/or mechanical domains [1]–[4]. The design process for these machines must also evolve to incorporate the unique flexibilities and limitations of AM.

While various aspects of electrical machines' production through AM have been studied including material characterization [5]–[8], and thermal and mechanical performance [9]–[11], there is a lack of research on the independent investigation of axial-asymmetry or non-uniformity in the third dimension. Quite a few authors have utilized such design topologies but only in a hybrid manner [12]. This paper aims to establish a starting point for the systematic inclusion of axial non-uniformity into the design process of electrical machines, by studying the interdependence of various design variables.

Since synchronous reluctance machine (SynRM) is a potential candidate for its production through AM, due to its relatively simple construction and wide range of applications [13]–[16], this study will focus on introducing and analyzing the effects of axial asymmetry on the main performance parameters of transversally laminated SynRMs. The results of this study will focus on analyzing mean torque and torque ripple, but the developed tool can also yield information on hysteresis and eddy-current loss patterns.

Section II of this article describes the idea of proposed asymmetry in detail. Section III describes the implemented design constraints in the context of the proposed asymmetry. Section IV explains the strategy and the respective parameters of the current simulation. In section V the yielded results are analyzed in the context of their interdependence with design parameters and simulation criteria. Section VI presents the conclusion and future works. In future works, the aim is to mathematically parametrize geometric shapes further and systematically interpret the results in the form of analytical equations.

II. Proposed Asymmetry

The design of an electrical machine typically requires an iterative approach to determine the geometric parameters based on various interdependent variables such as desired output parameters, design choices, constraints, and industry standards. One of the key desired characteristics is the output torque, which is represented mathematically using (1). This equation relates the relationship between torque (T) with the tangential stress ($\sigma_{F\,tan}$) acting on a rotor surface area (S_r) with the radius of cylinder (r_r) as the moment-of-arm. Equation (2) represents the same in terms of rotor volume (V_r).

$$T = \sigma_{F\,tan} r_r S_r \tag{1}$$

$$T = 2\,\sigma_{F\,tan} V_r \tag{2}$$

$$r_r\, S_r = 2\pi r^2 . l_{eq} = 2V_r \tag{3}$$

This work was supported by the Estonian Research Council grant (PRG-1827).

Authorized licensed use limited to: Tallinn University of Technology. Downloaded on April 09,2025 at 14:05:50 UTC from IEEE Xplore. Restrictions apply.

The above-presented equations characterize the conventional electrical machines where the design space is essentially 2-dimensional and the machine is kept uniform/symmetric in the third dimension. This is mainly due to the limitations imposed by the conventional production methods such as from pre-cut lamination sheets where the introduction of asymmetry in the third dimension makes the production cost and complexity, rise exponentially. With the advent of additive manufacturing technology, the design space for electrical machines expands and allows for the introduction of non-uniformity/asymmetry in the third dimension.

In the context of the above-presented analytical equations, it is evident that the torque output of the machine can be varied either by varying the tangential stress or the rotor volume. With additive manufacturing, the prospect of introducing asymmetry in the third dimension becomes available and the radius of the rotor can be changed axially. This would effectively vary the machine length, rotor surface area and resultantly, the rotor volume. This fact is illustrated in Fig. 1.

Examining the presented illustration in Fig. 1, it becomes apparent that by varying the rotor radius axially, the rotor surface area and effective length increase in both cases (Fig. 1 (a) and (c)). But since the torque is also subject to the variation in the moment-arm, the effective torque outcome is essentially proportional to the rotor volume (2). Equations (4)-(7) present the expressions for volume calculation of the geometries presented in Fig. 1.

$$r_1 < r_o < r_2 \tag{4}$$

$$V_1 = \int_0^{l_1} \pi\, r(x)^2 . dx \tag{5}$$

$$V_o = \pi\, {r_o}^2\, l_o \tag{6}$$

$$V_2 = \int_0^{l_2} \pi\, r(x)^2 . dx \tag{7}$$

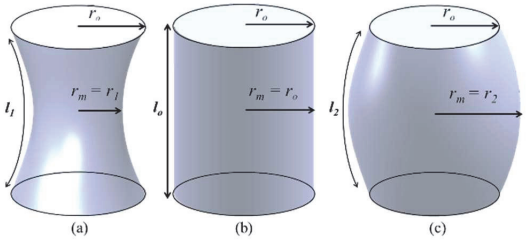


Fig. 1. Changing rotor geometry with the axially varying radius of the rotor. (a) mid-plane radius ($r_m = r_1$) less than the end-plane radius (r_o), (b) mid-plane radius equal to end-plane radius (r_o), (c) mid-plane radius ($r_m = r_2$) greater than the end-plane radius (r_o).

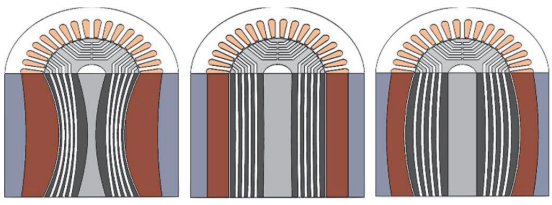


Fig. 2. Changing machine geometry with the axially varying radius of the rotor.

The proposed asymmetry of this paper is introduced in the benchmark symmetrical machine of [17], in steps from minimum to maximum value of mid-plane radius effectively transitioning the machine's internal geometry from hourglass to barrel-shape, as illustrated in Fig. 2.

III. Design Constraints

The proposed axial asymmetry in the rotor geometry was introduced by varying the rotor mid-plane radius in consecutive steps of 5 mm, from inward to outward direction. The major design constraints that were employed to introduce and investigate the effects of axial asymmetry, keeping in view the prospects offered by additive manufacturing, are as follows.

A. Machine Outer-volume

The rotor volume variation to achieve different power ratings of the machine can conventionally be achieved by uniformly varying the overall machine radius and/or stack length. But in this study, the focus is to investigate the effects of axial asymmetry and compare it with a similar axially-symmetric machine. For this, the first constraint employed is that the machine's outer stator volume i.e. outer stator radius and stack length is to be kept constant and only the machine internals such as stator inner-radius etc. will be varied in accordance with the varying rotor radius. The implementation of this constraint is also evident in Fig. 2.

B. Machine Air-gap

The airgap width is kept constant, i.e. the stator inner radius varies in accordance with the axially varying rotor outer radius.

C. Stator Slot/Tooth Dimensioning

With the stator inner radius varying in accordance with the rotor, it would affect the available space for stator slot/tooth width. A constraint on stator-tooth width and slot area needs to be implemented in this regard.

The winding parameters such as the number of winding turns/slot-conductors are kept the same as of the benchmark machine [17]. To house the same number of winding conductors in the slot, the slot area is kept constant axially. Also, the stator-tooth width is kept constant, to prevent over/under-saturation in stator teeth. The implementation of this constraint and consequent variation in slot height is illustrated in Fig. 3 and 4.

D. Flux-Barrier Dimensioning

With the axial variation in rotor radius, the available cross-sectional area for the flux barriers and flux guides at mid-plane also varies. The focus of this study was kept on keeping the flux-barrier width constant wherever possible.

In the case of decreasing mid-plane radius, the flux-barrier width was kept constant and consequently, the flux-guide width contracted due to reduced available cross-sectional area. With the increasing mid-plane radius, additional space becomes available at mid-plane and the flux-barrier width was increased along the q-axis.

The transition between the end-plane geometry and the varying mid-plane geometry was made through interconnecting splines.

Authorized licensed use limited to: Tallinn University of Technology. Downloaded on April 09,2025 at 14:05:50 UTC from IEEE Xplore. Restrictions apply.

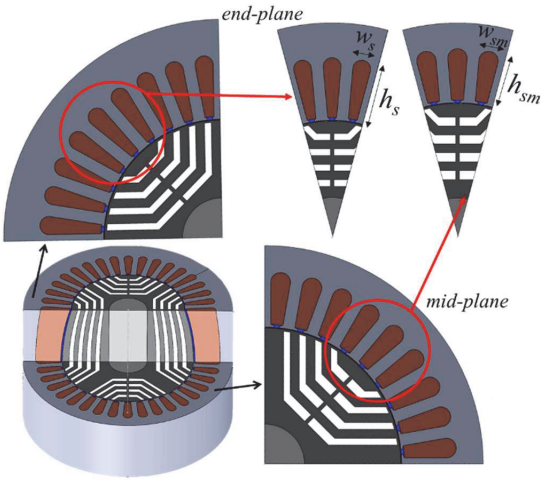


Fig. 3. Illustration of the design constraints implementation, via the cross-sectional view of the mid-plane and end-plane geometries for $r_2 > r_o$

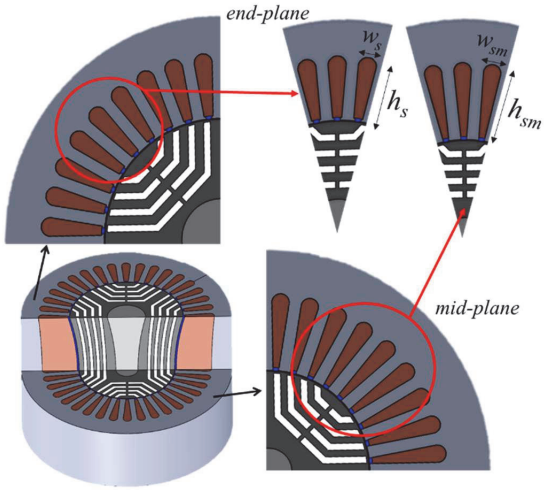


Fig. 4. Illustration of the design constraints implementation, via the cross-sectional view of the mid-plane and end-plane geometries for $r_m = r_1 < r_o$

IV. Simulation Procedure

Since the devised scheme of study is essentially iterative, an iterative tool based on MATLAB's OLE automation server was established which effectively communicates between the 3D geometry-developing CAD tool i.e. SOLIDWORKS and the FEA-analysis tool i.e. Simcenter-MAGNET. The base analytical calculations are made in MATLAB according to which the geometry is generated in SOLIDWORKS and after the FEA calculations in MAGNET, the results are brought back in MATLAB for further processing and analysis. The general block diagram of this iterative procedure is illustrated in Fig. 5. The creation of geometry in SOLIDWORKS and the FEA analysis in Simcenter-MAGNET is automated through the scripting in MATLAB. Since the machine is essentially identical around the mid-plane and at the pole axes, 1/8th of the machine was simulated in FEA to reduce the simulation complexity and runtime.

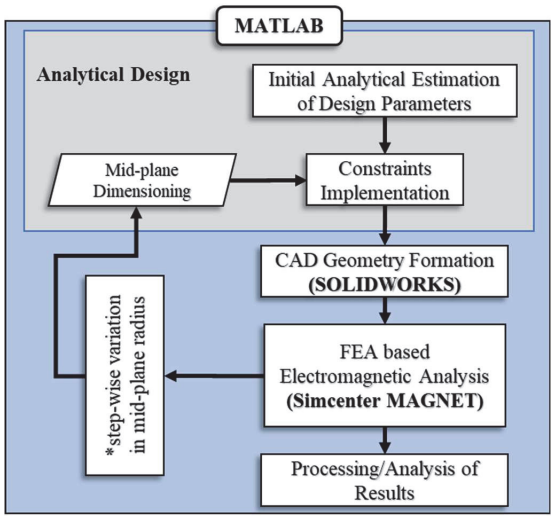


Fig. 5. Block diagram for the iterative simulation procedure.

Table-I presents the main design parameters of the benchmark machine (axially symmetric geometry) and the simulation parameters. The reference point for the comparison of simulation results was obtained by analyzing a symmetrical machine of [17], where the mid-plane radius (r_m) was set equal to the end-plane radius (r_o). The torque profile for the benchmark machine at rated parameters is presented in Fig. 6 (with a mean torque of 76.5 Nm). The respective flux density plot generated by FEA is presented in Fig. 7.

TABLE I. Main Design Parameters of the Benchmark Machine

Quantity	Value/Unit
Rated output power / torque	12 kW / ~ 76 Nm
Rated phase current	22 A
No. of poles	4 Nos.
Frequency	50 Hz
Air-gap flux density (magnetic loading)	0.85 Tesla
Linear current density (electric loading)	43.28 A/m
Machine stack length	147.3 mm
Stator-bore radius at end-plane, r_o	63.81 mm
Step size for mid-plane radius variation	5 mm
Min. stator-bore radius at mid-plane $r_1 < r_o$	38.81 mm
Max. stator-bore radius at mid-plane $r_2 > r_o$	93.81 mm
Time step for FEA simulation	0.1 mSec

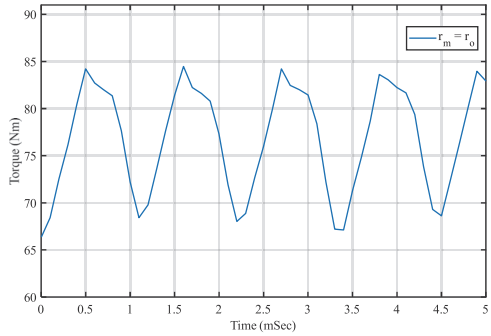


Fig. 6. Torque profile of the benchmark machine, at rated parameters

Authorized licensed use limited to: Tallinn University of Technology. Downloaded on April 09,2025 at 14:05:50 UTC from IEEE Xplore. Restrictions apply.

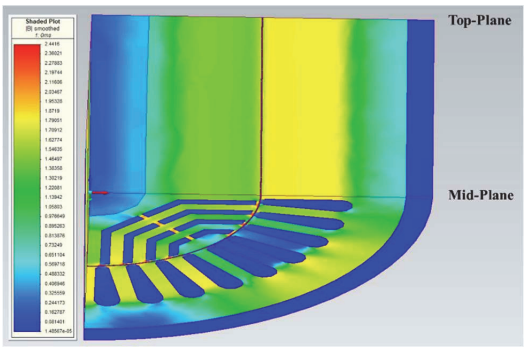


Fig. 7. Flux density plot (FEA) of the benchmark machine $r_m = r_o$, at rated parameters

For the complete simulation process, the mid-plane radius was varied in both directions i.e. inwards and outwards, in consecutive steps of 5mm. With the implementation of the design constraint dictating the constant outer radius, increased mid-plane radius results in a reduced stator yoke at mid-plane. The consequent increase in stator yoke saturation is bound to affect the maximum torque/load angle [18], [19]. The maximum load angle for each geometry was obtained by running a load-angle sweep at the rated current. The maximum load angle versus the mid-plane radius is presented in Fig. 8. Reference loading points for each individual geometry were then established by dividing the rated current and max load angle into ten equal steps. The complete set of results is presented in the next section for analysis and discussion.

V. Results and Discussion

A. Increasing Mid-plane Radius

Fig. 9 presents a sample torque profile for the increased mid-plane radius of the rotor i.e. $r_m > r_o$. Fig. 10 and 11 respectively present the FEA-calculated mean torque and ripple percentage versus the increasing mid-plane radius for different operating points of the machine, whereas Fig. 12 presents a sample flux density plot for the increased mid-plane radius of the rotor. Considering the increased mid-plane radius i.e. $r_m > r_o$, (2) suggests an increased output torque owing to the larger rotor surface and volume in comparison to the benchmark machine for which $r_m = r_o$. On the contrary, the FEA computed results indicate a reduction in mean torque.

To investigate this behaviour, consider the following formulations of tangential stress acting on the rotor surface.

$$\sigma_{F\,tan} = 1/2\,\hat{A}\hat{B}_\delta \cos\vartheta \tag{8}$$

$$\hat{A} = \hat{I_u}/\tau_{us} \tag{9}$$

where $\hat{B}_\delta$ is the peak airgap flux density, $\hat{A}$ is the linear current density around the outer periphery of the airgap, τ_{us} is the slot pitch, $\hat{I_u}$ is the slot current and $\cos\vartheta$ is phase-shift between $\hat{A}$ and $\hat{B}_\delta$.

The decreasing trend in mean-torque showcased by the results presented in Fig. 10, is due to the decrease in tangential stress acting on the rotor surface. The formulation of the tangential stress presented by (8) shows its dependence on the linear current density around the rotor periphery and on the airgap flux density. The increased rotor radius at mid-plane causes the stator slot-pitch to increase, causing the linear current density around the axial mid-plane to drop. Furthermore, keeping the outer stator radius constant, causes the stator yoke to saturate more around the axial mid-plane (refer to Fig. 12) which in turn causes the airgap flux density to drop too. This drop, in airgap flux density due to saturated stator yoke gets greater for higher operating currents of the machine, as also evident from the results of Fig. 10. The reduction in both contributing factors of tangential stress, with the increase in mid-plane radius of the rotor, causes an overall decreasing trend of the mean output torque of the machine.

Investigating the machine's behaviour for the amount of ripple in the output torque illustrates a potential benefit of the investigated axial asymmetry in the machine geometry. The improvement comes in the form of a reduced ripple percentage.

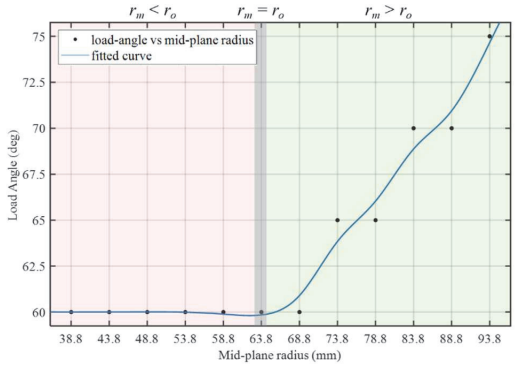


Fig. 8. Max.-torque yielding load-angle variation with varying mid-plane radius.

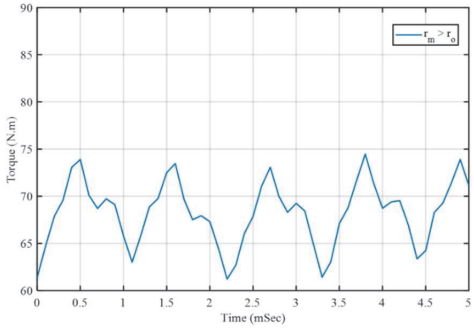


Fig. 9. Sample torque profile for increased mid-plane radius

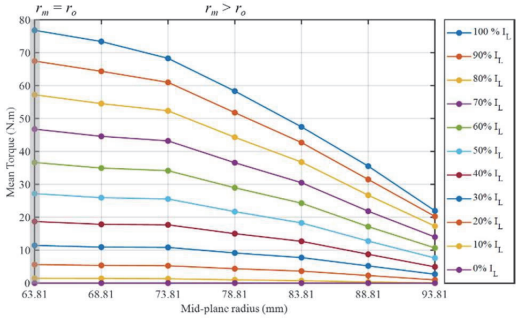


Fig. 10. Mean torque vs. increasing-plane radius (0-100% I_L)

Authorized licensed use limited to: Tallinn University of Technology. Downloaded on April 09,2025 at 14:05:50 UTC from IEEE Xplore. Restrictions apply.

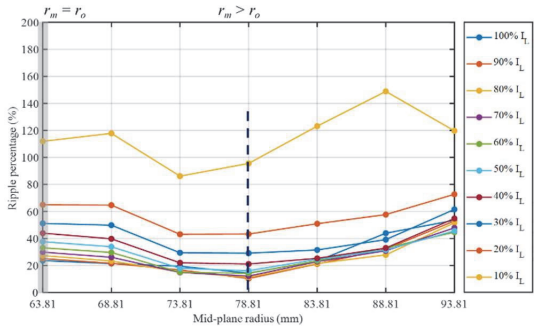


Fig. 11. Torque-ripple percentage vs. increasing mid-plane radius (0-100% I_L)

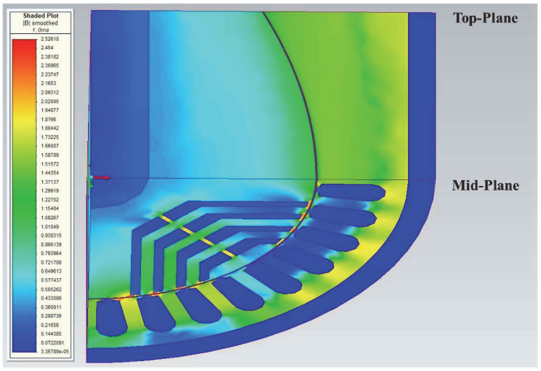


Fig. 12. Sample flux density plot (FEA) for $r_m > r_o$, at rated parameters

Fig. 11 demonstrates this behaviour, where the ripple percentage drops until a certain limit of increased radius (indicated by the dashed line on the plot) with a maximum of 25.78% decrease in torque ripple for the 23% increased mid-plane radius. This is a desired performance characteristic in any electrical machine for which the degree of axial asymmetry may be optimized against a reasonable compromise between output torque and ripple percentage.

B. Decreasing Mid-plane Radius

Fig. 13 presents a sample torque profile for the decreased mid-plane radius of the rotor i.e. $r_m < r_o$. Fig. 14 and 15 respectively present the FEA-calculated mean torque and ripple percentage versus the decreasing mid-plane radius for different operating points of the machine, whereas Fig. 16 presents a sample flux density plot for a decreased mid-plane radius of the rotor.

Referring to (8)-(9) and the previous discussion, a decreasing mid-plane radius causes the stator slot pitch to decrease which in turn forces the linear current density around the rotor periphery to follow an increasing trend. Additionally, with the decreased mid-plane radius of the rotor, the stator yoke height around the mid-plane increases. Because the normal machine design dictates operating the stator yoke near the knee (non-linear region) of the BH-curve (for the current benchmark design, it selected at 1.6Tesla for M400-50A), an increase in stator yoke height causes it to operate at lower saturated states even at high load currents (refer to Fig. 16). The stator yoke operating at lower saturated state, even at higher load currents, yields a higher air-gap flux density than the benchmark. The airgap flux density follows an increasing trend but only up until the stator yoke enters the linear operating region of the BH-curve. Further increase in stator yoke height won't cause any increased airgap flux density when compared to the same operating point of the benchmark machine.

The results presented in Fig. 14 showcase a slight initial increase in mean output torque (ranging from 0.7 to 1.30 % increased output torque for a 7.8 % decrease in the mid-plane radius of the currently presented machine geometry), in line with the previous discussion in the context of the tangential stress acting on the rotor surface. But shortly afterwards, the torque output starts following a decreasing trend. This decreasing trend is owing to the decrease in rotor volume, dominating the gains offered by increased linear current density and airgap flux density.

For the decreasing mid-plane radius, the results presented in Fig. 15 showcase an increased ripple percentage, once again

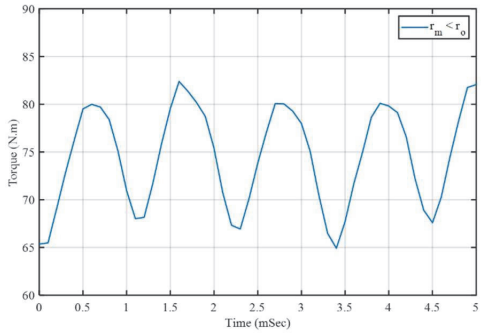


Fig. 13. Sample torque profile for decreased mid-plane radius

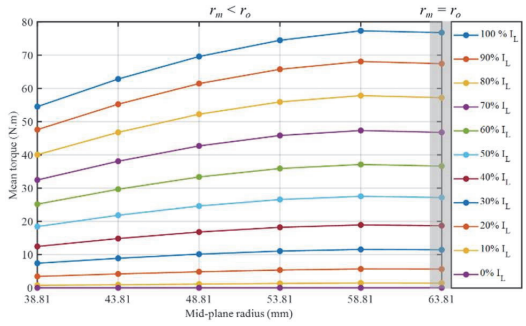


Fig. 14. Mean torque vs. decreasing mid-plane radius (0-100% I_L)

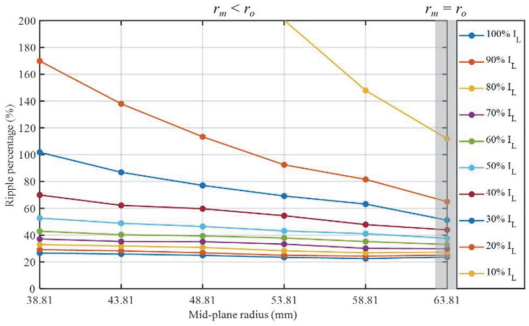


Fig. 15. Torque-ripple percentage vs. decreasing mid-plane radius (10-100% I_L)

Authorized licensed use limited to: Tallinn University of Technology. Downloaded on April 09,2025 at 14:05:50 UTC from IEEE Xplore. Restrictions apply.

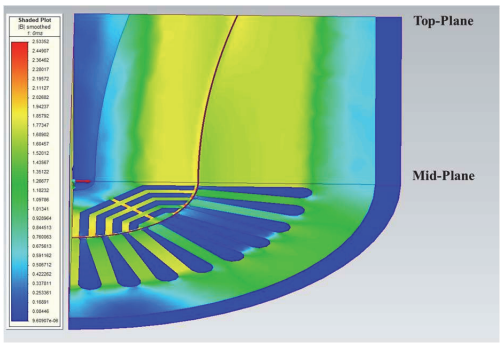


Fig. 16. Sample flux density plot (FEA) for $r_m < r_o$, at rated parameters

necessitating the introduction of an optimized degree of axial asymmetry against a reasonable compromise between output torque and ripple percentage.

VI. Conclusions and Future Work

This study presented an automated design analysis tool for the investigation of axially asymmetric/non-uniform design possibilities of electrical machines. The effort resulted in the development of an iterative tool based on MATLAB's OLE-automation-server which effectively realizes and analyzes asymmetric geometric possibilities for electrical machines. The relevance of such efforts becomes especially relevant in the context of utilizing additive manufacturing (AM) in electrical machine production.

The successful working of the design analysis tool was demonstrated by running a preliminary analysis for the introduction of axial asymmetry in synchronous reluctance machines (SynRMs). The yielded results are in reasonable agreement with the analytical reasoning, as discussed in the previous section. The analysis of results offers the possibility to study the interdependence between the geometrical and electrical parameters of the machine, as well as the selection of various design constraints. The design constraints implemented in the current study offer increased mean output torque to the detriment of increased torque ripple, for a decreased mid-plane radius. On the other hand, increased mid-plane radius results in a decreased mean output torque and a reduction of torque ripple.

With the results from implemented design constraints presented, the future work includes a parametrized/mathematical-equation-driven transition between the interconnecting end and mid-planes of the machine geometry (instead of utilizing the CAD-generated random splines). Mathematical parametrization of this transition between end-plane and mid-plane would result in precise analytical estimations even at the initial stages of the design procedure. Other future works include devising a strategy to better control the compromising electromagnetic parameters of the machine such as linear current and airgap-flux densities. Since the devised topologies are geometrically capable of producing higher torque densities but are limited due to electromagnetic parameters, the employment of attributes offered by advanced machine production technologies such as AM can help in overcoming the electromagnetic limitations through topology-optimized design strategies and enhanced/integrated cooling mechanisms etc.

References

[1] T. Pham, P. Kwon, and S. Foster, "Additive Manufacturing and Topology Optimization of Magnetic Materials for Electrical Machines—A Review," *Energies*, vol. 14, no. 2, p. 283, Jan. 2021.

[2] M. U. Naseer, A. Kallaste, B. Asad, T. Vaimann, and A. Rassõlkin, "A Review on Additive Manufacturing Possibilities for Electrical Machines," *Energies 2021, Vol. 14, Page 1940*, vol. 14, no. 7, p. 1940, Mar. 2021.

[3] R. Wrobel and B. Mecrow, "A Comprehensive Review of Additive Manufacturing in Construction of Electrical Machines," *IEEE Trans. Energy Convers.*, vol. 35, no. 2, pp. 1054–1064, Jun. 2020.

[4] R. Wrobel and B. Mecrow, "Additive manufacturing in construction of electrical machines-a review," in *Proceedings - 2019 IEEE Workshop on Electrical Machines Design, Control and Diagnosis, WEMDCD 2019*, Apr. 2019, pp. 15–22.

[5] H. Tiismus *et al.*, "Ac magnetic loss reduction of slm processed fe-si for additive manufacturing of electrical machines," *Energies*, vol. 14, no. 5, Mar. 2021.

[6] H. Tiismus, A. Kallaste, A. Belahcen, A. Rassolkin, and T. Vaimann, "Hysteresis loss evaluation of additively manufactured soft magnetic core," *Proc. - 2020 Int. Conf. Electr. Mach. ICEM 2020*, pp. 1657–1661, Aug. 2020.

[7] K. M. M. Billah, J. L. Coronel, M. C. Halbig, R. B. Wicker, and D. Espalin, "Electrical and Thermal Characterization of 3D Printed Thermoplastic Parts with Embedded Wires for High Current-Carrying Applications," *IEEE Access*, vol. 7, pp. 18799–18810, 2019.

[8] A. Selema *et al.*, "Evaluation of 3d-Printed Magnetic Materials for Additively-Manufactured Electrical Machines," *SSRN Electron. J.*, Nov. 2022.

[9] M. Sarap, A. Kallaste, P. S. Ghahfarokhi, H. Tiismus, and T. Vaimann, "Utilization of Additive Manufacturing in the Thermal Design of Electrical Machines: A Review," *Machines*, vol. 10, no. 4, Apr. 2022.

[10] M. Sarap, A. Kallaste, P. S. Ghahfarokhi, H. Tiismus, and T. Vaimann, "The Effect of Build Direction on the Thermal Conductivity of Additively Manufactured AlSi10Mg and Silicon-steel Samples," *2022 Int. Conf. Electr. Mach. ICEM 2022*, pp. 538–543, 2022.

[11] M. Sarap, A. Kallaste, P. S. Ghahfarokhi, H. Tiismus, and T. Vaimann, "Determining the Thermal Conductivity of Additively Manufactured Metal Specimens," pp. 1–4, Mar. 2022.

[12] J. Krishnasamy and M. Hosek, "Spray-Formed Hybrid-Field Traction Motor," in *SAE Technical Papers*, Mar. 2017, vol. 2017-March, no. March.

[13] N. Bianchi, S. Bolognani, E. Carraro, M. Castiello, and E. Fornasiero, "Electric Vehicle Traction Based on Synchronous Reluctance Motors," *IEEE Trans. Ind. Appl.*, vol. 52, no. 6, pp. 4762–4769, Nov. 2016.

[14] S. M. Taghavi and P. Pillay, "A mechanically robust rotor with transverse laminations for a wide-speed-range synchronous reluctance traction motor," *IEEE Trans. Ind. Appl.*, vol. 51, no. 6, pp. 4404–4414, Nov. 2015.

[15] E. Carraro, M. Morandin, and N. Bianchi, "Traction PMASR motor optimization according to a given driving cycle," *IEEE Trans. Ind. Appl.*, vol. 52, no. 1, pp. 209–216, Jan. 2016.

[16] S. V. Nair, K. Layek, and K. Hatua, "An Unequal Split Dual Three-Phase PMSM with Extended Torque-Speed Characteristics for Automotive Application," *IEEE Trans. Power Electron.*, vol. 37, no. 10, pp. 12437–12449, Oct. 2022.

[17] M. U. Naseer, A. Kallaste, B. Asad, T. Vaimann, and A. Rassõlkin, "Modified Initial Design Procedure for Synchronous Reluctance Motor," *2022 Int. Conf. Electr. Mach. ICEM 2022*, pp. 1969–1975, 2022.

[18] A. Vagati, M. Pastorelli, F. Scapino, and G. Franceschini, "Impact of cross saturation in synchronous reluctance motors of the transverse-laminated type," *IEEE Trans. Ind. Appl.*, vol. 36, no. 4, pp. 1039–1046, Jul. 2000.

[19] P. Rafajdus, V. Hrabovcova, P. Lehocky, P. Makys, and F. Holub, "Effect of Saturation on Field Oriented Control of the New Designed Reluctance Synchronous Motor," *Energies 2018, Vol. 11, Page 3223*, vol. 11, no. 11, p. 3223, Nov. 2018.

Authorized licensed use limited to: Tallinn University of Technology. Downloaded on April 09,2025 at 14:05:50 UTC from IEEE Xplore. Restrictions apply.

Publication V

M. U. Naseer, A. Kallaste, B. Asad, T. Vaimann, and A. Rassõlkin, “Modified Initial Design Procedure for Synchronous Reluctance Motor,” in ICEM 2022 XXV International Conference on Electrical Machines, 2022.

Modified Initial Design Procedure for Synchronous Reluctance Motor

Muhammad Usman Naseer, Ants Kallaste, Bilal Asad, Toomas Vaimann, Anton Rassõlkin

2022 International Conference on Electrical Machines (ICEM) | 978-1-6654-1432-6/22/$31.00 ©2022 IEEE | DOI: 10.1109/ICEM51905.2022.9910594

***Abstract* – This paper presents the basic design procedure for producing synchronous machines through conventional manufacturing techniques. The design procedure is explicitly adapted for synchronous reluctance machines with the proposed modifications, but individual portions can also be modified further for other machine types. The proposed changes in the design procedure also aim to establish a starting point for the systematic inclusion of design freedoms and limitations offered by additive manufacturing rather than their intuitive utilization.**

***Index Terms*-- AC machines, design tools, electric machines, rotating machines, three-dimensional printing**

I. Introduction

THE modern-day machine applications showcase an increasing demand for application-specific performance parameters. That includes improved electromagnetic, mechanical and thermal properties and other attributes such as integrated functionalities and higher power density. Recent advances in additive manufacturing (AM) techniques demonstrate promising results in these aspects through added flexibility in the three-dimensional realization of design, i.e. fabrication of complex/asymmetric geometrical structures and weight/size reduction through topology optimization [1], [2].

Considering the current state-of-the-art in AM and due to the relatively simple construction, least involvement of multi-material in the fabrication and wide-range applications, synchronous reluctance motor (SynRM) becomes a potential candidate for its production through AM [1]–[4]. SynRMs also offer fast response characteristics [5], [6], high torque density [7], [8] and higher efficiency [9] compared to other machine types. Apart from their typical utilization in constant speed applications, the latest developments in variable frequency drives make them a potential alternative to induction machines.

The basic aspects of synchronous machine design through the analytical procedure, somewhat comprehensively presented by various authors [10]–[12], have matured over time and are generally optimized for conventional manufacturing techniques. Recent literature also addresses improvements in individual performance parameters [13]–[21], which usually involves time and resource-consuming numerical modeling or prototyping. The design flexibilities offered by AM can also be analyzed through numerical modeling but are not preferable at the initial stage of the design process. The iterative nature of the initial design process makes it a complex and time-consuming job that must be avoided. This becomes more relevant in the context of mass-personalized production, which is the most significant feature of electrical machine production through AM.

This paper presents the conventional design procedure adapted for SynRM. The suggested modifications in the existing design procedure and execution strategy aim to establish a systematic approach, to incorporate the continuously evolving features of AM. It includes establishing the designer's enhanced control over optimizable parameters of interest and criteria, rather than relying on empirical knowledge of best practices (usually standardized for conventional manufacturing techniques).

Since the rotor core's electromagnetic properties are dependent on the printing methodology and structural topology, a rotor flux-barrier sizing approach is suggested based on the core's structural and magnetic characteristics. The verification of design outcomes in terms of operational parameters such as flux density assumptions and calculation of inductance ratio was done through numerical modeling. Future works include analytical measurement of *d* and *q-axis* inductances and the torque profile estimation to make initial design estimation fast and independent of complex modeling procedures.

II. Design Process

The design problem usually involves many interdependent variables classified into fixed and free variables. Most of the fixed variables comprise the desired output characteristics, i.e. output power, efficiency, torque or speed, and are assigned values accordingly. Additionally, some variables are assigned values per design constraints (i.e. frequency of the supply), specific design choices, or the empirical knowledge of well-established design practices. In contrast, other variables defining the machine's geometry are specified as free variables and are calculated in due order through iterative design calculations. Wherever required, free variables are also assigned initial assumptions to facilitate the design flow, and the process is re-iterated for the actual values calculated in the later steps. The design estimation process of [10] is generalized, yielding the initial design estimates of electrical machines. Whereas its adaptation for conventional synchronous machines is relatively simple. The block diagram showcasing the components and flow of the design process is presented in Fig. 1.

M. U. Naseer, A. Kallaste, B. Asad, T. Vaimann and A. Rassõlkin are with Department of Electrical Power Engineering and Mechatronics, Tallinn University of Technology, 19086 Tallinn, Estonia (e-mail: mnasee@taltech.ee, ants.kallaste@taltech.ee bilal.asad@taltech.ee, toomas.vaimann@taltech.ee, anton.rassolkin@taltech.ee).

Authorized licensed use limited to: Tallinn University of Technology. Downloaded on April 09,2025 at 14:06:58 UTC from IEEE Xplore. Restrictions apply.

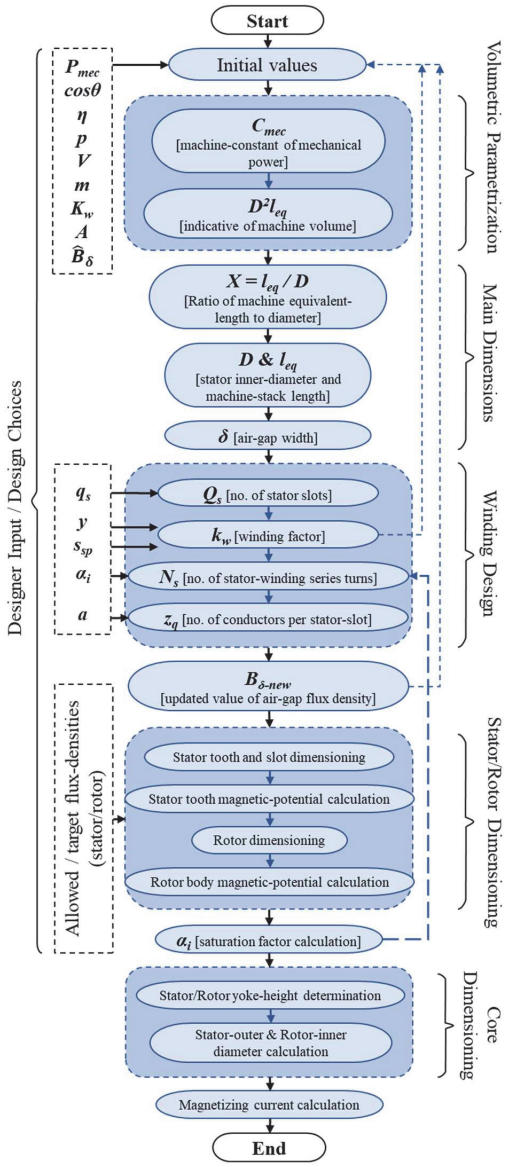


Fig. 1. Block diagram for initial design estimation of synchronous machines

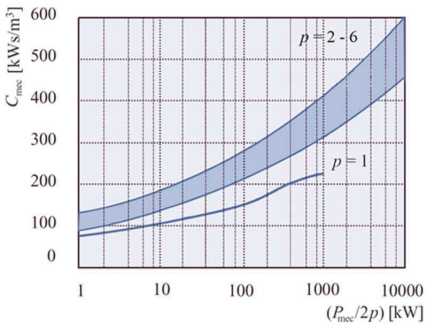


Fig. 2. Typical machine constant C_{mec} values as a function of machine power per-pole [10]

A. Initial Values

As explained in the previous text, the fixed variables with values assigned according to the machine's desired output characteristics and well-established design practices serve as the starting values for the analytical design procedure. These variables include rated output power-P_{mec} and terminal voltages-V, power factor-$cos\theta$, efficiency-η, number of pole pairs-p, number of phases-m etc. In addition to that, some free variables such as the winding factor-k_{w1} of the fundamental component, linear current density-A and air-gap flux density-$\hat{B}_\delta$ are also assigned some initial values. Their actual values will be calculated in later steps, and the design procedure will be re-iterated in due sequence.

B. Volumetric Parametrization

The machine's air-gap volume-V_{ag} is given by

$$V_{ag} = {}^{\pi}/_{4} D^2 l_{eq} \sim V_r \tag{1}$$

where l_{eq} is the machine's equivalent stack length, D is the air-gap diameter, and V_r is the rotor volume. Equating the machine output mechanical power in terms of air-gap volume, we get

$$P_{mec} = C_{mec} D^2 l_{eq} n_{syn} \tag{2}$$

where C_{mec} is the machine constant for mechanical power and n_{syn} is synchronous speed. The state-of-the-art in conventional manufacturing techniques suggests selecting the value of C_{mec} from the empirical knowledge of well-designed machines to get the volumetric estimate $D^2 l_{eq}$ from (2). The typical values of C_{mec} as a function of output mechanical power per-pole are given in Fig. 2.

C. Main Dimensions

The ratio of machine equivalent length to air-gap diameter-χ is set in accordance with the number of poles. The guidelines of the literature suggest calculating this ratio as follows

$$\chi = {}^{l_{eq}}/_{D} \approx {}^{\pi}/_{4\sqrt{p}} \tag{3}$$

Solving (2) and (3) yields the main dimension of the machine, i.e. D and l_{eq}.

For typical synchronous machines, the permitted armature reaction defines the minimum air-gap width-δ to avoid the excessive reduction in flux density under the pole area. This condition dictates the air-gap calculation as follows

$$\delta \geq {}^{1}/_{2}\, \alpha_{SM} \mu_o \tau_p {}^{A}/_{k_C \hat{B}_\delta} \tag{4}$$

where k_c is the carter factor, τ_p is the pole-pitch, μ_o is the permeability of free space, and α_{SM} is the relative pole width co-efficient ($\approx 2/\pi$ for sinusoidal flux distribution). This condition is valid for synchronous machines with wound-field rotors. But for the machines taking magnetizing current from the stator-phases, air-gap should be kept as minimum as manufacturing or fabrication procedure allows, to keep the magnetizing current as low as possible.

D. Winding Design

The winding design begins with the selection of the number of slots-per-pole-per-phase-q_s. To achieve a more sinusoidal current linkage, a large number of slots are the

Authorized licensed use limited to: Tallinn University of Technology. Downloaded on April 09,2025 at 14:06:58 UTC from IEEE Xplore. Restrictions apply.

desired feature. Still, it also affects the overall manufacturing cost due to the increased coils and end-winding associated copper losses. A suitable design choice for slot pitch is now required to achieve a balanced compromise between machine performance, manufacturing, and operation costs. The slot pitch-τ_{us} and total number of stator slots-Q_s is calculated as follows

$$Q_s = 2pmq_s \tag{5}$$

$$\tau_{us} = {}^{\pi D}/_{Q_s} \tag{6}$$

Improved machine performance parameters such as reduced harmonics, shorter end-windings, and improved sinusoidal current linkage can be achieved through layered and or short-pitched stator winding. Skewed stator slots contribute towards reduced slotting harmonics. Respective winding factors estimate the reduction in fundamental and higher-order harmonics and are calculated iteratively to achieve the desired results. The winding factors (combined winding factor-k_{wv}, skewing factor-k_{sqv}, pitch factor-k_{pv} and the distribution factor-k_{dv}) are calculated as follows

$$k_{dv} = \sin(v\frac{\pi}{2m}) \,/\, q\sin(v\frac{\pi}{2mq_s}) \tag{7}$$

$$k_{pv} = \sin(v\frac{y}{y_Q}\frac{\pi}{2}) \tag{8}$$

$$k_{sqv} = \sin(v\frac{\pi}{2}\frac{s_{sp}}{mq_s}) \,/\, (v\frac{\pi}{2}\frac{s_{sp}}{mq_s}) \tag{9}$$

$$k_{wv} = k_{dv} \times k_{pv} \times k_{sqv} \tag{10}$$

where y is the actual pitch of the coil (after short pitching), y_Q is the full pole pitch expressed in the number of slots, s_{sp} is the skewing of slots in terms of the number of slot pitches, and v is the harmonic number. The term y/y_Q in (8) represents the relative shortening in coil span. The winding factor for the fundamental component was assigned an initial value earlier. The process can be re-iterated against the actual calculated value at this stage.

The number of series turns per coil-N_s of the winding, and the number of conductors per slot-z_Q is calculated as follows. The calculation at this stage involves an unknown, α_i (arithmetic average of flux density per-pole, i.e. function of saturation), requiring a suitable assumption. The initial assumption for the unsaturated machine is taken here as an initial value, i.e. $0.65 \approx 2 / \pi$ for sinusoidal flux distribution.

$$N_s = \sqrt{2}E_m \,/\, \omega k_{w1} l_{eq} \tau_p \alpha_i \hat{B}_\delta \tag{11}$$

$$E_m = \pi^2 k_{w1} \hat{A} \hat{B}_\delta D^2 l_{eq} n_s \,/\, mI_s \tag{12}$$

$$I_s = P_{mec} \,/\, mV\,\eta\cos\theta \tag{13}$$

$$z_Q = 2amN_s \,/\, Q_s \tag{14}$$

where E_m is the induced emf of the stator phase winding, I_s is nominal stator current, and a is the number of parallel paths in the winding. The calculated value of z_Q may need to be rounded off to an even integer, resulting in an updated number of series turns. Equation (11) is utilized again at this stage to calculate the new value of air-gap flux density against the updated value of Ns. The design process is re-iterated against the updated value of air-gap flux density.

E. Stator / Rotor Dimensioning

The stator dimensioning for most machine types is similar and is based on the allowed or target flux density in various stator parts. The target flux density also depends on the magnetic characteristics of the core material. At this stage, stator teeth and slot dimension is done, whereas the yoke sizing will be done later in due sequence. By selecting a suitable apparent value of stator-tooth flux density-$\hat{B}'_{\mathrm{ds}}$ the stator tooth width-b_{ds} is calculated as follows

$$b_{ds} = l_{eq}\tau_{us} \,/\, k_{Fe}(l - n_v b_v) \cdot \hat{B}_\delta \,/\, \hat{B}'_{ds} \tag{15}$$

where n_v and b_v are the number and widths of ventilation ducts and k_{Fe} is the space factor for the core

The winding conductor cross-sectional area-S_{cs} and the required slot area-S_{cus} are determined according to the respective stator current and allowed current density-J_s of the selected conductor wire.

$$S_{cs} = I_s \,/\, aJ_s \tag{16}$$

$$S_{cus} = z_Q S_{cs} \,/\, k_{cus} \tag{17}$$

With the tooth width and required slot area determined, the slot dimensioning is done according to the stator slot's basic design choices, i.e. slot type and slot opening, etc. At this stage, the average slot width is more or less fixed due to the predetermined value of stator-tooth width. The main dimensioning is done in terms of slot height, in accordance with the area required to house z_q conductors i.e. S_{cus}.

The rotor's outer diameter is calculated as follows

$$D_r = D - 2\delta \tag{18}$$

whereas the detailed rotor dimensioning is dependent on the choice of specific machine type and construction, i.e. salient or non-salient pole synchronous machine, field excited or permanent magnet synchronous machine, synchronous reluctance machine (SynRM) etc. It is a vast and machine-type specific procedure and won't be covered here in a generalized manner. Since the main focus of this paper is the SynRM, a suggested scheme for the rotor dimensioning in that respect will be presented later in the text.

F. Saturation Factor and Magnetic Potential

The actual value for α_i, which was assigned an initial value to facilitate the design process, can be calculated at this stage. If the calculated value differs from the initial assumption, the process is re-iterated against the updated value. This involves calculating the magnetic potential of various machine parts by taking the line integral of magnetic field intensity-H within the respective machine part, as follows

$$U_m = \int H \,.\, dl \tag{19}$$

A two-step procedure (as described next) is adopted to determine the magnetic field intensity in individual machine parts. Earlier steps in the machine design process were executed by specifying apparent flux densities for each machine part. Flux weakening happens in the machine core due to flux leakage, and the actual flux density is given by (20). The second term in (20) represents the leakage flux and is proportional to the ratio of the area without magnetic material- S_u to that of the area with the magnetic material-S_d.

$$\hat{B}_d = \hat{B}_d{}' - (S_u \,/\, S_d)\,\mu_o \hat{H}_{dl} \tag{20}$$

Plotting (20) over the magnetization curve of the core material and finding the intersection point with the BH-curve

Authorized licensed use limited to: Tallinn University of Technology. Downloaded on April 09,2025 at 14:06:58 UTC from IEEE Xplore. Restrictions apply.

(as shown in Fig. 5, in the results section) gives the actual flux density, and the associated magnetic field intensity is utilized in (19) to calculate the magnetic potential of the respective machine part. The saturation factor k_{sat} and the corresponding actual value of α_i is calculated from empirical relations [10] as follows

$$k_{sat} = \left(\hat{U}_{m,s} + \hat{U}_{m,r}\right) / \hat{U}_{m,\delta} \quad (21)$$

$$\alpha_i = (1.24k_{sat} + 1) / (1.42k_{sat} + 1.57) \quad (22)$$

G. Core Dimensioning

The final core dimensioning takes place by defining the desired flux density of the stator and rotor yoke, i.e. a higher flux density yields lower yoke height but higher core losses, and vice versa. Designer intervention at this stage is required for a choice corresponding to the desired outcomes. The stator and rotor yoke heights are determined from (23)-(24).

$$h_y = \hat{\emptyset}_m / 2k_{Fe} l \hat{B}_y \quad (23)$$

$$\hat{\emptyset}_m = \alpha_i \hat{B}_\delta \tau_p l_{eq} \quad (24)$$

where h_y is the yoke height, $\hat{B}_y$ is the selected value of yoke flux density and $\hat{\emptyset}_m$ is the peak value of air-gap flux. The stator outer diameter is given by

$$D_{se} = D_s + 2\,(h_s + h_{ys}) \quad (25)$$

H. Magnetizing Current

The magnetizing current-$I_{s,mag}$ is calculated against the no-load magnetic potential of the machine, i.e. the fundamental component of current linkage-$\hat{\theta}_{s1}$.

$$\hat{U}_{m,total} = \hat{\theta}_{s1} = \frac{m\, k_{w1} N_s \sqrt{2}}{\pi p} I_{s,mag} \quad (26)$$

$$\hat{U}_{m,total} = \hat{U}_{m,\delta} + \hat{U}_{m,s} + \hat{U}_{m,r} + \hat{U}_{m,ys}/2 + \hat{U}_{m,yr}/2 \quad (27)$$

where $\hat{U}_{m,ys}$ and $\hat{U}_{m,yr}$ are the magnetic potentials of the stator and rotor yoke, respectively.

III. Suggested Modification in Design Procedure

The following modifications in the design procedure are suggested as an initial step towards incorporating AM features in the conventional design procedure.

A. Effect of Core's Structural Characteristics on Volumetric Parametrization

In any machine, torque production is achieved by tangential stress produced from the interaction of magnetic fields. The yield strength of the rotor material and structure defines the limit of tangential stresses that the rotor body can take. In terms of the machine's electromagnetic design parameters, the tangential stress-$\sigma_{F\,tan}$ is given by

$$\sigma_{F\,tan} = 1/2\, \hat{A}\hat{B}_\delta \cos\vartheta \quad (28)$$

where ϑ spatial phase shift between the fundamental distributions of air-gap flux density and linear current density. In terms of the machine's geometrical parameters, the torque production-T and the tangential stress are given as follows

$$T = \sigma_{F\,tan} r_r S_r \quad (29)$$

$$T = 1/2\, \sigma_{F\,tan} \pi D_r^{\,2} l_{eq} \quad (30)$$

$$\sigma_{F\,tan} = 2\,T / \pi D^2 l_{eq} \quad (31)$$

where r_r is the rotor radius and S_r is the rotor surface area. Equations (29)-(31) suggest that the interdependent quantities, i.e. tangential stress or rotor volume, need to be optimized for a specified value of required torque production. From the electrical-design point of view, the tangential stress (28) can be varied by the suitable design choice of linear current density or air-gap flux density.

From the standpoint of additive manufacturing, volumetric parameterization becomes a two-fold optimization problem due to the AM technology's various evolving aspects. First, the yield strength depends mainly on the core structure and printing methodology. Secondly, the magnetic properties of the printed material are not yet standardized and also depend majorly on the printing technology and parameters. These factors suggest the introduction of flexibility in the design strategy so that the designer has more control over the selection and choice of the fixed and optimizable parameters.

In contrast to the design procedure for conventional manufacturing techniques where the choice of C_{mec} (factor responsible for volumetric parameterization) is made from the empirical knowledge of well-designed machines, the suggested strategy involves calculating it in terms of machine design variables, as follows

$$C_{mec} = (V / E_m)\, \eta \cos\theta\, \pi^2 k_{w1} \hat{A} \hat{B}_\delta \quad (32)$$

Utilizing (28)-(32), the design values for $\hat{A}$ and $\hat{B}_\delta$ can be optimized against the chosen optimization criterion of the maximum allowed tangential stress. Fig. 3 illustrates the block diagram for the iterative optimization procedure. The top-left superscript in each block indicates the respective equation to be utilized. The optimizable and optimization criteria can be interchanged in accordance with the applicable constraints.

B. Rotor Flux-barrier Parametrization

The SynRM-rotor design guidelines suggest an initial parametrization of rotor flux barriers in a 50:50 ratio with the flux guides. This analytical approach yields a reasonable *d* and *q-axis* inductance ratio, but the number of flux barriers also significantly influence the inductance ratio. The number of flux barriers, if kept equal to one, yields the inductance

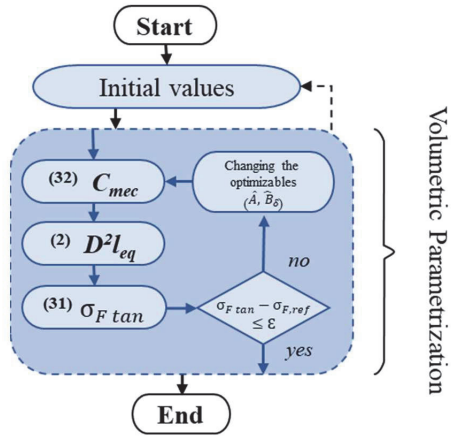


Fig. 3. Block diagram for optimizing design parameters against additively manufactured structural characteristics

Authorized licensed use limited to: Tallinn University of Technology. Downloaded on April 09,2025 at 14:06:58 UTC from IEEE Xplore. Restrictions apply.

ratio similar to typical synchronous machines having pole-shoe construction. This kind of construction gives L_d/L_q ratio in the range of 2-3. The flux barriers need to be increased to achieve higher inductance ratios. Iterative design analysis usually helps determine an optimized number and ratio of flux barriers. Further shape optimization of individual flux barriers is done in later design stages, utilizing more precise numerical modeling techniques.

The suggested initial parametrization of flux barriers is based on allowed flux density in the rotor body, i.e., keeping the core losses to the desired minimum (dependent on the core material and structural topology when utilizing AM). To commence the design procedure, the maximum flux density in the rotor flux-guide $\hat{B}_{fg}{}'$ must be proposed based on the material properties, i.e. BH-curve and loss characteristics. The flux-guide width-b_{fg} is calculated as follows

$$b_{fg} = l_{eq}\tau_{ur} / k_{Fe}(l - n_v b_v) \cdot \hat{B}_\delta / \hat{B}'_{fg} \quad (33)$$

where τ_{ur} is the rotor pitch for flux barriers, and $\hat{B}'_{fg}$ is the apparent flux density in the rotor core. From the calculated width of flux guide, the width of flux barrier-b_{fbr} is calculated as follows

$$b_{fbr} = \tau_{ur} - b_{fg} \quad (34)$$

IV. Results and Discussion

The presented design procedure was implemented in the form of a MATLAB algorithm where the possibility of designer intervention at designated places was made available to assign initial values (wherever required), define optimization criteria, and choose various design parameters by iteratively comparing the results.

A test run of the design procedure for the initial design estimation of an 11kW, 400V 3-phase synchronous reluctance motor was done, and the results are presented in Table 1 (in the chronological order of execution). The choice of χ, i.e. the ratio of machine length to diameter, was influenced by the fact that the motor was to be constructed by modifying an existing induction motor enclosure which only allowed for a particular value of χ. Since the SynRM has a non-excited rotor, the magnetizing current is drawn from the stator phases, necessitating the choice of minimum possible value for air-gap. Consequently, the air gap was chosen to be 0.5mm. A two-layered stator winding (for a better sinusoidal distribution of current linkage) with a short-pitching of two stator slots (to reduce higher-order harmonics) was opted, yielding a fundamental-component winding factor 0.901. Fig. 4 presents the winding factors for various higher-order harmonics.

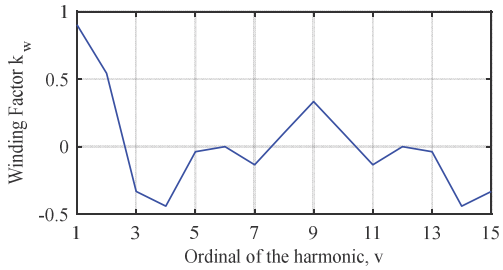


Fig. 4. Winding factor k_w for fundamental and higher-order harmonics

The stator/rotor dimensioning was done for the selected core material of M40050A, with various selected values of apparent flux densities in the respective portions of the machine (presented in Table 1). The process of determining the actual flux density and respective magnetic field strength for stator tooth-tip is shown in Fig. 5 for illustration purposes. Implementing Section-III (B) 's proposed scheme resulted in flux barrier and flux guide size of 4mm and 5mm, respectively. The estimated rotor design is illustrated in Fig. 6. Subsequent calculations of magnetic potential and saturation factor yielded a value of 0.654 for α_i, verifying the machine to be un-saturated at nominal operating conditions as intended. The machine's operating point, concerning the magnetic saturation level of core material, is indicated by the value of α_i and can be subsequently altered by a suitable selection of design parameters iteratively.

TABLE I
Initial Design Estimation of 11kW SynRM

Design Parameter	Value	Unit
Machine rated power	11	kW
Rated output torque	65.60	N·m
Terminal voltages (L-L)	400.00	V
Number of phases	03	No.
Number of poles	04	No.
Frequency	50	Hz
Rotational speed	1500	rpm
Efficiency	90	%
Power factor	0.65	--
Peak Air-gap flux density	0.85	T
Linear current density	42.7	
Air-gap width	0.5	mm
Stator bore-diameter	136	mm
Rotor diameter	135	mm
Machine stack length	156	mm
Number of stator slots	36	No.
Number of parallel paths in winding	02	No.
Number of winding layers	02	No.
Short pitching (in terms of stator slots)	02	No.
Slot skewing (in terms of stator slots)	00	No.
Winding factor k_{wl}	0.901	--
Rated stator current	22.1	A
Number of series coil turns	138	No.
Conductors per slot	46	No.
Flux density assumption for machine core	1.6	T
Stator tooth-width	6.4	mm
Stator-slot opening	2	mm
Stator-slot height	22.5	mm
Rotor flux-guide width	5	mm
Rotor flux-barrier width	4	mm
Stator-yoke height	21.3	mm
Stator outer-diameter	223	mm

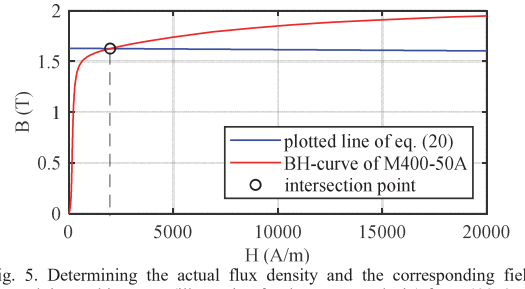


Fig. 5. Determining the actual flux density and the corresponding field strength in machine parts (illustration for the stator tooth-tip) for M40050A

Authorized licensed use limited to: Tallinn University of Technology. Downloaded on April 09,2025 at 14:06:58 UTC from IEEE Xplore. Restrictions apply.

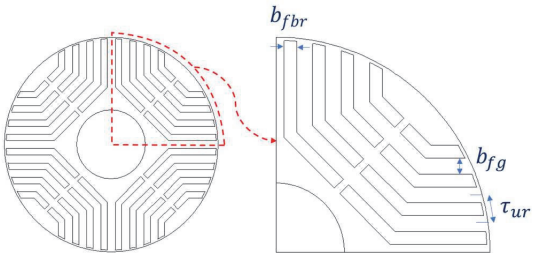


Fig. 6. Estimated rotor design from initial parameterization

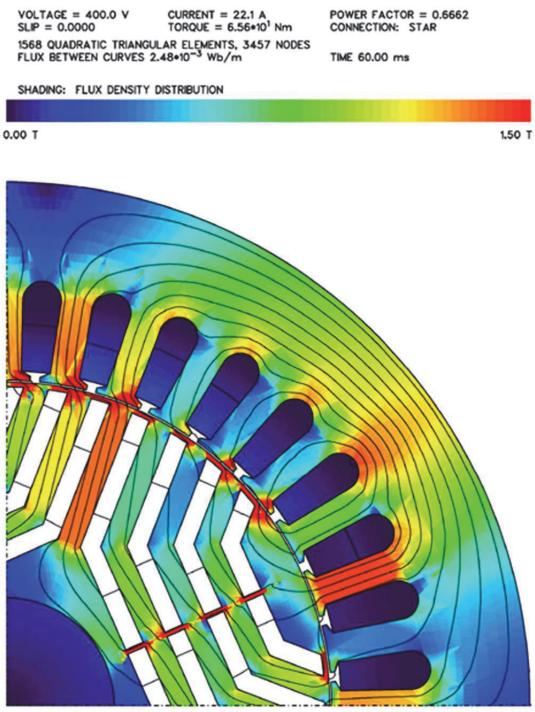


Fig. 7. Flux density distribution at nominal operating conditions

The design outcomes of the proposed modified analytical procedure were fed to finite element analysis (FEA)-based commercial design software Sincenter-MAGNET, verifying the flux density assumptions of the analytical design procedure (Fig. 7), giving a reasonable L_d/L_q ratio of 4.21.

V. Conclusion

The procedure and execution scheme of [10] is mainly standardized for conventional manufacturing techniques wherein the volumetric parametrization (responsible for power density) is done using empirical knowledge of mechanical power constant. The characteristics of any machine core are intrinsically interdependent, where a change in one parameter usually affects others. Additive manufacturing (AM) offers selective core characteristics mainly through structural topology optimization, which is otherwise difficult to attain through conventional manufacturing techniques (though currently very limited due to the AM technology's relative immaturity). Compared to the usual solid construction, the topology optimization affects the structural integrity of the printed machine parts, i.e. the upper limit of tangential stress. A modified volumetric parameterization is suggested in this article, where the machine's mechanical power constant is calculated from the optimized values of air-gap flux density and linear current density against the tangential-stress limit of the subject structural topology.

Next, the scope of the original design procedure addresses the typical permanent-magnet assisted or field excited synchronous machines, whereas the rotor design guidelines are only generalized. This paper suggests the rotor flux barrier parameterization based on magnetic characteristics of the core material, which provides flexibility in defining the operating region of the rotor core on the magnetization curve of printed material. This point is specifically important given the current state of the art in additive manufacturing, i.e. comparatively higher iron losses than the conventionally produced cores.

This submission is an initial step in the effort to develop a systematic design procedure, flexible enough to accommodate continuously evolving state-of-the-art at any stage of technological maturity in AM. The implemented algorithm is intended to provide a basis to build upon and develop the design scheme further in a scientific manner (to account for the offered prospects of AM such as performance parameter enhancements through the introduction of geometrical asymmetries and also the effect of structural topologies on the electromagnetic parameters of the machine). Regarding the synchronous reluctance machine in specific, the future work also includes the analytical calculation of *d* and *q-axis* inductances (main performance parameter) without having to utilize the resource and time-consuming numerical techniques such as FEA. A reliable standalone analytical model would also contribute towards a fast design iteration tool which is very important in achieving the possibility of mass-personalized production of electrical machines.

VI. References

[1] M. U. Naseer, A. Kallaste, B. Asad, T. Vaimann, and A. Rassõlkin, "A Review on Additive Manufacturing Possibilities for Electrical Machines," *Energies*, vol. 14, no. 7, p. 1940, Mar. 2021.

[2] T. Pham, P. Kwon, and S. Foster, "Additive Manufacturing and Topology Optimization of Magnetic Materials for Electrical Machines—A Review," *Energies*, vol. 14, no. 2, p. 283, Jan. 2021.

[3] N. Bianchi, S. Bolognani, E. Carraro, M. Castiello, and E. Fornasiero, "Electric Vehicle Traction Based on Synchronous Reluctance Motors," *IEEE Trans. Ind. Appl.*, vol. 52, no. 6, pp. 4762–4769, Nov. 2016.

[4] B. Ban, S. Stipetic, and M. Klanac, "Synchronous reluctance machines: Theory, design and the potential U se in traction applications," in *International Conference on Electical Drives and Power Electronics*, Sep. 2019, vol. 2019-September, pp. 177–188.

[5] S. J. Kang and S. K. Sul, "Highly dynamic torque control of synchronous reluctance motor," *IEEE Trans. Power Electron.*, vol. 13, no. 4, pp. 793–798, 1998.

[6] B. H. Bae and S. K. Sul, "A novel dynamic overmodulation strategy for fast torque control of high-saliency-ratio ac motor," *IEEE Trans. Ind. Appl.*, vol. 41, no. 4, pp. 1013–1019, Jul. 2005.

[7] R. R. Moghaddam, F. Magnussen, and C. Sadarangani, "Novel rotor design optimization of synchronous reluctance machine for high torque

Authorized licensed use limited to: Tallinn University of Technology. Downloaded on April 09,2025 at 14:06:58 UTC from IEEE Xplore. Restrictions apply.

density," *IET Conf. Publ.*, vol. 2012, no. 592 CP, 2012.
[8] M. N. F. Ibrahim, A. S. Abdel-Khalik, E. M. Rashad, and P. Sergeant, "An Improved Torque Density Synchronous Reluctance Machine With a Combined Star-Delta Winding Layout," *IEEE Trans. Energy Convers.*, vol. 33, no. 3, pp. 1015–1024, Sep. 2018.
[9] M. Villan, M. Tursini, M. Popescu, G. Fabri, A. Credo, and L. Di Leonardo, "Experimental comparison between induction and synchronous reluctance motor-drives," in *Proceedings - 2018 23rd International Conference on Electrical Machines, ICEM 2018*, Oct. 2018, pp. 1188–1194.
[10] J. Pyrhönen, T. Jokinen, and V. Hrabovcová, *Design of Rotating Electrical Machines*. John Wiley and Sons, 2008.
[11] T. A. Lipo, *Introduction to AC Machine Design*. 2017.
[12] I. Boldea and L. Tutelea, *Electric Machines. Steady State, Transients and Design with MATLAB*. CRC Press, 2010.
[13] A. Vagati, A. Canova, M. Chiampi, M. Pastorelli, and M. Repetto, "Design refinement of synchronous reluctance motors through finite-element analysis," *IEEE Trans. Ind. Appl.*, vol. 36, no. 4, pp. 1094–1102, Jul. 2000.
[14] Z. Wei, "Finite element computation of synchronous reluctance motor," in *ICMTCE2011 - Proceedings 2011 IEEE International Conference on Microwave Technology and Computational Electromagnetics*, 2011, pp. 391–394.
[15] C. Lee and I. G. Jang, "Topology optimization of multiple-barrier synchronous reluctance motors with initial random hollow circles," *Struct. Multidiscip. Optim.*, vol. 64, no. 4, pp. 2213–2224, Oct. 2021.
[16] G. Bacco and N. Bianchi, "Design Criteria of Flux-Barriers in Synchronous Reluctance Machines," *IEEE Trans. Ind. Appl.*, vol. 55, no. 3, pp. 2490–2498, May 2019.
[17] M. Degano, M. Di Nardo, M. Galea, C. Gerada, and D. Gerada, "Global design optimization strategy of a synchronous reluctance machine for light electric vehicles," *IET Conf. Publ.*, vol. 2016, no. CP684, 2016.
[18] N. Bernard, R. Missoum, L. Dang, N. Bekka, H. Ben Ahmed, and M. E. H. Zaim, "Design Methodology for High-Speed Permanent Magnet Synchronous Machines," *IEEE Trans. Energy Convers.*, vol. 31, no. 2, pp. 477–485, Jun. 2016.
[19] H. J. Kim, J. S. Jeong, M. H. Yoon, J. W. Moon, and J. P. Hong, "Simple Size Determination of Permanent-Magnet Synchronous Machines," *IEEE Trans. Ind. Electron.*, vol. 64, no. 10, pp. 7972–7983, Oct. 2017.
[20] S. Cai, J. Shen, H. Hao, and M. Jin, "Design methods of transversally laminated synchronous reluctance machines," *CES Trans. Electr. Mach. Syst.*, vol. 1, no. 2, pp. 164–173, Jul. 2020.
[21] C. Yang, H. Lin, J. Guo, and Z. Q. Zhu, "Design and analysis of a novel hybrid excitation synchronous machine with asymmetrically stagger permanent magnet," in *IEEE Transactions on Magnetics*, Nov. 2008, vol. 44, no. 11 PART 2, pp. 4353–4356.

VII. BIOGRAPHIES

Muhammad Usman Naseer was born in 1990 in Pakistan. He received his B.Sc. in Electrical Engineering from Islamia University of Bahawalpur, Pakistan in 2011 and MS degree from University of Engineering and Technology (UET), Lahore, Pakistan in 2017. He is currently a doctoral student at Tallinn University of Technology. His area of research includes electrical machines modeling, design and optimization.

Ants Kallaste was born in Pärnu, Estonia in 1980 and received his BSc, MSc and PhD degrees in electrical engineering from Tallinn University of Technology, Estonia, in 2004, 2006 and 2013 respectively. He is currently a Professor of Electrical Machines in Tallinn University of Technology, Department of Electrical Power Engineering and Mechatronics. In addition, he is holding the position of Head of Chair of Electrical Machines Research Group. He has spent several years in private engineering companies and visited numerous other research institutions. Amongst other research activities, Ants Kallaste is involved with expertise and consultations of private companies in the field of electrical machines, drives, and their diagnostics.

Bilal Asad was born in 1986 in Pakistan. He received his BSc in Electronics Engineering from The Islamia University of Bahawalpur and MSc in Electrical Engineering from University of Engineering and Technology (UET) Lahore, Pakistan in 2007 and 2011 respectively. Currently he is a PhD student in the Department of Electrical Power Engineering and Mechatronics, Tallinn University of Technology, Estonia and Department of Electrical Engineering and Automation, Aalto University, Espoo Finland. His area of interest includes design, modeling and fault diagnostics of electrical machines

Toomas Vaimann received his BSc, MSc and PhD degrees in electrical engineering from Tallinn University of Technology, Estonia, in 2007, 2009 and 2014 respectively. He is currently a senior researcher in Tallinn University of Technology, Department of Electrical Power Engineering and Mechatronics. He has been working in several companies as an electrical engineer. He is the member of IEEE, Estonian Society of Moritz Hermann Jacobi and Estonian Society for Electrical Power Engineering. His main research interest is the diagnostics of electrical machines.

Anton Rassõlkin was born in Tallinn, Estonia, in 1985. He received the BSc, MSc, and PhD degrees in electric drives and power electronics from Tallinn University of Technology (Estonia) in 2008, 2010, and 2014, respectively. In 2010 he received a Dipl.-Ing. degree in automatic from the University of Applied Science Giessen-Friedberg (Germany). He has been working in several companies as an electrical engineer and universities as a lecturer. Presently, he holds the position of professor in Mechatronics at the Department of Electrical Power Engineering and Mechatronics, School of Engineering, Tallinn University of Technology (TalTech). Moreover, he serves as a visiting professor at the Faculty of Control Systems and Robotics at ITMO University (St. Petersburg, Russia) and a visiting professor at the Faculty of Electrical Engineering Department of Power Electronics, Electrical Drives and Robotics at Silesian University of Technology (Gliwice, Poland). The main research interests are mechatronics and electrical drives, particularly for electric transportation, as well as autonomous vehicles. He is a Senior Member of IEEE and the Estonian Society of Moritz Hermann Jacobi.

Authorized licensed use limited to: Tallinn University of Technology. Downloaded on April 09,2025 at 14:06:58 UTC from IEEE Xplore. Restrictions apply.

Publication VI

M. U. Naseer, A. Kallaste, B. Asad, T. Vaimann, and A. Rassolkin, “Analytical modelling of synchronous reluctance motor including non-linear magnetic condition,” IET Electr Power Appl, Jan. 2022, doi: 10.1049/ELP2.12172.

Check for updates

Received: 8 November 2021 | Revised: 14 December 2021 | Accepted: 1 January 2022

IET Electric Power Applications

DOI: 10.1049/elp2.12172

The Institution of Engineering and Technology WILEY

ORIGINAL RESEARCH

Analytical modelling of synchronous reluctance motor including non-linear magnetic condition

Muhammad Usman Naseer | **Ants Kallaste** | **Bilal Asad** | **Toomas Vaimann** | **Anton Rassõlkin**

Department of Electrical Power Engineering and Mechatronics, Tallinn University of Technology, Tallinn, Estonia

Correspondence

Muhammad Usman Naseer, Department of Electrical Power Engineering and Mechatronics, Tallinn University of Technology, Akadeemia tee 5A/29, 19086 Tallinn, Estonia.
Email: mnasee@taltech.ee

Funding information

Eesti Teadusagentuur, Grant/Award Number: PSG-137

Abstract

This paper presents an analytical modelling technique based on modified winding function and co-energy analysis, for characterisation of synchronous reluctance machines, in conjunction with a hybrid algorithm for mapping of the machine's operating point on BH curve and the corresponding performance parameters in non-linear magnetic condition. The model successfully provides the mean torque and the torque profiles of a synchronous reluctance motor as a function of input current and load-angle in the magnetic linear and non-linear conditions. The obtained results of this proposed model are compared with finite-element-analysis (FEA) based commercial design software Simcentre-MAGNET. The comparison proves this model's capability to estimate the machine's performance parameters with considerable accuracy from an already established design analysis technique, FEA. The proposed modelling technique requires only a fraction of simulation runtime when compared to other design analysis techniques. Considering the accuracy of this modelling technique and the least requirement of computation resources and simulation time, this model can be used as an initial iterative-design tool for mass personalised, additively manufactured electrical machines where rapidness of the iterative design analysis tool is of paramount importance.

KEYWORDS

AC motors, mathematical analysis, non-linear estimation, synchronous machines, synchronous motors

1 | INTRODUCTION

The synchronous reluctance motor (SynRM) utilises variation in the reluctance of the magnetic path for electromagnetic energy conversion. Being a singly excited machine with high torque density [1, 2], high-speed applicability [3, 4] fault tolerance [5, 6], and fast response features [7, 8], makes it a promising alternative for induction as well as permanent magnet machines [9, 10], specifically for small to medium scale traction applications [11–13]. The relatively less involvement of multi-material in its fabrication and the absence of rotor windings or rotor cage results in lack of copper losses, improving its efficiency and making the fabrication process simple and economical compared with other kinds of machines [14].

Conventional manufacturing processes impose limitations on the realization of the geometrical structures, which are otherwise necessary for optimised performance parameters. Additive manufacturing (AM), having the capability to do so, has recently attracted the attention of various researchers and industries towards its employment in electrical machine fabrication [15, 16]. With AM, optimised, enhanced and mass personalised performance parameters can be obtained. To adequately support the process, specific design analysis tools giving a rapid and accurate estimation of machine performance parameters are needed to be developed for the initial iterative design procedure.

The performance evaluation of any electrical machine at the earliest phase of its design process is of paramount importance to avoid any intolerable outcomes resulting in

This is an open access article under the terms of the Creative Commons Attribution License, which permits use, distribution and reproduction in any medium, provided the original work is properly cited.

© 2022 The Authors. *IET Electric Power Applications* published by John Wiley & Sons Ltd on behalf of The Institution of Engineering and Technology.

reiteration of the whole process at an advanced stage. This evaluation can be done via measurements [17], analytical [18, 19] or numerical modelling techniques [20–22]. Performing practical measurements is time and resource-consuming for the initial design process and therefore not feasible. The finite-element-analysis (FEA)-based analysis gives accurate results, but it is also time-consuming, with simulation time rising exponentially when used iteratively for design variation analysis to optimise performance parameters.

Several methodologies have been proposed in the literature to define and optimise the rotor's initial geometrical parameters, such as number, location, and width of flux barriers. For example, the strategy often used, as illustrated in [23–26], selecting the number of rotor flux barriers as a function of stator slots and number of pole pairs yields the torque ripple within an acceptable limit. However, such guidelines are only generalized and do not provide insight towards the detailed output characteristics such as the torque profile of the machine. Numerical analysis techniques are essentially required at some later stage of the design process for improved estimation of the machine's operating characteristics [27]. But a rapid and highly accurate analytical model provides a better starting point for the optimization problem, resulting in less computational power and time required.

In [28], conformal mapping has been utilised to predict air-gap flux density and average torque of the machine with high accuracy. Still, it lacks in accurately estimating the torque profile of the machine. Winding function analysis (WFA) is relatively simple to implement in determining an electrical machine's magnetising inductances and performance parameters for steady-state and transient analyses [29]. However, while WFA-based papers mainly consider the air-gap throughout the machine periphery, a constant or approximated by cosine series functions [30], the modified winding function analysis (MWFA) considers the slot openings in the stator and the physical rotor geometry [31]. This essentially makes the air-gap a function of stator and rotor position. Various authors have implemented this approach on electrical machines [18, 32, 33], and the comparison of the winding function approach with FEA [34, 35] shows considerable agreement between results with the added advantage of simplicity and rapidness in the calculation procedure. As illustrated in the works mentioned earlier, the winding function approach is generally used for determining the average parameters of a machine with considerable accuracy in the linear magnetic condition. When considering the non-linear magnetic permeability of the material, deviation from practical measurements and FEA results occurs [18]. This paper proposes a strategy to include the effect of magnetic non-linearity of the material towards the machine's performance parameters, with the improved estimation of torque profile through stepped mapping of air-gap function. In addition, the effect of multilayer winding on resultant pole formation in the machine is also described.

In this paper, an analytical model for the characterisation of a transversally laminated anisotropic (TLA) rotor is developed and implemented on a previously designed SynRM. The machine inductances and electromagnetic torque (T_e) have been estimated for various input currents up to the rated value. Further, magnetic non-linearity has been included in estimating electromagnetic torque. The results of this analytical model have been compared with FEA for validation purposes. The results also show considerable agreement for various input currents and magnetic materials. This model can also be used for design variation analysis, as showcased in section-4.

In summary, the main contribution that this paper offers are:

- Simplistic and rapid procedure to obtain the machine's performance parameters through analytical modelling.
- Description of the analytical approach to include the effect of the layered stator winding on resultant pole formation.
- Precise estimation of torque profile from detailed mapping of air-gap and the rotor flux-barrier transitions.
- Defining the machine's operating zone on the BH-curve (curve characteristic of the magnetic properties) of the core material.
- Inclusion of the effect caused by the non-linear magnetic permeability of the core material on the performance parameters of the machine.
- The enormous reduction in simulation time (15 s) compared with the commercial FEA-based software (approximately 100 h) for similar value of temporal resolution for calculations.

The paper is organised such that Section 2 describes the modelling procedure starting from inductance to the electromagnetic torque calculation. Section-3 presents the hybrid algorithm to determine the machine's operating zone on the BH curve. Section-4 presents the results of the modelling procedure and their validation by comparison from FEA-based results. The proposed model's ability to reflect the design variation towards the performance parameters is also presented briefly in section-4. The conclusions are provided in section-5.

2 | ANALYTICAL MODELING PROCEDURE

The analytical model presented in this paper can be used for iterative design analysis of TLA SynRMs, to obtain the preliminary design parameters. These iterations can serve as a predesign tool for FEA, minimising the time and resources required for the overall design procedure. The proposed modelling and analysis procedure, MWFA, presented in this paper has previously been used for characterisation, fault and harmonic analysis of different electrical machines [32, 33, 36, 37]. However, in addition to the inclusion of the actual air-gap function, this model incorporates the non-linearity in magnetic properties of the material to precisely predict the output torque characteristics of the machine.

17518679, 2022, 4, Downloaded from https://ietresearch.onlinelibrary.wiley.com/doi/10.1049/elp2.12172 by Tallin Technical University, Wiley Online Library on [09/04/2025]. See the Terms and Conditions (https://onlinelibrary.wiley.com/terms-and-conditions) on Wiley Online Library for rules of use; OA articles are governed by the applicable Creative Commons License

This section presents the approach to calculate the machine's winding function, air-gap function, inductances, and electromagnetic torque. The approach is implemented on a predesigned SynRM [38], the main design parameters of which are presented in Figure 1 and Table 1.

The main performance parameter, that is, electromagnetic torque for SynRM with a TLA-rotor, is calculated using the co-energy analysis at different angular positions of the rotor and the respective input current. In an electromagnetic system, co-energy and torque are the functions of two independent variables, that is, inductance (L) and current (I), whereas L is the function of rotor position θ. The electromagnetic torque is given by

$$T_e = \frac{p}{2}[I]^T \left[\frac{\partial}{\partial\theta}[L(\theta)]\right][I] \tag{1}$$

where $[I]$ is the input current matrix, p is the number of pole pairs, and $\partial L(\theta)/\partial\theta$ is the inductance matrix derivative at the respective rotor angular position θ. The load angle δ is introduced towards the input current in the form of following equations:

$$I = \begin{bmatrix} I_{pk}\,\mathrm{Sin}(\omega t + \delta) \\ I_{pk}\,\mathrm{Sin}\left(\omega t - \frac{2\pi}{3} + \delta\right) \\ I_{pk}\,\mathrm{Sin}\left(\omega t + \frac{2\pi}{3} + \delta\right) \end{bmatrix} \tag{2}$$

This proposed modelling technique comprises the execution of two subsections in sequential order. First, the inductances at each rotor position of 360° mechanical rotation are calculated and stored in the offline section. Subsequently, electromagnetic torque is calculated in the online portion for the desired input current and loading angle, δ. The detailed steps for the modelling procedure are described in the following subsections.

2.1 | Inductance calculation

Through the modified winding function approach, the self and mutual inductances can be calculated in the following manner [39].

$$L_{xy}(\theta) = \mu_o r l \int_0^{2\pi} P(\theta,\beta).N_x(\theta,\beta).n_y(\theta,\beta).d\theta \tag{3}$$

For simplification of the calculation procedure, the integration in this equation can be replaced with mean value function [32].

$$L_{xy}(\theta) = 2\pi r \mu_o l \langle P(\theta,\beta).N_x(\theta,\beta).n_y(\theta,\beta)\rangle \tag{4}$$

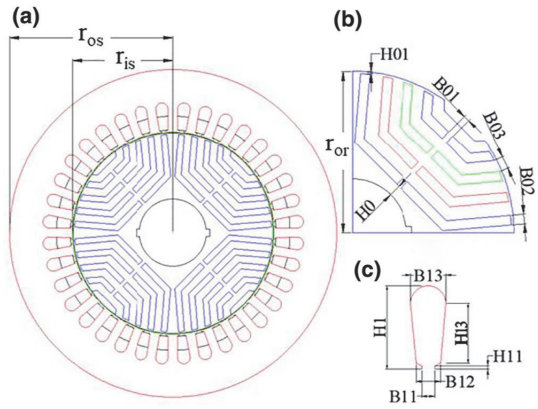


FIGURE 1 Machine geometry: (a) 2D-layout of stator and rotor, (b) rotor flux-barrier dimensions, (c) stator slot dimensions

TABLE 1 Machine parameters

Parameters	Value
Rated power	13426 VA
Rated current	20.3 A
Current angle for MTPA	67.5° elec.
Stator inner diameter	135.95 mm
Rotor outer diameter	135 mm
Air-gap length	0.95 mm
Stack length	200 mm
Number of poles	04
Number of stator slots	36
Core material	M400-50A
Number of winding turns per slot	23
Number of winding layers	02
H0	5 mm
H01	1 mm
H1	20 mm
H11	0.85 mm
H13	14.3 mm
B01	2.5 mm
B02	4 mm
B03	5 mm
B11	3 mm
B12	5.85 mm
B13	8.5 mm

Abbreviation: MTPA, maximum torque per ampere.

where r, $P(\theta,\beta)$, $N_x(\theta,\beta)$, $n_y(\theta,\beta)$ are the rotor's outer radius, air-gap permeance function and stator winding and turn functions, respectively. All of these are the functions of stator

17518679, 2022, 4, Downloaded from https://ietresearch.onlinelibrary.wiley.com/doi/10.1049/elp2.12172 by Tallin Technical University, Wiley Online Library on [09/04/2025]. See the Terms and Conditions (https://onlinelibrary.wiley.com/terms-and-conditions) on Wiley Online Library for rules of use; OA articles are governed by the applicable Creative Commons License

and rotor relative position, with β being the stator angle from a fixed reference point and θ is the rotor's relative position in stator frame of reference.

2.1.1 | Turn function and winding function

The winding function, $N(\theta)$, for the stator winding is defined by

$$N_x(\theta) = \left(n_x(\theta) - \frac{\langle P n_x \rangle}{\langle P \rangle}\right) \tag{5}$$

where N_x, n_x *and* $\langle P \rangle$ are the winding function, turn function and mean air-gap permeance. The machine under consideration has a double layer winding. The per-layer turn function for the phase-A winding is shown in Figure 2a. For each layer, a stator slot houses 23 numbers of winding turns. In order to get a better sinusoidal flux distribution, the winding layers are shifted relative to each other. The shift of one layer relative to the other yields a shift in magnetic axis of the resultant pole formation. This shift in the magnetic axis of stator poles can be calculated by Equations (6) and (7)

$$\theta_S = \left(\frac{\theta_m}{N_s}\right) N_l . N_{ss} \tag{6}$$

$$\theta_m = \frac{\theta_e}{p} \tag{7}$$

where θ_S, θ_m, N_s, N_l and N_{SS} are the amount of shift in magnetic axis, number of degrees for one complete rotation, number of stator slots, number of winding layers and the relative shift among the two layers (in terms of stator slots). The shift in magnetic axis can be simulated virtually by adding the individual winding functions of the layers and introducing a phase shift equivalent to θ_S in the machine's total winding function. The direction of phase shift is governed by the direction of overlap between the windings.

The resultant per-phase winding function of the machine under consideration is shown in Figure 2b. For a three-phase machine, the turn function and corresponding winding function for each phase are similar in shape but are displaced 120° apart. The net winding function of all phases is shown in Figure 3.

2.1.2 | Air-gap permeance function

The air-gap of the machine is divided into two parts, that is, one part is associated with the stator and the other associated with the rotor. The average air-gap thickness is given by

$$g_{\text{avg}} = \frac{r_{is} - r_{or}}{2} \tag{8}$$

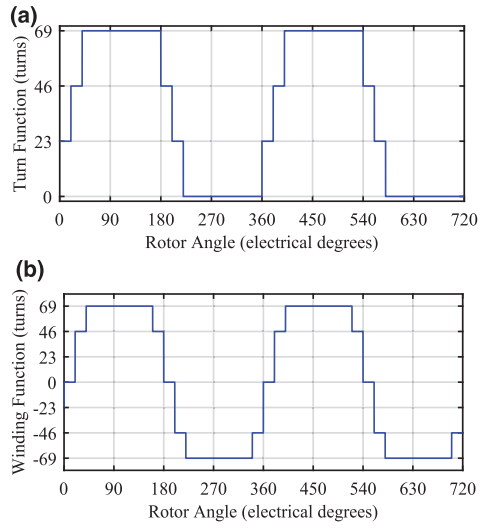


FIGURE 2 Phase-A: (a) per-layer turn function, (b) net winding function

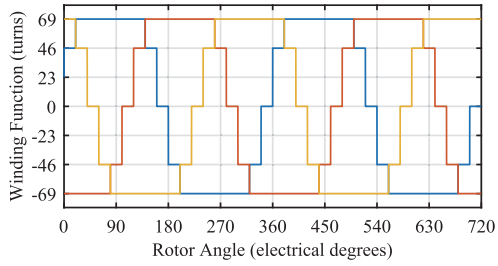


FIGURE 3 Winding function of the three-phase stator

where r_{is} and r_{or} are the inner radius of the stator and outer radius of the rotor, respectively. The air-gaps associated with stator and rotor are measured from a reference line marked at the centre of the air-gap that is, g_{avg}. The air-gap associated with the stator $g_s(\theta)$, incorporating the stator slot opening, is defined by stator geometry and is a function of rotor mechanical angle (θ) given by

$$g_s(\theta) = \begin{cases} g_{\text{avg}} & B_{11} \le \theta \le B_{11} + B_{tt} \\ g_{\text{avg}} + H_{11} & 0 \le \theta \le B_{11} \end{cases} \tag{9}$$

where H_{11}, B_{11} and B_{tt} are the length of the empty portion from the stator slot, the width of stator slot opening and stator tooth-tip, respectively. The machine's geometry is illustrated in Figure 1.

The rotor of the machine under consideration is smooth-surfaced, as shown in Figure 1a. Since the rotor has a uniform surface and no winding, neither would it affect the air gap physically nor have any specific winding function. The air-gap

17518679, 2022, 4, Downloaded from https://ietresearch.onlinelibrary.wiley.com/doi/10.1049/elp2.12172 by Tallin Technical University, Wiley Online Library on [09/04/2025]. See the Terms and Conditions (https://onlinelibrary.wiley.com/terms-and-conditions) on Wiley Online Library for rules of use; OA articles are governed by the applicable Creative Commons License

associated with the rotor $g_r(\beta)$ has a uniform thickness of g_{avg} throughout the rotor perimeter.

The air-gap permeance function is calculated by

$$P(\theta,\beta) = \frac{1}{g_s(\theta) + g_r(\theta,\beta)} \tag{10}$$

The stator and rotor associated air-gaps as a function of rotor angle θ are illustrated in Figure 4.

2.1.3 | Rotor flux-barrier translation

The principle of SynRM operation relies upon the insertion of flux barriers in the rotor body to create a difference of reluctance in the d-axis and q-axis flux paths. The reluctance of the magnetic path is directly proportional to path length and inversely proportional to the area. Since the insertion of flux barriers in the rotor body affects the availability of area for flux transmission and the flux barriers have low permeability than the rotor body, the magnetic path reluctance increases. This increased path reluctance can subsequently be translated towards the rotor associated air-gap in the form of increased air gap length.

The rotor is divided into individual sections corresponding to each flux barrier. The ratio of surface areas for each section, with and without flux barriers, gives the equivalent increase in the associated air-gap length. Equation (11) presented in the investigation [18] mainly governs this translation of flux barriers.

$$l_{fb} = \left[\left(\frac{A_1}{A_2}\right) - 1\right] l_{ag} \tag{11}$$

where l_{fb}, l_{ag}, A_1 and A_2 are the equivalent air-gap length for flux barrier, the actual air-gap length, area of the subsection without the flux barrier and the area of subsection with the flux barrier. In [18], the transition between flux barriers is represented linearly through a straight line. A slight modification to this equation and the detailed/step-wise mapping of transition between flux barriers yield a better mapping of the torque profile. The proposed modification in the equation mentioned above is that the rotor bridges, as indicated in Figure 5, are also incorporated.

Compared to Equation (11), the effective surface area with the flux-barrier increases by a factor proportional to the width of the bridge between flux barriers. In terms of rotor geometry presented in Figure 1, this bridge width is given as B01. The updated equation is

$$l_{fb} = \left[\left(\frac{A_1}{A_2 + kA_{RB}}\right) - 1\right] l_{ag} \tag{12}$$

where A_{RB} is the equivalent surface area of the bridge, and since this surface area bridges two individual flux paths, the value of k, in this case, is chosen to be 1/2. The air-gap function for rotor flux-barrier translation by the earlier and proposed approach for one rotor pole is presented in Figure 6a,b.

A comparison between the torque profiles obtained from the earlier approach, modified approach and FEA based

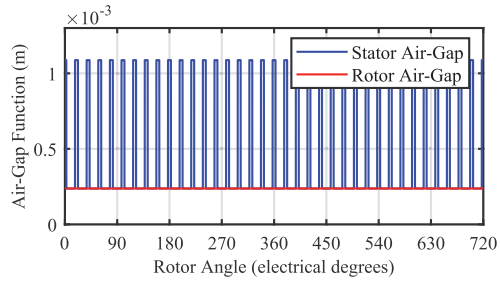


FIGURE 4 Stator and rotor associated air-gap function

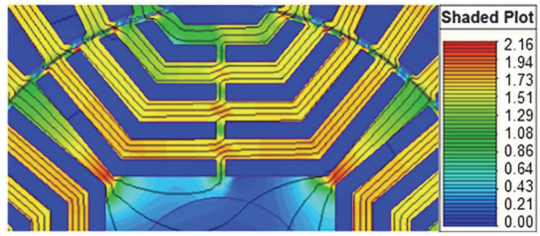


FIGURE 5 Flux path in rotor bridges

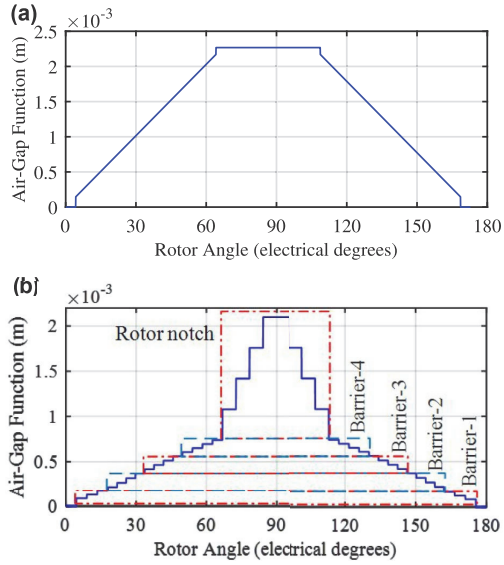


FIGURE 6 Rotor flux-barrier translation towards air-gap function (a) earlier approach Equation (11) with a linear transition between flux-barriers, (b) modified approach Equation (12) with a stepped transition between flux barriers

17518679, 2022, 4, Downloaded from https://ietresearch.onlinelibrary.wiley.com/doi/10.1049/elp2.12172 by Tallin Technical University, Wiley Online Library on [09/04/2025]. See the Terms and Conditions (https://onlinelibrary.wiley.com/terms-and-conditions) on Wiley Online Library for rules of use; OA articles are governed by the applicable Creative Commons License

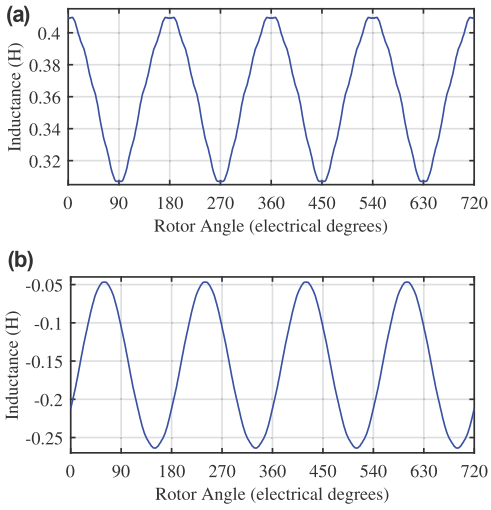


FIGURE 7 (a) Self-inductance of one phase, (b) mutual inductance between two phases

commercial software SIMCENTRE-MAGNET for the same operational parameters is provided in Figure 9a,b for illustration purposes.

The self and mutual inductances for stator phases are calculated by Equation (4). For illustration purposes, the self-inductance of phase A and mutual inductance between phase A and B are presented in Figure 7a,b. The self and mutual inductance profiles for other phases are similar to those illustrated in Figure 7 but displaced 120° apart.

2.2 | Torque calculation

With the inductances calculated for each rotor angle and stored offline, the electromagnetic torque is calculated using the co-energy method Equation (1) for various input current levels. The electromagnetic torque waveform for the machine under consideration, for peak input currents of 10 and 18 A at $\delta = 10°$ mechanical, is presented in Figure 8. Validation of these results by comparison with FEA will be presented in section-4 after including the effect of the material's non-linear magnetic properties.

3 | SATURATION DUE TO NON-LINEAR MAGNETIC PERMEABILITY

The current state of the art in MWFA-based characterisation of SynRM does not include the effect of non-linearity in the magnetic permeability of the machine's core material. This is because machine-geometry makes it a complex numerical problem to determine the machine's operating point on the

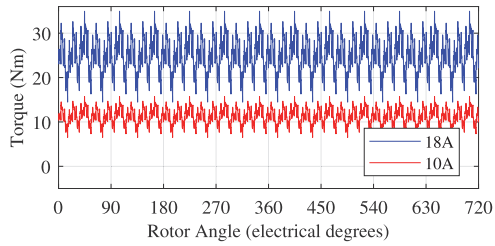


FIGURE 8 Electromagnetic torque waveform for input currents of 10 and 18 A

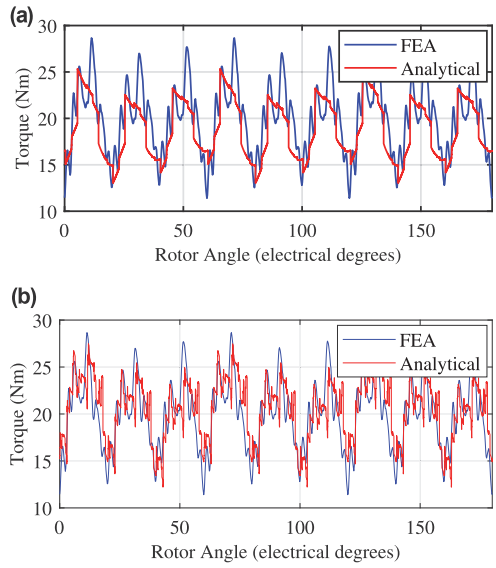


FIGURE 9 Torque profile for the same operational parameters (a) earlier approach Equation (11) with a linear transition between flux-barriers, (b) modified approach Equation (12) with a stepped transition between flux barriers

BH curve for any input current value. This proposed model presents a relatively easy, hybrid procedure to handle this.

In the original derivation of flux linkages and inductance calculation [39], the magnetomotive force (MMF) drop in the core is neglected. The material permeability is considered to be infinite, giving a linear air-gap MMF distribution corresponding to the input current that is,

$$\mathcal{F}_x(\theta) = N_x(\theta).i_x \tag{13}$$

The flux linkage λ between two phases of winding is given by

$$\lambda_{xy} = \frac{\mu_o r l}{g} \int_0^{2\pi} \mathcal{F}_x(\theta) n_y(\theta) d\theta \tag{14}$$

17518679, 2022, 4, Downloaded from https://ietresearch.onlinelibrary.wiley.com/doi/10.1049/elp2.12172 by Tallin Technical University, Wiley Online Library on [09/04/2025]. See the Terms and Conditions (https://onlinelibrary.wiley.com/terms-and-conditions) on Wiley Online Library for rules of use; OA articles are governed by the applicable Creative Commons License

$$L_{xy} = \frac{\lambda_{xy}}{i_x} = \frac{\mu_o r l}{g} \int_0^{2\pi} N_x(\theta) n_y(\theta) d\theta \quad (15)$$

where Equation (15) provides the basis for Equation (3) and lays the foundation for the MWFA approach.

Owing to the non-linear nature of material permeability, the air-gap MMF distribution and the resultant winding inductances become a non-linear function of the input current. This non-linearity of phase inductances, with respect to the input current, is introduced in the form of a permeability factor k_p in Equation (13–15). The value of k_p varies from 0 to 1, in accordance with material permeability, essentially reducing the air-gap MMF and hence the inductance. The value of k_p varies non-linearly according to relative permeability, depending upon the machine's operating point.

$$\mathcal{F}_x(\Phi) = k_p . N_x(\Phi) . I_x \quad (16)$$

$$L_{xy} = \frac{\lambda_{xy}}{i_x} = k_p . \frac{\mu_o r l}{g} \int_0^{2\pi} N_x(\theta) n_y(\theta) d\theta \quad (17)$$

$$T_e = k_p . \frac{p}{2} [I]^T \left[\frac{\partial}{\partial \theta} [L(\theta)] \right] [I] \quad (18)$$

$$k_p = \sqrt{2} \mu_r 10^{-4} \quad (19)$$

The machine being analysed in this paper is made of M400-50A. The relative permeability for this material rises from zero to a maximum of 64,868.9. Putting this in the empirical relation of Equation (19) gives $0 < \{k_p = \sqrt{2}\,(6468.9)\,10^{-4} = 0.91\} < 1$, as also illustrated in Figure 11 of the next section.

3.1 | Determination of the Machine's operating point

The derivative of the material's BH curve gives permeability (μ) and, when plotted versus H (magnetic field intensity), provides the permeability curve. The BH and permeability curves for M400-50A material are presented in Figure 10a,b, respectively. Determination of the machine's operating point relies on estimating the magnetic field intensity (H) produced in the air-gap by the respective input current. The generic formulation to calculate H is given by

$$H = \frac{N.I}{l} \quad (20)$$

where N, I and l are the number of turns in a coil, input current of the coil and mean length of the magnetic path. In the case of an electrical machine, for a fixed given geometry and circuit parameters, other factors in Equation (20) remain constant, and H is proportional to the input current that is,

$$H \propto I \quad (21)$$

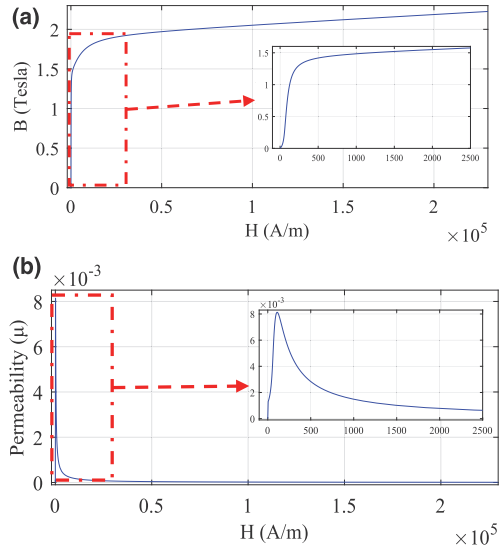


FIGURE 10 (a) BH curve, (b) permeability curve for M400-50A

To estimate the machine's operating point on the BH curve, a sweep for different values of Δ, defined by Equation (22), is made on the BH or permeability curve.

$$H = \Delta . I \quad (22)$$

where Δ controls the proportionality of H relative to the input current I, on the BH curve, as illustrated in Figure 11. The corresponding permeability value is used in Equation (19) to determine the permeability factor. The value of Δ is calculated iteratively through a hybrid algorithm presented in Figure 12. The reference or benchmark value of torque is obtained from FEA for a half cycle of the rated input current. The value of ε decides the error limit or accuracy of mapping.

The mapping procedure progresses such that for a specified value of the input current, the benchmark electromagnetic torque is calculated from FEA for almost a half cycle of the input current. For the same value of the input current, changing the value of Δ (in an iterative manner) changes the value of k_p and in turn, the value of electromagnetic torque is calculated by the analytical model. This analytical value is compared with the benchmark value against an error limit of ε. The value of ε is chosen according to the required accuracy of mapping.

Figure 11a–d shows the iterative procedure, B versus H for various values of Δ for the same input current range of 0–25 A, as an illustration. Once the required precision of mapping is achieved for a specific input current value, the respective value of Δ is fixed, and now, the operating zone of the machine on the BH curve can easily be estimated. For the complete input current range of the machine, H is calculated from Equation (22) and the corresponding values of μ_r are stored in 3D-lookup tables. In the online portion of the simulation, for each value

17518679, 2022, 4, Downloaded from https://ietresearch.onlinelibrary.wiley.com/doi/10.1049/elp2.12172 by Tallin Technical University, Wiley Online Library on [09/04/2025]. See the Terms and Conditions (https://onlinelibrary.wiley.com/terms-and-conditions) on Wiley Online Library for rules of use; OA articles are governed by the applicable Creative Commons License

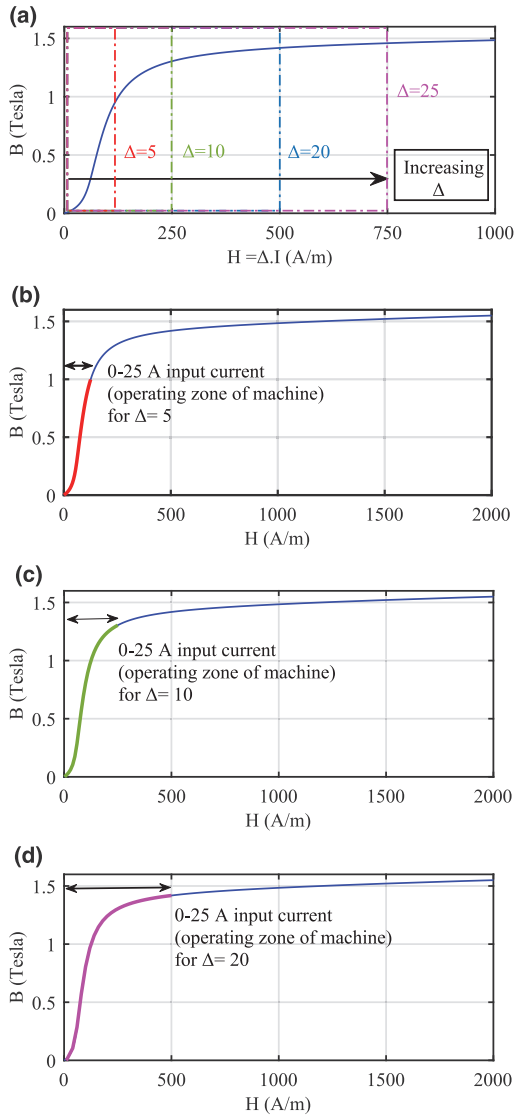


FIGURE 11 (a) BH curve mapping against input current for (b) Δ = 5, (c) Δ = 10, (d) Δ = 20

of the input current, the corresponding μ_r is obtained from the 3D-lookup table, the value of k_p is calculated and the corrected value of torque is calculated from Equation (18).

4 | RESULTS AND VALIDATION OF THE ANALYTICAL MODEL

Upon executing this mapping procedure for the machine under consideration, the optimised value of Δ is found out to be 13.5. The corresponding operating zone on the BH curve, its

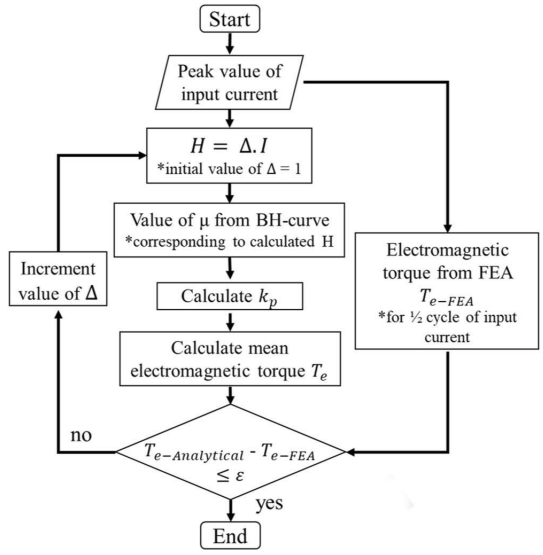


FIGURE 12 Block-diagram of the iterative procedure for determination of the machine's operating point on the BH curve and subsequent calculation of saturation factor k_p as a function of the input current

associated permeability curve and the value of k_p for an input current range of 0–25 A is shown in Figure 13. The 0–25 A input current range, though exceeding the rated current, that is, 20.3 A, is selected to test the model's ability to predict the performance parameters in overload conditions.

Air-gap MMF distribution for input currents of 10 and 15 A_{pk} at the load angle $\delta = 10°$ mechanical (with and without modulation by respective k_p) are presented in Figure 14a,b while the associated torque waveforms compared to the FEA results are shown in Figure 15a,b.

Figure 16 shows the comparison between the mean torque calculated by FEA and the proposed analytical model without including non-linearity in material permeability. For the linear magnetic condition, when plotted against the input current, the mean values of torque show a parabolic behaviour due to the squared value of I in Equation (1). Whereas, after the inclusion of magnetic non-linearity as in Equation (18), the obtained results shown in Figure 17a are within agreeable limits of the FEA results. For the validation purpose of this modelling technique, the comparison of mean torque calculated by this analytical procedure and FEA for different core materials is presented in Figures 17b,c.

4.1 | Validation of the modelling technique through frequency spectrum analysis

The proposed analytical model is a current-fed model which estimates the machine's performance characteristics in steady-state, utilised in the initial design stage. In FEA based

17518679, 2022, 4, Downloaded from https://ietresearch.onlinelibrary.wiley.com/doi/10.1049/elp2.12172 by Tallin Technical University, Wiley Online Library on [09/04/2025]. See the Terms and Conditions (https://onlinelibrary.wiley.com/terms-and-conditions) on Wiley Online Library for rules of use; OA articles are governed by the applicable Creative Commons License

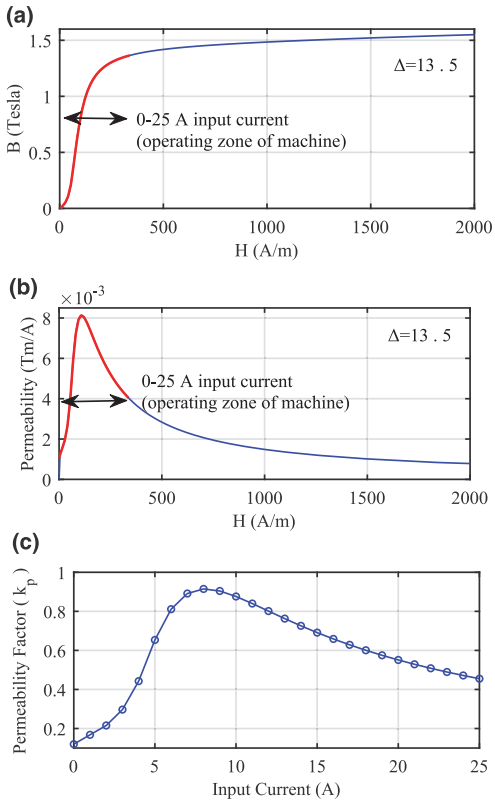


FIGURE 13 Operating zone of the machine under consideration on (a) BH curve, (b) permeability curve, (c) value of K_p versus input current

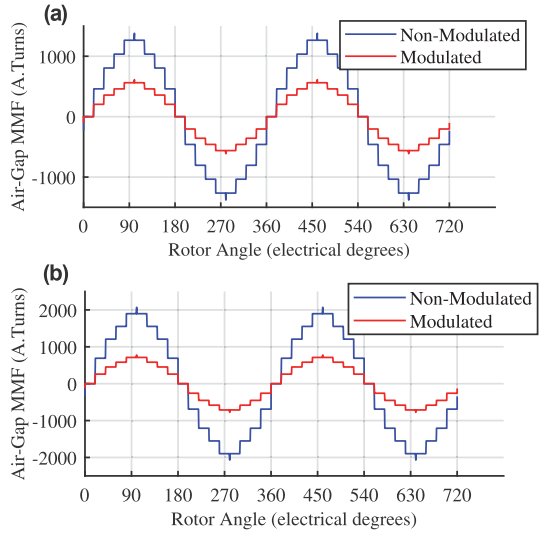


FIGURE 14 Air-gap MMF with and without the inclusion of saturation factor k_p, for input currents of (a) 10 A, (b) 15 A

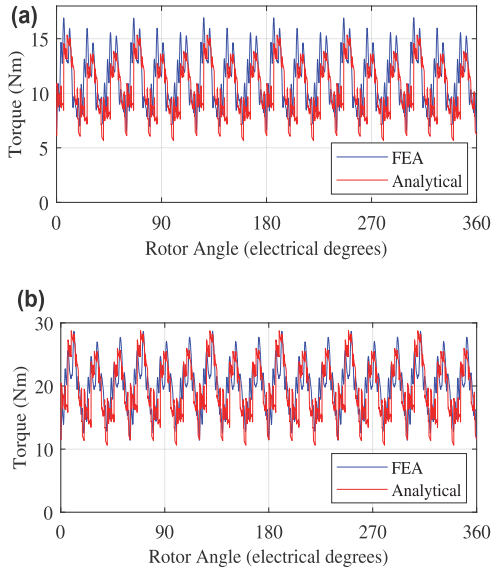


FIGURE 15 Torque waveform comparison with finite-element-analysis results, $\delta = 10°$ mechanical (a) 10 A, (b) 15 A

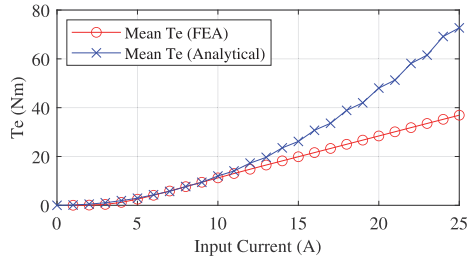


FIGURE 16 Comparison of mean torque calculation by the analytical model without the inclusion of non-linearity in magnetic permeability and finite-element-analysis (FEA)

simulations, it is possible to current-feed the machine to get the steady-state torque profile compared with the analytical model (done in the previous section). Whereas in practical measurements, the machine is in-fact voltage-fed, and the performance characteristics also involve transient characteristics. Frequency spectrum analysis comes in handy to validate the analytical model against the experimental results. A reasonable agreement and presence of significant frequency components in both cases, analytical and practical, validate the modelling technique. The SynRM under test can be fed through the grid or a converter for practical measurements.

For the grid fed SynRM, relatively fewer harmonics will be introduced into the machine's performance characteristics. But, the steady-state operation of the machine would not be possible since no control mechanism is in place. The machine will be subjected majorly to the transient state of operation

17518679, 2022, 4, Downloaded from https://ietresearch.onlinelibrary.wiley.com/doi/10.1049/elp2.12172 by Tallin Technical University, Wiley Online Library on [09/04/2025]. See the Terms and Conditions (https://onlinelibrary.wiley.com/terms-and-conditions) on Wiley Online Library for rules of use; OA articles are governed by the applicable Creative Commons License

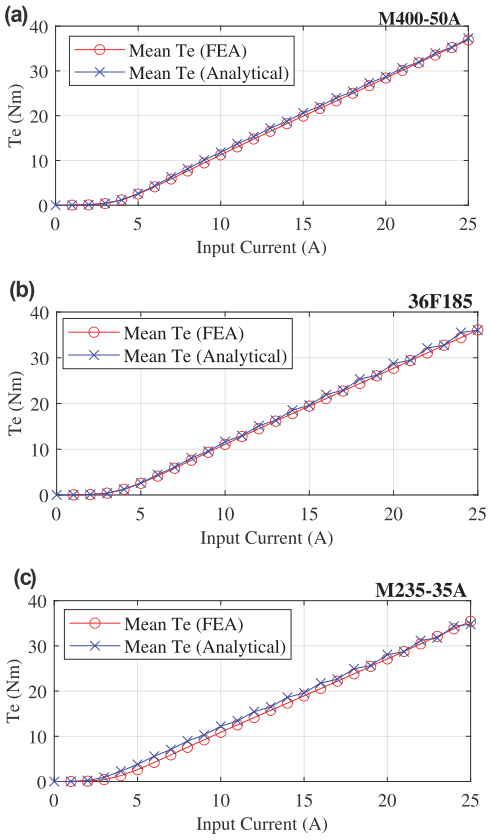


FIGURE 17 Comparison of mean torque calculation by the proposed analytical model (under non-linear magnetic condition) and finite-element-analysis (FEA) for different materials: (a) M400-50A, (b) 36F185, (c) M235-35A

due to speed and torque fluctuations. For the converter-fed SynRM, the control over the machine's torque-speed characteristics would be better, and the machine can be run in a steady state. But in that case, the converter's switching harmonics will be introduced into the machine performance characteristics. For this paper's aimed scope, to avoid the converter fed harmonics, the SynRM under test is fed through the grid, and a frequency spectrum comparison between practical results of the torque profile from grid-fed SynRM and the analytical model is presented for validation purposes.

The SynRM is fed from the grid, coupled through a torque-speed sensor (NCTE S4000-250-1), with an induction motor (IM) acting as a load. The loading IM is run through an industrial inverter (ABB ACS-600) in direct-torque-control (DTC) mode. The same loading motor is initially utilised to bring the SynRM-shaft near synchronous speed before switching the grid supply. Figures 18a,b present the comparison of the frequency spectrum. The harmonics visible in the spectrum are caused by various reasons but are mainly due to the stepped configuration of winding distribution, the stator slot openings and flux barrier transitions in the rotor etc. These harmonics are also indicative of speed and torque ripples. The slight deviation between the frequency spectrum of the analytical model and practical measurements is due to the presence of additional grid and load-side inverter-fed harmonics. that is, Figure 18a presents the comparison of the analytical model with the practical measurement when the load-side inverter is switched off whereas, Figure 18b presents the spectrum comparison when the load-side inverter is switched on. The inverter harmonics get imposed on the toque waveform even at minor load imposition. Another factor responsible for deviation from practical measurements is that the machine is modelled in two dimensions in the proposed modelling scheme. A successive approximation of the third dimension is made to get the overall performance characteristics. As evident from Figure 18a, the main harmonic components from practical measurements are present and in good agreement with the frequency spectrum of the proposed analytical model.

The ultimate goal of this article is to formulate a simple and fast analytical model for the initial design characterisation of SynRM. This analytical model, requiring less computing power and time, can be utilised effectively for the initial design iteration procedure necessary for the AM process. To determine the accuracy and applicability of the proposed model against other design characterising numerical techniques, a comparison of this model with an FEA-based solution is made. The obtained results for different input current levels and load angle δ are presented in Figure 19a,b. The results of this proposed model and FEA are shown for different load angle values in each plot.

Comparing the results of two different methods for each value of the input current shows that the proposed model has an acceptable agreement with the established design characterisation method of FEA. Compared to other analytical analysis techniques, these results show a better mapping of torque profiles with only a slight deviation at the peak points. This deviation can be designated to the presence of localised saturations happening in complex structures of the machine's body, as evident from the FEA-based flux distribution shown in Figure 5. The deviation in torque profile is also partly owed to the low temporal resolution of FEA results as the higher temporal resolution results in an exponential increase of simulation time.

4.2 | Design parameter analysis

This analytical model's ability to reflect the effect of various design parameters on the output performance parameters is shown in this section. This model can handle the machine design's major parameters, such as the number of stator slots, turns per slot, the effect of layered winding, stator-teeth parameters, air-gap length, and rotor geometry. From the rotor perspective, the rotor pole-arc to the pole-pitch ratio (determined from the end-point location of the biggest flux barrier) and the width of flux barriers play an important role in

17518679, 2022, 4, Downloaded from https://ietresearch.onlinelibrary.wiley.com/doi/10.1049/elp2.12172 by Tallin Technical University, Wiley Online Library on [09/04/2025]. See the Terms and Conditions (https://onlinelibrary.wiley.com/terms-and-conditions) on Wiley Online Library for rules of use; OA articles are governed by the applicable Creative Commons License

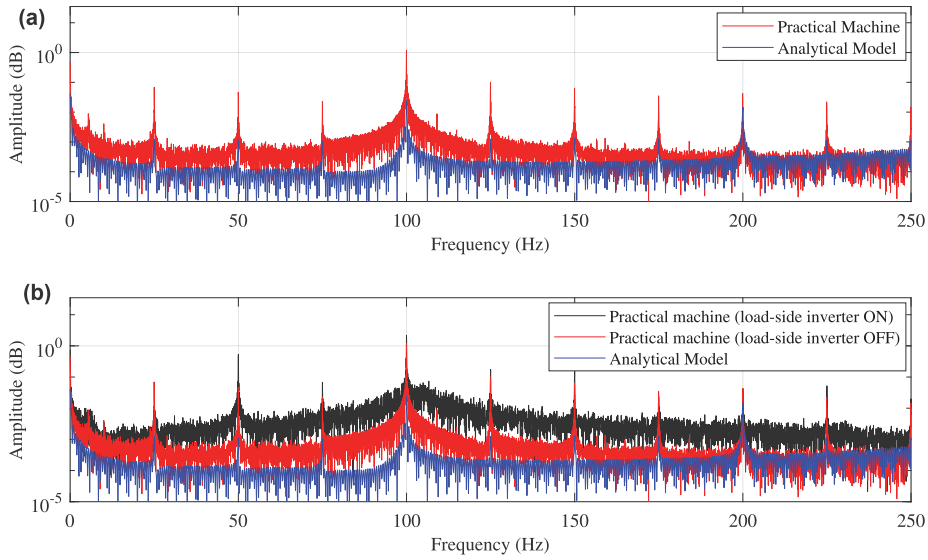


FIGURE 18 Frequency spectrum (0–250 Hz) of the synchronous reluctance motor (SynRM) torque using the proposed analytical model and practical measurement. (a) with inverter controlling the coupled induction motor (IM), turned OFF, (b) with inverter controlling the coupled IM, turned ON

determining the output performance parameters. Figure 20a,b show the air-gap function and associated torque profile for two different values of pole-arc to pole-pitch ratios, with all other parameters remaining constant at input current of 15 A and $\delta = 10°$. The results illustrate the effect of the smallest change in design parameters on the machine performance. Decreasing the pole-arc increased the mean torque value from 20.5 to 22.6 Nm, and the ripple percentage changed from 33.1% to 36.7%.

As the width of flux barriers also affects the available area for *d*-axis flux, for illustration purposes, the flux barrier width increase of 1 mm is made in the design of base SynRM having rotor air-gap function shown in Figure 6. The new air-gap function is shown in Figure 21a, and its associated torque profile at input current of 15 A and $\delta = 10°$ is shown in Figure 21b. With the increase in flux barrier width and consequent reduction in available area for *d*-axis flux, the mean torque output reduced from 20.5 to 19.6 Nm. The ripple percentage also changed from 33.18% to 31.4%.

The model can also be modified to predict the stator parameter variations. Therefore, it is evident that with the ability of this modelling procedure to meet the application requirements by a suitable change in design parameters, it can serve as an initial design tool.

As with the model presented in [18], the measurements made for low currents showed a symmetrical behaviour to the FEA based results and practical measurements. However, the authors reported deviation from symmetrical behaviour at higher input currents, that is, the proximity of rated input current levels. This deviation is mainly owed to the saturation of the ferromagnetic core. The proposed model of this paper addresses this deficiency to a large extent by including the effect of material permeability on the machine performance parameters. The accuracy in obtaining the torque profiles is also greatly enhanced from detailed mapping of stator air-gap and the transition between rotor flux barriers.

The effect of localised saturation should be included in this analytical model to precisely predict the torque profiles. However, for the objective of this paper, the obtained accuracy is reasonable. This proposed model can be utilised for examining the effect of various design parameters such as stator geometry, stator winding parameters, the physical geometry of the rotor and flux barriers on the TLA-rotor SynRM's performance, as shown previously. Hence it is a relatively simple, fast and accurate tool for the initial design parameter iterations. The comparison of simulation runtime for both FEA and Analytical procedures is presented in Table 2.

5 | CONCLUSION

The MWFA based analytical modelling of SynRM was presented in this paper, which utilises the simple electromagnetic coupling equations. By implementing the MWFA approach, instead of considering the constant air-gap or by representing it with cosine function, the air gap function was obtained from detailed mapping of actual rotor and stator geometry. The effect of rotor flux-barrier translation towards the rotor associated air-gap was improved by including the effect of rotor bridges. This, in conjunction with the stepped transition between individual flux-barriers, produced a better mapping of torque profile when compared to FEA results

17518679, 2022, 4, Downloaded from https://ietresearch.onlinelibrary.wiley.com/doi/10.1049/elp2.12172 by Tallin Technical University, Wiley Online Library on [09/04/2025]. See the Terms and Conditions (https://onlinelibrary.wiley.com/terms-and-conditions) on Wiley Online Library for rules of use; OA articles are governed by the applicable Creative Commons License

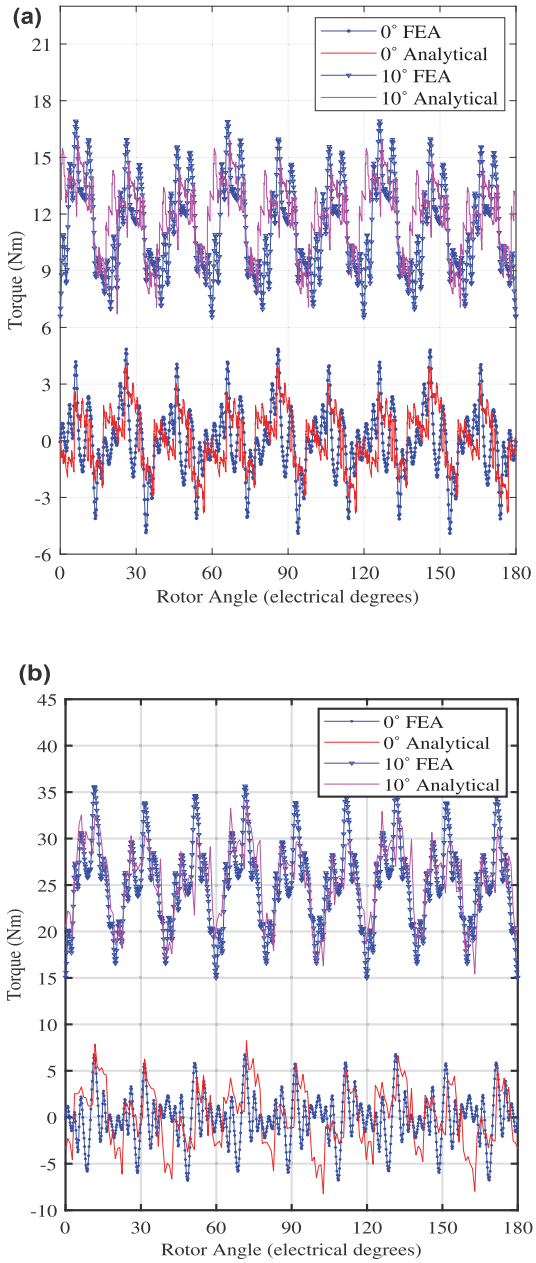


FIGURE 19 Torque profile for different load angles δ: (a) 10 A, (b) 18 A

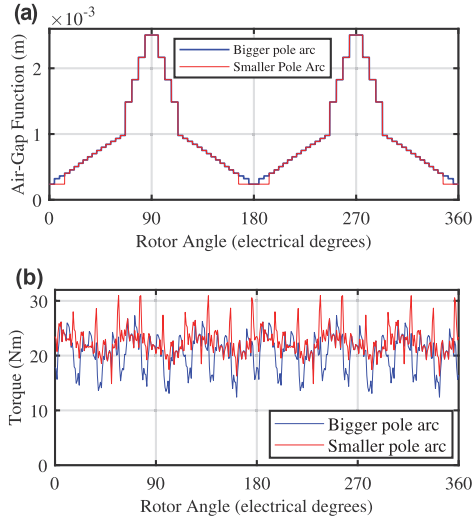


FIGURE 20 (a) Air-gap function for design variation in pole arc (b) associated torque profile for the respective design variation

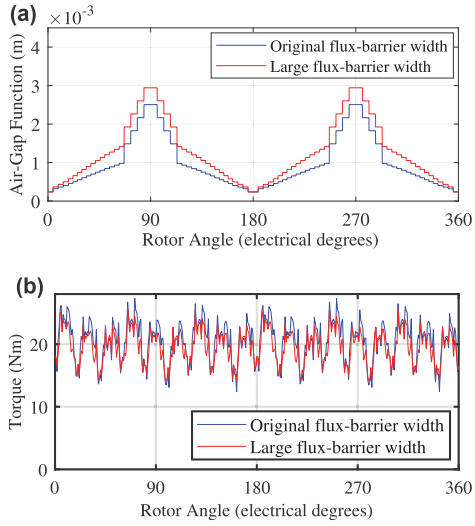


FIGURE 21 (a) Air-gap function for design variation in flux-barrier width (b) associated torque profile for the respective design variation

demonstrated in the last section of this paper. The influence of material permeability as a function of input current on the air-gap flux and resultantly on machine inductances and electromagnetic torque was introduced as a multiplier in the torque equation. This effectively mapped the machine operation in the magnetic non-linear region.

The implementation strategy of the proposed model was such that the calculation of turn and winding functions, air-gap permeance function and resultant inductances for each rotor position (from 0 to 2π mechanical degrees) was done by running an offline MATLAB-script. The calculated values of inductances were stored in 3D-lookup tables as a function of rotor position. The torque calculation was made in the online environment of SIMULINK-MATLAB, where the respective change in the lookup table index was made to

17518679, 2022, 4, Downloaded from https://ietresearch.onlinelibrary.wiley.com/doi/10.1049/elp2.12172 by Tallin Technical University, Wiley Online Library on [09/04/2025]. See the Terms and Conditions (https://onlinelibrary.wiley.com/terms-and-conditions) on Wiley Online Library for rules of use; OA articles are governed by the applicable Creative Commons License

TABLE 2 Simulation runtime comparison for same temporal resolution and machine runtime (4 s), FEA versus analytical

Type of modelling	Simulation runtime	
Analytical	Tuning via hybrid FEA-Analytical procedure (one-time procedure)	15–20 min
	Each subsequent iteration	15 s
FEA	Per-iteration	Approx. 100 h

Abbreviation: FEA, finite element analysis.

calculate the performance parameters for each rotor position, The procedure outlined in this paper is intended to shift the majority of initial design-iteration related computational-load from FEA to the analytical method by yielding information about the air-gap MMF, torque profiles, effect of design variation on output performance parameters and in the meantime, also considering the global saturation of core material. This gives less time and computational effort for the initial iteration intensive design process and a better starting point for the FEA-based design iteration stage. Utilising only FEA for these iterations takes enormous time and computational resources. The current state of the art in WFA of SynRM lacks the mapping of machine behaviour in the non-linear magnetic condition, which is usually near rated current and is very important for design considerations. This model presents a hybrid procedure to tackle this issue, where initial involvement of FEA takes place only for tuning purposes, usually taking 20 min. After the said tuning, the model works stand-alone in all the operating zones of the machine; magnetic-linear as well as non-linear magnetic conditions. Once the model is tuned, it does simulate any temporal resolution of the machine's performance parameters in mere seconds. In iteration intensive procedures, this is very important where each FEA-based iteration takes hours to simulate even a few seconds of machine performance. Utilising this procedure would take a considerable load off from the FEA-dependent initial design iterations.

The electromagnetic torque estimated by the simulation of the proposed model was compared with FEA-based results. The FEA-based simulation was done in Simcentre-MAGNET, a commercial design analysis software by Siemens Digital Industries. The comparison, along with the frequency spectrum analysis, shows reasonable accuracy of the proposed model in terms of torque profile and the mean-torque value for most of the input current range. The slight deviation in results obtained from this model versus FEA and practical machine results is because, at the present stage, the analytical model considers the estimated geometry and hence only considers the effect of global saturation. Even so, the comparison of results obtained from this analytical model with FEA demonstrates its applicability as a design and analysis tool. For prospects in this line of research, the model's accuracy can further be improved by incorporating the localised saturations happening in various machine parts such as stator teeth etc., through suitable air-gap modulation. As discussed earlier, while presenting the frequency spectrum analysis, this model estimates the steady state performance parameters. Modifying this model's online portion and the transformation of calculated inductances to the d-q plane offers the possibility of yielding the dynamic torque. This, in turn, can be employed to perform transient analyses for machine diagnostic, condition monitoring and control applications such as maximum torque per ampere vector control strategy.

ACKNOWLEDGEMENTS

This work was supported by the Estonian Research Council grant (PSG-137).

CONFLICT OF INTEREST

The authors declare no conflict of interest.

DATA AVAILABILITY STATEMENT

Data available on request from the authors.

ORCID

Muhammad Usman Naseer https://orcid.org/0000-0002-1682-9169

REFERENCES

1. Moghaddam, R.R., Magnussen, F., Sadarangani, C.: Novel rotor design optimization of synchronous reluctance machine for high torque density. IET Conf. Publ. 592, 1–4 (2012). https://doi.org/10.1049/CP.2012.0256
2. Ibrahim, M.N.F., et al.: An improved torque density synchronous reluctance machine with a combined star-delta winding layout. IEEE Trans. Energy Convers. 33(3), 1015–1024 (2018). https://doi.org/10.1109/TEC.2017.2782777
3. Babetto, C., Bacco, G., Bianchi, N.: Synchronous reluctance machine optimization for high-speed applications. IEEE Trans. Energy Convers. 33(3), 1266–1273 (2018). https://doi.org/10.1109/TEC.2018.2800536
4. Babetto, C., Bacco, G., Bianchi, N.: Analytical power limits curves of high-speed synchronous reluctance machines. IEEE Trans. Ind. Appl. 55(2), 1342–1350 (2019). https://doi.org/10.1109/TIA.2018.2875663
5. Babetto, C., Bianchi, N.: Synchronous reluctance motor with dual three-phase winding for fault- tolerant applications. Proc. - 2018 23rd Int. Conf. Electr. Mach. ICEM, September, 2297–2303 (2018). https://doi.org/10.1109/ICELMACH.2018.8506771
6. Wang, B., et al.: A fault-tolerant machine drive based on permanent magnet-assisted synchronous reluctance machine. IEEE Trans. Ind. Appl. 54(2), 1349–1359 (2018). https://doi.org/10.1109/TIA.2017.2781201
7. Kang, S.J., Sul, S.K.: Highly dynamic torque control of synchronous reluctance motor. IEEE Trans. Power Electron. 13(4), 793–798 (1998). https://doi.org/10.1109/63.704161
8. Bae, B.H., Sul, S.K.: A novel dynamic overmodulation strategy for fast torque control of high-saliency-ratio ac motor. IEEE Trans. Ind. Appl. 41(4), 1013–1019 (2005). https://doi.org/10.1109/TIA.2005.851042
9. Heidari, H., et al.: A review of synchronous reluctance motor-drive advancements. Sustain. Times. 1313(2), 729 (2021). https://doi.org/10.3390/SU13020729
10. Babetto, C., et al.: High speed motors: a comparison between synchronous PM and reluctance machines. IEEE Energy Convers. Congr. Expo.

17518679, 2022, 4, Downloaded from https://ietresearch.onlinelibrary.wiley.com/doi/10.1049/elp2.12172 by Tallin Technical University, Wiley Online Library on [09/04/2025]. See the Terms and Conditions (https://onlinelibrary.wiley.com/terms-and-conditions) on Wiley Online Library for rules of use; OA articles are governed by the applicable Creative Commons License

ECCE. 2017-January, 3927–3934 (2017). https://doi.org/10.1109/ECCE.2017.8096689
11. Bianchi, N., et al.: Electric vehicle traction based on synchronous reluctance motors. IEEE Trans. Ind. Appl. 52(6), 4762–4769 (2016). https://doi.org/10.1109/TIA.2016.2599850
12. Taghavi, S.M., Pillay, P.: A mechanically robust rotor with transverse laminations for a wide-speed-range synchronous reluctance traction motor. IEEE Trans. Ind. Appl. 51(6), 4404–4414 (2015). https://doi.org/10.1109/TIA.2015.2445819
13. Carraro, E., Morandin, M., Bianchi, N.: Traction PMASR motor optimization according to a given driving cycle. IEEE Trans. Ind. Appl. 52(1), 209–216 (2016). https://doi.org/10.1109/TIA.2015.2477479
14. Rassõlkin, A., et al.: Life cycle analysis of electrical motor drive system based on electrical machine type. Proc. Est. Acad. Sci. 69(2), 162–177 (2020). https://doi.org/10.3176/PROC.2020.2.07
15. Pham, T., Kwon, P., Foster, S.: Additive manufacturing and topology optimization of magnetic materials for electrical machines—a review. Energies. 14(2), 283 (2021). https://doi.org/10.3390/en14020283
16. Naseer, M.U., et al.: A review on additive manufacturing possibilities for electrical machines. Energies. 14(7), 1940 (2021). https://doi.org/10.3390/EN14071940
17. Bedetti, N., Calligaro, S., Petrella, R.: Stand-still self-identification of flux characteristics for synchronous reluctance machines using novel saturation approximating function and multiple linear regression. IEEE Trans. Ind. Appl. 52(4), 3083–3092 (2016). https://doi.org/10.1109/TIA.2016.2535413
18. Maroufian, S.S., Pillay, P.: Torque characterization of a synchronous reluctance machine using an analytical model. IEEE Trans. Transp. Electrif. 4(2), 506–516 (2018). https://doi.org/10.1109/TTE.2018.2794828
19. Seo, J.H., Choi, H.S.: Analytical modeling for calculating cogging torque in interior permanent magnet machine with multi flux-barriers. IEEE Trans. Appl. Supercond. 24(3), 1–4 (2014). https://doi.org/10.1109/TASC.2014.2304835
20. Mohr, M., et al.: A finite element-based circuit model approach for skewed electrical machines. IEEE Trans. Magn. 50(2), 837–840 (2014). https://doi.org/10.1109/TMAG.2013.2280292
21. Venegas, V., et al.: A finite element approach for the calculation of electrical machine parameters at high frequencies. IEEE Power Eng. Soc. Gen. Meet. PES (June, 2007). https://doi.org/10.1109/PES.2007.386274
22. Zhang, Y., et al.: A finite element-analytical method for electromagnetic field analysis of electric machines with free rotation. IEEE Trans. Magn. 42(10), 3392–3394 (2006). https://doi.org/10.1109/TMAG.2006.879441
23. Fratta, A., et al.: Evaluation of torque ripple in high performance synchronous reluctance machines. Conf. Rec. - IAS Annu. Meet. (IEEE Ind. Appl. Soc.). 1, 163–170 (1993). https://doi.org/10.1109/IAS.1993.298919
24. Vagati, A., et al.: Design of low-torque-ripple synchronous reluctance motors. IEEE Trans. Ind. Appl. 34(4), 758–765 (1998). https://doi.org/10.1109/28.703969
25. Vagati, A., et al.: Design refinement of synchronous reluctance motors through finite-element analysis. IEEE Trans. Ind. Appl. 36(4), 1094–1102 (2000). https://doi.org/10.1109/28.855965
26. Bacco, G., Bianchi, N.: Design criteria of flux-barriers in synchronous reluctance machines. IEEE Trans. Ind. Appl. 55(3), 2490–2498 (2019). https://doi.org/10.1109/TIA.2018.2886778
27. Degano, M., et al.: Global design optimization strategy of a synchronous reluctance machine for light electric vehicles. IET Conf. Publ. 2016, CP684 (2016). https://doi.org/10.1049/CP.2016.0253
28. Tessarolo, A.: Modeling and analysis of synchronous reluctance machines with circular flux barriers through conformal mapping. IEEE Trans. Magn. 51(4), 1–11 (2015). https://doi.org/10.1109/TMAG.2014.2363434
29. Mishra, C., Routray, A., Mukhopadhyay, S.: A computationally efficient winding function method for calculation of inductances in an asymmetric induction motor. Elec. Power Compon. Syst. 35(1), 43–61 (2007). https://doi.org/10.1080/15325000600815456
30. Nandi, S.: Modeling of induction machines including stator and rotor slot effects. IEEE Trans. Ind. Appl. 40(4), 1058–1065 (2004). https://doi.org/10.1109/TIA.2004.830764
31. Faiz, J., Tabatabaei, I.: Extension of winding function theory for nonuniform air gap in electric machinery. IEEE Trans. Magn. 38(6), 3654–3657 (2002). https://doi.org/10.1109/TMAG.2002.804805
32. Asad, B., et al.: Modified winding function-based model of squirrel cage induction motor for fault diagnostics. IET Electr. Power Appl. 14(9), 1722–1734 (2020). https://doi.org/10.1049/IET-EPA.2019.1002
33. Doulatshah, A., Naderi, P.: Eccentricity fault detection of a salient-pole synchronous machine using modified winding function approaches and finite element method. 7th Power Electron. Drive Syst. Technol. Conf. PEDSTC 2016, February, 29–34 (2016). https://doi.org/10.1109/PEDSTC.2016.7556833
34. Boubakar, F., et al.: A three dimensional finite element method analysis and winding function theory for torque ripple reducing in reluctance machine. Proc. 2016 8th Int. Conf. Model. Identif. Control. ICMIC 2016, November, 418–423 (2016). https://doi.org/10.1109/ICMIC.2016.7804148
35. Lubin, T., et al.: Comparison between finite-element analysis and winding function theory for inductances and torque calculation of a synchronous reluctance machine. IEEE Trans. Magn. 43(8), 3406–3410 (2007). https://doi.org/10.1109/TMAG.2007.900404
36. Obe, E.S.: Calculation of inductances and torque of an axially laminated synchronous reluctance motor. IET Electr. Power Appl. 4(9), 783–792 (2010). https://doi.org/10.1049/IET-EPA.2009.0197
37. Nandi, S.: A detailed model of induction machines with saturation extendable for fault analysis. IEEE Trans. IN Appl. 40(5), 1302–1309 (2004). https://doi.org/10.1109/TIA.2004.834101
38. Orlova, S., et al.: Design of rotors for synchronous reluctance motor: analytical treatment and optimization. 2019 21st Eur. Conf. Power Electron. Appl. EPE 2019 ECCE Eur, September (2019). https://doi.org/10.23919/EPE.2019.8914760
39. Lipo, T.A.: Analysis of Synchronous Machines, 2nd ed. CRC Press (2017)

How to cite this article: Naseer, M.U., et al.: Analytical modelling of synchronous reluctance motor including non-linear magnetic condition. IET Electr. Power Appl. 16(4), 511–524 (2022). https://doi.org/10.1049/elp2.12172

17518679, 2022, 4, Downloaded from https://ietresearch.onlinelibrary.wiley.com/doi/10.1049/elp2.12172 by Tallin Technical University, Wiley Online Library on [09/04/2025]. See the Terms and Conditions (https://onlinelibrary.wiley.com/terms-and-conditions) on Wiley Online Library for rules of use; OA articles are governed by the applicable Creative Commons License

Publication VII

M. U. Naseer, A. Kallaste, B. Asad, T. Vaimann, and A. Rassolkin, “Modified Winding Function Analysis of Synchronous Reluctance Motor for Design Iteration Purposes,” IEEE Trans Magn, pp. 1–1, 2022, doi: 10.1109/TMAG.2022.3164189.

Modified Winding Function Analysis of Synchronous Reluctance Motor for Design Iteration Purposes

Muhammad Usman Naseer, Ants Kallaste, Bilal Asad, Toomas Vaimann, and Anton Rassõlkin

Department of Electrical Power Engineering and Mechatronics, Tallinn University of Technology, 19086 Tallinn, Estonia

This article proposes a hybrid analytical modeling procedure for the performance parameter estimation of synchronous reluctance machine, including its operation in the region of magnetic saturation. The proposed model better estimated the torque profile through improved translation and stepped transition of rotor flux barriers. The non-linear operation is simulated by considering the global saturation and estimating the machine's operating point on the magnetization curve of the core material. The procedure formulation focuses on improving the accuracy and rapidness of the iterative design process. The obtained results are validated against an already established design analysis technique, finite-element analysis, and the frequency spectrum analysis of practical machine results. With the improved accuracy and the least requirement of simulation runtime and computational resources, the modeling procedure can be utilized as an initial design iteration tool.

***Index Terms*— AC machines, analytical models, electromagnetic modeling, rotating machines, rotor, stator, torque measurement.**

I. Introduction

THE synchronous reluctance motor (SynRM), having high torque density, fault tolerance, and fast response features, has widespread industrial use, particularly in traction applications [1], [2]. Relatively least usage of multi-material fabrication and the absence of permanent magnets lower its manufacturing and maintenance costs. An accurate design analysis procedure is essential to design the machine reliably according to the application requirements. The machine's performance parameters can be evaluated using prototyping, analytical modeling techniques [3], and finite-element analysis (FEA) [4]. Like every other machine, the design process of SynRMs is usually iterative and requires the analysis of machine output parameters at every stage. A rapid and accurate design iteration tool is paramount for the production processes aimed at mass-personalized production. To adequately support the iteration-intensive design procedures, design analysis tools having the ability to rapidly and accurately estimate the performance parameters over the complete range of the machine's operation, i.e., in the linear and non-linear region of magnetic permeability, are required. Failure to yield the output parameters in the complete operating range necessitates the employment of FEA at an earlier stage of the design iterations [5], resulting in a significant requirement of computational resources and simulation runtime.

This article focuses on improving the output parameter estimation capability of modified winding function analysis (MWFA)-based analytical modeling technique for transversally laminated-anisotropic (TLA) SynRMs with significantly reduced simulation time, improved accuracy, and applicability. The proposed analytical procedure considers the effect of the multi-layered short-pitched stator winding, yields accurate torque profile through improved rotor flux barrier translation, and estimates the machine's output performance parameters over its complete range of operation by mapping its operating point on the magnetization curve of the core's material through a hybrid algorithm. With the machine's operating point determined, the torque estimation can be carried out in the magnetically saturated region with considerable accuracy. This hybrid approach is less computation-intensive and requires less simulation runtime per iteration. Hence, the procedure can be effectively utilized in the initial design iterations, taking a significant computational load off the independent FEA-based design analysis stage.

Manuscript received 10 February 2022; revised 10 March 2022; accepted 28 March 2022. Date of publication 1 April 2022; date of current version 26 August 2022. Corresponding author: M. U. Naseer (e-mail: mnasee@taltech.ee).

Color versions of one or more figures in this article are available at https://doi.org/10.1109/TMAG.2022.3164189.

Digital Object Identifier 10.1109/TMAG.2022.3164189

II. Modeling Procedure

The modeling procedure progresses so that the machine's circuit parameters, such as stator-phase inductances as a function of rotor position, are calculated for one complete rotation by executing an offline MATLAB script. The performance parameter estimation is carried out in the online section of SIMULINK by solving the electromagnetic coupling model. This mainly involves the estimation of electromagnetic torque by (1) against the load angle and input current

$$T_e = \frac{p}{2}[I]^T\left[\frac{\partial}{\partial\theta}[L(\theta)]\right][I] \tag{1}$$

where $[I]$ is the input current matrix, $\partial L(\theta)/\partial\theta$ is the derivative of the inductance matrix at the corresponding rotor position θ, and p is the number of pole pairs. The load angle is introduced in the form of phase shift in the input current waveform. The block diagram for modeling procedure is presented in Fig. 1.

A. Inductance Calculation

The stator phase inductances are calculated by (2) as a function of rotor position, where the mean value function is utilized to simplify the calculation procedure [6]

$$L_{xy}(\theta) = 2\pi\,\mu_o rl\langle P(\theta,\alpha)\cdot N_x(\theta,\alpha)\cdot n_y(\theta,\alpha)\rangle \tag{2}$$

0018-9464 © 2022 IEEE. Personal use is permitted, but republication/redistribution requires IEEE permission.
See https://www.ieee.org/publications/rights/index.html for more information.

Authorized licensed use limited to: Tallinn University of Technology. Downloaded on April 09,2025 at 14:09:30 UTC from IEEE Xplore. Restrictions apply.

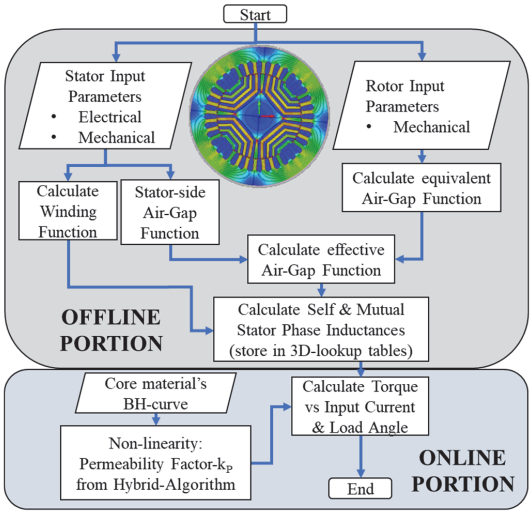


Fig. 1. Block diagram for modeling procedure.

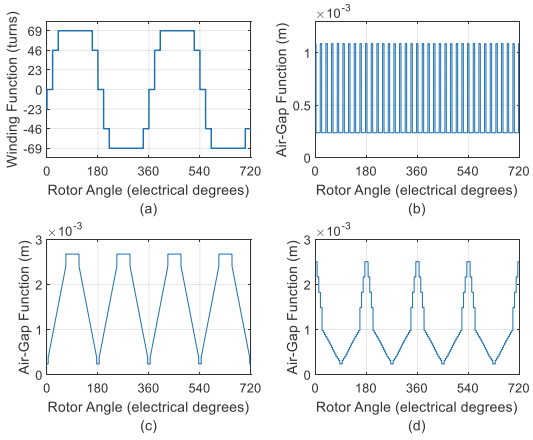


Fig. 2. (a) Per-phase winding function, (b) stator air-gap function and rotor equivalent air-gap function, (c) earlier approach, and (d) proposed approach.

where r, l, $P(\theta, \alpha)$, $n_y(\theta, \alpha)$, and $N_x(\theta, \alpha)$ are the rotor radius, machine stack length, permeance function of air gap, stator turn function, and stator winding function, respectively, θ is the rotor relative position in the stator reference frame, and α is the stator relative position from a stationary reference frame. The air-gap permeance is given by

$$P(\theta, \alpha) = {}^{1}\!/_{g_s(\theta) + g_r(\theta, \alpha)} \tag{3}$$

where $g_s(\theta)$ is the stator side air-gap function and $g_r(\theta, \alpha)$ is the rotor side air-gap function, calculated from an intermediate reference point of the air gap, i.e., g_{avg}. Since the stator for induction motor and SynRM is similar, the procedure to define stator air-gap function, stator turn, and winding function is identical to as described in [6]. The SynRM rotor houses only the flux barriers, causing a difference between the rotor's d- and q-axis path reluctance. The flux barriers can be interpreted toward the corresponding rotor air-gap function, with reluctance being a function of magnetic path length. The analytical procedure to resolve the rotor flux barriers into an equivalent rotor-associated air-gap length will be discussed later in the following.

1) Effect of Short-Pitched Layered Stator Winding: In the machines with multi-layered short-pitched stator winding, for improved sinusoidal-MMF distribution, the magnetic axis of the resultant stator pole shifts. For the winding function analysis of SynRMs, this shift in the stator-pole axis needs to be considered. Otherwise, this relative shift between the stator-pole axis and rotor position acts as a load angle. This shift can be quantified as follows:

$$\theta_s = \left({}^{\theta_e}\!/_{pN_s}\right) n_{ss}.n_l \tag{4}$$

where n_l, n_{ss}, N_s, θ_e, and θ_s are the number of the stator winding layers, short pitching in terms of the number of stator slots, the total number of stator slots, electrical degrees for one rotation, and the resultant shift in stator-pole axis, respectively. The change in stator-pole axis is accounted for by adding the per-layer winding functions and phase shifting the resultant by θ_s.

2) Flux Barrier Translation: Since the reluctance is proportional to the path length, the increased q-axis path reluctance can be translated as an increased air-gap length. The increase in air-gap length is majorly governed by the relation presented in [3]. The proposed modification in the equation to consider the effect of bridges in the rotor flux barriers and the stepped transition among flux barriers produces an improved estimation of torque profile. The modified equation for the flux barrier translation is given as follows:

$$l_{fb} = \left[\left({}^{A_1}\!/_{A_2 + \gamma A_{RB}}\right) - 1\right] l_{ag} \tag{5}$$

where l_{ag}, A_{RB}, A_1, A_2, and l_{fb} are the actual air-gap length of the machine, the equivalent surface area of the rotor bridge, the surface area of the rotor section in the absence of flux barrier, the reduced surface area of rotor section after the insertion of the flux barrier, and the effective air-gap length for the respective flux barrier, respectively. Since each rotor bridge serves two flux guides, the value of γ is set to 1/2. The equivalent rotor air-gap function by the earlier and proposed approaches is presented in Fig. 2(c) and (d), respectively. The associated torque profile estimations and their comparisons with results obtained from FEA are shown in Fig. 3(c) and (d), respectively.

3) Effect of Non-Linear Magnetic Permeability: The original derivation mentioned in [7], which serves as the basis for MWFA, considers the MMF drop in the core negligible, resulting in infinite permeability. This assumption makes the air-gap MMF linear with regard to the input current, i.e.,

$$\mathcal{F}_x(\theta) = N_x(\theta) i_x \tag{6}$$

whereas in reality, the material's magnetic properties are nonlinear, making the air-gap magnetic voltage and inductances

Authorized licensed use limited to: Tallinn University of Technology. Downloaded on April 09,2025 at 14:09:30 UTC from IEEE Xplore. Restrictions apply.

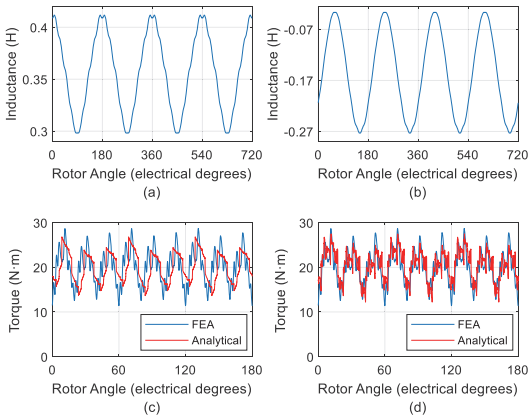


Fig. 3. Stator phase: (a) self-inductance, (b) mutual inductance and torque profile estimation, (c) earlier approach versus FEA, and (d) proposed approach versus FEA.

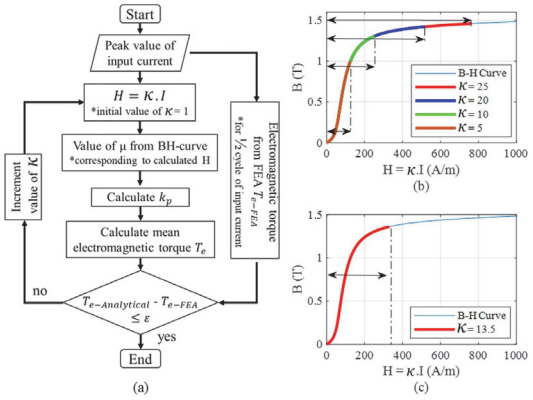


Fig. 4. (a) Block diagram for the iterative procedure to map the machine's operating region on the magnetization curve. (b) B–H curve mapping against input current range of 0–25 A, for κ = 5, 10, 20, and 25. (c) κ = 13.5 (1/m) optimized value for the predesigned machine, operating zone for the input current of 0–25 A.

non-linear with regard to the input current. A permeability factor k_p is introduced in (6) to incorporate this behavior. k_p is a function of the material's relative permeability, and depending on the machine's operating point on the magnetization curve, the corresponding value of relative permeability is used in the empirical relation (10) to calculate it

$$\lambda_{xy} = \frac{\mu_o rl}{g}\int_0^{2\pi} \mathcal{F}_x(\theta) n_y(\theta) d\theta \tag{7}$$

$$L_{xy} = \frac{\lambda_{xy}}{i_x} = k_p.\frac{\mu_o rl}{g}\int_0^{2\pi} N_x(\theta) n_y(\theta) d\theta \tag{8}$$

$$T_e = k_p.\frac{p}{2}[I]^T\left[\frac{\partial}{\partial\theta}[L(\theta)]\right][I] \tag{9}$$

$$k_p = \sqrt{2}\mu_r 10^{-4}. \tag{10}$$

4) Machine's Operating Region on Magnetization Curve: The main task in determining the machine's operating point on the magnetization curve is to estimate the magnetic field intensity (H) against the value of the stator input current. The general formula to compute H dictates that for fixed circuit parameters and geometry, the magnetic field intensity is proportionate to the input current (I), i.e.,

$$H = \kappa I \tag{11}$$

where κ ($1/m$) is a proportionality constant. Fig. 4(b) shows the process of sweeping (11) on the magnetization curve, for the machine's input current range of 0–25 A, against different values of κ. It can be seen that κ effectively controls the scaling of magnetic field intensity (function of input current) on the magnetization curve. The value of κ is optimized iteratively by executing a hybrid algorithm, as shown in Fig. 4(a). For the rated input current, the value of κ is optimized against a reference output torque obtained from running FEA-based calculations for almost a half cycle of rated input current. The error limit ε defines the precision of the mapping procedure.

After carrying out the mapping procedure and with the value of κ optimized, the operating region of the machine

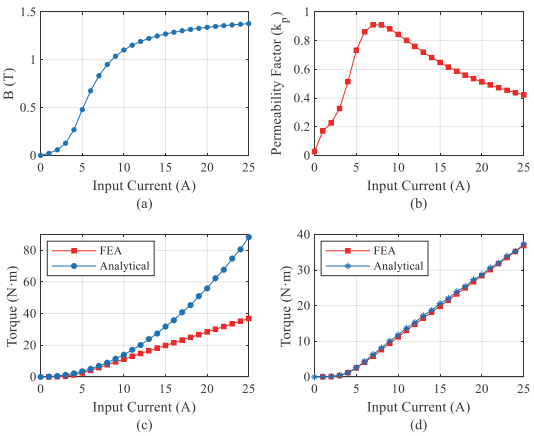


Fig. 5. (a) Estimated operating region of the machine on the B–H curve, B versus $H = \kappa I$; (b) k_p versus input current; (c) torque estimation versus input current, earlier approach versus FEA; and (d) torque estimation versus input current, proposed approach versus FEA.

on the magnetization curve can be mapped readily, as shown in Fig. 4(c). Against the value of input current, the corresponding permeability from the magnetization curve can be obtained and used to calculate k_p, i.e., with the value of κ fixed, H is calculated from (11) against the whole input current range of the machine. The corresponding values of flux density (B) and k_p (function of μ_r) are obtained from the magnetization/permeability curve and stored in the lookup table. Fig. 5(a) and (b) shows the values of B and k_p for the whole input current range of the machine under consideration.

B. Torque Calculation

For any input current value, the corresponding k_p is evaluated, and the estimation of torque is carried out by

Authorized licensed use limited to: Tallinn University of Technology. Downloaded on April 09,2025 at 14:09:30 UTC from IEEE Xplore. Restrictions apply.

executing (9) in the online section of the Simulink. The torque profile estimation for the pre-designed machine under consideration [8], against the input current of 15 A $\delta = 10°$ mechanical, is presented in Fig. 3(d). This hybrid analytical approach against FEA and practical tests will be validated in Section III.

III. Results and Validation

Upon implementing the described modeling procedure for a predesigned SynRM and executing the hybrid mapping procedure, the obtained value for κ is set to be 13.5. The corresponding per-phase winding function, the stator air-gap function, and the rotor's equivalent air-gap function from the earlier and proposed approaches are presented in Fig. 2(a)–(d), respectively. Stator-phase self-inductance and mutual inductance as a function of rotor position are presented in Fig. 3(a) and (b), respectively, with the associated torque estimation shown in Fig. 3(d). Fig. 5(a) presents the result of the hybrid mapping procedure, indicating the estimated values of B in the machine core versus input current.

The torque profile estimation from the proposed hybrid analytical approach presented in Fig. 3(d) shows considerable agreement with FEA results. The comparison of mean torque calculation obtained from analytical and FEA-based modeling is presented in Fig. 5(c) and (d). The FEA simulation was done through a commercial design analysis software, Simcenter-MAGNET by Siemens Digital Industries. The FEA simulation was done in a manner to simulate the steady-state operation of the machine making it current fed, with speed of rotation kept constant at synchronous speed. The load angle variation was incorporated by introducing a relative shift between the stator-field magnetic axis and the rotor core. The simulation step size for analytical and FEA simulation was set equal to 0.1 ms.

Without taking the non-linear magnetic permeability into account, the results from (1) depict a deviating trend from the FEA-based results, after approximately half the rated input current, see Fig. 5(c). While utilizing the hybrid mapping algorithm and introducing k_p, the torque calculation from (9) yields analogous results compared to FEA, see Fig. 5(d).

The proposed hybrid analytical model is current-fed and produces steady-state torque estimation at synchronous speed. The FEA simulations also allow for the current-fed simulation of the machine characteristics, i.e., performance parameters in steady-state operation. In contrast, the machine was fed directly from the grid for practical tests, to avoid inverter-fed harmonics. Since the tests were performed without any control algorithm, the steady-state operation was not possible, necessitating validation through the frequency spectrum analysis. The frequency spectrum analysis for the proposed technique and practical measurements is presented in Fig. 6. The harmonics in both of these spectrums are produced for several reasons but are primarily due to flux barrier transitions in the rotor, the stator slot openings, the stepped configuration of winding distribution, and so on. They also indicate the presence of torque and speed ripples. The slight deviations from the proposed model and practical results are also due to some additional grid-fed harmonics. As evident from the presented frequency spectrum comparison, the main harmonic components from experimental measurements exist and are in good agreement with the results of the proposed analytical model.

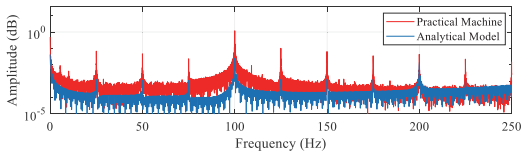


Fig. 6. Frequency spectrum comparison of SynRM torque, the proposed hybrid analytical procedure, and the practical test.

IV. Conclusion

In this article, a hybrid analytical procedure to evaluate the machine's output performance parameters in the regions of non-linear magnetic permeability is proposed, which is usually near rated current and is vital for design purposes. FEA was involved initially for tuning purposes, only taking 20 min. Afterward, the model worked independently in all the operating regions of the machine and simulated any amount of machine runtime in mere seconds. This reduction of simulation runtime per iteration is significant compared to FEA-based models taking multiple hours per iteration.

The analytical modeling procedure was modified to accommodate the multi-layer, short-pitched stator winding. The torque profile estimation was also improved through an improved rotor flux barrier translation and a stepped transition scheme among the individual flux barriers. Considering the accuracy and rapidness of this modeling procedure, it can potentially be utilized as an effective initial design analysis and iteration tool.

References

[1] R. R. Moghaddam, F. Magnussen, and C. Sadarangani, "Novel rotor design optimization of synchronous reluctance machine for high torque density," in *Proc. IET Conf. Publications*, no. 592, 2012, p. 32.

[2] N. Bianchi, S. Bolognani, E. Carraro, M. Castiello, and E. Fornasiero, "Electric vehicle traction based on synchronous reluctance motors," *IEEE Trans. Ind. Appl.*, vol. 52, no. 6, pp. 4762–4769, Nov. 2016.

[3] S. Maroufian and P. Pillay, "Torque characterization of a synchronous reluctance machine using an analytical model," *IEEE Trans. Transport. Electrific.*, vol. 4, no. 2, pp. 506–516, Jun. 2018.

[4] Z. Wei, "Finite element computation of synchronous reluctance motor," in *Proc. IEEE Int. Conf. Microw. Technol. Comput. Electromagn. (ICMTCE)*, May 2011, pp. 391–394.

[5] F. Uberti, L. Frosini, and L. Szabó, "A new design procedure for rotor laminations of synchronous reluctance machines with fluid shaped barriers," *Electronics*, vol. 11, no. 1, p. 134, Jan. 2022.

[6] B. Asad, T. Vaimann, A. Belahcen, A. Kallaste, A. Rassõlkin, and M. N. Iqbal, "Modified winding function-based model of squirrel cage induction motor for fault diagnostics," *IET Electr. Power Appl.*, vol. 14, no. 9, pp. 1722–1734, Sep. 2020.

[7] T. A. Lipo, *Analysis of Synchronous Machines*, 2nd ed. Boca Raton, FL, USA: CRC Press, 2017.

[8] S. Orlova, V. Pugachov, A. Rassõlkin, A. Kallaste, and T. Vaimann, "Design of rotors for synchronous reluctance motor: Analytical treatment and optimization," in *Proc. 21st Eur. Conf. Power Electron. Appl. (EPE ECCE Europe)*, Sep. 2019, pp. P.1–P.10.

Authorized licensed use limited to: Tallinn University of Technology. Downloaded on April 09,2025 at 14:09:30 UTC from IEEE Xplore. Restrictions apply.

Publication VIII

B. Asad, T. Vaimann, A. Belahcen, A. Kallaste, A. Rassõlkin, H. V. Khang, P. S. Ghahfarokhi, **M. U. Naseer**, and M. N. Iqbal, "The Modeling and Investigation of Slot Skews and Supply Imbalance on the Development of Principal Slotting Harmonics in Squirrel Cage Induction Machines," IEEE Access, vol. 9, pp. 165932–165946, 2021, doi: 10.1109/ACCESS.2021.3134331.

IEEE Access
Multidisciplinary ⋮ Rapid Review ⋮ Open Access Journal

Received November 23, 2021, accepted December 6, 2021, date of publication December 10, 2021,
date of current version December 24, 2021.

Digital Object Identifier 10.1109/ACCESS.2021.3134331

The Modeling and Investigation of Slot Skews and Supply Imbalance on the Development of Principal Slotting Harmonics in Squirrel Cage Induction Machines

BILAL ASAD[1,2], (Member, IEEE), TOOMAS VAIMANN[1], (Senior Member, IEEE), ANOUAR BELAHCEN[2], (Senior Member, IEEE), ANTS KALLASTE[1], (Senior Member, IEEE), ANTON RASSOLKIN[1], (Senior Member, IEEE), HUYNH VAN KHANG[3], (Senior Member, IEEE), PAYAM SHAMS GHAHFAROKHI[1,4], (Member, IEEE), MUHAMMAD U. NASEER[1], (Member, IEEE), AND MUHAMMAD N. IQBAL[1], (Member, IEEE)

[1]Department of Electrical Power Engineering and Mechatronics, Tallinn University of Technology, 19086 Tallinn, Estonia
[2]Department of Electrical Engineering and Automation, Aalto University, 00076 Aalto, Finland
[3]Department of Engineering Sciences, Faculty of Engineering and Science, University of Agder, 4879 Grimstad, Norway
[4]Department of Electrical Machines and Apparatus, Riga Technical University, Riga LV-1658, Latvi

Corresponding author: Bilal Asad (bilal.asad@aalto.fi)

This work was supported by European Economic Area (EEA)/Norway Grants 2014–2021 (Industrial Internet Methods for Electrical Energy Conversion Systems Monitoring and Diagnostics).

ABSTRACT A discrete winding function analysis (DWFA) based approach for the modelling of skewed rotor cage-type induction motor with minimal simulation time is presented in this paper. The rotor slot skew has a significant attenuating impact on principal slotting harmonics (PSH) or rotor slotting harmonics (RSH). These harmonics can play a significant role in sensor-less speed estimation and condition monitoring of induction machines. The advanced fault diagnostic algorithms are becoming increasingly dependent on the fast and accurate mathematical models of electrical machines. The most accurate models are based on the finite element method (FEM), but the computational complexity and the required simulation time make them unsuitable for model-dependent fault diagnostic algorithms. Moreover, as most models are 2D, they cannot incorporate axial asymmetries such as rotor slot skews. Furthermore, most analytical models, such as modified winding function analysis (MWFA), depend upon the continuous integration functions, increasing complexity while implementing them in the online environment in digital signal processing boards. To resolve all those issues, DWFA based model is proposed in this paper, which can simulate the majority of the faults in negligible time compared to the corresponding FEM models. The impact of slot skews and unbalanced power supply on the current spatial harmonics is studied, and the results are compared with the practical measurements taken from the laboratory setup.

INDEX TERMS Analytical models, discrete-time systems, condition monitoring, electrical machines, electromagnetic modeling, fault diagnosis, induction motors.

I. INTRODUCTION

The role of induction machines in modern-day society is indispensable because of their simple and rugged structure, low cost, easy maintenance and reliability. Their dominant and frequent use increases the importance of their mathematical models not only for design and control but also for their condition monitoring. As the faults in electrical machines are degenerative, their detection at the embryonic stage is of crucial importance to avoid any catastrophic situation. Varieties of very mature diagnostic algorithms, which do not depend upon the model of the system, are available in the

The associate editor coordinating the review of this manuscript and approving it for publication was Dazhong Ma.

This work is licensed under a Creative Commons Attribution 4.0 License. For more information, see https://creativecommons.org/licenses/by/4.0/

literature. However, with the increasing trend of industrial inverters, conventional diagnostic algorithms such as MCSA do not remain straightforward. Moreover, those techniques may also vary according to the motor working environment. The common diagnostic techniques that do not depend upon the motor model are MCSA, thermal analysis, acoustic analysis, stray flux monitoring, partial discharge analysis, air gap flux monitoring etc. [1].

The conventional diagnostic techniques related problems can be avoided by using advanced model-dependent condition monitoring techniques. The reliable model-based diagnostic algorithms depend upon the accurate and fast mathematical models of induction motors. These models can be used for the fault identification and severity estimation [2], [3], for the training of multi-agent systems [4], for the development of vector classifiers [5, for the comparison of fault indexes [6], for online parameters estimation [7], [8], and motor drives [9, etc. Among several model-dependent condition monitoring techniques, the artificial intelligence (AI) based fault diagnostic techniques are gaining heightened popularity [10]. The only challenge with AI techniques is the requirement of big data for training purposes. The training data set should have as many healthy and faulty cases as possible for better reliability of the diagnostic algorithm.

The collection of big data with all possible faulty cases is very challenging from the industry as well as from the laboratory environments. From industry, it is difficult because of the limited number of faulty machines working due to preventive maintenance. Moreover, the training data set should have signals with very well-defined types and severity of the fault so that they can be considered as benchmark signals. On the other hand, from the laboratory, it is difficult as a limited number of destructive tests can be performed due to economic limitations.

The only possible solution is the mathematical model that can simulate various faults within an acceptable duration of time. The mathematical models can be broadly classified into two categories: Analytical and Numerical. A typical example of numerical models is the finite element method (FEM) based models. The FEM based models can give promising results as almost all practical aspects can be included [11]–[13], making them suitable for design problems. Those aspects can be related to material, geometry and winding configuration. The only problem with FEM modeling is the amount of simulation time that is not feasible for fault diagnostic algorithms. These models cannot easily become the part of drive because of associated limited computational resources. Moreover, these models are not feasible for inverse problem theory where observables are mapped towards the unknowns. The reason for this is the FEM solution related large matrices whose inverse solution cannot give stable and unique results. The most common example of analytical models is the magnetic circuit coupling (MCC) based models. In these models, the electrical circuit's equations are used for the simulation of performance parameters. The most common MCC models are the winding function analysis (WFA) based models where machine design parameters can be defined with the help of Fourier summation or conditional analytical equations.

Considerable work has already been reported in this domain. For example, The authors of [14] simulated stator short circuit faults in squirrel cage induction motor (SQIM) using winding function analysis (WFA) while the broken rotor bars were presented in [15]. The authors of [16] used this approach to analyze various faults, such as stator phase disconnection, broken bars, and broken end rings. The WFA approach for the analysis of adjustable speed drive applications is presented in [17], [18]. The modelling of a permanent magnet machine with a fractional slot concentrated winding can be studied in [19]. In most of the WFA based models, the air gap is considered constant, making the model unsuitable for implementing eccentricity-based faults. Moreover, the effects of stator and rotor slot openings cannot be studied. These studies may also include the effects of general and local saturations. Furthermore, these models are unsuitable for sensor-less speed drive systems as the principal slotting harmonics (PSH) are potentially ignored.

These problems can be solved using the modified winding function analysis (MWFA) method, where the slot openings of the stator and rotor can be considered by making the air gap a function of the stator and rotor relative position. The authors in [20] extended the WFA based method to simulate electrical machines with a non-uniform air gap. The use of the MWFA to model the stator and rotor slot effects for speed sensor-less drive systems is presented in [21]. The static and dynamic eccentricities are presented in [22] and [23], respectively. Unlike [21], where the air gap permeance is approximated by cosine series functions, [24] used the actual stator and rotor slot opening functions and a medium magnetic equipotential surface to simulate the machine. By doing so, the authors obtained results very close to the ones obtained from FEM. The simulation time was further reduced by exploiting the symmetry of the rotor cage, however, it is not valid in the case of faulty machines. The primary approximation frequently used in all the papers cited earlier is that; the machine is symmetrical in the axial direction, which is not always true. In most machines, the rotor slots are skewed to attenuate the rotor slotting harmonics (RSH). Those harmonics are attenuated for the reduction of speed and torque ripples. In this paper, a novel technique for implementing rotor skews is proposed. In continuation of [25], this paper has the following attractive features.

- Unlike most of the papers where an integral function is solved for the calculation of inductances, in this research, a discrete mean value equation is proposed. The derived mean value equation reduces the computational complexity and the integral calculation-based approximations.
- The proposed DWFA formula is further extended to incorporate the machine's axial asymmetries such as rotor slots skew.

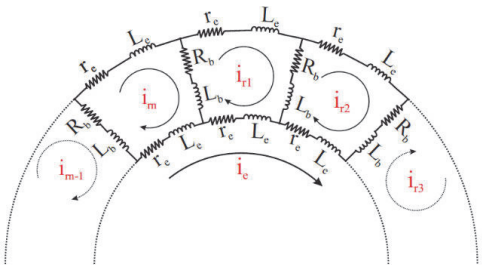


FIGURE 1. The equivalent circuit diagram of rotor cage.

- Unlike most of the papers where the spatial harmonics are defined with the help of Fourier summation of the selective number of harmonics, in this paper the winding functions and the air gap is defined with the help of conditional analytical expressions. The approximations related to the self-defined number of harmonics and their amplitude can be avoided by doing so.
- The impact of rotor slot skews on PSH amplitude is studied, while in most of the papers, it is neglected.
- The impact of negative sequence currents on the development of spatial harmonics is investigated.
- The model is divided into online and offline portions. All the inductances are calculated in the offline portion, and the results are saved in 3-D lookup tables. Once the offline calculation is done, most of the faults can be simulated in the online portion without doing unnecessary offline calculations again.

II. THE ANALYTICAL MODEL

The induction machines are magnetically coupled electrical circuits. Mostly the primary windings are static and associated with the stator side, while secondary windings are associated with the rotor and rotate with it. The magnetic coupled circuits theory-based voltage equations of a squirrel cage induction motor are described as;

$$\boldsymbol{V}_s = \boldsymbol{I}_s\boldsymbol{R}_s + \frac{d}{dt}\boldsymbol{\varphi}_s, \tag{1}$$

$$\boldsymbol{0} = \boldsymbol{I}_r\boldsymbol{R}_r + \frac{d}{dt}\boldsymbol{\varphi}_r, \tag{2}$$

where **V**s, **I**s, **I**r, **R**s and **R**r are vectors containing stator three-phase voltage, stator three-phase current, stator resistances, and rotor resistances. While φs and φr are the stator and rotor fluxes, respectively. The voltage matrix on the rotor side is zero because the end rings are short-circuiting the rotor phases that are bars in cage-induction machines.

The following equations present the detailed description of voltage equations of stator and rotor in the form of matrices that makes the implementation of the model easier (3) and (4), as shown at the bottom of the next page.

The matrix elements with subscript "s" and "r" are respective stator and rotor associated entries. The dimension of rotor related matrices depends upon the number of bars in it plus one more which corresponds to the end ring. The end ring-related rows and columns shown in (4) could be neglected because their value is minimal and the end ring current is approximately zero because all rotor phases are equally mechanically spaced. Nevertheless, neglecting them can cause the problems of singularities while taking the inverse of matrices, and the end ring faults cannot be implemented. The equivalent circuit diagram of the rotor cage is shown in Figure (1), from where (4) can be written using simple voltage equations.

The stator flux is the function of stator self and mutual inductances and their corresponding currents (5).

$$\boldsymbol{\varphi}_s = \boldsymbol{L}_{ss}\boldsymbol{I}_s + \boldsymbol{L}_{sr}\boldsymbol{I}_r, \tag{5}$$

where $\boldsymbol{L}_{ss}$ and $\boldsymbol{L}_{sr}$ are matrices containing stator and rotor self and mutual inductances, as presented below:

$$\boldsymbol{L}_{ss} = \begin{bmatrix} L_{aas} & L_{abs} & L_{acs} \\ L_{bas} & L_{bbs} & L_{bcs} \\ L_{cas} & L_{cbs} & L_{ccs} \end{bmatrix},$$

$$\boldsymbol{L}_{sr} = \begin{bmatrix} L_{ar1} & L_{ar2} & \cdots & L_{ari} & \cdots & L_{arn} & L_{are} \\ L_{br1} & L_{br2} & \cdots & L_{bri} & \cdots & L_{brn} & L_{bre} \\ L_{cr1} & L_{cr2} & \cdots & L_{cri} & \cdots & L_{crn} & L_{cre} \end{bmatrix},$$

$$\boldsymbol{L}_{sr} = \begin{bmatrix} L_{ar1} & L_{ar2} & \cdots & L_{ari} & \cdots & L_{arn} & 0 \\ L_{br1} & L_{br2} & \cdots & L_{bri} & \cdots & L_{brn} & 0 \\ L_{cr1} & L_{cr2} & \cdots & L_{cri} & \cdots & L_{crn} & 0 \end{bmatrix},$$

The subscripts a,b,c, and r represent entries related to the stator and rotor phases.

Similarly, rotor fluxes can be represented as:

$$\boldsymbol{\varphi}_r = \boldsymbol{L}_{rs}\boldsymbol{I}_s + \boldsymbol{L}_{rr}\boldsymbol{I}_r = \boldsymbol{L}_{sr}^T\boldsymbol{I}_s + \boldsymbol{L}_{rr}\boldsymbol{I}_r, \tag{6}$$

$$L_{rr} = \begin{bmatrix} L_{r1r1} & L_{r1r2} & \cdots & L_{r1ri} & \cdots & L_{r1rn} & L_{r1re} \\ L_{r2r1} & L_{r2r2} & \cdots & L_{r2ri} & \cdots & L_{r2rn} & L_{r2re} \\ \vdots & \vdots & \vdots & \vdots & \vdots & \vdots & \vdots \\ L_{rir1} & L_{rir2} & \cdots & L_{riri} & \cdots & L_{rirn} & L_{rire} \\ \vdots & \vdots & \vdots & \vdots & \vdots & \vdots & \vdots \\ L_{rnr1} & L_{rnr2} & \cdots & L_{rnri} & \cdots & L_{rnrn} & L_{rnre} \\ L_{rer1} & L_{rer2} & \cdots & L_{reri} & \cdots & L_{rern} & L_{rere} \end{bmatrix}$$

The rotor end-ring leakage inductance depends upon the number of rotor phases (n_b), the number of stator phases (m), the number of pole pairs (P), the bar length (l_{bar}), stator effective length (l_s), a factor ($\nu = 0.18$ for $P > 1$) and the average ring diameter (D_r) as in (7) [24].

$$L_e = \mu_o \frac{n_b}{3mP^2}\left((l_{bar} - l_s) + \nu\frac{\pi D_r}{2P}\right), \tag{7}$$

III. THE FORMATION OF DWFA METHOD AND INCORPORATING ROTOR SKEW

Other than the leakage, various magnetization inductances in induction machines can be classified as; stator-stator self, stator-stator mutual, stator-rotor mutual, rotor-rotor self and rotor-rotor mutual inductances. The main contributing factors among many for these inductances are stator and rotor winding configurations, air gap permeance functions, radius,

and the machine's length. According to the winding function based theory, those inductances can be calculated using (8).

$$L_{ij}(\theta e) = \mu_o rl \int_0^{p\pi} \mathrm{P}(\theta e, \alpha) N_i(\theta e, \alpha) n_j(\theta e, \alpha) d\theta e, \tag{8}$$

where μ_o is the permeability of the free space, r is the mid-air-gap radius of the machine, l is the effective length of the machine, $\mathrm{P}(\theta_e, \alpha)$ is the inverse air gap permeance function, $\mathrm{N}(\theta_e, \alpha)$ is the winding function, and $\mathrm{n}(\theta_e, \alpha)$ is the turn function. The theta (θ_e) and alpha (α) are the rotor and stator angles from a fixed reference point. These angles can be electrical or mechanical and will be equal in the case of a two-pole machine.

The integrator shows the summation of all rotor position-dependent variables multiplied at each position in the continuous-time domain. The usual integration calculation is based on the area under the curve, which can be calculated using the trapezoidal rule. Unfortunately, this rule not only increases the error but also increases the complexity of the integral solution. To avoid those problems, (8) can be reduced to a mean value function, as shown by (9).

$$L_{ij}(\theta e) = p\pi\mu_o l < r_g((\theta e, \alpha)\mathrm{P}((\theta e, \alpha) N_i((\theta e, \alpha) n_j((\theta e, \alpha) >, \tag{9}$$

Since all the inductances are supposed to be calculated at different rotor positions from 0 to 2π mechanical, the problem is no longer in the continuous-time domain. Instead, it can be considered in a discrete-time domain where all rotor position-dependent functions can be defined as vectors having "n" elements. Then, all those vectors can be multiplied in an element-wise manner. Finally, the average can be calculated by adding the elements of the resultant vector and dividing it by the total number of steps as shown by (10). By doing so, the integral complexity with the increasing number of rotor position-dependent variables does not remain a problem anymore. Moreover, the exploitation of constant air gap and complex analytical representation of various inductances as in [26], [27] can be easily avoided.

$$L_{ij}(\theta e) = \frac{p\pi\mu_o l}{n} \times \sum_{k=1}^{n} \left(r_g((\theta e, \alpha)\mathrm{P}((\theta e, \alpha) N_i((\theta e, \alpha) n_j((\theta e, \alpha)\right)_k \tag{10}$$

where the element-wise multiplication of all rotor position-dependent variables will create a vector of "n" elements. All elements are then added and divided by "n" to get the mean value.

Till this point, the machine is in two dimensions (x, y) while the third axial dimension is neglected. Usually, the induction machines in the axial direction are considered symmetrical, which is not always true. The most common reason for axial asymmetry is the stator and rotor slot skews, which reduce speed and torque ripples.

The rotor slot skews can be included by introducing a third angle known as skew angle (α_{sk}). The rotor can be divided into "n" number of segments in the axial direction, and the inductances of all segments can be calculated separately. Since all segments are serially attached, the final inductance vector will be equal to the sum of all individual segment vectors, as shown by (11) and (12).

$$L_{ij}(\theta e) = \frac{p\pi\mu_o}{n} \times \left[l_1 \sum_{k=1}^{n} \left(r_{g1}((\theta e, \alpha)\, P_1((\theta e, \alpha) N_{i1}((\theta e, \alpha) n_{j1}((\theta e, \alpha)\right)_k \right.$$

$$\begin{bmatrix} v_{as} \\ v_{bs} \\ v_{cs} \end{bmatrix} = \begin{bmatrix} R_{as} & 0 & 0 \\ 0 & R_{bs} & 0 \\ 0 & 0 & R_{cs} \end{bmatrix} \begin{bmatrix} i_{as} \\ i_{bs} \\ i_{cs} \end{bmatrix} + \frac{d}{dt} \begin{bmatrix} \varphi_{as} \\ \varphi_{bs} \\ \varphi_{cs} \end{bmatrix}, \tag{3}$$

$$\begin{bmatrix} 0 \\ 0 \\ \vdots \\ 0 \\ 0 \\ 0 \end{bmatrix} = \begin{bmatrix} 2(R_b + r_e) & -R_b & 0 & 0 & \dots & 0 & -R_b & -r_e \\ -R_b & 2(R_b + r_e) & -R_b & 0 & \dots & 0 & 0 & -r_e \\ 0 & -R_b & 2(R_b + r_e) & -R_b & \dots & 0 & 0 & -r_e \\ \vdots & \vdots & \vdots & \vdots & \vdots & \vdots & \vdots & \vdots \\ 0 & 0 & 0 & 0 & \dots & 2(R_b + r_e) & -R_b & -r_e \\ -R_b & & 0 & 0 & \dots & -R_b & 2(R_b + r_e) & -r_e \\ -r_e & -r_e & -r_e & -r_e & \dots & -r_e & -r_e & n_b re \end{bmatrix} * \begin{bmatrix} i_{r1} \\ i_{r2} \\ i_{r3} \\ \vdots \\ i_{r(n-1)} \\ i_{rn} \\ i_{re} \end{bmatrix} + \frac{d}{dt} \begin{bmatrix} \varphi_{r1} \\ \varphi_{r2} \\ \varphi_{r3} \\ \vdots \\ \varphi_{r(n-1)} \\ \varphi_{rn} \\ \varphi_{re} \end{bmatrix} \tag{4}$$

$$+ l_2 \sum_{k=1}^{n} \left(r_{g2}((\theta e, \alpha) P_2((\theta e, \alpha) N_{i2}((\theta e, \alpha) n_{j2}((\theta e, \alpha)) \right)_k + \ldots + l_n \sum_{k=1}^{n} \left(r_{gn}((\theta e, \alpha) P_n((\theta e, \alpha) N_{in}((\theta e, \alpha) n_{jn}((\theta e, \alpha)) \right)_k \Bigg] \tag{11}$$

$$L_{ij}(\theta e) = \frac{p\pi\mu_o}{n} \times \sum_{s=1}^{n} \sum_{k=1}^{n} \left[l_s \begin{pmatrix} r_{gs}((\theta e, \alpha, \alpha_{sk}) \times P_s((\theta e, \alpha, \alpha_{sk}) \\ \times N_{is}((\theta e, \alpha, \alpha_{sk}) \times n_{js}((\theta e, \alpha, \alpha_{sk}) \end{pmatrix} \right]_k \tag{12}$$

All rotor position-dependent variables can be defined by shifting the corresponding reference vector by n elements for each segment. The number of shifting elements depends upon the number of segments and the samples per segment, as shown by (13) and (14).

$$l_{seg} = \frac{l_{ef}}{n_{seg}} \tag{13}$$

$$samples_{seg} = \frac{(sampes\ per\ skew\ angle\ in\ terms\ of\ stator\ slots)}{n_{seg}}$$
$$\alpha_{sk} = \text{skew angle} = n\ stator\ slot\ pitch \tag{14}$$

where l_{seg} is the segment length, l_{ef} is the rotor effective length, n_{seg} are the total number of segments in the axial direction.

All these inductances are saved in 3D tables as a function of rotor position. To calculate the machine performance parameters such as currents, fluxes, torque and speed, the pre-saved matrices are called as a function of rotor position. In the online simulation environment, the rotor position shall be used to index the corresponding 2D matrix. The main equations for the simulation of the machine's global variables are shown in (15) and (16).

$$T_e = \frac{1}{2}\left(\frac{p}{2}\right)\left(\boldsymbol{I}_r^T \frac{d}{d\theta}\boldsymbol{L}_{rs}\boldsymbol{I}_s + \boldsymbol{I}_s^T \frac{d}{d\theta}\boldsymbol{L}_{sr}\boldsymbol{I}_r\right), \tag{15}$$

$$J\frac{d}{dt}\omega_m = T_e - T_L - B_f\omega_m, \tag{16}$$

IV. THE PSH GENERATION CRITERIA

The leading causes of high-frequency current harmonics are the changing air gap and the non-sinusoidal distributed stator and rotor winding functions. Due to these factors, the air gap MMF distribution does not remain perfectly sinusoidal but becomes the function of the rotor position. These frequency components always remain present in the frequency spectrum of any healthy induction machine and yield speed and torque ripples. However, their amplitude can be attenuated by using an appropriate winding distribution on the stator side and putting a skewed cage on the rotor side. The eccentricity and principal slotting harmonics (PSH) or rotor slotting harmonics (RSH) in a squirrel cage induction machine can be described by the following equation;

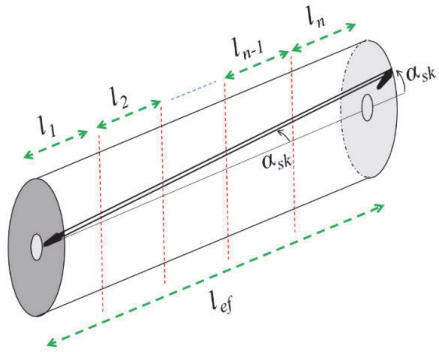


FIGURE 2. The description of rotor skew angle.

$$f_{ecce} = \left[(kn_b \pm n_d)\left(\frac{1-s}{P}\right) \pm v \right] fs, \tag{17}$$

And the mixed eccentricity by:

$$f_{ecce} = f_s \pm kf_r, \quad k = 1, 2, 3, \ldots \tag{18}$$

where n_d is the dynamic eccentricity which is 0 for static and 1, 2, 3, ... for dynamic eccentricity. n_b is the number of rotor bars, s is the slip, P is the number of pole pairs, k is any positive integer, ν is the power supply based harmonic order, and f_s is the fundamental supply frequency.

Not all combinations of n_b and P can produce PSH in the current and voltage spectrum. The air gap MMF based harmonics, also known as PSH or RSH, will develop in stator voltage and current if any element from the set of P(6m ± 1) is equal to the stator winding based pole pair number of the space harmonics defined by $(Q - N_b - Pn)$ or $(Q - N_b + Pn)$ [21].

More precisely, the PSH or RSH will develop in the frequency spectrum if the following equality holds [28].

$$n_b = 2P\,[3\,(m \pm q) \pm r] \tag{19}$$

where m ± q = 0, 1, 2, 3 . . . and r = 0 or 1.

Out of two fundamental PSH components, one is more significant than the other. The most significant or PSH1 depends upon the winding distributions or air gap MMF distribution. The least significant component (PSH2) is due to the reverse rotating field because of the negative sequence currents. Even if PSH2 is absent in the simulation results, or the machine is not a PSH machine, the voltage imbalance and constructional imperfections can generate them in the healthy practical machine. Moreover, the changing air gap due to the stator and rotor slot openings also contribute to the production of PSH2. The following is the list of crucial factors that can have a direct influence on the presence and the amplitude of PSH components;

- Stator and rotor MMF
- Slot permeance functions
- Material saturation (flux fringing, rotor bridges)

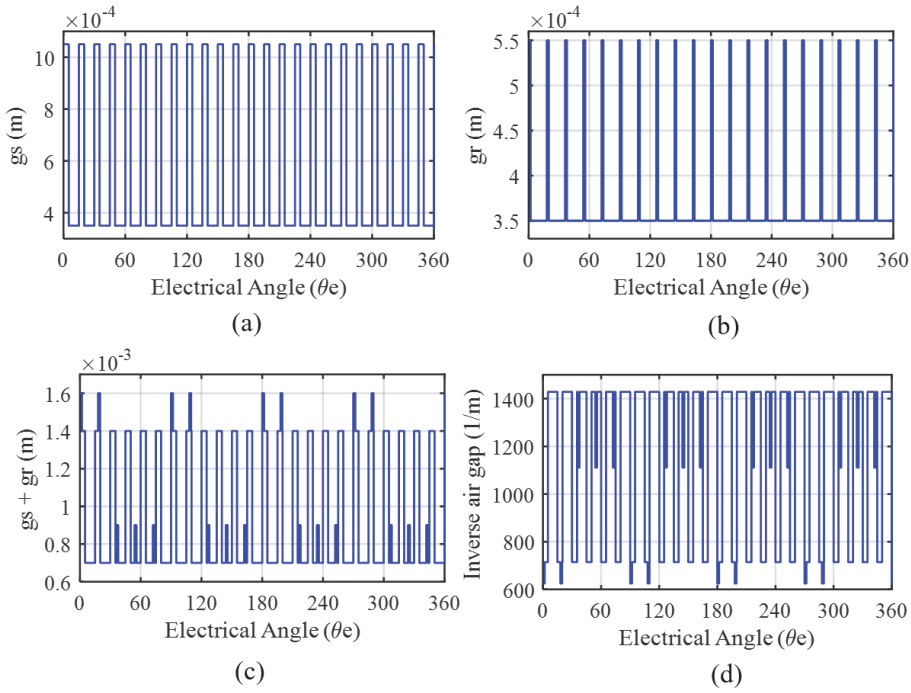


FIGURE 3. The air gap function of (a) the stator (gs), (b) the rotor (gr), (c) the net equivalent (gs+gr), and (d) the inverse air gap function at a specific rotor position.

- Slots skew
- Machine asymmetry (inherent eccentricity, unbalanced stator windings etc.)
- Unbalanced supply voltages

V. THE AIR-GAP AND WINDING FUNCTIONS

$$g_s(\theta e) = \begin{cases} r_g + h_{11}, & 0 \le \theta e \le B_{11} \\ r_g, & B_{11} < \theta e \le (B_{11} + B_{tt}), \end{cases} \quad (20)$$

$$g_r(\theta e, \alpha) = \begin{cases} r_g + h_{21}, & 0 \le \theta e \le B_{21} \\ r_g, & B_{21} < \theta e \le (B_{11} + B_{rt}), \end{cases} \quad (21)$$

The stator and rotor slot openings are the main reasons of the non-uniform air gap. From the air gap mid-point, the stator g_s (θe) and rotor g_r (θe, α) associated air gaps with the inclusion of slot openings can be defined using conditional analytical expressions.

Where B_{11}, B_{tt}, B_{21}, B_{rt}, h_{11}, h_{21}, r_g are the width (in terms of angle) of the stator slot opening, stator tooth tip, rotor slot opening, rotor tooth tip, stator slot depth without winding, the rotor bar depth, and the height of air gap centre respectively. The geometrical description of the stator and rotor slots can be found in [25].

The total air gap is the sum of both air gaps and changes with moving rotor, as shown in Figure (3). The extended lines in the total and the inverse air gaps are the locations where stator and rotor slot openings coincide with each other.

Similarly, the stator and rotor winding functions can be defined. Again, the stator winding function is stepped distributed, and on the rotor side, each pair of subsequent rotor bars represent each rotor phase, as shown in Figure (4).

VI. SIMULATION RESULTS

Each rotor segment produces the inductance profile similar to the adjacent segment but shifted by a specific number of samples described in equation (14).

The number of samples depends upon the number of samples per segment. Moreover, the number of shifted copies of the inductance profile depends upon the number of rotor segments. Figure 5 (a) shows the stator-rotor mutual inductance as the function of rotor position while the entire rotor is divided into four equally spaced segments. All shifted copied of the inductance profile will remain within the skew angle equal to one stator slot pitch in the motor under investigation. Since all segments are axially connected, the total inductance will be equal to the sum of all individual vectors. The final inductance profile tends to become smooth as the skew angle is introduced, as shown in Figure 5 (b). Figure 5 (a)-(b) intends to describe slot-related ripples' attenuation in the inductance profile as the skewed bar is considered. However, the length is taken as constant in all cases until this point for ease of understanding.

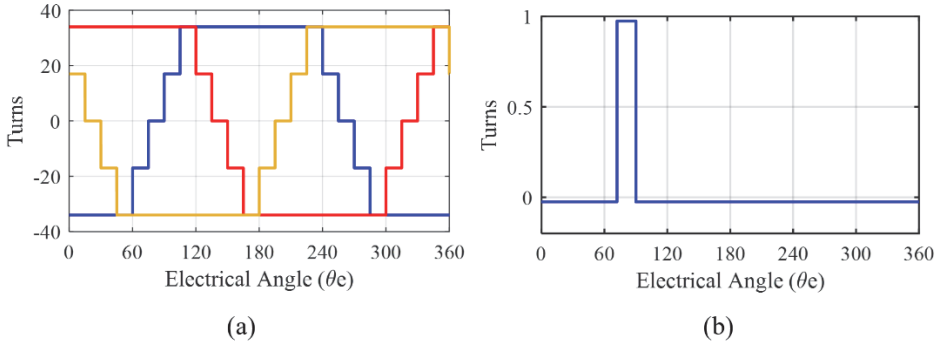


FIGURE 4. The winding functions (a) a three-phase stator, (b) one loop of the rotor.

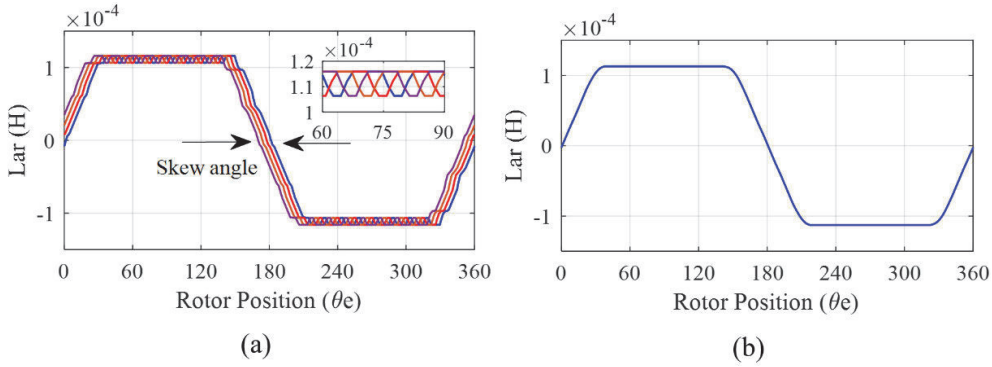


FIGURE 5. The stator-rotor mutual inductance, (a) for each segment (4 segments), (b) the final inductance.

Figure (6) shows the smoothing of all inductances with the inclusion of rotor slot skew. For comparison, the rotor is initially considered as a single piece without any skew. Then the rotor core is axially divided into forty equal segments with slot skew angle equal to one stator slot pitch. The blue line shows the inductance behaviour with the stepping rotor by considering it as non-skewed. The red lines show the smoothing of the inductance profiles when the skew is considered. The inductance profiles not only increases the smoothness but also reduce the peak-to-peak ripple magnitude. Since the machine has 48 stator slots, 40 rotor slots and 4 poles, the number of cycles of changing inductance till 120 degrees electrical angle are 8 on rotor-rotor and about 6.67 on stator-stator related inductances. However, the total number of cycles is 40 in stator related while 48 in rotor related inductances. The design parameters, such as winding functions and air-gaps, are defined by the vectors, each having a size equal to 10 × Qs × nb (19200). The vector size equal to the integral multiple of the number of stator and rotor slots avoids the problems of fractional number while implementing the equations. The rotor step size is equal to one sample, which corresponds to 0.0375 degrees electrical, giving better resolution.

The corresponding derivatives are shown in Figure (7), where it is evident that the rate of change of inductances with respect to the rotor position decreases significantly with the inclusion of rotor slot skew. The rate of changing inductances can be further reduced by increasing the skew angle.

The simulated phase currents with non-skewed and skewed rotor bars are shown in Figure (8) (a) and (b), respectively. In both cases, the pre-saved inductance matrices are used in an online environment. The simulation is performed with 19200 rotor steps equal to ten times the number of stator and rotor slots. As already discussed, the selection of an appropriate number of rotor steps is very crucial for simulation without any error. The number of rotor steps should be such that; it is divisible with the number of stator slots; it is divisible with the number of rotor bars—otherwise, any fractional value while calculating samples per slot pitch will lead to an error. Moreover, the number of rotor segments should equally divide the number of samples corresponding to the skew angle. All these conditions can be achieved by considering the rotor steps equal to "k" times the number of stator and rotor slots (21). The rotor slot skew based reduction in torque ripples is shown in Figures (8) (c) and (d). While for better comparison both skewed and non-skewed rotor based

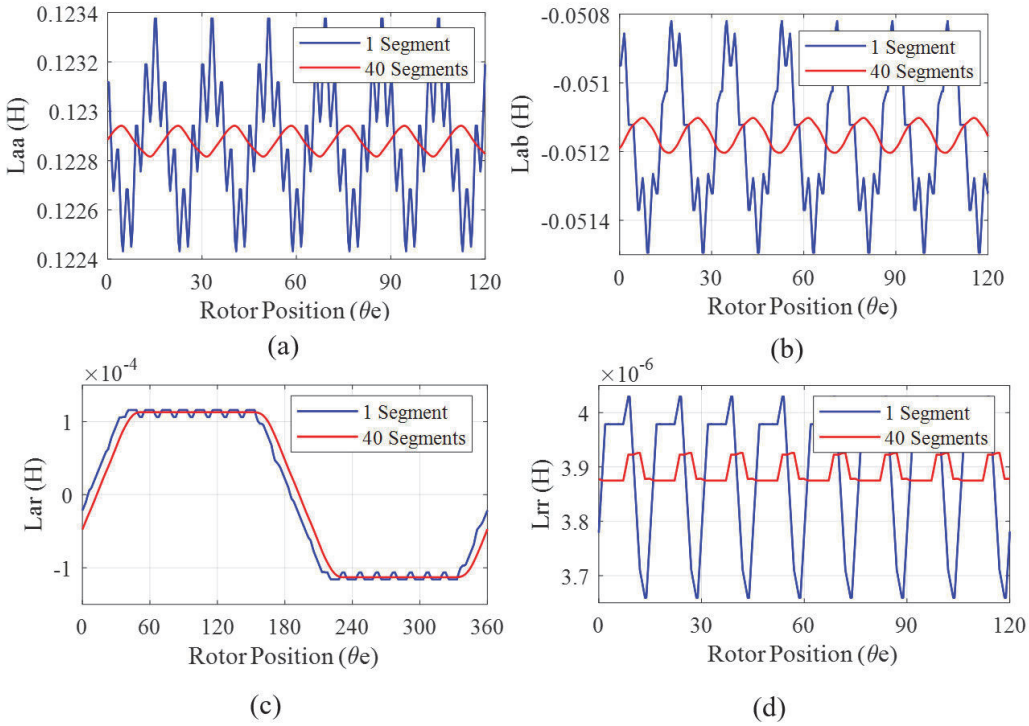


FIGURE 6. The calculated inductances with (red) and without (blue) rotor slots skew, (a) stator to stator self (Laa), (b) stator to stator mutual (Lab), (c) stator to the rotor (Lar), and (d) rotor to rotor (Lrr) concerning the rotor position.

torque profiles are shifted across the zero line.

$$f_s = k \times Q_s \times n_b; \quad k = 1, 2, 3, \ldots. \tag{22}$$

The simulated currents are much smoother with a skewed rotor than the corresponding rotor with non-skewed rotor bars. It is due to the attenuation of the PSH harmonics, as shown in Figure (9). In the machine under investigation with 40 rotor bars, two pole pairs, zero dynamic eccentricity, and 0.0067 slip, the PSH1 and PSH2 components will develop at 883 Hz and 983 Hz theoretically according to the equation (17). The machine is a PSH machine as it holds the equality given by equation (19). Both harmonics are attenuated from 0.04922 A and 0.0617 A to 0.00398 A and 0.00914 A, respectively while the same Hamming window is used for all cases.

Although, the skew angle attenuates the PSH components quite significantly. It should be appropriately optimized as, on the one hand, it attenuates the high-frequency components, but on the other hand, it decreases the machine power. Table 1 shows the impact of rotor bar skews in terms of stator slot pitch. It is clear that with the increase in the slot skew, the amplitude of PSH components decreases but slip increases with constant load. Similarly, the mean generated torque reduces under constant slip conditions. Therefore, the best practice is to make skew angle equal to one stator slot pitch as it is in the machine under investigation.

TABLE 1. The effect of slot skew on slip and generated torque.

Skew angle/slot pitch	RSH1 (Hz)	RSH2 (Hz)	Mean torque (N-m) for S=0.0667	Slip for the load (125N-m)
0	0.04249	0.06170	121.56	0.0667
1	0.00398	0.00914	119.95	0.0691
2	0.00215	0.00727	113.50	0.0752
3	0.00204	0.00625	99.55	0.1342
4	0.00142	0.00460	81.07	unstable

TABLE 2. The development of PSH with skewed rotor.

Simulation slip	RSH1 (Hz)	RSH2 (Hz)	RSH1 (A)	RSH2 (A)
0.0030	946.96	1047	0.00047	0.0005
0.035	914.90	1015	0.00231	0.0048
0.05	899.90	1000	0.00332	0.0068
0.0667	883.17	983.27	0.00454	0.0075

It is worth mentioning here that the current spectrum in Figures 9 and 10 are of phase current that is why both PSH1 and PSH2 components are visible. However, in the case of a perfectly symmetrical machine with a balanced supply PSH2 component will disappear from the line current.

As described by equation (17), the slotting harmonics are the function of slip in terms of frequency and amplitude. Figure (10) shows the movement of these components as the slip increases from 0.0030 to 0.05. The skew in

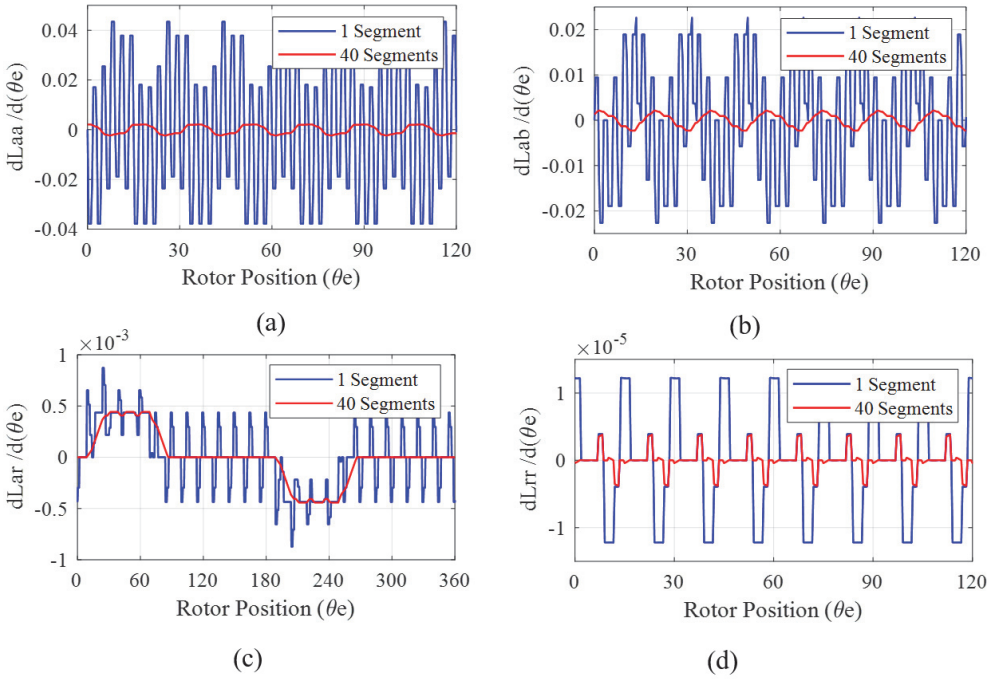


FIGURE 7. The derivative of the inductances with (red) and without (blue) rotor slot skews (a) stator to stator self (Laa), (b) stator to stator mutual (Lab), (c) stator to the rotor (Lar), and (d) rotor to rotor (Lrr) with respect to the rotor position.

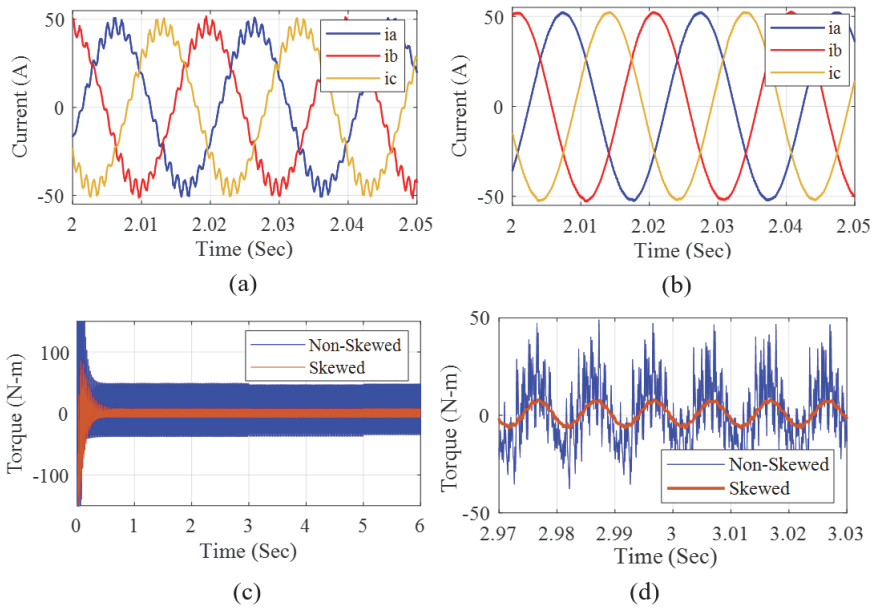


FIGURE 8. The stator currents with the rotor in (a) 2D without slot skew, (b) 3D with slot skew equal to one stator slot pitch, (c) the comparison of torque profile with and without rotor slot skews, (d) the zoomed comparison of torque profile with and without skews.

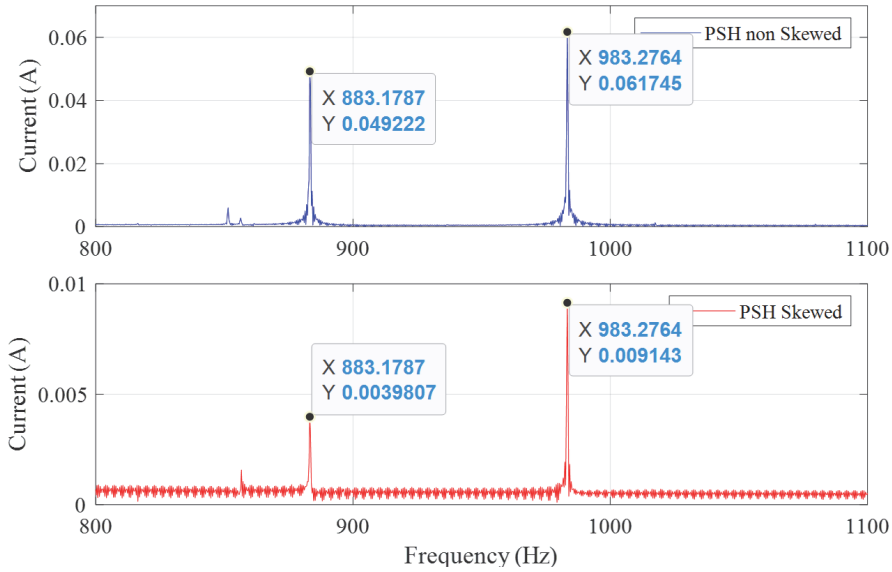


FIGURE 9. The development of PSH1 and PSH2 with and without slot skew in phase current.

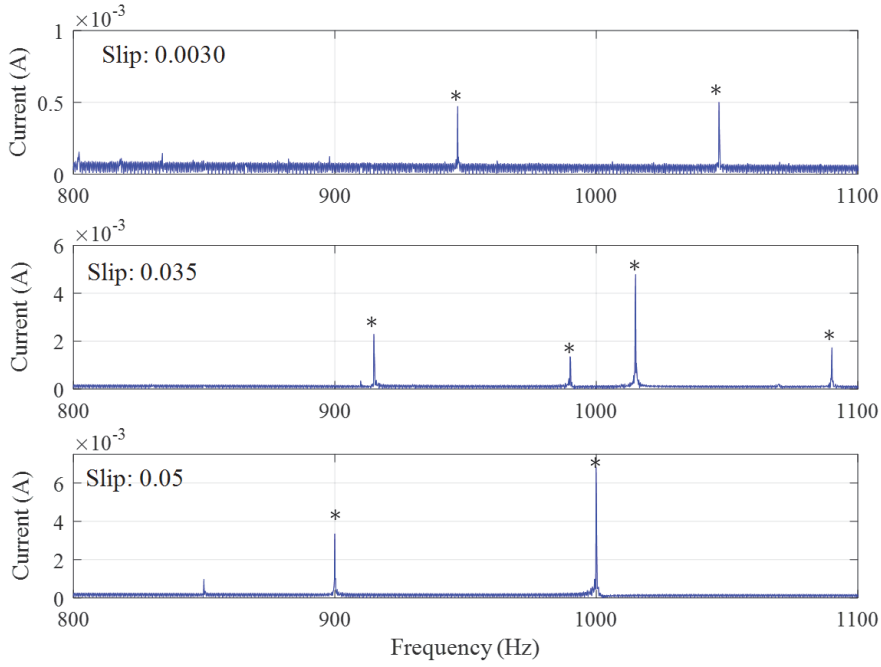


FIGURE 10. The development of PSH1 and PSH2 with skewed rotor bars while the PSH2 is present because the phase current is taken into consideration here.

slots changes the rotor winding function, which affects the PSH1 component while the PSH2 is very prominent here because the phase currents are considered. The frequency and amplitude of fundamental slotting harmonics are given in table 2.

In the line currents, the PSH2 components are cancelled out as shown in Figure (11). The development of PSH2 in the line current depends upon the non-linear behaviour of the magnetic material, local saturation on tooth tips, the fringing effects, any asymmetry in machine and supply unbalances.

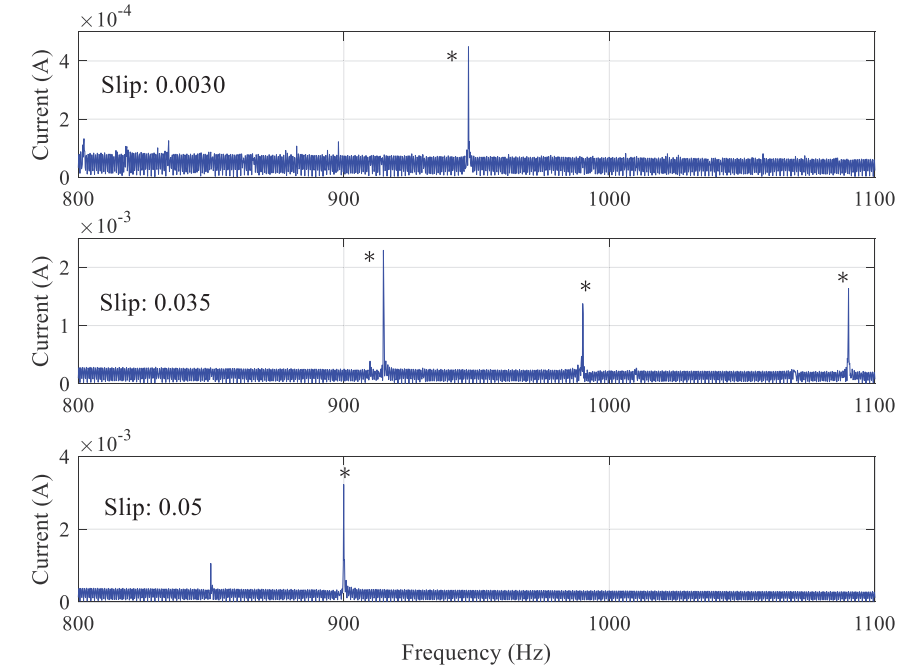


FIGURE 11. The development of PSH1 and cancellation of PSH2 with skewed rotor bars as the line currents are considered here while the supply is perfectly balanced.

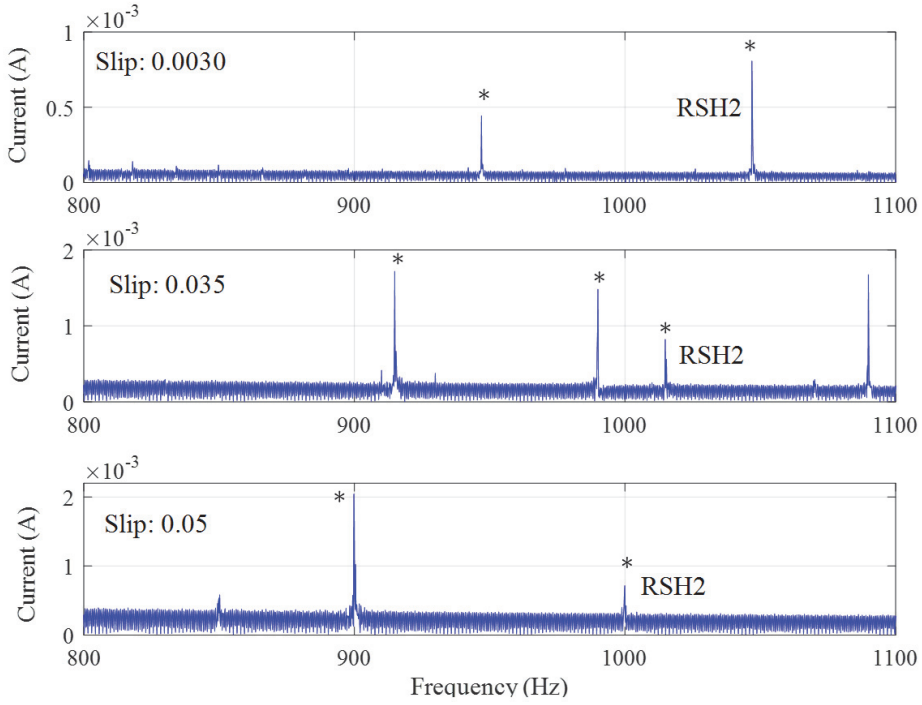


FIGURE 12. The development of PSH2 when the supply is made unbalanced according to the measured voltages from the supply side given in table 3.

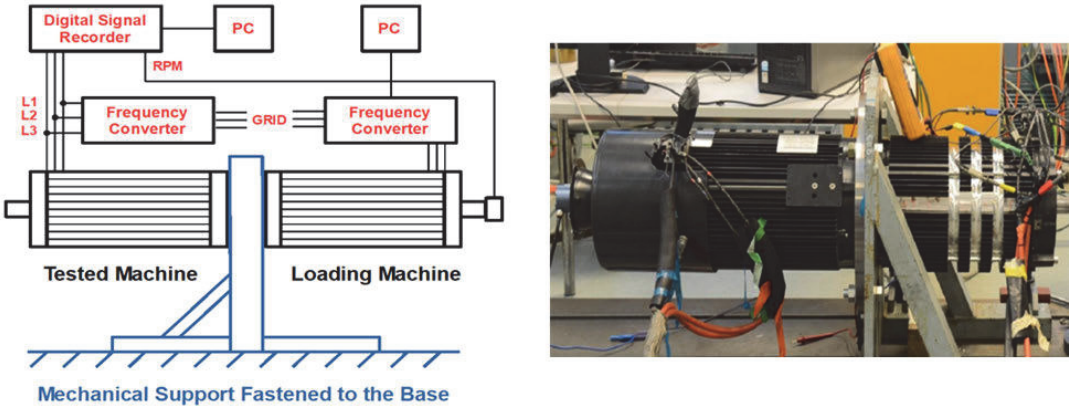


FIGURE 13. The experimental setup, block diagram (left), test rig (right).

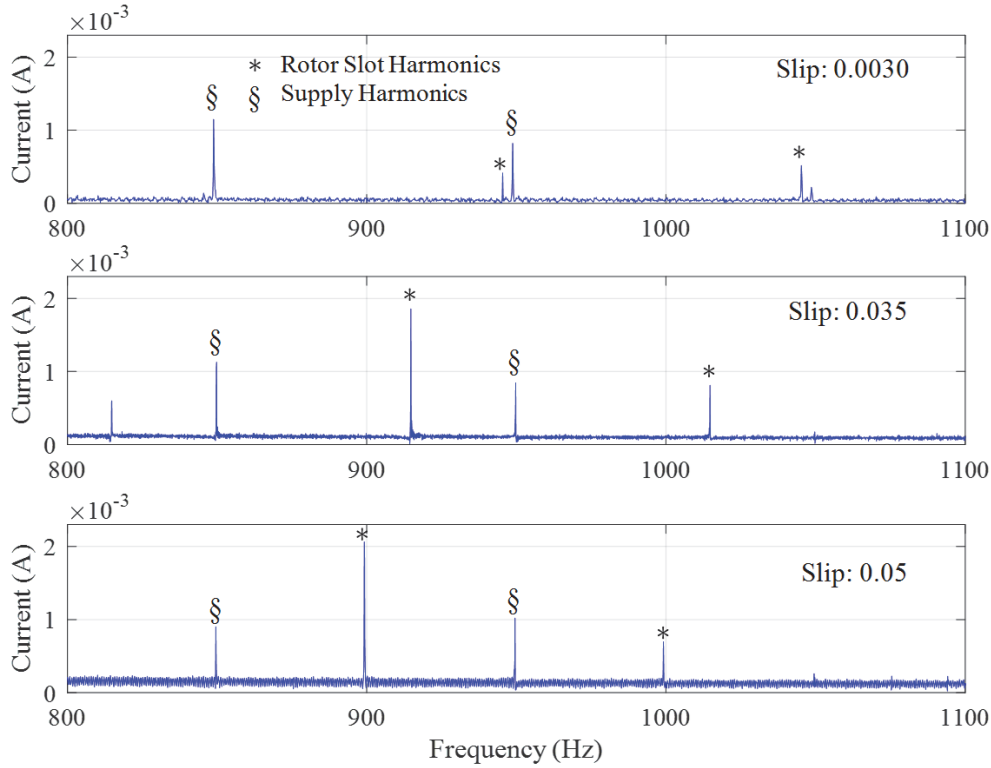


FIGURE 14. The PSH1 and PSH2 in practical measurements.

The tooth tip saturation and flux fringing effects can be simulated by reducing the height of stator and rotor slot openings however are neglected here. The development of the PSH2 component due to unbalanced supply is shown in Figure (12). For better understanding, the supply voltage in simulation is made the same as measured from the practical setup.

VII. PRACTICAL SETUP AND RESULTS

For experiments and measurements, a test rig is prepared, consisting of two identical motors coupled back to back as shown in Figure 13. One machine is under investigation while the other is acting as a load. Both machines are mounted on the same mechanical base and coupled through their shafts. The loading machine is fed through the inverters

TABLE 3. The supply based negative and zero sequence voltages.

slip	Va (V)	Vb (V)	Vc (V)	Zero seq. (V)	+ive seq. (V)	-ive seq. (V)
0.0030	191.747	190.256	190.522	0.557	188.711	0.557
0.035	192.436	191.155	187.878	1.233	188.241	1.235
0.05	194.418	189.331	191.131	1.533	188.765	1.533

TABLE 4. The development of PSH with skewed rotor in practical measurement.

Sr. No.	Parameter	Symbol	Value
1	Rated speed	N_r	1400 rpm@50 Hz
2	Rated power	P_r	18 kW@50 Hz
3	Connection	Y, Δ	Star (Y)
4	Power factor	cosφ	0.860
5	Number of poles	P	4
6	Number of rotor bars skewed	N_{rb}	40
7	Number of stator slots	Ns	48

TABLE 5. The development of PSH with skewed rotor in practical measurement.

Slip (Healthy)	RSH1 (Hz)	RSH2 (Hz)	RSH1 (A)	RSH2 (A)
0.0030	945.40	1045.20	0.00042	0.0005
0.035	914.76	1014.76	0.00189	0.0008
0.05	899.23	999.21	0.00233	0.0007

to improve its controllability for various load levels. Grid feeds the machine under investigation. The stator currents and voltages are measured using the Dewetron transient recorder. The measured signals' sampling frequency is 10 kHz, and the measurement time is 70 seconds, giving an excellent resolution of the frequency spectrum. The selection of appropriate sampling frequency also reduces the problems related to aliasing and mirror frequency components. The quality of supply voltage in the sense of negative and zero sequence components is presented in Table 3.

The negative sequence components result is flux rotating in opposite direction to the main flux. It results in the development of the RSH2 component with a corresponding increase in speed and torque ripples. The specifications of the machine under investigation are given in table 4.

The most prominent causes of current harmonics in induction machines are; supply, winding and inherent eccentricity based harmonics. Moreover, since both machine and its supply are not ideal, the factors such as, negative sequence currents generating reverse rotating field, the material local saturation points, flux fringing, the stator winding asymmetry, the skinning and proximity effects, the thermal effects on the resistance and leakage flux can also affect the slotting harmonics. As discussed earlier, most of these factors affect the PSH2 component quite significantly. This is why PSH2 is lower in amplitude than the PSH1 component, as described in Figure (14) and table 5.

The simulation results are in a very good agreement with the practical results. The RSH1 components obtained from simulation have almost same amplitude as the ones obtained from the practical measurements. However, a slight difference in RSH2 is due to neglecting the non-linear behaviour of magnetic material and local saturation of stator and rotor tooth tips. The material saturation can be included by using the B-H curve as a lookup table in the online section of the model, while local saturation can be incorporated by modulating the air gap and can be considered as future work in this domain.

VIII. CONCLUSION

A new approach for the modelling of a skewed rotor based squirrel cage induction motor has been presented in this paper. The conversion of a 2D continuous integration based winding function to a 3D discrete mean value equation, the definition of the air gap and winding functions using conditional analytical expressions and the inclusion of rotor slots skew are the crucial features of the proposed model.

For implementation, the model is divided into offline and online portions. All inductances and resistances are calculated as a function of rotor position in the offline portion, and results are saved in the 3D lookup table. The pre-saved results are then used in the online portion for the simulation of the performance parameters. By doing so, the offline calculations do not need to be calculated in the online portion, which decreases the simulation time considerably. As discussed in [25], the proposed model takes only three minutes per segment for the offline calculations while the online section takes only a few seconds to simulate the global parameters of the motor. This fact makes the model a good candidate for model-dependent condition monitoring algorithms. In comparison the FEM models can take several days to simulate the machine in 3D. In the light of the results and discussion following are the concluding remarks of the model.

- Since the model considers all design parameters as conditional analytical expressions, it is suitable for analyzing machine under various healthy and faulty scenarios. The fault cases may include broken rotor bars, broken end rings, static and dynamic eccentricity and stator short circuits.
- Since the model takes negligible simulation time compared to the corresponding FEM models, it is suitable for model-dependent fault diagnostic algorithms and drives where sensor-less speed estimation is required. The location of PSH components can be used for the estimation of slip without speed sensors.
- The transformation of the conventional integration based winding function formula to discrete mean value equation reduces the simulation time and computational complexity. Moreover, the integration constant related issues are also resolved.

- Unlike conventional winding function-based models where the harmonics are defined using Fourier series, the proposed model considers the design parameters and calculate the performance parameters. Thus, this approach reduces the problems of self-defined number, frequency and amplitude of current harmonics.
- *Most importantly*, the model can incorporate axial asymmetries in the machine, the rotor slot skews can be easily simulated. It is observed that with skewed rotor bars, the PSH has quite a different amplitude, which is impossible to study using conventional winding function based 2D models. The same is true in the case of 2D FEM models. Moreover, the 3D FEM models are computationally so intense that they do not remain suitable for model-dependent fault diagnostic algorithms and drives.
- It is observed that the PSH1 depends upon the winding configurations while PSH2 depends upon material, design and supply related asymmetries.
- The supply based negative sequence currents play a significant role in the development of PSH2 with the resultant increase in the speed and torque ripples.

As the model is suitable for the implementation of almost all faults and can simulate the results in negligible time as compared to the FEM models. With its increased applicability to incorporate axial asymmetry, it can be a very good choice for model-dependent fault diagnostic techniques.

REFERENCES

[1] B. Asad, T. Vaimann, A. Belahcen, A. Kallaste, A. Rassõlkin, and M. N. Iqbal, "Broken rotor bar fault detection of the grid and inverter-fed induction motor by effective attenuation of the fundamental component," *IET Electr. Power Appl.*, vol. 13, no. 12, pp. 2005–2014, Dec. 2019.

[2] M. Ojaghi, R. Aghmasheh, and M. Sabouri, "Model-based exact technique to identify type and degree of eccentricity faults in induction motors," *IET Electr. Power Appl.*, vol. 10, no. 8, pp. 706–713, Sep. 2016.

[3] G. Trejo-Caballero, H. Rostro-Gonzalez, R. de Jesus Romero-Troncoso, C. H. Garcia-Capulin, O. G. Ibarra-Manzano, J. G. Avina-Cervantes, and A. Garcia-Perez, "Multiple signal classification based on automatic order selection method for broken rotor bar detection in induction motors," *Elect. Eng.*, vol. 99, no. 3, pp. 987–996, 2017.

[4] R. H. C. Palácios, I. N. da Silva, A. Goedtel, and W. F. Godoy, "A novel multi-agent approach to identify faults in line connected three-phase induction motors," *Appl. Soft Comput.*, vol. 45, pp. 1–10, Aug. 2016.

[5] M. O. Mustafa, D. Varagnolo, G. Nikolakopoulos, and T. Gustafsson, "Detecting broken rotor bars in induction motors with model-based support vector classifiers," *Control Eng. Pract.*, vol. 52, pp. 15–23, Jul. 2016.

[6] V. Ghorbanian and J. Faiz, "A survey on time and frequency characteristics of induction motors with broken rotor bars in line-start and inverter-fed modes," *Mech. Syst. Signal Process.*, vols. 54–55, pp. 427–456, Mar. 2015.

[7] S. H. Saïd, M. F. Mimouni, F. M'Sahli, and M. Farza, "High gain observer based on-line rotor and stator resistances estimation for IMs," *Simul. Model. Pract. Theory*, vol. 19, no. 7, pp. 1518–1529, Aug. 2011.

[8] A. Sapena-Bano, F. Chinesta, M. Pineda-Sanchez, J. V. Aguado, D. Borzacchiello, and R. Puche-Panadero, "Induction machine model with finite element accuracy for condition monitoring running in real time using hardware in the loop system," *Int. J. Elect. Power Energy Syst.*, vol. 111, pp. 315–324, Oct. 2019.

[9] M. Jemli, H. B. Azza, and M. Gossa, "Real-time implementation of IRFOC for single-phase induction motor drive using dSpace DS 1104 control board," *Simul. Model. Pract. Theory*, vol. 17, no. 6, pp. 1071–1080, Jul. 2009.

[10] M. D. Prieto, G. Cirrincione, A. G. Espinosa, J. A. Ortega, and H. Henao, "Bearing fault detection by a novel condition-monitoring scheme based on statistical-time features and neural networks," *IEEE Trans. Ind. Electron.*, vol. 60, no. 8, pp. 3398–3407, Aug. 2013.

[11] V. Mukherjee, M. F. Far, F. Martin, and A. Belahcen, "Constrained algorithm for the selection of uneven snapshots in model order reduction of a bearingless motor," *IEEE Trans. Magn.*, vol. 53, no. 6, pp. 1–4, Jun. 2017.

[12] M. F. Far, F. Martin, A. Belahcen, P. Rasilo, and H. A. A. Awan, "Real-time control of an IPMSM using model order reduction," *IEEE Trans. Ind. Electron.*, vol. 68, no. 3, pp. 2005–2014, Mar. 2021.

[13] M. F. Far, F. Martin, A. Belahcen, L. Montier, and T. Henneron, "Orthogonal interpolation method for order reduction of a synchronous machine model," *IEEE Trans. Magn.*, vol. 54, no. 2, pp. 1–6, Feb. 2018.

[14] G. M. Joksimovic and J. Penman, "The detection of inter-turn short circuits in the stator windings of operating motors," *IEEE Trans. Ind. Electron.*, vol. 47, no. 5, pp. 1078–1084, Oct. 2000.

[15] J. Milimonfared, H. M. Kelk, S. Nandi, A. D. Minassians, and H. A. Toliyat, "A novel approach for broken-rotor-bar detection in cage induction motors," *IEEE Trans. Ind. Appl.*, vol. 35, no. 5, pp. 1000–1006, Sep. 1999.

[16] H. A. Toliyat and T. A. Lipo, "Transient analysis of cage induction machines under stator, rotor bar and end ring faults," *IEEE Trans. Energy Convers.*, vol. 10, no. 2, pp. 241–247, Jun. 1995.

[17] H. A. Toliyat, T. A. Lipo, and J. C. White, "Analysis of a concentrated winding induction machine for adjustable speed drive applications. I. Motor analysis," *IEEE Trans. Energy Convers.*, vol. 6, no. 4, pp. 679–683, Dec. 1991.

[18] H. A. Toliyat, T. A. Lipo, and J. C. White, "Analysis of a concentrated winding induction machine for adjustable speed drive applications. II. Motor design and performance," *IEEE Trans. Energy Convers.*, vol. 6, no. 4, pp. 684–692, Dec. 1991.

[19] A. M. El-Refaie, T. M. Jahns, and D. W. Novotny, "Analysis of surface permanent magnet machines with fractional-slot concentrated windings," *IEEE Trans. Energy Convers.*, vol. 21, no. 1, pp. 34–43, Mar. 2006.

[20] J. Faiz and I. Tabatabaei, "Extension of winding function theory for nonuniform air gap in electric machinery," *IEEE Trans. Magn.*, vol. 38, no. 6, pp. 3654–3657, Nov. 2002.

[21] S. Nandi, "Modeling of induction machines including stator and rotor slot effects," *IEEE Trans. Ind. Appl.*, vol. 40, no. 4, pp. 1058–1065, Jul. 2004.

[22] H. A. Toliyat, M. S. Arefeen, and A. G. Parlos, "A method for dynamic simulation of air-gap eccentricity in induction machines," *IEEE Trans. Ind. Appl.*, vol. 32, no. 4, pp. 910–918, Jul./Aug. 1996.

[23] J. Faiz and M. Ojaghi, "Unified winding function approach for dynamic simulation of different kinds of eccentricity faults in cage induction machines," *IET Electr. Power Appl.*, vol. 3, no. 5, p. 461, 2009.

[24] A. Marfoli, P. Bolognesi, L. Papini, and C. Gerada, "Mid-complexity circuital model of induction motor with rotor cage: A numerical resolution," in *Proc. 13th Int. Conf. Electr. Mach. (ICEM)*, Sep. 2018, pp. 277–283.

[25] B. Asad, T. Vaiman, A. Belahcen, A. Kallaste, A. Rassolkin, and M. N. Iqbal, "Modified winding function-based model of squirrel cage induction motor for fault diagnostics," *IET Electr. Power Appl.*, vol. 14, pp. 1–11, May 2020.

[26] M. Harir, A. Bendiabdellah, A. Chaouch, and N. Benouzza, "Modelling of induction motor including skew effect using MWFA for performance improvement," *Int. J. Elect. Comput. Eng.*, vol. 7, no. 12, pp. 1737–1743, Jan. 2014.

[27] J. M. Gojko, D. D. Momir, and O. B. Aleksandar, "Skew and linear rise of MMF across slot modelling-winding function approach," *IEEE Trans. Energy Convers.*, vol. 14, no. 3, pp. 315–320, Sep. 1999.

[28] S. Nandi, S. Ahmed, and H. A. Toliyat, "Detection of rotor slot and other eccentricity related harmonics in a three phase induction motor with different rotor cages," *IEEE Trans. Energy Convers.*, vol. 16, no. 3, pp. 253–260, Sep. 2001.



BILAL ASAD (Member, IEEE) was born in Pakistan, in 1986. He received the B.Sc. degree in electronics engineering from The Islamia University of Bahawalpur, in 2007, the M.Sc. degree in electrical engineering from the University of Engineering and Technology (UET) Lahore, Pakistan, in 2011, and the Ph.D. degree under cotutelle dual degree program from the Department of Electrical Power Engineering and Mechatronics, Tallinn University of Technology, Estonia, and the Department of Electrical Engineering and Automation, Aalto University, Espoo, Finland, in 2021. His research interests include signal processing, design, modeling, and fault diagnostics of electrical machines.



TOOMAS VAIMANN (Senior Member, IEEE) was born in Pärnu, Estonia, in 1984. He received the B.Sc., M.Sc., and Ph.D. degrees in electrical engineering from the Tallinn University of Technology, Estonia, in 2007, 2009, and 2014, respectively.

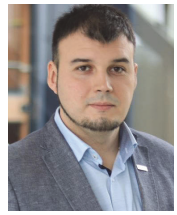
He is currently a Senior Researcher with the Department of Electrical Engineering, Tallinn University of Technology. Internationally, he has been a Postdoctoral Researcher with the Department of Electrical Engineering and Automation, Aalto University, Espoo, Finland, and works as a Visiting Professor with the Faculty of Control Systems and Robotics, ITMO University, St. Petersburg, Russia. He has been working in several companies as an Electrical Engineer. He is a member of Estonian Society of Moritz Hermann Jacobi and Estonian Society for Electrical Power Engineering. His research interest includes diagnostics of electrical machines.



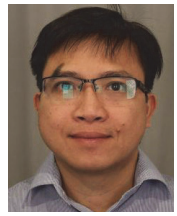
ANOUAR BELAHCEN (Senior Member, IEEE) is currently a Professor in computational electromechanics with Aalto University, Finland. He has authored or coauthored more than 90 journal articles and several conference papers, many of them are the results of joint international cooperation, e.g., with French, German, Austrian, Spanish, Italian, Belgian, Portuguese, and Chinese research groups. His research interests include numerical modeling of electrical machines, magnetic materials characterization and modeling, coupled magneto-mechanical problems, magnetic forces and magnetostriction, iron losses, and fault diagnostics of electrical machines. He is a Senior Member of the IEEE Society and a member of the first Board (AdCom) of the ICEM NPO, which manages the ICEM conferences and a member of the ICS board, which manages the COMPUMAG conference. He is a regular participant in the major conferences in his field, including COMPUMAG, CEFC, ICEM and SDEMPED, where he has been acting as the Session Chair and Track Chair. At the university level, he is the Deputy Head of his department and the Director of the Master's Programme in automation and electrical engineering with more than 100 students entering the programme each year. He is also the Deputy Head of the Quality of Education Committee (QEC), responsible for the assessment of teaching and learning. Besides his work at Aalto University, he has been working as an Invited Professor with the Tallinn University of Technology, Estonia, since 2011, where he has been teaching subject related to electrical machines and supervising Ph.D. and postdoctoral researchers.



ANTS KALLASTE (Senior Member, IEEE) was born in Pärnu, Estonia, in 1980. He received the B.Sc., M.Sc., and Ph.D. degrees in electrical engineering from the Tallinn University of Technology, Estonia, in 2004, 2006, and 2013, respectively. He is currently a Professor in electrical machines with the Department of Electrical Power Engineering and Mechatronics, Tallinn University of Technology. In addition, he is holding the position of the Head of Chair of the Electrical Machines Research Group. He is a member of the Estonian Society of Moritz Hermann Jacobi.



ANTON RASSOLKIN (Senior Member, IEEE) was born in Tallinn, Estonia, in 1985. He received the B.Sc., M.Sc., and Ph.D. degrees in electric drives and power electronics from the Tallinn University of Technology, Estonia, in 2008, 2010, and 2014, respectively, and the Dipl.-Ing. degree in automatic from the University of Applied Science Giessen-Friedberg, Germany, in 2010.



HUYNH VAN KHANG (Senior Member, IEEE) received the B.Sc. degree in electrical engineering from the Ho Chi Minh City University of Technology, Ho Chi Minh City, Vietnam, in 2002, the M.Sc. degree in electrical engineering from Pusan National University, Busan, South Korea, in 2008, and the D.Sc. (Tech.) degree in electrical engineering from Aalto University, Espoo, Finland, in 2012.

He was an Associate Professor in electrical power engineering with the University of Agder, Grimstad, Norway, from 2013 to 2019, where he is currently a Professor with the Department of Engineering Sciences. His research interests include electrical machines, condition-based maintenance, and applied power electronics.



PAYAM SHAMS GHAHFAROKHI (Member, IEEE) was born in Iran, in 1986. He received the B.Sc. degree in electrical power engineering from IAUN, Iran, in 2010, the M.Sc. degree in electrical power engineering from Newcastle University, U.K., in 2011, and the Ph.D. degree in electrical engineering and machines from the Tallinn University of Technology, Estonia, in 2019. He is currently a Senior Researcher and a Postdoctoral Researcher with the Department of Electrical Machines and Apparatus, Riga Technical University, Latvia. His research interests include electromagnetic design and thermal management of PM and synchronous reluctance electrical machines.



MUHAMMAD U. NASEER (Member, IEEE) was born in Pakistan, in 1990. He received the B.Sc. degree in electrical engineering from the Islamia University of Bahawalpur, in 2011, and the M.Sc. degree from the University of Engineering and Technology (UET), Lahore, Pakistan. He is currently pursuing the Ph.D. degree with the Tallinn University of Technology. His research interests include electrical machines modeling, design, and optimization.



MUHAMMAD N. IQBAL (Member, IEEE) was born in Pakistan, in 1988. He received the B.Sc. degree in electronics engineering from the Islamia University of Bahawalpur, in 2008, the M.S. degree from the University of New South Wales, Australia, and the Ph.D. degree from the Tallinn University of Technology, in 2021. His research interests include energy consumption modeling and power quality.

Curriculum vitae

Personal data

Name:	Muhammad Usman Naseer
Date of birth:	01-12-1990
Place of birth:	Pakistan
Citizenship:	Pakistan

Contact data

E-mail:	muhammad.naseer@taltech.ee usman.naseer.eductaional@gmail.com

Education

2021–2025	**PhD**, Department of Electrical Power Engineering and Mechatronics, Tallinn University of Technology, Estonia
2014–2015	**PGTP**, Nuclear Power Plant Technology, CHASCENT-Chashma, Mianwali, Pakistan
2012–2017	**MSc**, Department of Electrical Engineering, University of Engineering and Technology, Lahore, Pakistan
2007–2011	**BSc**, Department of Electrical Engineering, The Islamia University of Bahawalpur, Pakistan

Language competence

English	Fluent
Estonian	Beginner
Urdu	Native
Punjabi	Native

Professional employment

2023–2025	Early-stage Researcher (1.00) Department of Electrical Power Engineering and Mechatronics, Tallinn University of Technology, Estonia
2015–2021	Senior Engineer (1.00) National Tokamak Fusion Program, Islamabad-Pakistan
2012–2014	Junior Lecturer (1.00) Department of Electrical Engineering, The Islamia University of Bahawalpur, Pakistan

Industrial Property

- A method for contouring an airgap profile in an electromagnetic device, Owners: Department of Electrical Power Engineering and Mechatronics, School of Engineering, Tallinn University of Technology, Authors: Muhammad Usman Naseer, Ants Kallaste, Toomas Vaimann, Priority number: P202500004, Priority date: 09.01.2025.

Projects

- PRG1827 “Additively Manufactured Electrical Machines” (01.01.2023−31.12.2027), Principal Investigator: Ants Kallaste, Tallinn University of Technology, School of Engineering, Department of Electrical Power Engineering and Mechatronics. Financier: Estonian Research Council
- LEEEV23104 “Consultation Services Agreement” (27.09.2023−27.09.2024); Principal Investigator: Toomas Vaimann, Tallinn University of Technology, School of Engineering, Department of Electrical Power Engineering and Mechatronics (coordinator), Financier: Private Company

Elulookirjeldus

Isikuandmed

Nimi:	Muhammad Usman Naseer
Sünniaeg:	01-12-1990
Sünnikoht:	Pakistan
Kodakondsus:	Pakistani

Kontaktandmed

E-post:	muhammad.naseer@taltech.ee usman.naseer.eductaional@gmail.com

Hariduskäik

2021–2025	**PhD**, Elektroenergeetika ja mehhatroonika instituut, Tallinna Tehnikaülikool, Estonia
2014–2015	**PGTP**, Tuumaelektrijaama tehnoloogia, CHASCENT-Chashma, Mianwali, Pakistan
2012–2017	**MSc**, Elektrotehnika osakond, Tehnika- ja Tehnoloogiaülikool, Lahore, Pakistan
2007–2011	**BSc**, Department of Electrical Engineering, The Islamia University of Bahawalpur, Pakistan

Keelteoskus

inglise keel	kõrgtase
eesti keel	algtase
urdu keel	emakeel
pandžabi keel	emakeel

Teenistuskäik

2023–2025	Nooremteadur (1.00) Elektroenergeetika ja mehhatroonika instituut, Tallinna Tehnikaülikool, Estonia
2015–2021	Vaneminsener (1.00) National Tokamak Fusion Program, Islamabad-Pakistan
2012–2014	Nooremlektor (1.00) Department of Electrical Engineering, The Islamia University of Bahawalpur, Pakistan

Tööstusomand

- Meetod õhupilu profiili profileerimiseks elektromagnetilises seadmes; Omanikud: Tallinna Tehnikaülikool, Tallinna Tehnikaülikool, Inseneriteaduskond, Elektroenergeetika ja mehhatroonika instituut; Autorid: Muhammad Usman Naseer, Ants Kallaste, Toomas Vaimann; Prioriteedi number: P202500004; Prioriteedi kuupäev: 09.01.2025.

Projektid

- PRG1827 “Kihtlisandustehnoloogial põhinevad elektrimasinad” (01.01.2023−31.12.2027); Vastutav täitja: Ants Kallaste; Tallinna Tehnikaülikool, Inseneriteaduskond, Elektroenergeetika ja mehhatroonika instituut; Finantseerija: Sihtasutus Eesti Teadusagentuur
- LEEEV23104 “Konsultatsiooniteenuste leping” (27.09.2023−27.09.2024); Vastutav täitja: Toomas Vaimann; Tallinna Tehnikaülikool, Inseneriteaduskond, Elektroenergeetika ja mehhatroonika instituut; Finantseerija: Eraettevõte

ISSN 2585-6901 (PDF)
ISBN 978-9916-80-302-8 (PDF)